UNIVERSITY OF TRENTO

Doctoral School in Civil, Environmental and Mechanical Engineering

Curriculum 3. Modelling and Simulation

Chiara Colombo

Development of a multiscale 1D-0D cardiovascular model to investigate orthostatic stress responses

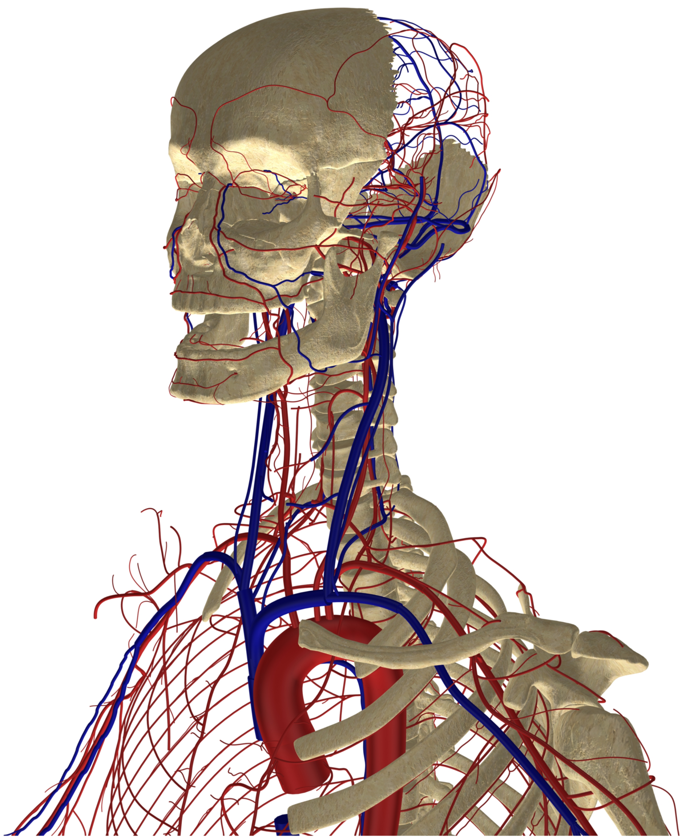

2025 - Doctoral thesis

UNIVERSITY OF TRENTO - Italy
Department of Civil, Environmental
and Mechanical Engineering

Doctoral School in Civil, Environmental and Mechanical Engineering
Curriculum 3. Modelling and Simulation - XXXVII cycle

Doctoral Thesis - January 2026

Chiara Colombo

Development of a multiscale 1D-0D cardiovascular model to investigate orthostatic stress responses

Supervisors
Annunziato Siviglia - University of Trento
Lucas Omar Müller - University of Trento

Credits of the cover image: Sansuke M. Watanabe (Blanco et al. (2015); Müller et al. (2023))

University of Trento
Doctoral School in Civil, Environmental and Mechanical Engineering
http://web.unitn.it/en/dricam
Via Mesiano 77, I-38123 Trento
Tel. +39 0461 282670 / 2611 - dicamphd@unitn.it

Summary

The study of orthostatic stress effects on the cardiovascular system has gained significant attention since the 1960s, initially driven by the space race, and more recently by advances in medicine and technology. The full extent of the physiological responses to orthostatic stress still remains not fully understood, owing to the complex interplay between multiple body systems and external factors that influence cardiovascular function. To address this complexity, increasingly sophisticated computational models of the cardiovascular system have been developed.

The accuracy of these models in reproducing physiological responses to orthostatic stress depends on the physical description of the problem, on the numerical methods used to approximate the solution, and on the representation of the physiological mechanisms involved. A clear and realistic formulation of the physical processes is essential for capturing the fundamental features of the modeled interactions. At the same time, numerical aspects can significantly influence the accuracy and reliability of simulations. Finally, the extent to which the model captures the complexity of regulatory responses directly impacts the model's ability to reflect real-world behavior under orthostatic stress.

This Ph.D. thesis tackles all these challenges, presenting an extension of the anatomically detailed arterial-venous network (ADAVN) model, a multiscale model originally developed to reproduce hemodynamics of the entire circulation with high anatomical fidelity. The ADAVN model comprises a unique 3D spatial characterization of both arterial and venous networks that captures the anatomical geometry of the human vasculature. Blood flow in these networks is described using partial differential equations (PDEs) in one-dimension (1D). In particular, it adopts a 1D blood flow model, where a viscoelastic tube law is used to represent the mechanics of the vessels' wall. To incorporate the effects of gravity, an additional term has been introduced in the governing equations of the 1D blood flow model, leading to a novel and unique cardiovascular model that accounts for gravitational influences in both arterial and venous networks based on vessels' geometrical properties.

The first part of this thesis focuses on examining how different parameterizations of selected tube laws alter the mathematical properties (namely hyperbolicity and genuine non-linearity of characteristic fields) of the considered 1D blood flow model. We investigate how constraining admissible parameter ranges influences the tube law's ability to fit human and ovine experimental data. Notably, we demonstrate that the viscoelastic tube law, employed in the ADAVN model, preserves the mathematical properties of the 1D blood flow model despite the imposed parametrization, making it a robust tool for further developments of the ADAVN model.

The second part of this thesis addresses the challenge of accurately computing the numerical solution of our model. To this end, we propose a well-balanced high-order

path-conservative numerical method capable of solving non-conservative hyperbolic PDEs. This method is able to describe steady-state solutions in presence of geometric- and algebraic-type source terms, as well as to correctly estimate transient solutions. Particularly, we show its crucial ability to accurately reproduce hydrostatic pressure distributions when applied to solve the 1D blood flow model with gravity in complex vascular networks.

The third part of this thesis is dedicated to the physiological aspects of the cardiovascular response to orthostatic stress. Due to the reduced availability of data on the venous system and the limited understanding of the regulatory mechanisms involved, we collaborated with a team of physiologists from the University of Auckland (New Zealand) to answer specific questions regarding the lack of venous data and the functioning of the regulatory mechanisms, aiming to clarify how these elements coordinate to regulate blood flow and pressure under different orthostatic conditions. We present the outcomes of this collaboration, detailing the design of an experiment to collect relevant physiological data in compliance with ethical and privacy standards. We describe the recruitment of volunteers, the data acquisition, and the processing of raw measurements into meaningful metrics for model validation. Notably, we underline that the collected data confirm existing findings in literature and provide new insights into the venous system and the regulatory mechanisms.

Finally, the last part of this thesis concentrates on simulating orthostatic stress using the extended ADAVN model. This application integrates all previously developed theoretical knowledge, numerical tools and incorporates the acquired experimental data. We detail the simulation setup and validate the obtained results. Furthermore, we identify the current limitations of the ADAVN model and highlight the aspects that require further refinement to capture the key physiological mechanisms involved in the cardiovascular response to orthostatic stress.

This thesis brings together multidisciplinary studies that represent an important first step towards the development of a cardiovascular model capable of reproducing essential physiological processes during postural transitions. The resulting framework offers a valuable tool for advancing our understanding of the cardiovascular system's response to orthostatic stress.

Acknowledgements

First and foremost, I would like to express my sincere gratitude to my supervisors, prof. Annunziato Siviglia and prof. Lucas O. Müller. Without your precious guidance, constant availability, and unwavering support, this work would not have been possible. Your expertise and encouragement have been fundamental throughout this journey, and I would not be where I am today without you. Thank you from the bottom of my heart.

I would also like to thank the reviewers, prof. Valerio Caleffi and prof. Leif R. Hellevik, for taking the time to carefully read my thesis and for providing valuable feedback and insightful comments that helped improve the quality of this work.

I wish to thank my parents, Vincenza and Giancarlo. Your unconditional love, patience, and constant encouragement have supported me in every step of my academic path and beyond. Thank you for always believing in me, for giving me the strength and motivation to pursue my goals, and for always being there for me. I would not be who I am today without you.

I would also like to thank my boyfriend Gabriele for his love, support, and understanding throughout this journey. Thank you for standing by my side during both the stressful and rewarding moments, for your encouragement, for your laughter that brightened even the most challenging moments, and for the joy and color you brought into my life during this time. Your presence made this experience lighter and more meaningful, and I am deeply grateful to have shared it with you.

I wish to thank my housemates, Davide, Sameer, Fiorenzo, Elisa and Tommaso, for their support and companionship throughout these years. Thank you for making our home a place of comfort, for the shared moments, conversations, and unforgettable parties that helped me disconnect from work and recharge. Your presence turned everyday life into a source of joy and made this period truly memorable.

I would also like to thank all my colleagues at DICAM and at the mathematics department, who over the past years have been not only office mates but also dear friends. Thank you for sharing this journey with me, for the stimulating discussions, mutual support, and countless moments of collaboration and laughter. Working alongside you made even the most demanding days more enjoyable and enriched both my academic experience and my personal growth.

I would also like to express my sincere gratitude to prof. Gonzalo D. Maso Talou and to all the colleagues I had the pleasure of working with during my visiting period at the Auckland Bioengineering Institute in New Zealand. Thank you for the warm welcome, the stimulating discussions, and the inspiring research environment. This experience was both professionally enriching and personally rewarding, and it significantly contributed to my growth as a researcher.

Finally, I would like to thank all the people I met along this journey, whether at conferences, workshops, or in everyday academic life. The exchanges of ideas, shared experiences, and meaningful connections have greatly enriched both my research and my personal path. I am also grateful to friends and to everyone who supported me in ways large or small and whom I may not have mentioned individually. Each of you contributed to this journey more than you know.

Funding

This work has been supported by the Italian Ministry of Education, Universities and Research (MUR), in the framework of the project DICAM-EXC (Departments of Excellence 2023-2027, grant L232/2016).

The author also acknowledges the financial support of the European Union under NextGenerationEU, Mission 4, Component 2 - PRIN 2022 (D.D. 104/22), project title: Immersed methods for multIscale and multiphysics problems, CUP: E53D2300592 0006.

Contents

Summary **i**

Acknowledgements **iii**

1 Introduction **1**

1.1 1D cardiovascular models 2

1.2 0D cardiovascular models 5

1.3 Multiscale 1D-0D cardiovascular models with gravity 7

1.4 Parametrization and validation of multiscale cardiovascular models with gravity 9

1.5 Objectives of this thesis 11

2 Tube law parametrization using in vitro data for one-dimensional blood flow in arteries and veins **13**

2.1 Introduction 14

2.2 Materials and Methods 16

2.2.1 Mathematical model for blood flow in collapsible tubes 16

2.2.2 The elastic model 17

2.2.2.1 Governing equations 17

2.2.2.2 Eigenstructure 18

2.2.2.3 Characteristic fields 20

2.2.3 The viscoelastic model 22

2.2.3.1 Governing equations 22

2.2.3.2 Eigenstructure 23

2.2.3.3 Characteristic fields 24

2.2.4 Tube law parameter estimation 25

2.2.4.1 In vitro data 25

2.2.4.2 Estimation procedure setup 27

2.3 Results 32

2.4 Discussion 32

2.4.1 Accuracy 32
2.4.2 Averaged estimated parameters 38
2.5 Conclusion 41

3 Well-balanced high-order method for non-conservative hyperbolic PDEs with source terms: application to one-dimensional blood flow equations with gravity 43
3.1 Introduction 44
3.2 Numerical method 46
3.2.1 Stationary solution identification 48
3.2.2 The well-balanced DET solver 48
3.2.3 Spatial reconstruction 51
3.2.4 Summary of the method 53
3.3 Numerical tests 54
3.3.1 Scalar case: Burgers' equation 54
3.3.2 System case: hyperbolized blood flow equations 56
3.3.2.1 Efficiency analysis for a single blood vessel (ICA test) 58
3.3.2.2 Empirical convergence rates for ICA test 60
3.3.2.3 Well-balance property for the ADAN86 geometry (deadman test) 60
3.3.2.4 Transient simulation for ADAN86 61
3.4 Discussion 64
3.5 Conclusion 66

4 Quantitative analysis of physiological responses to orthostatic stress during the head-up tilt test 69
4.1 Introduction 69
4.2 Methods 71
4.2.1 Ethical approval 71
4.2.2 Participants 71
4.2.3 Experimental protocol 72
4.2.4 Experimental measurements 73
4.2.5 Data analysis 75
4.3 Results 76
4.4 Discussion 76
4.4.1 Stroke volume 76

4.4.2 Cardiac output 77
4.4.3 Heart rate 79
4.4.4 Blood pressure 80
4.4.5 Cerebral inflow 82
4.4.6 Cerebral outflow 85
4.4.7 Peripheral arteries 89
4.4.8 Other blood vessels: femoral vein and inferior vena cava 92
4.4.9 Further considerations 93
4.5 Conclusion 94

5 Modeling cardiovascular responses to orthostatic stress 97
5.1 Introduction 97
5.2 Methodology 98
5.2.1 The ADAVN model: extension with gravity 98
5.2.2 Simulation setups 101
5.3 Results and discussion 103
5.3.1 Supine position simulations: Gravity vs. No gravity 104
5.3.2 Postural simulations: Supine vs. Upright 106
5.3.3 Upright position simulations: Effects of manual calibration 110
5.4 Conclusion 115

6 Conclusion 119
6.1 Mathematical formulation of the tube law 119
6.2 Numerical methodology 120
6.3 Acquisition of experimental data 121
6.4 Modeling cardiovascular responses to orthostatic stress 121
6.5 Limitations and future works 122
6.6 Concluding remarks 124

Appendix A Background 125
A.1 The human cardiovascular system 125
A.2 The effects of orthostatic stress on the human cardiovascular system 129
A.3 The ADAVN model 133

Appendix B Supplementary material to Chapter 2 137

Appendix C Supplementary material to Chapter 3 **147**
C.1 Solution to RP (3.23) for the BFEs 147
C.2 Additional results related to the third-order implementation of the method . . . 151

Appendix D Supplementary material to Chapter 4 **155**

References **159**

Chapter 1

Introduction

Mathematical models have become essential tools for investigating cardiovascular physiology, enabling noninvasive assessment of blood flow, pressure, and tissue perfusion under both normal and pathological conditions (Alastruey et al., 2011; Albanese et al., 2016; Caddy et al., 2024; Quarteroni et al., 2017; Taylor and Figueroa, 2009). In recent years, a wide range of cardiovascular models of the human circulatory system have been developed to analyze different physiological and pathological aspects of cardiovascular function. Depending on the level of spatial resolution and physical detail, cardiovascular models can be classified into three main categories: three-dimensional (3D), one-dimensional (1D), and zero-dimensional (0D) models. 3D models are commonly employed to simulate the mechanical and hemodynamic behavior of specific organs, such as the heart (Zingaro et al., 2023) or the liver (Bonfiglio et al., 2010). At the core of most 3D cardiovascular models lie the Navier–Stokes equations, which govern the motion of blood as an incompressible, viscous fluid. These equations provide a detailed description of local hemodynamics, enabling the computation of velocity fields, pressure distributions, and wall shear stresses within complex vascular geometries. To achieve a more realistic simulation of physiological environments, 3D models are commonly integrated into fluid–structure interaction (FSI) frameworks, which describe the interaction between a deformable structure, like the walls of a blood vessel or an organ, and the fluid flow. Such coupling captures the bidirectional interplay between blood dynamics and wall motion, thereby improving the model's predictive capability but also increasing its computational cost. Consequently, the numerical solution of these models requires an adequate spatial and temporal discretization, making simulations computationally demanding, particularly when extended to large portions of the vascular network. For these reasons, 3D cardiovascular models are typically applied to study localized phenomena of interest (Formaggia et al., 2009). To address these limitations, reduced-order formulations based on 1D or 0D representations are often adopted. These simplified models retain the essential hemodynamic relationships derived from the Navier–Stokes framework while substantially reducing computational cost, thereby allowing for efficient simulation of systemic circulation and of specific vascular regions (Duanmu et al., 2019; Mynard and Smolich, 2015). They are particularly useful for simulating systemic responses under different physiological or pathological conditions and can be effectively coupled with 3D models or with models describing the control mechanisms of the nervous system to provide a comprehensive representation of cardiovascular function (Blanco et al., 2009). In this context, multiscale 1D-0D models play a crucial role by integrating processes that occur across different spatial and temporal scales. The development of such models requires the definition of both 1D and 0D models, and their subsequent coupling. This integrated framework enables the simultaneous investigation of local and global phenomena, capturing the interactions between different cardiovascular mechanisms. By coupling models with different spatial scales, multiscale models enhance predictive accuracy and provide a wider understanding of how localized phenomena, such as those arising from diseases or interventions, can influence overall cardiovascular performance (Blanco and Müller, 2025; Blanco et al., 2009; Quarteroni et al., 2017; Shi et al., 2011).

1.1 1D cardiovascular models

Here, we briefly describe the 1D cardiovascular models, which represent one of the main components of multiscale 1D-0D frameworks. 1D cardiovascular models are derived from cross-sectional averaging the Navier–Stokes equations under the assumptions that blood vessels are axially symmetric and that the blood flow is predominantly laminar (Canić et al., 2006; Formaggia et al., 2009; Hughes and Lubliner, 1973). In these models, the vascular network is represented as a series of compliant tubes as the one showed in figure 1.1, where each segment is characterized by spatially varying parameters such as the reference radius or the wall elasticity. Each vessel is then interconnected with the others at their inlets, outlets, or both, forming the complete vascular network of interest. In this work, we consider extensive vascular networks that include both arterial and venous segments, as shown in figures 1.2 and 1.3.

Each blood vessel is represented as impermeable and deformable tubular control volume, while the blood is assumed to behave as an incompressible Newtonian fluid flowing primarily in the axial direction with an axisymmetric velocity profile. Under these assumptions, the mechanics of blood flow along a single blood vessel can be described by the mass conservation and momentum balance partial differential equations (PDEs), which read

$$\begin{cases} \partial_t A + \partial_x q = 0, \\ \partial_t q + \partial_x \left(\frac{q^2}{A} \right) + \frac{A}{\rho} \partial_x p = R \frac{q}{A} + A g_x, \end{cases} \tag{1.1}$$

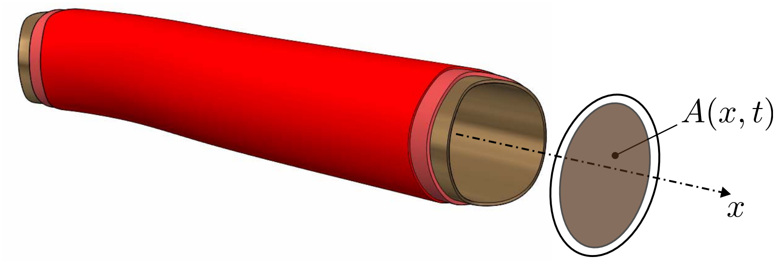

Figure 1.1: Schematic representation of a blood vessel. Axially symmetric vessel configuration in three space dimensions at time t, with an indication of the cross-sectional area A(x,t).

where x is the axial coordinate along the vessel, and t is the time. The unknowns are the cross-sectional area of the vessel lumen $A(x,t) \in \mathbb{R}^+ \setminus \{0\}$, the flow rate $q(x,t) \in \mathbb{R}$ and the cross-sectional averaged internal pressure $p(x,t) \in \mathbb{R}$. $R \in \mathbb{R}^-$ is the negative coefficient of the friction term, while $\rho \in \mathbb{R}^+$ is the blood density. Finally, $g_x(x) \in \mathbb{R}$ is the projection of gravity along the vessel's axis defining the gravity term.

System (1.1) has three unknowns but only two equations, therefore, an additional relation must be introduced. This relation, commonly referred to as the closure condition, describes the mechanical behavior of the vessel wall by linking the average internal pressure $p(x,t)$ to the corresponding cross-sectional area $A(x,t)$. This pressure–area relationship, known as the tube law, can be formulated in different ways depending on the physical characteristics of the vessel wall that one intends to capture. The selection of an appropriate tube law is crucial for accurately representing the wave propagation phenomena that govern the hemodynamic behavior of the modeled vascular system. Additionally, the parametrization of the chosen tube law is a critical aspect, as it determines both the physical properties of the represented blood vessels, such as the stiffness or the compliance, and the mathematical properties of the resulting 1D blood flow model.

The complete 1D formulation enables the computation of pressure and flow wave propagation along the vessels, capturing important features of pulse wave transmission throughout the arterial and venous systems (Alastruey et al., 2011; Avolio, 1980; Formaggia et al., 2003). Furthermore, it provides a favorable balance between physiological accuracy and computational efficiency, making 1D blood flow model particularly useful for studying global hemodynamic phenomena.

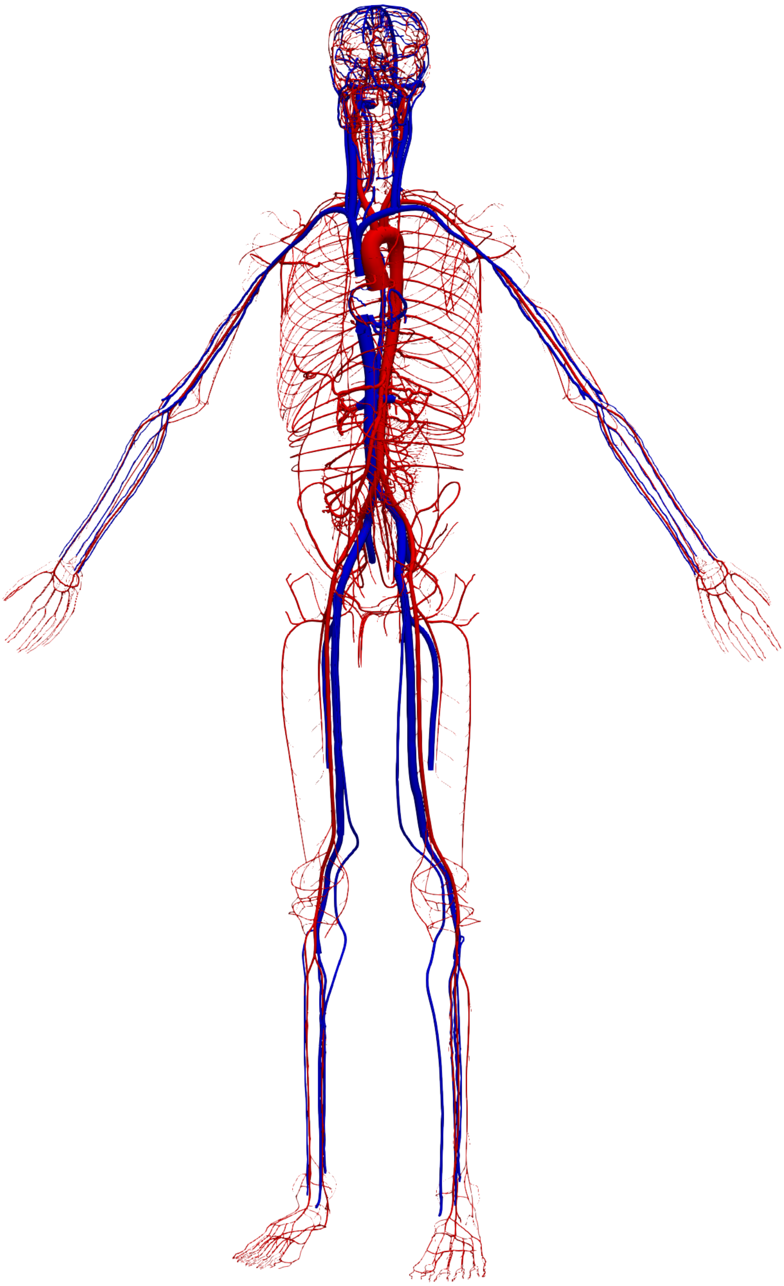

Figure 1.2: ADAVN. Arterial (red) and venous (blue) networks of the Anatomically Detailed Arterial-Venous Network model (Müller et al., 2023).

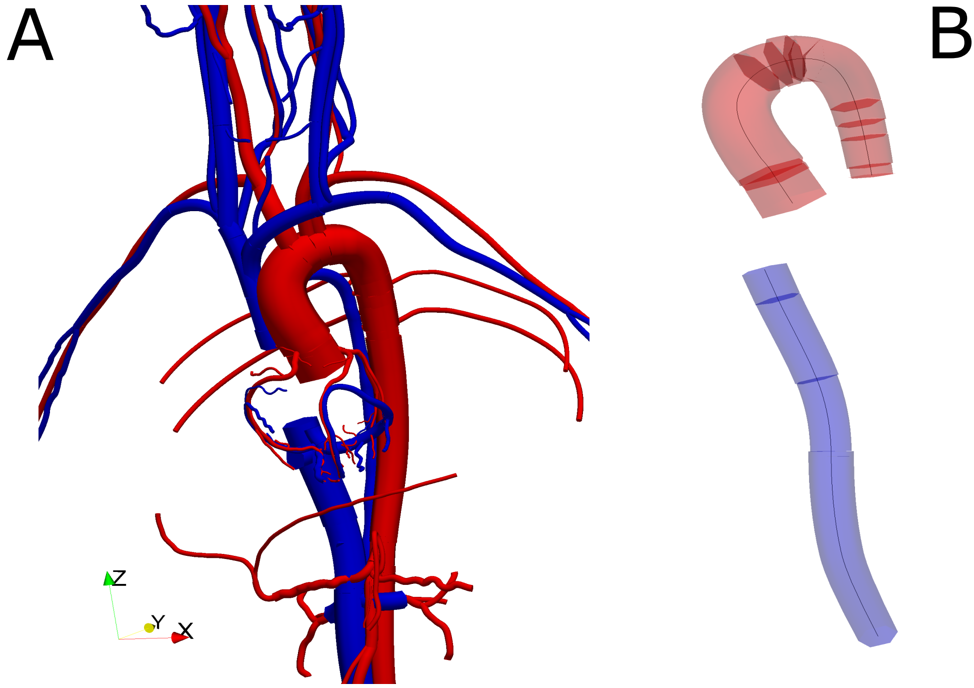

Figure 1.3: Thoracic cavity. A) Zoom on the thoracic cavity of ADAVN86, the reduced version of ADAVN, showing the 3-dimensionality of the network. B) Focus on the aortic arch (light red) and the inferior vena cava (light blue), showing the vessels' centerlines (black curves) used for the 1D modeling.

1.2 0D cardiovascular models

0D models, also known as lumped-parameter models, provide a highly simplified yet powerful representation of the cardiovascular system. In these models, spatial variations in pressure and blood flow are neglected, and each vascular compartment is described by global variables representing average hemodynamic quantities. The governing equations are ordinary differential equations (ODE) derived from the principles of mass and momentum conservation (eq. (1.1)) by applying spatial averaging to the system variables. These equations are commonly represented through an analogy with electrical circuits, where pressure, flow, compliance, resistance, and inertance correspond to voltage, current, capacitance, resistance, and inductance, respectively (Shi et al., 2011). The simplest 0D model that can be considered is a two-element circuit arranged in series, consisting of a resistive element with constant resistance R and a capacitive element with constant compliance C. Figure 1.4 shows a schematic representation of this 0D model, indicating the direction of flow Q. Based on this representation, the governing equations

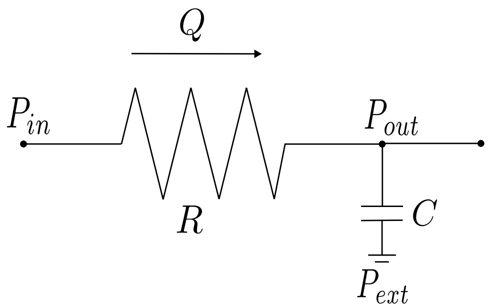

Figure 1.4: Schematic representation of a RC electric circuit. Sketch of a resistance-capacitance (RC) electric circuit with indication of the direction of flow Q.

for blood flow and pressure are given by

$$Q = \frac{P_{in} - P_{out}}{R} \tag{1.2}$$

and

$$P_{out} = \frac{V - V_0}{C} + P_{ext}, \tag{1.3}$$

where P_{in} and P_{out} are the pressures at the left and right of the resistive element R, respectively. These two pressures depends on the composition of the considered 0D model and can either come from model's input, boundary conditions at which the 0D model is connected, or computed with the previously reported equation. V is the volume circulating in the capacitor C, V_0 is a reference unstressed volume and P_{ext} is the external pressure acting on the capacitor C, and thus on the cardiovascular compartment this 0D model is representing.

Despite their simplicity, 0D models are particularly valuable for investigating the global behavior of the cardiovascular system and its regulatory mechanisms. Owing to their simplified mathematical formulation, expressed through ODEs, they enable efficient simulations of the cardiovascular interactions and long-term circulatory adaptations. They are widely employed to represent the function of the heart, the pulmonary and respiratory systems, and different components of the systemic circulation, including the microcirculation or specific anatomical regions, such as the abdomen, the lower limbs, and the cerebral region. Thereby, 0D models are well suited for large-scale studies and real-time applications. Moreover, they can be seamlessly coupled with higher-dimensional (1D or 3D) models to provide boundary conditions, facilitating multiscale modeling of cardiovascular functions (Blanco et al., 2009; Shi et al., 2011).

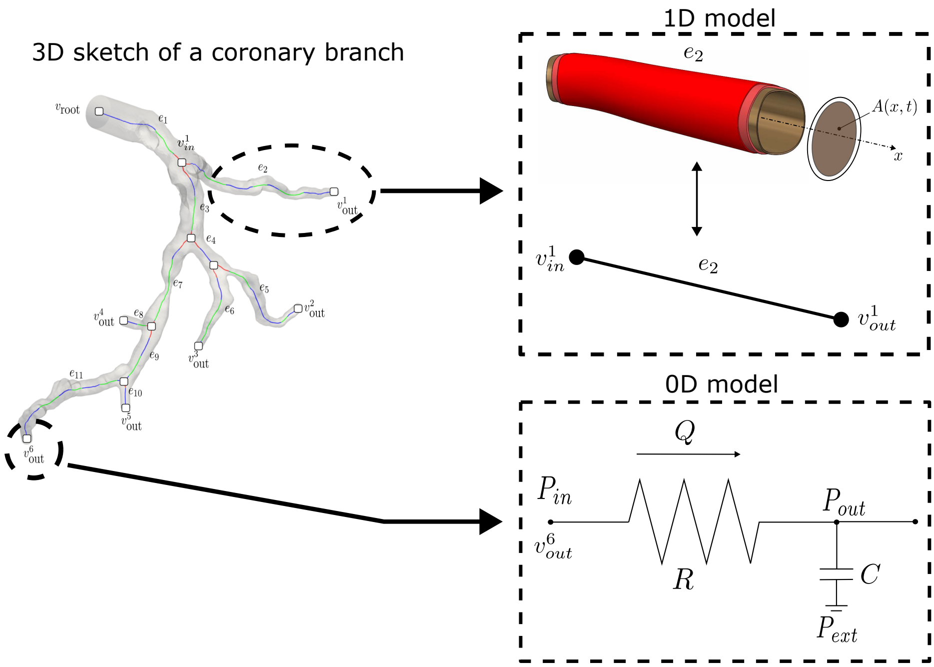

Figure 1.5: Example of a multiscale 1D-0D cardiovascular model. Multiscale model of a coronary branch. Blood flow in each of the 11 blood vessels is described using a 1D model, while 0D models are connected to the outlets of the terminal vessels, v_{out}, to represent the microcirculation.

1.3 Multiscale 1D-0D cardiovascular models with gravity

Both 1D and 0D approaches offers distinct advantages and trade-offs in terms of spatial resolution, physiological detail, and computational cost. Consequently, recent research has increasingly focused on multiscale frameworks that integrate these approaches to combine anatomical realism with systemic physiological accuracy. A representative example of a multiscale cardiovascular model is illustrated in figure 1.5, which depicts a coronary branch. The model comprises eleven coronary arteries interconnected to form a small vascular network. Blood flow in each vessel is described using a 1D formulation. At the inlet of the branch, v_{root}, a boundary condition is applied to represent a typical coronary inflow, whereas at the outlets of the terminal vessels, v_{out}, each is coupled to a 0D model representing the microcirculation that bridges the arterial and venous domains.

The present work is developed within this broader framework of multiscale cardiovascular modeling. Specifically, to investigate the effects of gravity on the human cardiovascular system, we adopt a 1D model of the complete circulation coupled with 0D models to represent localized hemodynamic interactions, including the function of the heart, the pulmonary system, the microcirculation and the valve dynamic (Müller et al., 2023). A detailed description of the state-of-the-art multiscale model is provided in appendix A. The choice of adopting such modeling framework is motivated by its ability to balance computational cost and physiological accuracy. Compared with 3D models, which provide highly detailed spatial representations but are computationally expensive, 1D models offer a simplified yet physiologically meaningful description of wave propagation phenomena along the vascular network at a lower computational cost. At the same time, 1D models preserve spatial information on pressure and flow distribution throughout the considered vascular network, thereby capturing essential hemodynamic features that are neglected by fully 0D models due to their focus on global hemodynamic relationships. By coupling the 1D representation of the major vessels with 0D components describing localized circulatory regions, the proposed approach combines the strengths of both 1D and 0D models, enabling efficient and physiologically meaningful simulations of the cardiovascular system.

Within this class of multiscale 1D-0D models, the majority of the cardiovascular models do not account for gravity and, consequently, cannot capture orthostatic stress responses, that is the cardiovascular adjustments elicited by gravity during postural changes (see appendix A for a detailed description of the physiological mechanisms underlying orthostatic stress). Most of these models have been developed to represent the supine position, under the simplifying assumption that blood vessels lie within a coplanar configuration. In this orientation, the vessel plane is perpendicular to the gravitational vector, and gravitational effects on blood flow can thus be neglected (Alastruey et al., 2011; Boileau et al., 2015). This simplification is further justified by the fact that most clinical and experimental data used for model calibration are obtained in the supine position (Gerlach et al., 2021; van Assen et al., 2023). However, neglecting gravity limits the applicability of such models to physiological conditions involving postural transitions or orthostatic stress, where hydrostatic pressure significantly influence venous return and the overall hemodynamic regulation.

In the past 70 years, increasing attention has been devoted to extending cardiovascular models to incorporate gravitational influences, enabling the study of postural changes and orthostatic stress. A representative example is the model developed by Heldt et al. (2002) (and reference therein), which employs a fully 0D formulation to simulate the hemodynamic responses to orthostatic stress. Similarly, the studies by Melchior et al. (1992) and Olufsen et al. (2004) investigated orthostatic stress responses using variants of fully 0D models coupled with representations of autonomic nervous system control mechanisms. In a similar manner, the works by Snyder and Rideout (1969) and van Heusden et al. (2006) examined the influence of gravitational effects on the venous circulation, also employing fully 0D formulations. Other examples include the models developed by Murillo and Garcia-Navarro (2023) and Zhang et al. (2017), which feature a 1D representation of both arterial and venous vascular trees, together with the gravitational pressure gradients acting along the entire vascular network. However, these models do not explicitly account for the neural control mechanisms of the autonomic nervous system. A more comprehensive approach was proposed by Fois et al. (2022), who combined a 1D arterial network with a 0D venous network, incorporating gravitational pressure gradients in both domains as well as the autonomic regulatory mechanisms governing cardiovascular control. It is important to note, however, that all these models still rely on the assumption of vascular coplanarity, meaning that blood vessels are considered to lie within a single plane. As a result, while gravitational effects are included, the 3D anatomical distribution of vessels in the human body, and its associated impact on hydrostatic pressure gradients, remains idealized. Beyond the scope of orthostatic stress and postural transitions, several other modeling efforts have investigated the role of gravity under different physiological and environmental conditions. These include studies focused on cardiovascular responses to microgravity exposure, linear and rotational accelerations, and varying gravitational loads during exercise or aerospace conditions. While these models are not discussed here in detail, the interested reader is referred to comprehensive reviews and specialized works in this field (see e.g. Blanco and Müller (2025)).

1.4 Parametrization and validation of multiscale cardiovascular models with gravity

Building upon the formulation of multiscale 1D–0D cardiovascular models, an important aspect concerns their parametrization and validation, which determine the physiological fidelity and predictive capability of the simulations (Albanese et al., 2016; Quarteroni et al., 2017). In fact, the development of such models depends crucially on the parameters used to represent the phenomena of interest. These parameters define a comprehensive set of anatomical and physiological quantities that collectively describe the geometry, mechanics, and hemodynamics of the entire circulation. Geometric parameters such as vessel lengths, radii, and branching patterns are typically extracted from imaging data or anatomical databases, while wall stiffness, peripheral resistances, and compliances are often calibrated to reproduce physiological targets such as mean arterial pressures, cardiac output, or pulse wave velocity (Mynard and

Smolich, 2015; Reymond et al., 2009; Steinman, 2002). Due to the complexity of the coupled 1D–0D network, many parameters cannot be directly measured and must be estimated through various techniques, including inverse modeling, optimization procedures or machine learning approaches (Argus et al., 2022; Saxton et al., 2023). Validation of the full system model then requires comparison between simulated and measured hemodynamic quantities at multiple locations within the network to ensure that both global and local dynamics are accurately represented. Achieving robust parametrization and validation is therefore essential to establish the model's credibility and to enable its use for predictive or patient-specific applications (Eck et al., 2017).

The same considerations apply when developing cardiovascular models that account for the effects of gravity on blood flow distribution and pressure regulation. In these models, accurate parametrization remains essential to capture posture-dependent variations in vascular resistance, compliance, and venous return (Fois et al., 2022; van Heusden et al., 2006). However, a major challenge lies in the limited availability of experimental and clinical data suitable for validation under different gravitational conditions. Most hemodynamic measurements used for parameter estimation and model calibration are obtained in the supine position, while data acquired during standing or in other positions, where hydrostatic effects become significant, are relatively scarce. This scarcity, especially concerning the venous behavior and the control mechanisms of the autonomic nervous system, of posture-specific data complicates both the identification of parameters governing gravitational responses and the rigorous validation of the model predictions, ultimately limiting the reliability of simulations aimed at reproducing postural cardiovascular dynamics (Ursino and Magosso, 2003).

In summary, although current multiscale 1D–0D cardiovascular models have advanced our understanding of posture-related hemodynamics, significant physiological uncertainties remain, particularly regarding autonomic regulation and venous mechanics. These limitations prevent the development of predictive models capable of reproducing the full spectrum of cardiovascular responses observed during orthostatic stress. Addressing these limitations requires the integration of more physiologically consistent representations of neural and venous dynamics, supported by targeted experimental data for model calibration and validation. The following section outlines the specific objectives of this work, which are designed to address some of these challenges and contribute to the development of more comprehensive and physiologically accurate cardiovascular models.

1.5 Objectives of this thesis

The main objective of this work is to extend an existing multiscale 1D–0D cardiovascular model that has a unique 3D spatial characterization of both arteries and veins by incorporating the effects of gravity.

To achieve this, the work builds upon the Anatomically Detailed Arterial–Venous Network (ADAVN) model (Müller et al., 2023) and its reduced formulations (Blanco et al., 2015, 2020). The key strength of the ADAVN model lies in its high degree of anatomical fidelity, as it retains the real 3D geometry and spatial configuration of both arterial and venous networks (see figures 1.2 and 1.3). Each vessel of these networks is represented within an anatomically realistic 3D domain, modeled as a tubular structure, consistent with established principles of descriptive anatomy (Blanco et al., 2015). Unlike the other models that assume a coplanar vascular layout, thereby limiting the ability to accurately compute hydrostatic pressure distributions along the vascular network, this anatomically realistic framework explicitly accounts for the actual positioning of vessels throughout the body. As a result, it enables a more physiologically consistent investigation of gravitational and postural effects on human circulation, overcoming a limitation commonly present in previous modeling approaches and serving as the foundation for our work.

In the context of this work, the state-of-the-art ADAVN model, described in detail in appendix A, has been extended to incorporate gravitational terms, as discussed in chapter 5. This extension, however, was not straightforward and required addressing several technical and physiological challenges. The accuracy and reliability of the resulting model in reproducing physiological responses to orthostatic stress depend critically on three key components:

- the physical formulation of the problem,
- the numerical methodology employed to ensure its stable and efficient solution,
- the representation of control mechanisms, particularly those related to autonomic nervous system, which are essential for reproducing realistic adaptive responses to postural changes.

In the following chapters, each of these aspects is discussed in detail. Chapter 2 is devoted to the identification of a clear and realistic formulation of the tube law, the constitutive relationship that describes the mechanical behavior of the vessel wall, demonstrating the superiority of the viscoelastic description in capturing realistic vessel wall behavior. Chapter 3 introduces a well-balanced high-order path-conservative numerical scheme capable of accurately solving the governing equations of blood flow in the presence of gravitational effects, thereby ensuring robust and reliable simulations. Chapter 4 complements these modeling and numerical advances with experimental data acquired in collaboration with physiologists from the University of Auckland (New Zealand), addressing key knowledge gaps in venous dynamics and autonomic control. Finally, chapters 5 and 6 integrate these elements within the ADAVN framework to simulate the cardiovascular response to orthostatic stress, assess the model's physiological fidelity, and identify current limitations and directions for future research.

Chapter **2**

Tube law parametrization using in vitro data for one-dimensional blood flow in arteries and veins

Chiara Colombo, Annunziato Siviglia, Eleuterio F. Toro, Daniel Bia, Yanina Zócalo, and Lucas O. Müller

The deformability of blood vessels in one-dimensional blood flow models is typically described through a pressure-area relation, known as the tube law. The most used tube laws take into account the elastic and viscous components of the tension of the vessel wall. Accurately parametrizing the tube laws is vital for replicating pressure and flow wave propagation phenomena. Here, we present a novel mathematical-property-preserving approach for the estimation of the parameters of the elastic and viscoelastic tube laws. Our goal was to estimate the parameters by using ovine and human in vitro data, while constraining them to meet prescribed mathematical properties. Results show that both elastic and viscoelastic tube laws accurately describe experimental pressure-area data concerning both quantitative and qualitative aspects. Additionally, the viscoelastic tube law can provide a qualitative explanation for the observed hysteresis cycles. The two models were evaluated using two approaches: (i) allowing all parameters to freely vary within their respective ranges and (ii) fixing some of the parameters. The former approach was found to be the most suitable for reproducing pressure-area curves.

This chapter has been published as: *Colombo C., Siviglia A., Toro E. F., Bia D., Zócalo Y., Müller L. O. Tube law parametrization using in vitro data for one-dimensional blood flow in arteries and veins. Int. J. Numer. Meth. Biomed. Engng. 2024; 40(4):e3803. doi:10.1002/cnm.3803*

2.1 Introduction

In silico models have become increasingly important in modern medical research as a means of simulating and quantifying pressure and flow pulse waveforms in the circulatory system (Formaggia et al., 2009), since they can simulate the behavior of the circulatory system under both healthy and pathological conditions (Liang et al., 2018; Mynard and Smolich, 2015). Among all the mathematical models used to describe the cardiovascular system, an important role is played by one-dimensional (1D) models, which have shown to provide accurate prediction of pressure and flow wave propagation on large arterial and venous networks (Alastruey et al., 2011; Boileau et al., 2015; Mynard and Smolich, 2015; Müller and Toro, 2014; Reymond et al., 2009). These models are governed by systems of evolutionary partial differential equations (PDEs) of hyperbolic or hyperbolic-dominant type, and provide a reasonable balance between computational cost and accuracy (Xiao et al., 2014).

These models consider the deformability of blood vessels by incorporating the so-called *tube law*, which relates the blood pressure to the wall tension. In turn, wall tension is normally described in terms of strain, for purely elastic models, and in terms of strain and strain rate for viscoelastic models (Bia et al., 2014). This coupling of fluid dynamics with vessel's mechanical properties depends on the composition of the vessel wall, which in turn is determined by its function (Burton, 1954). While tube laws used in 1D models can consider several different phenomena contributing to the wall tension (Formaggia et al., 2003), in this work we focus on elastic and viscoelastic tube laws, which in turn are the most common used ones. Elastic tube laws (elastic models) consider a purely elastic response to the vessel wall to deformation (Brook et al., 1999; Müller and Toro, 2014; Pedley et al., 1996), while viscoelastic tube laws (viscoelastic models) consider a viscoelastic response, incorporating the viscous properties of the vessel wall neglected in elastic models (Bertaglia et al., 2020; Bia et al., 2014; Formaggia et al., 2003; Müller et al., 2016).

Both elastic and viscoelastic tube laws are characterized by parameters that represent vessels' geometrical and mechanical properties (Battista et al., 2016; Bia et al., 2014). These parameters are typically derived from more complex models (Quarteroni et al., 2000), or by analyzing temporal data for pressure-area dynamics, which are obtained from in vitro or in vivo experiments. By utilizing this data, it is possible to extract the values of the parameters associated with a specific formulation (either elastic or viscoelastic) and use them to evaluate the model's ability to reproduce real wave patterns (Alastruey et al., 2011; Reymond et al., 2009) and study structural and functional differences among vessels (Bia Santana et al., 2007; Valdez-Jasso et al., 2011; Zócalo et al., 2013). However, parameter values cannot be arbitrary. Certain constrains are derived from physical considerations, while others might be needed if specific mathematical properties of the 1D blood flow model are required. Elastic models are typically governed by quasi-linear first-order PDE systems, where the parameters of the tube law are chosen such that the model is of hyperbolic type (Müller and Toro, 2014; Spilimbergo et al., 2021; Toro and Siviglia, 2013), allowing for the use of numerical methods of the Godunov type (Toro, 2009). Other approaches are also available. Elastic models can indeed be linearized and a solution, either analytical or semi-analytical, can be found in terms of Fourier series expansions (Flores et al., 2016; Sazonov and Nithiarasu, 2019). Viscoelastic models are usually governed by quasi-linear second-orders PDEs systems of parabolic type (Alastruey et al., 2011; Formaggia et al., 2003) and can be solved applying different numerical approaches. One approach consists in using the Galerkin method, where the solution is expanded in terms of a set of basis functions, and the equations are projected onto these functions to obtain a system of algebraic equations (Alastruey et al., 2011; Quarteroni, 2012). Another approach consists in using the operator splitting technique, where the original problem is split into a convective and a diffusive subproblem that are solved sequentially (Formaggia et al., 2003; Toro, 2009). A third alternative approach is to transform the initial parabolic problem into an hyperbolic problem using the Cattaneo's relaxation approach (Cattaneo, 1958). This third method has been effectively applied to viscoelastic models (Montecinos and Toro, 2014; Montecinos et al., 2014), and enables the use of standard Godunov-type numerical methods.

In this work we assess how constraining tube law parameters to obtain certain mathematical properties of 1D blood flow model affects the capacity of the tube law to fit experimental data. Specifically, we consider two widely employed tube laws, the elastic tube law as described in Pedley et al. (1996) and the viscoelastic tube law as described in Alastruey et al. (2011). For the estimation procedure we use in vitro pressure and area time series extracted from ovine and human donors. These estimates must not only satisfy physiological requirements to correctly reproduce pressure waveforms, but also ensure that the mathematical nature (namely hyperbolicity and genuine non-linearity characteristic fields (Toro, 2009)) of the 1D blood flow model is preserved. To this end, since elastic and viscoelastic tube laws give rise to hyperbolic and parabolic systems of PDEs, respectively, we reformulate the parabolic problem as an hyperbolic system following Montecinos et al. (2014). We then study the mathematical properties of the two systems of PDEs and ensure that the structure of the PDE systems is strictly hyperbolic with genuinely non-linear and/or linearly degenerate characteristic fields. These properties ensure the well posedness of certain initial- and initial-boundary value problems involving these 1D blood flow models (Bressan, 2000).

2.2 Materials and Methods

2.2.1 Mathematical model for blood flow in collapsible tubes

We consider the impermeable and deformable tubular control volume showed in Fig. 2.1 and assume a Newtonian incompressible fluid flowing in the axial direction x with an axisymmetric velocity profile. In such conditions, 1D blood flow in major vessels is described by two PDEs, representing mass conservation and momentum balance. The model reads

$$\begin{cases} \partial_t A + \partial_x q = 0, \\ \partial_t q + \partial_x \left(\frac{q^2}{A}\right) + \frac{A}{\rho}\partial_x p = f, \end{cases} \tag{2.1}$$

where x is the axial coordinate along the vessel (Fig. 2.1) and t is the time. The unknowns are the cross-sectional area of the vessel lumen $A(x,t) \in \mathbb{R}^+ \setminus \{0\}$, the flow rate $q(x,t) \in \mathbb{R}$ and the cross-sectional averaged internal pressure $p(x,t) \in \mathbb{R}$. The friction term f, depends on the local velocity profile which is assumed a priori, while ρ is the blood density.

System (2.1) has more unknowns than equations, hence a closure condition must be introduced. This closure condition is given by the tube law, which relates the averaged internal pressure $p(x,t)$ to the cross-sectional area $A(x,t)$.

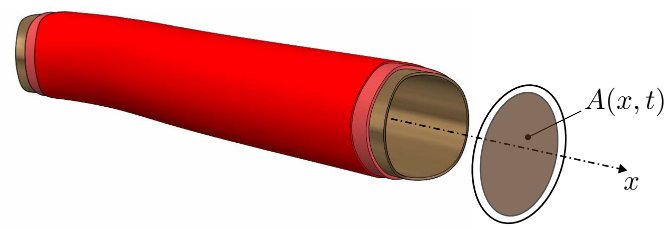

Figure 2.1: Vessel configuration. Axially symmetric vessel configuration in three space dimensions at time t, with an indication of the cross-sectional area $A(x,t)$. The vessel wall consists of three layers: the tunica intima (in brown), the tunica media (light red) and the tunica adventitia (in red). Each of these layers has a specific role. The function of the tunica media is to supply mechanical strength and contractile power to the vessel. Therefore, it is predominantly composed of smooth muscle cells, immersed in a matrix of elastin and collagen fibers. More details about the tunica media can be found in Levick (2009) and in Burton (1954), together with more information on the roles of the other layers and their composition.

2.2.2 The elastic model

Here we adopt an elastic tube law (Brook et al., 1999; Pedley et al., 1996; Siviglia and Toffolon, 2013; Toro and Siviglia, 2013) of the form

$$p(x,t) = p_{ext}(x,t) + \psi(A(x,t);A_0,K,m,n,p_0), \tag{2.2}$$

where $p_{ext}(x,t)$ is the external pressure, assumed equal to zero. $\psi(A(x,t);A_0,K,m,n,p_0)$ represents the elastic component of the tube law and is given by

$$\psi(A(x,t);A_0,K,m,n,p_0) = K\phi(A(x,t);A_0,m,n) + p_0, \tag{2.3}$$

with

$$\phi(A(x,t);A_0,m,n) = \left[\left(\frac{A(x,t)}{A_0}\right)^m - \left(\frac{A(x,t)}{A_0}\right)^n\right]. \tag{2.4}$$

In this work, all the parameters are considered constant in space and time. Particularly, $A_0 \in \mathbb{R}^+ \setminus \{0\}$ denotes the cross-sectional area at equilibrium, $K \in \mathbb{R}^+ \setminus \{0\}$ represents the the stiffness coefficient of the vessel wall, $p_0 \in \mathbb{R}$ is the reference cross-sectional averaged pressure, while parameters $m \in \mathbb{R}$ and $n \in \mathbb{R}$ intend to mimic the hyperelastic nature of vessel walls and the behavior during collapse, respectively.

The adopted tube law allows to describe experimentally observed pressure-area relations over a wide pressure range. These relations are determined by the biological composition of the wall of vessels (Burton, 1954), which contains elastine, collagen fibers and smooth muscle cells. It is well known that, for increasing positive transmural pressures ($p_{tm}(x,t) = p(x,t) - p_0$), the stiffness of vessels raise, due to the gradual recruitment of collagen fibers, determining a characteristic hyperelastic behaviour. On the other hand, for negative transmural pressures, vessels will undergo collapse, resulting in the buckling of the vessel wall and the consequent increment in stiffening for decreasing transmural pressures. The intermediate region between the collapse-related buckling region and the hyperelastic one, is a range where the vessel exhibits maximum compliance (or minimal stiffness). Further details on this subject are available in Caro et al. (2012) and Fung (1997).

2.2.2.1 Governing equations

We consider a mathematical model consisting of system (2.1), along with tube law (2.2). Since we are interested in the eigenstructure of the resulting system, we will restrict our study to the homogeneous case. The resulting system can be written in quasi-linear form as follows

$$\partial_t \boldsymbol{Q} + \boldsymbol{B}(\boldsymbol{Q})\partial_x \boldsymbol{Q} = \boldsymbol{0}, \tag{2.5}$$

where the vector of unknowns $\boldsymbol{Q}$ is

$$\boldsymbol{Q} = [A, q]^T \in \Omega, \tag{2.6}$$

with

$$\Omega = \{(A, q) \in \mathbb{R}^+ \setminus \{0\} \times \mathbb{R}\}. \tag{2.7}$$

The matrix of coefficients $\boldsymbol{B}(\boldsymbol{Q})$ is given by

$$\boldsymbol{B}(\boldsymbol{Q}) = \begin{bmatrix} 0 & 1 \\ c_E^2 - u^2 & 2u \end{bmatrix}, \tag{2.8}$$

where $u = q/A$, and

$$c_E = \sqrt{\frac{A}{\rho} K \partial_A \phi} \tag{2.9}$$

is the wave speed. Next we study some mathematical properties of system (2.5).

2.2.2.2 Eigenstructure

The eigenstructure of system (2.5) is given by the eigenvalues and the corresponding eigenvectors of coefficient matrix (2.8). Eigenvalues of matrix (2.8) are

$$\lambda_1 = u - c_E \quad \text{and} \quad \lambda_2 = u + c_E. \tag{2.10}$$

The corresponding right eigenvectors are

$$\boldsymbol{R}_1(\boldsymbol{Q}) = \begin{bmatrix} 1 \\ u - c_E \end{bmatrix}, \quad \text{and} \quad \boldsymbol{R}_2(\boldsymbol{Q}) = \begin{bmatrix} 1 \\ u + c_E \end{bmatrix}. \tag{2.11}$$

The mathematical nature of this model depends on parameters m and n of the elastic tube law (2.2) (Spilimbergo et al., 2021; Toro and Siviglia, 2013). System (2.5) is strictly hyperbolic if λ_1 and λ_2 are real and distinct. Since $u \in \mathbb{R}$, we need to check if $c_E \in \mathbb{R}^+ \setminus \{0\}$. Therefore, we need to verify that the argument of the squared root of the wave speed (2.9) is positive. Since $A > 0$, $\rho > 0$, $K > 0$ for physical reasons, we only need to verify that

$$\partial_A \phi > 0. \tag{2.12}$$

Simple manipulations give

$$m \left(\frac{A}{A_0} \right)^m > n \left(\frac{A}{A_0} \right)^n. \tag{2.13}$$

Introducing $a = A/A_0$, we write inequality (2.13) as

$$m(a)^m > n(a)^n. \tag{2.14}$$

We see that

- if $a < 1$, then
  - I) if $m, n > 0$, then for a given m, $\exists v_1, v_2 \in \mathbb{R}^+ \setminus \{0\}$ s.t. $n \in (0, v_1) \cup (v_2, +\infty)$,
  - II) if $m \leq 0, n \geq 0$, then there is no solution,
  - III) if $m, n < 0$, then inequality (2.14) holds true only if $n < m$,
  - IV) if $m > 0, n \leq 0$, then inequality (2.14) holds always true,
- if $a > 1$, then
  - I) if $m, n > 0$, then inequality (2.14) holds true only if $n < m$,
  - II) if $m \leq 0, n \geq 0$, then there is no solution,
  - III) if $m, n < 0$, then for a given m, $\exists v_3, v_4 \in \mathbb{R}^- \setminus \{0\}$ s.t. $n \in [v_3, v_4]$,
  - IV) if $m > 0, n \leq 0$, then inequality (2.14) holds always true,
- if $a = 1$, then
  - I) if $m, n > 0$, then inequality (2.14) holds true only if $n < m$,
  - II) if $m \leq 0, n \geq 0$, then there is no solution,
  - III) if $m, n < 0$, then inequality (2.14) holds true only if $n < m$,
  - IV) if $m > 0, n \leq 0$, then inequality (2.14) holds always true.

Fig. 2.2 displays a graphical example of the previous cases, while the full derivation of the above conclusions can be seen in Colombo (2021). Fig. 2.2 shows contour plots with binary output of the function $y(m, n; a) = m(a)^m - n(a)^n$, where the black regions represent the sectors where inequality (2.14) holds true for the given $a > 0$ and the given combination of m and n. Since inequality (2.14) must hold true $\forall a > 0$, all the previous cases must be satisfied simultaneously. Combining them (Fig. 2.2f), we obtain that our system is strictly hyperbolic when

$$m > 0 \quad \text{and} \quad n \leq 0. \tag{2.15}$$

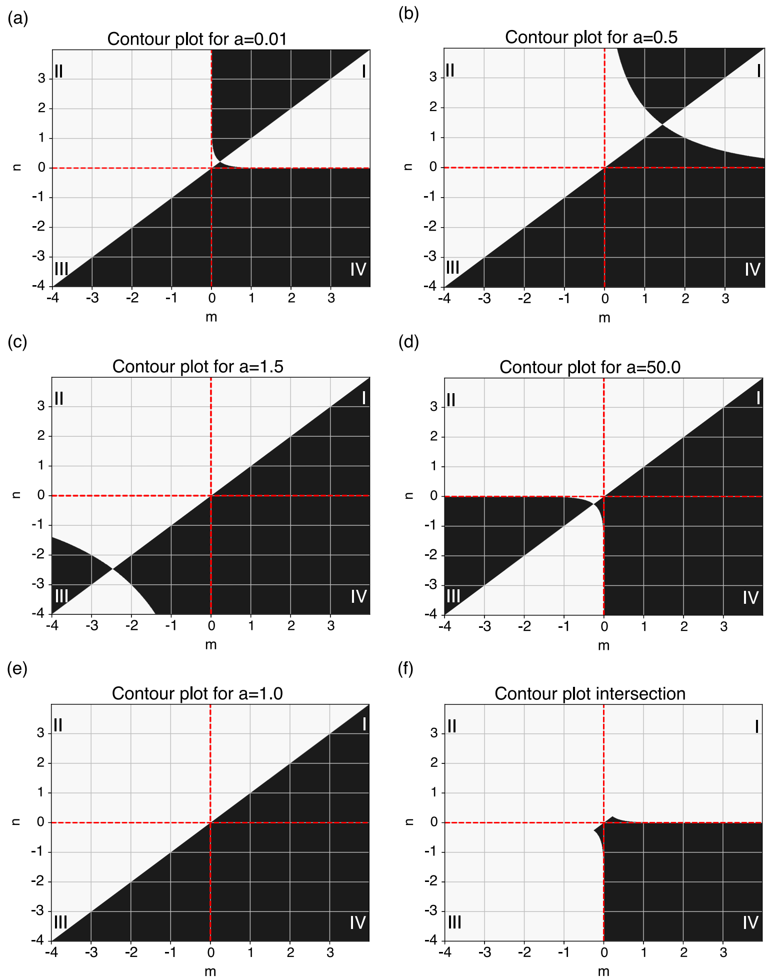

Figure 2.2: Contour plots with binary output. Panels (a)-(e) display different contour plots with binary output of the function $y(m,n;a) = m(a)^m - n(a)^n$ for 5 given $a > 0$. Panel (f) displays a contour plot with binary output obtained by intersecting the previous 5 panels. Black sections are regions where $y(m,n;a) > 0$. It is worth remarking that the mismatch between the analytical solution and the results in panel (f) (small spots in quadrants I and III) is due to the particular choice we made for a. A perfect match could be obtained by selecting $a \to 0$ and $a \to \infty$.

2.2.2.3 Characteristic fields

Parameters m and n control which are the families of waves present in the solution of system (2.5). In particular, genuinely non-linear characteristic fields will give rise to shocks or rarefactions, while linearly degenerate characteristic fields generate contact discontinuities (Toro, 2009). Genuine non-linearity is a desirable property of hyperbolic systems of conservation laws. In fact, problems involving genuinely non-linear characteristic fields are significantly easier to analyze and discretize with respect to problems that present non genuinely non-linear characteristic fields. As a consequence, most general well-posedness results for initial value problems regarding hyperbolic systems of partial differential equations are available for systems having either genuinely non-linear or linearly degenerate characteristic fields (Bressan, 2000). Characteristic fields are said to be genuinely non-linear if the following inequalities are fulfilled

$$\nabla\lambda_1(\boldsymbol{Q})\cdot\boldsymbol{R}_1(\boldsymbol{Q}) < 0 \quad \forall \mathbf{Q}\in\Omega, \tag{2.16a}$$

$$\nabla\lambda_2(\boldsymbol{Q})\cdot\boldsymbol{R}_2(\boldsymbol{Q}) > 0 \quad \forall \mathbf{Q}\in\Omega, \tag{2.16b}$$

where $\nabla\lambda_i(\boldsymbol{Q})$ is the gradient of λ_i. Particularly, for the problem under consideration the following holds

$$\nabla\lambda_i(\boldsymbol{Q})\cdot\boldsymbol{R}_i(\boldsymbol{Q}) = \left(\frac{\partial}{\partial A}\lambda_i + \lambda_i\frac{\partial}{\partial q}\lambda_i\right), \quad i=1,2. \tag{2.17}$$

Expressing the partial derivatives, relation (2.17) becomes

$$\begin{aligned}\nabla\lambda_i(\boldsymbol{Q})\cdot\boldsymbol{R}_i(\boldsymbol{Q}) &= \pm\frac{K}{2\rho c_E}\left(3\partial_A\phi + A\partial_A^{(2)}\phi\right) = \\ &= \pm\frac{K}{2\rho c_E A}\left[m(m+2)\left(\frac{A}{A_0}\right)^m - n(n+2)\left(\frac{A}{A_0}\right)^n\right], \quad i=1,2.\end{aligned} \tag{2.18}$$

Under the assumption that $m>0$, $n\le 0$, since $K>0$, $\rho>0$, $c_E>0$, $A>0$, $A_0>0$, we need to solve the following inequality

$$m(m+2)\left(\frac{A}{A_0}\right)^m - n(n+2)\left(\frac{A}{A_0}\right)^n > 0. \tag{2.19}$$

Introducing again $a = A/A_0$, we write inequality (2.19) as

$$m(m+2)(a)^m - n(n+2)(a)^n > 0. \tag{2.20}$$

It is possible to show that

- if $a<1$, then for a given m, $\exists v_5 \in [-m-2,-2)$ s.t. $n\in[v_5,0]$,
- if $a>1$, then for a given m, $\exists v_6 < -2$ s.t. $n\in(v_6,0]$,
- if $a=1$, then for a given m, $n\in[-m-2,0]$.

These three cases must be satisfied simultaneously, thus their combination gives

$$m>0 \quad \text{and} \quad n\in[-2,0]. \tag{2.21}$$

Conditions (2.21) for parameters m and n guarantee that the 1D elastic model is strictly hyperbolic and its characteristic fields are genuinely non-linear.

2.2.3 The viscoelastic model

Here we adopt the following viscoelastic tube law (Alastruey et al., 2011; Canić et al., 2006; Formaggia et al., 2003; Müller et al., 2016)

$$p(x,t) = p_{ext}(x,t) + \psi(A(x,t);A_0,K,m,n,p_0) + \varphi(A(x,t);A_0,\Gamma)\partial_t A, \tag{2.22}$$

where the term involving $\partial_t A$ with

$$\varphi(A(x,t);A_0,\Gamma) = \frac{\Gamma}{A_0\sqrt{A(x,t)}}, \tag{2.23}$$

represents its viscous component. $\Gamma \in \mathbb{R}^+$ is a parameter related to the viscosity of the vessel wall (Alastruey et al., 2011), assumed constant in space and time.

2.2.3.1 Governing equations

We consider the 1D blood flow model consisting of system (2.1), along with tube law (2.22). The resulting system can be reformulated following the procedure exposed in Montecinos et al. (2014) and in Montecinos and Toro (2014) to obtain an hyperbolic system of PDEs. Specifically, we introduce a new variable $\Psi \in \mathbb{R}$ and a relaxation parameter $\varepsilon \in \mathbb{R}^+ \setminus \{0\}$ as well as the following additional evolutionary equation for Ψ

$$\partial_t \Psi = \frac{1}{\varepsilon}(\partial_x q - \Psi). \tag{2.24}$$

This results in the following property

$$\Psi \to \partial_x q, \quad \text{as } \varepsilon \to 0, \tag{2.25}$$

so that one can recover the original parabolic problem for small relaxation parameter ε. We then formulate the viscoelastic tube law (2.22) as

$$p(x,t) = p_{ext}(x,t) + \psi(A(x,t);A_0,K,m,n,p_0) - \varphi(A(x,t);A_0,\Gamma)\Psi. \tag{2.26}$$

Finally we write the system in quasi-linear form as in (2.5). The vector of unknowns is

$$\boldsymbol{Q} = [A,q,\Psi]^T, \tag{2.27}$$

and the matrix of coefficients is

$$\boldsymbol{B}(\boldsymbol{Q}) = \begin{bmatrix} 0 & 1 & 0 \\ c_V^2 - u^2 & 2u & -\frac{A}{\rho}\varphi \\ 0 & -\frac{1}{\varepsilon} & 0 \end{bmatrix}, \tag{2.28}$$

where

$$c_V = \sqrt{c_E^2 + \frac{\varphi\Psi}{2\rho}} = \sqrt{\frac{A}{\rho}K\partial_A\phi + \frac{\varphi\Psi}{2\rho}} \tag{2.29}$$

is the wave speed. System (2.5) with (2.24) and (2.25) constitutes a relaxation system whose solutions approximate those of the original viscoelastic system.

2.2.3.2 Eigenstructure

The eigenstructure of the system is given by the eigenvalues of matrix (2.28) and the corresponding eigenvectors. The eigenvalues are

$$\lambda_1 = u - \tilde{c}, \quad \lambda_2 = 0, \quad \lambda_3 = u + \tilde{c}, \tag{2.30}$$

where the wave speed is

$$\tilde{c} = \sqrt{c_V^2 + \frac{A\varphi}{\rho\varepsilon}} = \sqrt{\frac{A}{\rho}K\partial_A\phi + \frac{\varphi\Psi}{2\rho} + \frac{A\varphi}{\rho\varepsilon}}. \tag{2.31}$$

The right eigenvectors are

$$\boldsymbol{R}_1(\boldsymbol{Q}) = \begin{bmatrix} 1 \\ u - \tilde{c} \\ -1/\varepsilon \end{bmatrix}, \quad \boldsymbol{R}_2(\boldsymbol{Q}) = \begin{bmatrix} 1 \\ 0 \\ \frac{(c_V^2 - u^2)\rho}{\varphi A} \end{bmatrix}, \quad \boldsymbol{R}_3(\boldsymbol{Q}) = \begin{bmatrix} 1 \\ u + \tilde{c} \\ -1/\varepsilon \end{bmatrix}. \tag{2.32}$$

The eigenstructure allows us to study the hyperbolicity of the system, as we did for the elastic model. Specifically, it is possible to prove that the system of conservation laws is strictly hyperbolic, i.e. the eigenvalues are real and distinct, if

$$\frac{A}{\rho}K\partial_A\phi + \frac{\varphi\Psi}{2\rho} + \frac{A\varphi}{\rho\varepsilon} > 0. \tag{2.33}$$

After some algebraic manipulations, we obtain that inequality (2.33) is equivalent to

$$\frac{\partial p}{\partial A} - \frac{1}{\varepsilon}\frac{\partial p}{\partial \Psi} > 0. \tag{2.34}$$

However we cannot identify any mathematical constrains on the parameters since relation (2.34) has not a closed form. We observe that if $\varphi > 0$, then

$$\frac{\partial p}{\partial \Psi} = -\varphi < 0. \tag{2.35}$$

Thus, we can always choose a $\varepsilon > 0$ small enough such that inequality (2.34) is satisfied and the system is strictly hyperbolic, independently of the sign of $\frac{\partial p}{\partial A}$. Additionally, since the viscoelastic tube law (2.22) is an extension of the elastic tube law (2.2), we also observe that we are able to resume the properties of the elastic model when the viscoelasticity coefficient is set to zero. Specifically, we have that the elastic component of the viscoelastic tube law is a monotonically increasing function of the cross-sectional area A, i.e.

$$\left(\frac{\partial p}{\partial A} - \frac{1}{\varepsilon}\frac{\partial p}{\partial \Psi}\right)\bigg|_{\varphi=0} = \frac{\partial p}{\partial A}\bigg|_{\varphi=0} = \frac{\partial \psi}{\partial A} = K\partial_A \phi > 0, \tag{2.36}$$

which is equivalent to condition (2.12).

2.2.3.3 Characteristic fields

Here we analyze the nature of the characteristic fields. It is easy to see that λ_2-characteristic field is linearly degenerate. Instead, it is possible to prove that λ_1-, λ_3-characteristic fields are genuinely non-linear. It holds

$$\nabla\lambda_i(\boldsymbol{Q})\cdot\boldsymbol{R}_i(\boldsymbol{Q}) = \left(\frac{\partial}{\partial A}\lambda_i + \lambda_i\frac{\partial}{\partial q}\lambda_i - \frac{1}{\varepsilon}\frac{\partial}{\partial \Psi}\lambda_i\right), \quad i = 1,3. \tag{2.37}$$

Computing the partial derivatives, relation (2.37) becomes

$$\nabla\lambda_i(\boldsymbol{Q})\cdot\boldsymbol{R}_i(\boldsymbol{Q}) = \pm\left(\frac{\partial \tilde{c}}{\partial A} + \frac{\tilde{c}}{A} - \frac{1}{\varepsilon}\frac{\partial \tilde{c}}{\partial \Psi}\right), \quad i = 1,3. \tag{2.38}$$

If we rewrite the expression of $\tilde{c}$ (2.31) as follows

$$\tilde{c} = \sqrt{\frac{A}{\rho}K\partial_A\phi + \frac{\varphi\Psi}{2\rho} + \frac{A\varphi}{\rho\varepsilon}} = \sqrt{\frac{A}{\rho}\frac{\partial p}{\partial A} - \frac{A}{\rho\varepsilon}\frac{\partial p}{\partial \Psi}} = \sqrt{c_V^2 - \frac{A}{\rho\varepsilon}\frac{\partial p}{\partial \Psi}}, \tag{2.39}$$

expression (2.38) becomes

$$\nabla\lambda_i(\boldsymbol{Q})\cdot\boldsymbol{R}_i(\boldsymbol{Q}) = \pm\left(\frac{c_V}{\tilde{c}}\frac{\partial c_V}{\partial A} - \frac{1}{2\tilde{c}}\frac{1}{\rho\varepsilon}\frac{\partial p}{\partial \Psi} - \frac{1}{2\tilde{c}}\frac{A}{\rho\varepsilon}\frac{\partial^2 p}{\partial \Psi\partial A} + \frac{\tilde{c}}{A} - \frac{1}{\varepsilon}\frac{c_V}{\tilde{c}}\frac{\partial c_V}{\partial \Psi}\right), \quad i = 1,3. \tag{2.40}$$

Noting that

$$\frac{\partial c_V}{\partial \Psi} = \frac{1}{2c_V}\frac{A}{\rho}\frac{\partial^2 p}{\partial \Psi\partial A}, \tag{2.41}$$

and that

$$\frac{\partial p}{\partial \Psi} = -\varphi, \quad \frac{\partial^2 p}{\partial \Psi\partial A} = \frac{\varphi}{2A}, \tag{2.42}$$

we obtain

$$\nabla \lambda_i(\boldsymbol{Q}) \cdot \boldsymbol{R}_i(\boldsymbol{Q}) = \pm \left(\frac{c_V}{\tilde{c}} \frac{\partial c_V}{\partial A} + \frac{\tilde{c}}{A} \right). \tag{2.43}$$

Since $\tilde{c} > 0$, we need to prove that

$$c_V \frac{\partial c_V}{\partial A} + \frac{\tilde{c}^2}{A} > 0. \tag{2.44}$$

Recalling the expression of the wave speed $\tilde{c}$ (2.31), where it appears as denominator the relaxation parameter ε, we conclude that, under the assumption that the system is strictly hyperbolic, we can always choose $\varepsilon > 0$ small enough such that inequality (2.44) is fulfilled and λ_1-, λ_3-characteristic fields are genuinely non-linear. Hence, the parameters have no explicit mathematical constraints, only needing to satisfy physiological ones. As a result, we can reduce the hypotheses on the fitting parameters, with respect to the elastic model, because the viscoelastic model preserves its nature even when we relax conditions (2.12) (or equivalently (2.15)) and consider $m \in \mathbb{R}$ and $n \in \mathbb{R}$.

2.2.4 Tube law parameter estimation

We are interested in estimating parameters K, m, n, Γ of tube laws (2.2) and (2.22) by fitting ovine and human in vitro data. Here, we introduce the in vitro data and we describe the methodology that we used for the evaluation of the parameters.

2.2.4.1 In vitro data

The experimental data used in this study (Bia et al., 2014; Bia Santana et al., 2007; Zócalo et al., 2007) consist of multiple sets of pressure-diameter time series acquired from 12 adult sheep and from 15 humans.

All protocols applied to record the data were approved by the Research and Development Council of the Universidad de la Republica (Uruguay) and were conducted in accordance with the guide for the care and use of laboratory animals (Council, 1996).

For all the data (ovine and human), pressure values (in mmHg) have been recorded through the usage of a solid-state microtransducer (Model P2.5, 1200 Hz frequency response; Konigsberg Instruments, Pasadena, CA, USA). Vascular diameters have been measured with a pair of ultrasonic gauges (5 MHz; 2 mm diameter) sutured to the adventitia. A sonomicrometer (Triton Technology Inc., San Diego, CA, USA) has been used to convert transit time (1580 m/s) to distance.

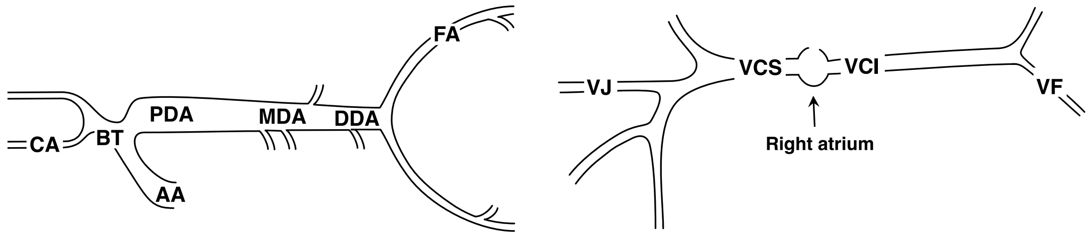

(a) Ovine systemic arterial network

(b) Ovine veins' network

Figure 2.3: Schematic representation of the ovine vessels' network, with the indication of the main vessels. Panel (a) on the left, the ovine systemic arterial network. AA: ascending aorta, BT: brachiocephalic trunk, CA: carotid artery, PDA: proximal descending aorta, MDA: medial descending aorta, DDA: distal descending aorta, FA: femoral artery. Panel (b) on the right, the ovine veins' network. VJ: jugular vein, VCS: superior vena cava, VCI: inferior vena cava, VF: femoral vein. Adapted from Battista et al. (2016) and Zócalo et al. (2007)

The measures of ovine data have been taken in different vessels: seven arteries of the systemic circulation, i.e. carotid artery (CA), brachiocephalic trunk (BT), ascending aorta (AA), proximal descending aorta (PDA), medial descending aorta (MDA), distal descending aorta (DDA) and femoral artery (FA), two arteries of the pulmonary circulation, i.e. main pulmonary artery (PT) and left pulmonary artery (LPA), and four veins, i.e. inferior vena cava (VCI), superior vena cava (VCS), jugular vein (VJ) and femoral vein (VF) (Fig. 2.3). In vitro tests for ovine arteries have been carried out at physiological pressure, while ovine veins have been tested under both low (L - physiological) and high (H - arterial values range) pressure (Bia et al., 2014; Zócalo et al., 2007). The aforementioned prefixes shall be utilised henceforth in the text, tables, and illustrations to specify the data that is being referenced. The methodology used to record ovine data can be divided into two parts (Bia et al., 2007, 2014; Zócalo et al., 2007). Firstly, the animals have been anesthetized and segments of the selected vessels have been delimited in vivo using two suture stitches. Following this, pressure and diameter sensors have been instrumented on each segment before excision, and in vivo data have been subsequently collected. During the second phase, the sheep have been euthanized and their instrumented segments have been carefully removed and mounted in custom cannulae within the flow circuit (in vitro system). They have been then immersed and perfused with oxygenated Tyrode's solution at a temperature of $37°C$ and a pH of 7.4. The same in vivo vessels' length has been maintained in the process. After a period of adaptation of 15 min, in vitro measures of pressure and diameter have been gathered. Pressure and diameter signals from 10 to 20 consecutive cycles have been sampled simultaneously every 5 ms (sampling rate = 200 Hz). Pressure levels and stretch rates ("heart rate") similar to those observed in sheep have been chosen. The previously acquired in vivo data have been used to confirm the adequate quality of the diameter and pressure signals and to generate in vitro pressure waveforms that simulate the morphology of the pressure waveforms found in vivo.

For both human and sheep data, pressure values (in mmHg) and diameter values (in mm) were recorded under dynamic conditions. The recordings for human data have been done for two types of vessels at high pressure: saphenous vein (Saf) and femoral artery (Fem). These segments have been obtained from donors in a condition of brain death with aseptic surgical techniques, during multiple organ and tissue harvesting (Bia Santana et al., 2007). The methodology utilized to record this data is comparable to that used for ovine data (Bia et al., 2007). Prior to vessels removal, the segments have been measured and marked with two suture stitches. Subsequently, they have been cut off and fitted onto the same in vitro setup for biomechanical testing. Throughout this process, efforts have been made to maintain the length of the in vivo vessels. Pressure and diameter signals from 10 to 20 consecutive cycles have been simultaneously sampled every 5 ms (sampling rate = 200 Hz), using pressure levels and stretch rates ("heart rate") similar to those observed in humans.

A typical example of the acquired in vitro data is shown in Fig. 2.4a.

2.2.4.2 Estimation procedure setup

Here, we detail the procedure utilized in our study to derive parameter estimates from in vitro data. Fig. 2.4 shows a conceptual scheme of this process.

Starting from the acquired in vitro data (Fig. 2.4a), we preprocessed all the pressure-diameter time series. Specifically, for each type of vessel we had several datasets containing the samples acquired (Table 2.1). Each of these datasets consisted of a time series of pressure and diameter values for more than a single cycle. For all the time series we have identified the peaks (red dots in Fig. 2.4a) and the troughs (red crosses in Fig. 2.4a) in the curves. The peaks are the moments of maximum pressure (diameter), while the troughs are the moments of minimum pressure (diameter). By identifying the peaks and troughs in the pressure-diameter time series, we extracted the data associated with individual cycles. We then calculated the mathematical mean over multiple cycles to obtain average signals. These averages are represented by an area-pressure loop, obtained considering the extracted pressures and the circular areas, whose diameters correspond to the extracted ones. These loops describe on average the behavior of the vessels along a single cardiac cycle. An example of such loops can be seen in Fig. 2.4b1, where the gray curve represents the raw in vitro data, the black curve is the average signal, the

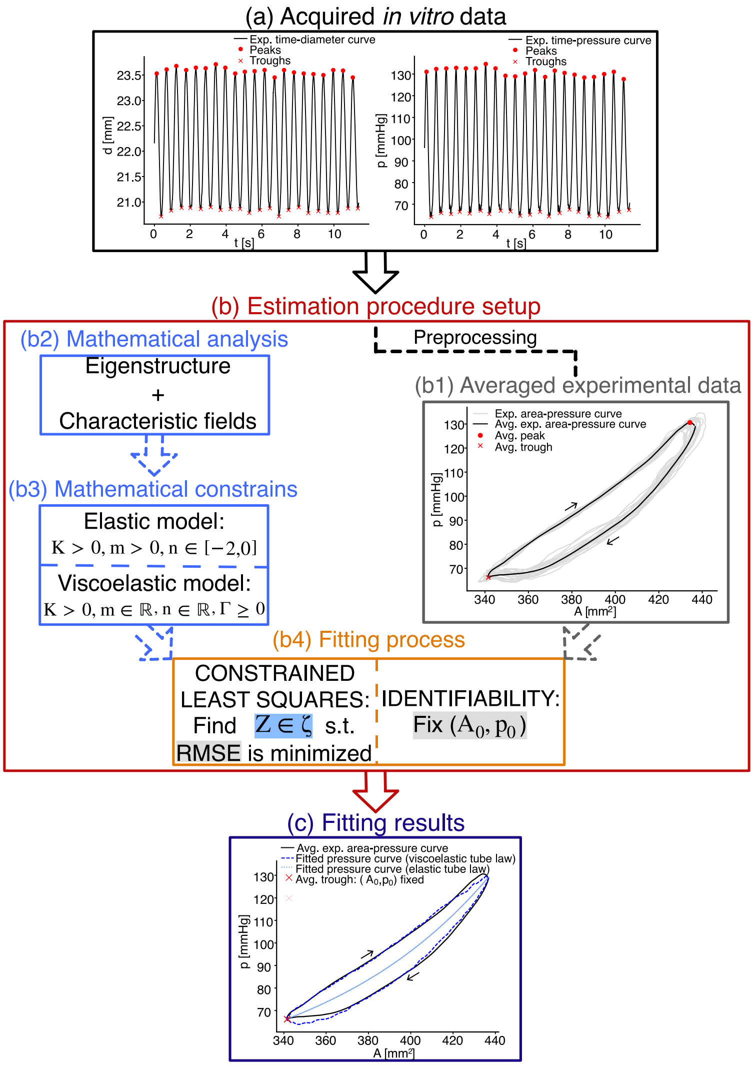

Figure 2.4: Conceptual scheme of the methodology used for the parameter estimation process. Overview of the process showing the input, which is an example of acquired in vitro data (a), the estimation procedure (b) to pass from the input to the output, and the output, which is the final fitting result (c). The estimation procedure (b) is composed of different steps. A phase of preprocessing of the acquired in-vitro data is used to obtain the averaged experimental data (b1). Instead the mathematical analysis (b2) of the two considered models is used to ensure that the mathematical properties of the models in which we are interested are preserved, through mathematical constrains (b3) on the parameters that must be fulfilled. All these steps are then used in the fitting process (b4) that gives us the final results. Specifically, it focuses on two aspects. Firstly, we fix A_0 and p_0 to enhance the identifiability of the other parameters. Secondly, the other parameters, which are represented by the vector $\boldsymbol{Z} = [K, m, n, \Gamma]$, were determined through minimising the root mean squared errors (RMSE). The range ζ within which the parameters must fall is outlined in Table 2.2.

red cross is the averaged trough, and the red dot is the averaged peak. The descending branch, connecting the averaged peak to the averaged trough, represents the relaxation phase. Here we observe a steep decrease of both pressure and vessel area. The ascending branch, connecting the averaged trough to the averaged peak, represents the loading phase. During this phase, pressure and area initially increase slowly due to vessel's compliance, then the increase becomes steep, as the vessels stiffen when subjected to higher pressures. The obtained averaged experimental data (Figure 2.4b1) were then saved and the fitting process (Fig. 2.4b4) was applied to these averaged curves.

We now introduce the constrains derived from the mathematical analysis. Recalling that our goal is to fit experimental data while ensuring that the use of such parameters in 1D blood flow models results in hyperbolic mathematical problems with genuine nonlinear characteristic fields (Fig. 2.4b3). As outlined in sections 2.2.2.2 and 2.2.2.3, the parameters of the elastic tube law (2.2) have to satisfy the following mathematical constrains

$$K > 0, \quad m > 0 \quad \text{and} \quad n \in [-2, 0]. \tag{2.45}$$

Similarly, in sections 2.2.3.2 and 2.2.3.3, we demonstrated that the parameters of the viscoelastic tube law (2.22) have to fulfill the following constrains

$$K > 0, \quad m \in \mathbb{R}, \quad n \in \mathbb{R} \quad \text{and} \quad \Gamma \geq 0. \tag{2.46}$$

The fitting process is the final step of the estimation procedure setup (Fig. 2.4b4) and it takes advantage of all the previous steps. Here, we used the constrained least squares technique to identify the parameters that best fit tube laws (2.2) and (2.22) to the observed in vitro data. Additionally, we fixed A_0 and p_0 to increase the identifiability of the remaining parameters, making the estimation process more accurate. We extracted the values of A_0 and p_0 in the averaged troughs (red cross in Fig. 2.4b1) to ensure that these values were as precise as possible, given the minimal motion of the vessels at those points in the cycle. To provide an overview of the obtained results, Table 2.1 displays the values for A_0 and p_0 in terms of minimum, average and maximum for every type of vessel. The decision to fix A_0 and p_0 is based on two main reasons. Firstly, it is a common practice in hemodynamics to fix these parameters as A_0 and p_0 can be derived from experimental area-pressure data. Secondly, a local sensitivity and collinearity analysis (results not reported here, (Colombo, 2021)) showed that pressure $p(x,t)$ is very sensitive to changes in A_0. Therefore, we fixed it to avoid that the estimation problem was affected by inaccurate A_0 estimates.

The constrained least squares problem (Fig. 2.4b4) reads

$$\text{Find } \boldsymbol{Z} \in \zeta \text{ such that } f(\boldsymbol{Z}) \text{ is minimized.} \tag{2.47}$$

Table 2.1
Statistics of A_0 and p_0. Minimum, average and maximum values in the averaged trough of the parameters A_0 and p_0 for all the vessel types (Vess.).

Vess.	Num.*	A_0 [mm^2]			p_0 [mmHg]		
		Min.	Avg.	Max.	Min.	Avg.	Max.
Sheep systemic arteries							
AA	12	289.58	365.01	415.86	63.01	68.65	77.88
BT	11	248.83	304.80	489.15	60.79	66.78	74.08
CA	11	39.11	53.13	65.14	61.47	66.28	71.67
DDA	11	221.77	230.98	247.27	55.99	63.33	68.53
FA	11	21.87	26.60	32.64	61.63	67.97	72.84
MDA	11	247.50	267.49	279.74	54.88	63.52	69.43
PDA	11	263.78	284.87	294.97	59.28	65.31	71.68
Sheep pulmonary arteries							
LPA	11	138.93	179.45	242.89	9.91	12.14	14.85
PT	10	327.43	399.00	459.56	9.92	12.18	15.07
Sheep veins at high (H) pressure							
HVCI	5	255.39	318.32	377.11	63.32	70.12	74.31
HVCS	8	203.59	239.32	258.09	63.86	75.81	90.23
HVF	5	25.81	28.32	31.73	78.80	83.42	87.23
HVJ	8	67.99	152.54	258.11	67.14	79.96	101.16
Sheep veins at low (L) pressure							
LVCI	10	174.35	271.30	372.28	-2.13	1.73	4.07
LVCS	12	76.09	128.65	227.40	-0.68	2.39	6.97
LVF	30	19.62	27.32	42.22	0.55	10.39	28.64
LVJ	10	28.54	75.18	148.47	0.12	3.57	12.07
Human vessels							
Fem	30	23.69	43.90	55.53	54.93	73.58	107.24
Saf	20	27.11	41.37	48.46	52.81	68.61	102.03

*Number of available sets of data for each type of vessel

$\boldsymbol{Z}$ is the vector representing the parameters to estimate. For the elastic tube law (2.2), $\boldsymbol{Z} = [K,m,n]$, while for the viscoelastic tube law (2.22), $\boldsymbol{Z} = [K,m,n,\Gamma]$. ζ is a subset of either $\mathbb{R}^3$ (elastic tube law) or $\mathbb{R}^4$ (viscoelastic tube law) representing the parameter space. $f(\boldsymbol{Z})$ is the objective function we need to minimize, whose expression is determined by the residual vector $\boldsymbol{r}(\boldsymbol{Z})$. Its i-th component is given by

$$r_i(\boldsymbol{Z}) = p_{exp}(t_i) - p_{approx}(\boldsymbol{Z};t_i), \tag{2.48}$$

where $p_{exp}(t)$ is the experimental area-pressure relation $\forall t \in \mathbb{R}^+$, obtained from the averaged experimental data (black curve in Fig. 2.4b1), while $p_{approx}(\boldsymbol{Z};t)$ is the pressure curve that we

Table 2.2
Parameter estimations summary. The performed estimations have been summarized, with each case being identified by a specific name. The elastic tube law is represented by the letter E, while the viscoelastic tube law is represented by the letter V.

Elastic tube law				
Case	K	m	n	Γ
E1	$K>0$	$m>0$	$n\in[-2,0]$	$\Gamma=0$
E2	$K>0$	$m=10.0$	$n=-1.5$	$\Gamma=0$
E3	$K>0$	$m=0.5$	$n=0.0$	$\Gamma=0$
E4	$K>0$	$m\in\mathbb{R}$	$n\in\mathbb{R}$	$\Gamma=0$

Viscoelastic tube law				
Case	K	m	n	Γ
V1	$K>0$	$m>0$	$n\in[-2,0]$	$\Gamma>0$
V2	$K>0$	$m=10.0$	$n=-1.5$	$\Gamma>0$
V3	$K>0$	$m=0.5$	$n=0.0$	$\Gamma>0$
V4	$K>0$	$m\in\mathbb{R}$	$n\in\mathbb{R}$	$\Gamma>0$

want to parametrize and that must satisfy relation (2.2) or (2.22). We decided to evaluate the accuracy of the estimation process computing the root mean squared error (RMSE) between $p_{exp}(t)$ and $p_{approx}(\boldsymbol{Z};t)$, normalized with respect to the pressure range. Thus, the objective function reads

$$f(\boldsymbol{Z}) = \text{RMSE} = \frac{\sqrt{\frac{1}{n_r}\sum_{i=1}^{n_r}(r_i(\boldsymbol{Z}))^2}}{\max\limits_{i=1,\dots,n_r}[p_{exp}(t_i)] - \min\limits_{i=1,\dots,n_r}[p_{exp}(t_i)]}, \tag{2.49}$$

where n_r is the size of $\boldsymbol{r}(\boldsymbol{Z})$. We solved the constrained least squares problem applying a constrained non-linear optimization technique, called Trust Region Reflective (Branch et al., 1999; Nocedal and Wright, 1999). This method produces a solution only when the convergence conditions have been met. Specifically, we have implemented a termination tolerance for both cost function modification and change in independent variables, set at 10^{-15}.

We performed 4 estimations for each tube law (Table 2.2) using the described setup. For each estimation we performed 100 optimizations, defining each time a new random uniformly distributed initial guess, to ensure the convergence of the optimization process. Our aim was to compare the models, and investigate any differences between values of the parameters found in literature (Brook et al., 1999; Formaggia et al., 2003; Müller and Toro, 2014; Siviglia and Toffolon, 2013) and those obtained from our multiple estimations. Cases E1 and V1 are derived from constraints (2.45), while cases E4 and V4 come from constraints (2.46). Cases E2, E3, V2, and V3 are based on literature examples (Brook et al., 1999; Formaggia et al., 2003; Müller and Toro, 2014; Siviglia and Toffolon, 2013), where m and n are fixed, and K and Γ are allowed to vary. The different cases define the subset ζ.

2.3 Results

Quantitative results are displayed in Fig. 2.5 for each vessel type in terms of average (central dot), minimum (lower whisker) and maximum (upper whisker) RMSEs. The 5 panels on the left display the results for the estimations obtained using the elastic tube law (cases E1-E4), while the 5 panels on the right display the estimations for the viscoelastic tube law (cases V1-V4). Additionally, Table 2.3 reports the values assumed by the averaged RMSEs for the different vessel types and the different estimation cases.

Qualitative results are shown in Figs. 2.6 and 2.7 in terms of fitted pressure curves (p_{approx}). These curves were derived by using the estimated parameters as input data for tube laws (2.2) and (2.22), in addition to the cross-sectional areas obtained from the experiments. Additionally, the time derivative in the viscoelastic tube law (2.22) has been discretized using the forward finite difference approximation. In each plot we have reported in black the considered experimental area-pressure curve, in blue the fitted pressure curve obtained with the elastic estimation cases E1-E4 and in red the fitted pressure curve obtained with the viscoelastic estimation cases V1-V4. The experimental area-pressure curve refer to HVCI for Fig. 2.6 and to LVCI for Fig. 2.7. Additionally, Fig. B.1, B.2, B.3 of appendix A show qualitative results for AA, LPA and Fem, respectively.

Finally, Fig. 2.8 displays the values of the estimated parameters for six selected vessel types and for all the four viscoelastic estimation cases V1-V4, in terms of average (central dot), minimum (lower whisker) and maximum (upper whisker) values. The exact values of the average estimated parameters for case V1 and all vessel types are reported in Table 2.4. Whereas in appendix A, Tables B.1, B.2, B.3 report the exact values of the averaged estimated parameters for estimation cases V2-V4, and Tables B.4, B.5, B.6, B.7 report the exact values of the averaged estimated parameters for estimation cases E1-E4.

2.4 Discussion

2.4.1 Accuracy

This section presents a comprehensive evaluation of the obtained results, with emphasis on accuracy and reliability of the parameter estimations made. After examining Fig. 2.5 and Table 2.3, it becomes apparent that there is a noticeable pattern when comparing E1 to E4, as well as V1 to V4. These cases, which are based on constraints (2.45) and (2.46), demonstrate relatively similar average RMSEs for all types of vessels. This suggests that constraining m and

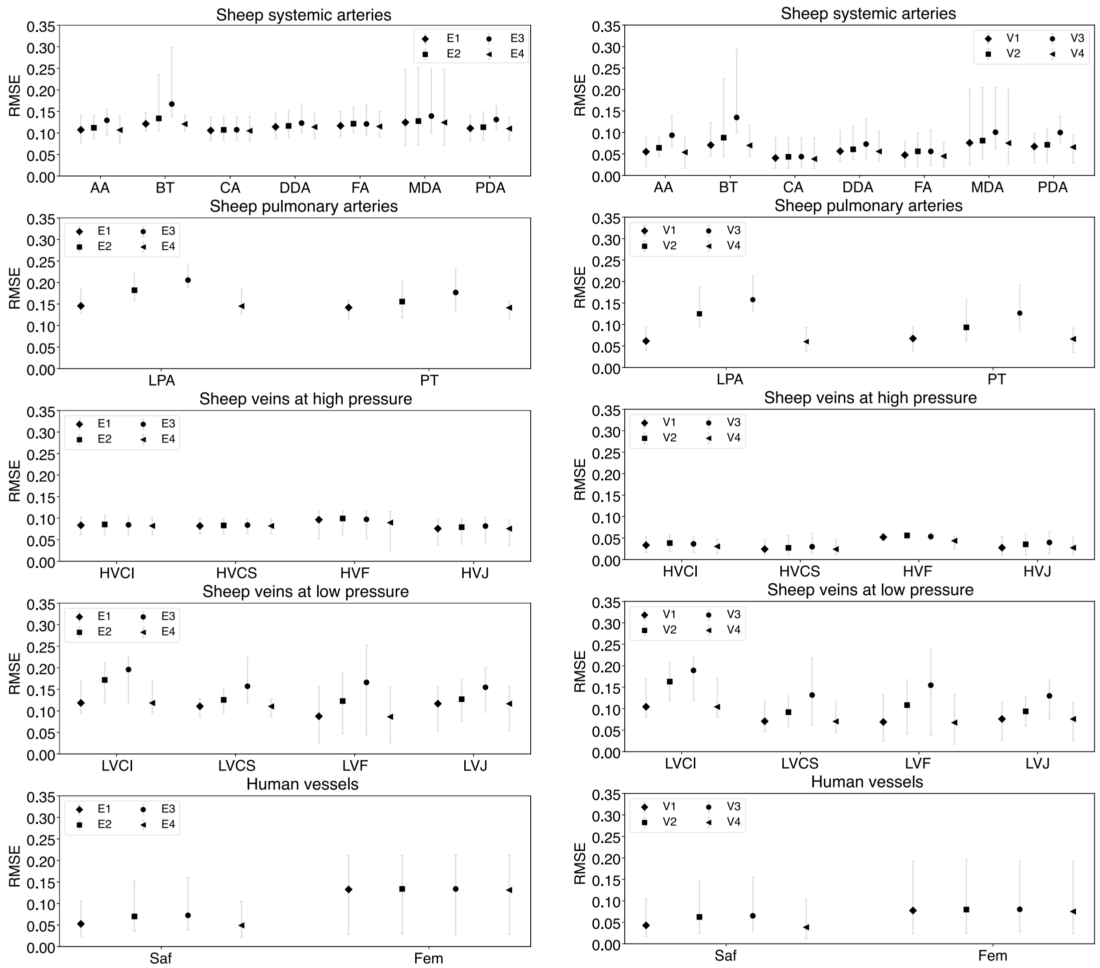

Figure 2.5: RMSEs for all the vessel types and for both the elastic and the viscoelastic tube laws. Average (central dot), minimum (lower whisker) and maximum (upper whisker) RMSEs for each vessel type. On the left, results of the four estimates with the elastic tube law (cases E1-E4). On the right, results of the four estimates with the viscoelastic tube law (cases V1-V4).

n, as we did in E1 and V1 cases, has not a big impact on the accuracy of the estimations. The parameters consistently adopt the optimal configuration of values to achieve the lowest RMSE. More importantly, this aspect allowed us to verify the influence of constraints on estimations, particularly for the elastic tube law (2.2). Upon analyzing the results in Table B.7, that report the obtained estimates of parameters for case E4, we can clearly observe that the estimates of n are always below -2 or above 0. This implies that constraints (2.45) are never met. Hence, the phenomenon we describe using parameters obtained from this fitting (case E4) might lead to the generation of waves that are not present in the cardiovascular system. It is evident that

Table 2.3
Averaged RMSEs. Averaged RMSEs for all the estimation cases (E1-E4 and V1-V4) and for all the vessel types (Vess.).

Vess.	Num.*	Averaged RMSE							
		E1	E2	E3	E4	V1	V2	V3	V4
Sheep systemic arteries									
AA	12	0.11	0.11	0.13	0.11	0.06	0.06	0.09	0.05
BT	11	0.12	0.13	0.17	0.12	0.07	0.09	0.13	0.07
CA	11	0.11	0.11	0.11	0.10	0.04	0.04	0.04	0.04
DDA	11	0.11	0.12	0.12	0.11	0.06	0.06	0.07	0.06
FA	11	0.12	0.12	0.12	0.11	0.05	0.06	0.06	0.04
MDA	11	0.12	0.13	0.14	0.12	0.08	0.08	0.10	0.08
PDA	11	0.11	0.11	0.13	0.11	0.07	0.07	0.10	0.07
Sheep pulmonary arteries									
LPA	11	0.15	0.18	0.21	0.15	0.06	0.13	0.16	0.06
PT	10	0.14	0.16	0.18	0.14	0.07	0.09	0.13	0.07
Sheep veins at high (H) pressure									
HVCI	5	0.08	0.09	0.08	0.08	0.03	0.04	0.04	0.03
HVCS	8	0.08	0.08	0.08	0.08	0.02	0.03	0.03	0.02
HVF	5	0.10	0.10	0.10	0.09	0.05	0.06	0.05	0.04
HVJ	8	0.08	0.08	0.08	0.08	0.03	0.04	0.04	0.03
Sheep veins at low (L) pressure									
LVCI	10	0.12	0.17	0.20	0.12	0.10	0.16	0.19	0.10
LVCS	12	0.11	0.13	0.16	0.11	0.07	0.09	0.13	0.07
LVF	30	0.09	0.12	0.17	0.09	0.07	0.11	0.15	0.07
LVJ	10	0.12	0.13	0.15	0.12	0.08	0.09	0.13	0.08
Human vessels									
Fem	30	0.13	0.13	0.13	0.13	0.08	0.08	0.08	0.08
Saf	20	0.05	0.07	0.07	0.05	0.04	0.06	0.07	0.04

*Number of available sets of data for each type of vessel

while constraining m and n is not essential when dealing with the viscoelastic tube law (2.23), it is crucial when we use the elastic tube law (2.2).

Our results (see Fig. 2.5 and Table 2.3) show also that average RMSEs for cases E2, E3 and V2, V3 are higher compared to those for cases E1, E4, and V1, V4. By allowing for estimation of m and n in a tube law (cases E1, E4, and V1, V4), we enhance the precision of the parameter estimation. The greater weight of uncertainty and errors in cases E2, E3, and V2, V3 is due to the limited number of adjustable parameters (K and Γ) in these cases. Conversely, in cases E1, E4, and V1, V4, all parameters can vary freely and reach the optimal configuration, resulting in smaller RMSEs. Additionally, the cases that present the highest errors are always E3 and V3.

Therefore, if m and n cannot be estimated, but they have to be fixed, then values $m = 10.0$ and $n = -1.5$ (E2 and V2 cases) should be used instead of $m = 0.5$ and $n = 0.0$ (E3 and V3 cases).

Finally, if we compare average RMSEs for elastic cases E1-E4 (Fig. 2.5 left panels) with average RMSEs for viscoelastic cases V1-V4 (Fig. 2.5 right panels), for all the vessel types, we observe that average RMSEs for the viscoelastic cases are lower than those of the elastic cases. Therefore viscoelasticity cannot be neglected and the viscoelastic tube law should be used instead of the elastic tube law, whenever possible.

Studying now qualitative results, if we compare Fig. 2.6a (2.7a) with Fig. 2.6d (2.7d), namely the curves obtained considering cases E1 (V1) and E4 (V4), we cannot see any clear distinction among them. This is in agreement with the previous results, where we showed that averaged RMSEs for these cases are similar. Although the pressure curves fitted for case E4 showed in Fig. 2.6d and Fig. 2.7d resemble the experimental pressure curves, it is important to note that this outcome may not be replicated in more complex vessel networks. Instead, when comparing panels (a) and (d) with panels (b) and (c), it is evident that the fitted pressure curves obtained from cases E1, E4, and V1, V4 (with m and n allowed to vary) better approximate the experimental area-pressure curves, particularly in the case of LVCI (Fig. 2.7). By fixing m and n in cases E2, E3, and V2, V3, we limit the ability to capture the non-linearity of the curve to only K and Γ. If all four parameters are allowed to change, as expected a better fit can be found. This scenario corresponds to what we have underlined previously in terms of averaged RMSEs, even though the differences between E2 (V2) and E3 (V3) cases are not qualitatively detectable. The pressure curves in panels (b) and (c) of both Fig. 2.6 and Fig. 2.7 are very similar.

Finally, if we look at Fig. 2.6 and 2.7, it is clear that the hysteresis cycles are better captured by the red dashed lines, which are the fitted curves obtained using the viscoelastic tube law. The agreement between these curves and the experimental area-pressure curves is satisfactory, especially in V1 and V4 cases. Instead the blue lines, which represent the fitted curves obtained with the elastic tube law, approximate the hysteresis with straight lines and slightly overestimate the pressure peaks in the pressure-time curves. These final considerations are significant because they confirm again our quantitative results and because similar observations have been made also by other authors (Alastruey et al., 2011; Battista et al., 2016).

Before proceeding further, a remark has to be made. Among all the datasets that we used for this study, we observed that some of them present averaged experimental area-pressure curves with squeezed or twisted hysteresis cycles. Despite the particular shape of these averaged experimental data, the estimation process was only slightly affected. The obtained RMSEs for these particular datasets all belong to the upper whiskers (Fig. 2.5) of the vessel types the datasets refer to. However, they never assume the maximum RMSE value. Therefore, we

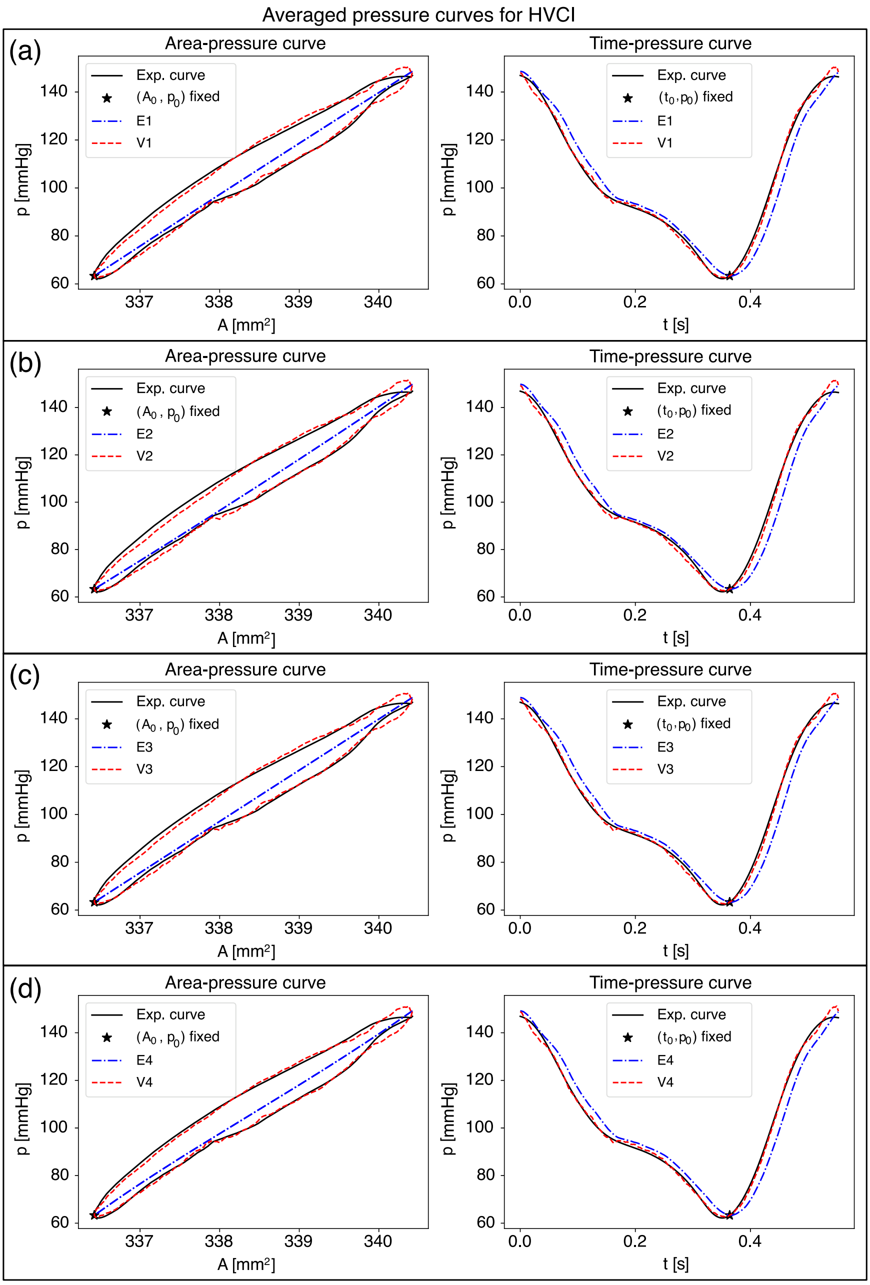

Figure 2.6: Fitted pressure curves for HVCI. Comparison between experimental and fitted pressure curves for all the estimation cases of an example dataset of VCI at high (H) pressure. Black solid lines represent averaged experimental area-pressure and time-pressure curves, blue dash-dot lines represent the fitted curves obtained considering the elastic cases E1-E4, while red dashed lines represent the fitted curves obtain considering the viscoelastic cases V1-V4.

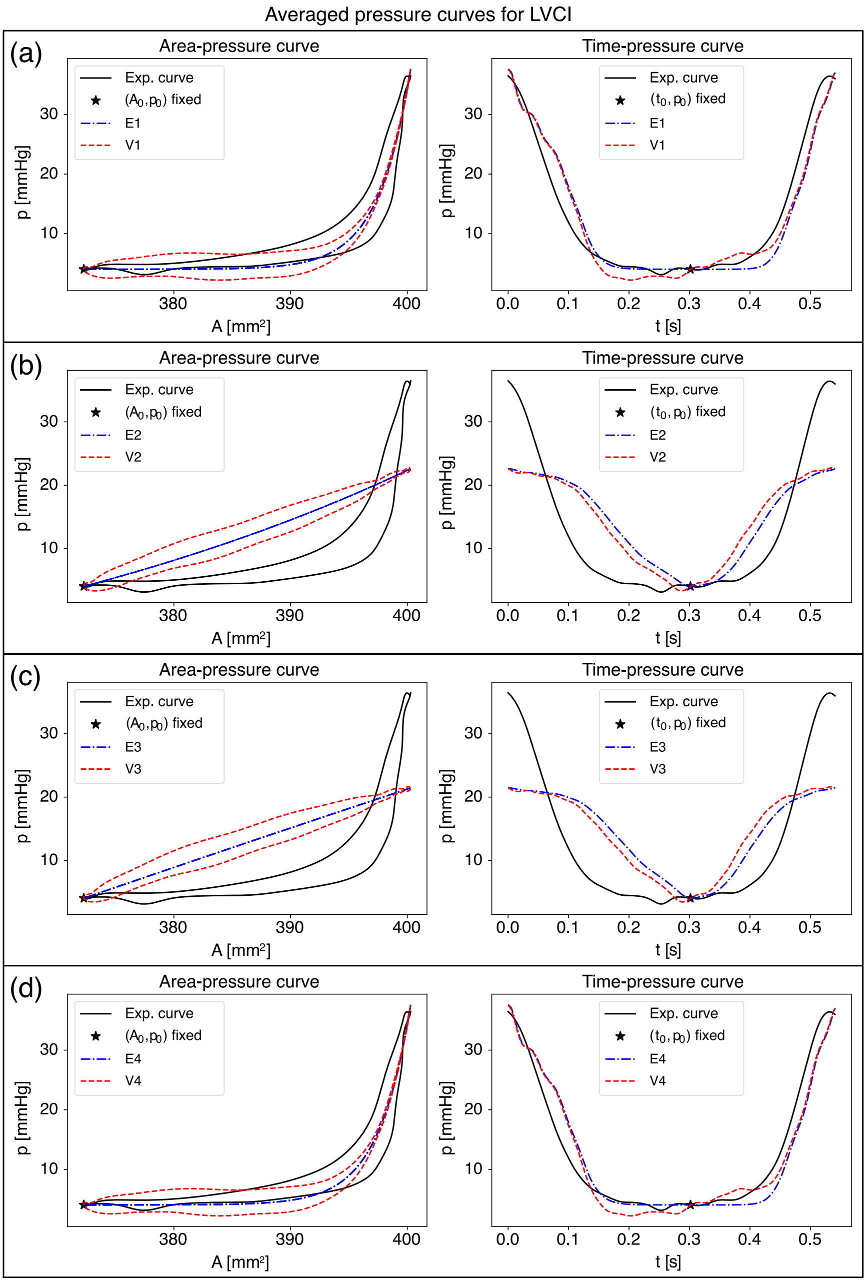

Figure 2.7: Fitted pressure curves for LVCI. Comparison between experimental and fitted pressure curves for all the estimation cases of an example dataset of VCI at low (L) pressure. Black solid lines represent averaged experimental area-pressure and time-pressure curves, blue dash-dot lines represent the fitted curves obtained considering the elastic cases E1-E4, while red dashed lines represent the fitted curves obtain considering the viscoelastic cases V1-V4.

decided to maintain these datasets as part of the study. Nevertheless, it means that the tube laws we are considering are not able to reproduce this kind of waveforms. A more sophisticated tube law that encompasses additional physical factors should be examined, such as the tube laws utilised in Bertaglia et al. (2020) or in Valdez-Jasso et al. (2011).

2.4.2 Averaged estimated parameters

The ability of the viscoelastic tube law (2.22) to better approximate the behavior of the experimental area-pressure relations has been demonstrated in the previous section, where quantitative and qualitative comparisons between elastic and viscoelastic models have been made. Nevertheless, the elastic tube law is still widely used, thanks to its simpler formulation and its good representation of the dominating effect, the elastic response to vessel wall's deformations. However, predictably, when modeling hysteresis cycles, viscoelasticity is crucial. This is also confirmed by the averaged estimated parameters obtained with the viscoelastic tube law. If we examine the last panel in Fig. 2.8, which shows the results obtained for the viscoelasticity parameter Γ, it is worth noting that the average estimates across all cases and those specific to individual vessel types are nearly indistinguishable, despite the variability of the estimates of the different datasets of a specific vessel type can be significant. This observation is confirmed by results reported in Table 2.4 and Tables B.1, B.2, B.3, which clearly show that Γ values for individual vessel types are very similar. This indicates that Γ is distinct for a specific vessel type and can be accurately estimated. Additionally, if we study the differences between vessel types, we observe how Γ estimated values have an order of magnitude of difference between pulmonary and systemic arteries. Our results show that the viscoelasticity of LPA and PT is lower than the viscoelasticity of the systemic arteries and assume a value around 4.76 Pa s m. Conversely, systemic arteries range between 13.69 and 93.89 Pa s m, with an increase in Γ from AA towards DDA. This is in agreement with the observations made by Bia et al. (2014), where the authors showed that the increase in the viscoelasticity depends on the amounts of collagen and smooth muscle cells, components of the vessel walls (Burton, 1954; Levick, 2009). As for the ovine veins, rather different values of Γ have been obtained for the same type of veins at low and high pressure. Particularly, results for data regarding high pressure veins produced a viscoelasticity coefficient that is at least one order of magnitude greater than low pressure veins. This is in agreement with different studies (Zócalo et al., 2013), where it has been observed that veins viscoelasticity has the functional role of energy dissipation and adaptive response to hemodynamic overload conditions.

Observing now the panels for K, m and n parameters of Fig. 2.8, we see that the values

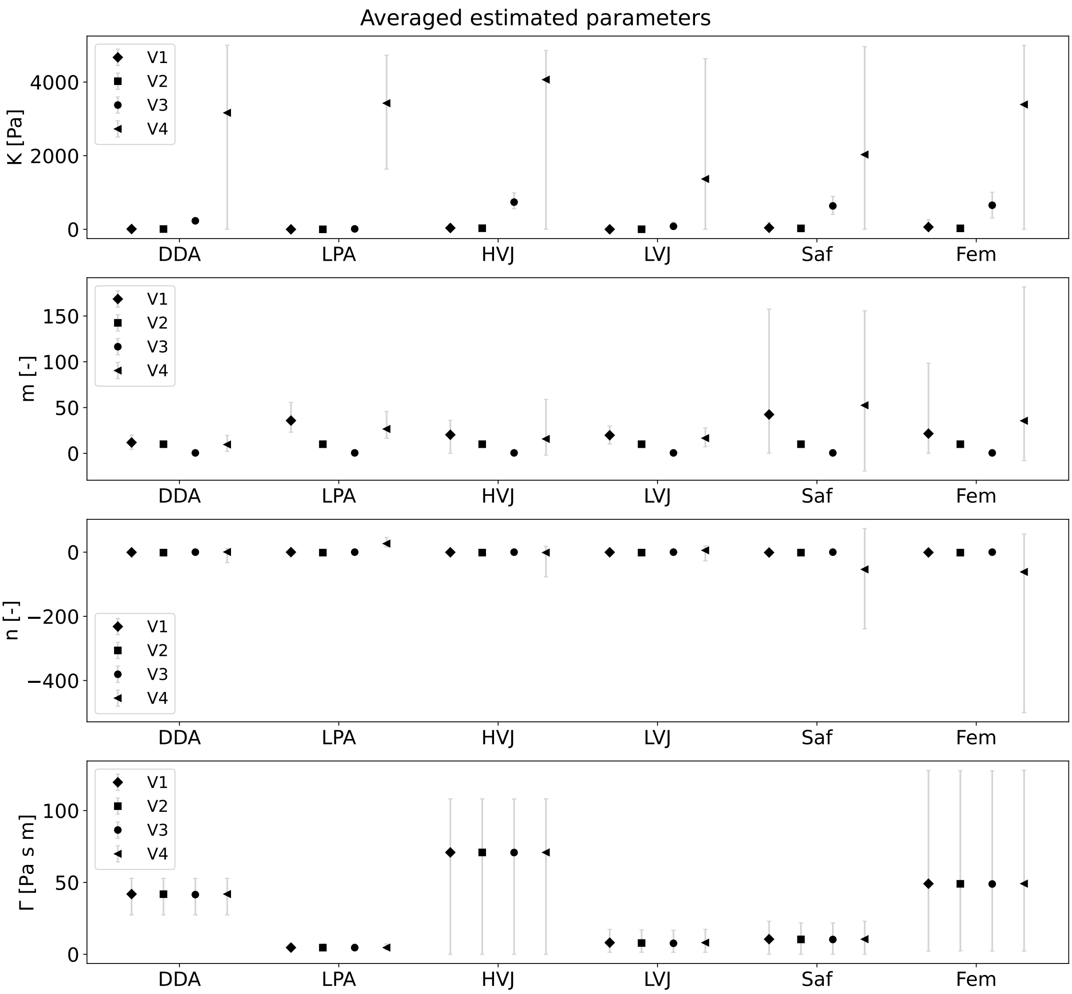

Figure 2.8: Averaged estimated parameters of the viscoelastic tube law. Averaged (central dot), minimum (lower whisker) and maximum (upper whisker) estimated parameters of the viscoelastic tube law for six selected vessel types and for all the viscoelastic estimation cases V1-V4.

of the three parameters can change and modify themselves to always have the best approximation of the experimental data. Nevertheless, analyzing Tables 2.4 and B.3, we note how the estimated values of the stiffness coefficient K increase from AA towards DDA. Different studies on arterial wall composition (Bia et al., 2014) show that the quantity of elastin directly influences arterial wall compliance and that there is an increase in compliance from peripheral arteries to the aortic root, thus the increase we observed in K aligns with such physiological observations. Moreover, we observe that the values of K are higher for muscular arteries, such as the peripheral arteries CA and FA, compared to other ovine arteries. This is noteworthy as

Table 2.4
Averaged estimated parameters of the viscoelastic tube law for V1 estimation case.

Vess.	Num.*	K [kPa]	m [–]	n [–]	Γ [Pa s m]
Sheep systemic arteries					
AA	12	1.78	8.31	-0.83	13.69
BT	11	1.13	14.80	-1.27	19.26
CA	11	202.74	14.21	-1.27	93.89
DDA	11	8.68	11.85	-0.55	41.89
FA	11	40.16	9.30	-0.91	22.61
MDA	11	4.27	8.67	-1.36	19.66
PDA	11	2.02	10.96	-1.64	16.01
Sheep pulmonary arteries					
LPA	11	0.02	35.78	-0.00	4.66
PT	10	0.13	20.85	-0.00	4.86
Sheep veins at high (H) pressure					
HVCI	5	274.83	7.98	-1.60	214.50
HVCS	8	88.23	14.25	-0.25	140.46
HVF	5	97.18	6.22	-2.00	28.44
HVJ	8	36.47	20.31	-0.50	70.88
Sheep veins at low (L) pressure					
LVCI	10	19.29	64.22	-0.80	7.04
LVCS	12	0.75	15.34	-1.33	8.70
LVF	30	3.45	21.54	-0.87	4.16
LVJ	10	0.65	19.78	-0.40	8.09
Human vessels					
Fem	30	62.07	21.54	-0.93	49.12
Saf	20	41.73	42.41	-1.20	10.52

*Number of available sets of data for each type of vessel

K is proportional to the Young's elastic modulus, to the vessel wall thickness and to the inverse of the vessel radius (Alastruey et al., 2011). Thus, since CA and FA have smaller diameters respect the other considered arteries, the small radius can lead to higher values of K in these two cases. The higher values of CA and FA are also coherent with the fact that external vessels have thicker walls than inner vessels because they must be able to resist also to external forces that could deform them (Levick, 2009). Instead, ovine veins exhibit even higher estimated values of K compared to arteries. But in this case the explanation of high values is connected with the presence of collagen. Veins indeed are more compliant at low pressure values than arteries, but for high pressures they become very stiff (Zócalo et al., 2013).

Regarding the other two parameters (m and n), central panels of Fig. 2.8 show that the obtained averaged estimated m and n for cases V1 and V4 differ from the literature values that we were considering (V2, V3 cases). Specifically, it can be read in Tables 2.4 and B.3 how all the estimated values of m range between 6.22 and 64.22, and this is in line with the fact that for $m > 1$ vessels tend to become stiffer as deformations grow, as it happens for real vessels. When a value of $m < 1$ is assumed, the described behavior is the opposite. Vessels tend to be softer for high pressure values, but this is against physiological observations. Thus, this is a further confirmation that case V3 ($m = 0.5$ and $n = 0.0$) and in general any value of $m < 1$, should not be adopted if large vessel deformations are to be modelled.

2.5 Conclusion

In this work, we estimated the parameters of elastic and viscoelastic tube laws using in vitro data from ovine and human sources. Our methodology involved constraining the parameters to specific ranges in order to maintain prescribed mathematical properties.

The results we obtained demonstrate that both the elastic and the viscoelastic tube laws can replicate the in vitro experimental data. Nevertheless, we noted that the elastic tube law cannot depict the experimentally observed hysteresis cycles owing to the absence of the viscous term in its formulation. Furthermore, it has been noted that the viscoelastic tube law provides a quantitative and qualitative description of all in vitro data utilised in this study. However, the law's viscous component requires improvement to represent more tightly or twisted hysteresis cycles effectively. A dependency on pressure, similar to the one proposed in Bertaglia et al. (2020), should be included to achieve better capture of these particular hysteresis cycles.

Within this study, it was demonstrated that the constraining procedure is essential for obtaining accurate estimates that can be utilised in more complex blood vessel networks, particularly when considering the elastic tube law. The calibrated models are appropriate for representing the pressure-area relationship under experimentally observed pressure conditions. If specific phenomena, such as vessels' collapse or stiffening, need to be described, new parameterizations of the tube laws are necessary. In fact, the tube laws we are currently considering are incomplete. Proper generalisation of both low and high-pressure regimes can be achieved simultaneously by adding new non-linear terms to the mathematical formulation of the tube laws or by coupling the models we are considering with other specific models to describe the particular phenomena.

Finally, we also tested the two tube laws by allowing all their parameters to vary freely within their respective ranges and by fixing some of their parameters. We observed that it is desirable to adopt the first approach ("leaving the parameters free") to ensure that the experimental pressure-area curves are reproduced adequately. Nevertheless, we also observed that anyhow it is possible to fix some of the parameters of the tube laws, but careful consideration must be given to the chosen values.

Chapter **3**

Well-balanced high-order method for non-conservative hyperbolic PDEs with source terms: application to one-dimensional blood flow equations with gravity

Chiara Colombo, Caterina Dalmaso, Lucas O. Müller, and Annunziato Siviglia

The present work proposes a well-balanced finite volume-type numerical method for the solution of non-conservative hyperbolic partial differential equations (PDEs) with source terms. The method is characterized, first, by the use of a recently introduced high-order spatial reconstruction, based on generalized Riemann problem information from the previous time level. Such reconstruction is well-balanced up to order three, compact, efficient and easy to implement. Second, the method incorporates a well-balanced space-time evolution operator, which allows for well-balanced fully explicit time evolution. The accuracy and efficiency of the method are assessed on both a scalar problem (Burgers' equation) and a nonlinear PDE system (hyperbolized one-dimensional blood flow equations with gravity and friction, and with variable mechanical and geometrical properties). The well-balanced property is verified by showing that numerically-determined stationary solutions are preserved up to machine precision. The order of accuracy in space and time is validated through empirical convergence rate studies. Additionally, the performance of the method is assessed on a network of 86 arteries, under both stationary and transient conditions.

This chapter is under review in the Journal of Computational Physics.
It has also been published on ArXiv repository as: *Colombo C., Dalmaso C., Müller L. O., Siviglia A. Well-balanced high-order method for non-conservative hyperbolic PDEs with source terms: application to one-dimensional blood flow equations with gravity. http://arxiv.org/abs/2509.22190*

3.1 Introduction

Several physical phenomena can be modeled through non-conservative hyperbolic PDEs with source terms. Notable examples include the shallow water equations (SWEs) with moving bottom topography (Siviglia et al., 2022), the multilayer SWEs with variable density (Guerrero Fernández et al., 2022), the Euler equations with gravity (Bermudez et al., 2016; Gaburro et al., 2018), and the characterization of blood flow within vessels having variable physical properties (Müller and Toro, 2013; Toro and Siviglia, 2013). The solution of such equations in the presence of discontinuities (shock waves) poses several challenges, as the conservative form of the equations no longer holds. One of the main issues is the definition of jump relations across a discontinuity, which has been addressed by Dal Maso et al. (1995) interpreting the jump relations as Borel measures dependent on the path connecting the two sides of the discontinuity.

A second issue is the description of steady-state solutions in the presence of geometric- and/or algebraic-type source terms, which can be discontinuous (Murillo et al., 2019). Such solutions should be accurately captured by the numerical methods used to solve the considered PDEs. Moreover, they should be recovered after small perturbations in the initial data, in order to avoid spurious oscillations that might cause significant deviations from the exact solution (Castro Díaz et al., 2007; Guerrero Fernández et al., 2022). A numerical scheme able to preserve the correct balance between advective and source terms was initially introduced in 1994 for the SWEs by Bermudez and Vazquez (1994), paving the way for the numerous first- and high-order approaches developed in the last thirty years for different systems of balance laws (Berberich et al., 2021; Castro and Parés, 2020; Castro Díaz et al., 2007; Gómez-Bueno et al., 2021; Gosse, 2000; Greenberg et al., 1997; Guerrero Fernández et al., 2022; Parés and Parés-Pulido, 2021), with a particular focus on variants of the SWEs (Canestrelli et al., 2009; Chacón Rebollo et al., 2003; Guerrero Fernandez et al., 2020; Guerrero Fernández et al., 2022; Noelle et al., 2006) and Euler equations (Bermudez et al., 2016; Chandrashekar and Zenk, 2017; Desveaux et al., 2016; Gaburro et al., 2018; Grosheintz-Laval and Käppeli, 2019; Käppeli and Mishra, 2014). Nowadays, numerous methods are also available for the solution of blood flow equations (BFEs), tailored to the preservation of some or all stationary solutions of the system (well-balanced and fully well-balanced methods, respectively). Many of these methods were devised to treat space-varying geometrical and physical properties of the vasculature, friction and gravity (Britton and Xing, 2020; Delestre and Lagrée, 2013; Ghitti et al., 2020; Li et al., 2018; Murillo and Garcia-Navarro, 2015, 2023; Müller and Toro, 2013; Spilimbergo et al., 2021).

Recently, Castro and Parés (2020) and Guerrero Fernández et al. (2022) proposed a generic strategy for the development of well-balanced high-order methods in the finite volume and discontinuous Galerkin frameworks, testing them on hyperbolic PDEs with continuous and discontinuous source terms. One of the main obstacles to the development of well-balanced methods is the construction of a well-balanced reconstruction operator (Castro and Parés, 2020), since standard reconstruction operators such as ENO, WENO and MUSCL (Harten, 1989; Liu et al., 1994; van Leer, 1979) are not usually well-balanced. Indeed, these methods are based on standard interpolation techniques, and there is no guarantee that stationary solutions of the considered PDEs belong to the same class of reconstruction functions. A strategy to modify standard reconstruction operators so that they are well-balanced for all stationary solutions of the considered PDEs has been proposed by Castro et al. (2008). However, this approach requires the solution of a nonlinear system of equations, which might have multiple or no solutions, and might be computationally expensive (Castro and Parés, 2020).

In this paper, we present a numerical method that combines the novel centered reconstruction technique by Montecinos et al. (2025) with the well-balancing approach by Castro and Parés (2020) and Guerrero Fernández et al. (2022). The method is developed within the path-conservative framework, using the high-order solver of Müller et al. (2016) and the well-balancing strategy of Guerrero Fernández et al. (2022), which relies on the knowledge of families of stationary solutions. The reconstruction technique (Montecinos et al., 2025) requires, at each time step and in every computational cell, the cell average of the solution at the current time level and the solution of a generalized Riemann problem (GRP) at the cell interfaces from the previous time level. Provided that the GRP solver being used is well balanced, this minimal data dependence guarantees the well-balancing of the reconstruction technique by construction up to the third order, while also making the technique highly efficient and easy to implement.

In the following, we show that the resulting numerical method is well-balanced up to order three, testing it on both a scalar problem represented by the Burgers' equation, and a PDE system given by the hyperbolized one-dimensional BFEs presented in Montecinos et al. (2014), including variable geometrical and mechanical vessel properties, friction and a spatially variable C^0 gravity term. The gravity term, in particular, is defined, depending on the considered test, either as a constant quantity, a smooth function or a polyline computed from anatomical data.

The rest of the work is structured as follows. Section 3.2 illustrates the proposed well-balanced numerical method, detailing the spatial reconstruction procedure (Montecinos et al., 2025) and our modifications to the local space-time prediction and time evolution steps described in Müller et al. (2016). Section 3.3 presents the numerical tests performed to assess the accuracy and efficiency of the solver. Numerical results are discussed in section 3.4. Conclusions are drawn in section 3.5.

3.2 Numerical method

We consider the following system

$$\begin{cases} \partial_t \mathbf{Q} + \mathbf{A}(\mathbf{Q})\partial_x \mathbf{Q} = \mathbf{S}(\mathbf{Q}), & x \in \Omega, \quad t \in \mathscr{T}, \\ \mathbf{Q}(x,0) = \mathbf{Q}_0(x), \end{cases} \tag{3.1}$$

where $t \in \mathscr{T}$ and $x \in \Omega$ are time and space independent variables, with $\Omega = [x_A, x_B] \subset \mathbb{R}$ a one-dimensional spatial domain and $\mathscr{T} = [0, t^K] \subset \mathbb{R}_0^+$ a temporal domain. $\mathbf{Q}(x,t) \in \mathscr{B}_Q$ is the state vector, with $\mathscr{B}_Q \subset \mathbb{R}^\nu$ the space of the admissible states, $\mathbf{Q}_0(x) \in \mathscr{B}_Q$ is the initial condition, $\mathbf{S}(\mathbf{Q}(x,t)) \in \mathbb{R}^\nu$ is the source vector, and $\mathbf{A}(\mathbf{Q}(x,t)) \in \mathbb{R}^{\nu \times \nu}$ is the system matrix with real and distinct eigenvalues. If $\mathbf{A}(\mathbf{Q})$ is the Jacobian of the system, then the previous equation reduces to a classical balance law.

Our goal is to construct a numerical scheme that preserves stationary solutions in the framework of path-conservative numerical methods. We begin by identifying the stationary solutions of problem (3.1) as described below. Let $\mathbf{Q}^*(x) \in \mathscr{B}_Q$, $\forall x \in \Omega$, be the stationary solution of problem (3.1), then it holds

$$\mathbf{A}(\mathbf{Q}^*)\partial_x \mathbf{Q}^* = \mathbf{S}(\mathbf{Q}^*). \tag{3.2}$$

Subtracting eq. (3.2) from eq. (3.1) (Guerrero Fernández et al., 2022), we obtain an equivalent problem given by

$$\begin{cases} \partial_t \mathbf{Q} + \mathbf{A}(\mathbf{Q})\partial_x \mathbf{Q} - \mathbf{A}(\mathbf{Q}^*)\partial_x \mathbf{Q}^* = \mathbf{S}(\mathbf{Q}) - \mathbf{S}(\mathbf{Q}^*), & x \in \Omega, \quad t \in \mathscr{T}, \\ \mathbf{Q}(x,0) = \mathbf{Q}_0(x). \end{cases} \tag{3.3}$$

Then, we discretize the spatial domain Ω into N computational cells $S_i = [x_{i-\frac{1}{2}}, x_{i+\frac{1}{2}}]$, with $i = 1, \ldots, N$, and the temporal domain $\mathscr{T}$ into K computational cells $T^n = [t^n, t^{n+1}]$ with $n = 0, \ldots, K-1$. Integrating eq. (3.3) in space and time over the control volume $V_i^n = S_i \times T^n$, we obtain the following numerical scheme

$$\mathbf{Q}_i^{n+1} = \mathbf{Q}_i^n - \frac{1}{\Delta x}\Big(\mathbf{B}_i - \mathbf{B}_i^*\Big) - \frac{\Delta t^n}{\Delta x}\Big(\mathbf{D}^-_{i+\frac{1}{2}} + \mathbf{D}^+_{i-\frac{1}{2}}\Big) + \Delta t^n \Big(\mathbf{S}_i - \mathbf{S}_i^*\Big), \tag{3.4}$$

where

$$\mathbf{Q}_i^n \approx \frac{1}{\Delta x}\int_{x_{i-\frac{1}{2}}}^{x_{i+\frac{1}{2}}} \mathbf{Q}(x,t^n)\,dx, \tag{3.5}$$

$$\mathbf{B}_i \approx \int_{t^n}^{t^{n+1}} \int_{x_{i-\frac{1}{2}}}^{x_{i+\frac{1}{2}}} \mathbf{A}(\mathbf{Q})\partial_x \mathbf{Q} dx dt, \quad \mathbf{B}_i^* \approx \int_{t^n}^{t^{n+1}} \int_{x_{i-\frac{1}{2}}}^{x_{i+\frac{1}{2}}} \mathbf{A}(\mathbf{Q}^*)\partial_x \mathbf{Q}^* dx dt, \tag{3.6}$$

$$\mathbf{S}_i \approx \frac{1}{\Delta x \Delta t^n} \int_{t^n}^{t^{n+1}} \int_{x_{i-\frac{1}{2}}}^{x_{i+\frac{1}{2}}} \mathbf{S}(\mathbf{Q}) dx dt, \quad \mathbf{S}_i^* \approx \frac{1}{\Delta x \Delta t^n} \int_{t^n}^{t^{n+1}} \int_{x_{i-\frac{1}{2}}}^{x_{i+\frac{1}{2}}} \mathbf{S}(\mathbf{Q}^*) dx dt, \tag{3.7}$$

and

$$\mathbf{D}^{\pm}_{i+\frac{1}{2}} \approx \frac{1}{\Delta t^n} \int_{t^n}^{t^{n+1}} D^{\pm}_{i+\frac{1}{2}} \left(\mathbf{Q}^-_{i+\frac{1}{2}}(t), \mathbf{Q}^+_{i+\frac{1}{2}}(t), \mathbf{\Psi}\left(\mathbf{Q}^-_{i+\frac{1}{2}}(t), \mathbf{Q}^+_{i+\frac{1}{2}}(t), s \right) \right) dt. \tag{3.8}$$

$\Delta x = x_{i+\frac{1}{2}} - x_{i-\frac{1}{2}}$ is the mesh spacing, and $\Delta t^n = t^{n+1} - t^n$ is the n-th time step. $\mathbf{Q}_i^n$ denotes the i-th cell average at time t^n, $\mathbf{B}_i$ and $\mathbf{B}_i^*$ are the non-conservative products of the i-th cell, $\mathbf{S}_i$ and $\mathbf{S}_i^*$ are the numerical source terms of the i-th cell, while $\mathbf{D}^{\pm}_{i+\frac{1}{2}}$ are the numerical fluctuations across the interface $x_{i+\frac{1}{2}}$. $D^{\pm}_{i+\frac{1}{2}}\left(\mathbf{Q}^-_{i+\frac{1}{2}}, \mathbf{Q}^+_{i+\frac{1}{2}}, \mathbf{\Psi}\right)$ are the jump terms on the cells boundaries, also called fluctuations, that arise from the solution of a Riemann problem (RP) at the cell interface $x_{i+\frac{1}{2}}$. They depend on the left and right states at the cell interface $\mathbf{Q}^{\pm}_{i+\frac{1}{2}}(t)$, and on the integration path $\mathbf{\Psi}\left(\mathbf{Q}^-_{i+\frac{1}{2}}, \mathbf{Q}^+_{i+\frac{1}{2}}, s\right)$. Here, we compute them as described in Müller and Toro (2013). The integration path $\mathbf{\Psi}$ is a parametric arc in the parameter $s \in [0,1]$ that is used to connect the left and right states $\mathbf{Q}^{\pm}_{i+\frac{1}{2}}(t)$. Multiple path choices are possible. Theoretical details on the choice of paths are given in Parés (2006). Here, we adopt the segment path for the Burgers' equation, and a modification of it for the BFEs (Müller and Toro, 2013). The left and right states $\mathbf{Q}^{\pm}_{i+\frac{1}{2}}(t)$ are space-time reconstructed data that are extrapolated to both sides of the cell interface $x_{i+\frac{1}{2}}$. These space-time reconstructed data are space-time predictions of the sought solution $\mathbf{Q}(x,t)$, computed with a local implicit discontinuous Galerkin scheme. Here, we adopt a modified version of the Dumbser-Enoux-Toro GRP solver (Dumbser et al., 2008) that uses spatial reconstruction polynomials as initial data. These polynomials are computed through a reconstruction procedure that exploits GRP-based predictions from the previous time step to construct the reconstructions at the current step. Together, the GRP solver and the spatial reconstruction technique, described in detail below, provide the quantities required for evaluating the integrals in (3.4), thereby yielding a high-order numerical scheme in both space and time.

In order to have a fully explicit evolution of the data $\mathbf{Q}_i^{n+1}$ at each time step, we have to approximate integrals appearing in eq. (3.4) with the desired order of accuracy. The numerical fluctuations $\mathbf{D}^{\pm}_{i+\frac{1}{2}}$ (3.8) are computed as follows. First, we solve a classical RP for system in (3.3) with initial condition defined as

$$\mathbf{Q}(x,t^n) = \begin{cases} \mathbf{Q}^-_{i+\frac{1}{2}} & \text{if } x < x_{i+\frac{1}{2}}, \\ \mathbf{Q}^+_{i+\frac{1}{2}} & \text{if } x > x_{i+\frac{1}{2}}, \end{cases} \tag{3.9}$$

in order to compute the jump terms $D^{\pm}_{i+\frac{1}{2}}$ (Müller and Toro, 2013). Then, we approximate the time integral in eq. (3.8) using a second- or third-order quadrature rule with Gaussian quadrature nodes and Lagrange interpolation polynomials defined on these nodes. In analogous manner, the numerical sources $\mathbf{S}_i$ and $\mathbf{S}_i^*$ in (3.7), and the two non-conservative products $\mathbf{B}_i$ and $\mathbf{B}_i^*$ in (3.6) are approximated with the same quadrature rule in both space and time.

3.2.1 Stationary solution identification

In this section, we describe the procedure that, at each time step t^n, and for each computational cell S_i, we use to identify a suitable stationary solution $\mathbf{Q}^*(x)$ of problem (3.1) defined in each of the $P(=2,3)$ quadrature points x_p, $p = 0,\dots,P-1$ used in the numerical scheme. To this end, we discretize each computational cell S_i into $P-1$ intervals $[x_{p-1}, x_p]$ of length h. Then, we identify a succession of P values $\{\mathbf{Q}^*_{i,p}\}_{p=0}^{P-1}$ representing the approximated stationary solution in each node x_p. Specifically, this succession is obtained by applying the Runge-Kutta method (RK) of order P and with P stages to eq. (3.2). In this work, we consider the second-order RK with 2 stages, and the third-order RK with 3 stages. In both cases, the standard Butcher tableau with coefficients a_{jk}, b_j, and c_j is employed. Therefore, we compute $\mathbf{Q}^*(x_p) \approx \mathbf{Q}^*_{i,p}$ for $p > 0$ as

$$\begin{cases} \mathbf{Q}^*_{i,p+1} = \mathbf{Q}^*_{i,p} + h\sum_{j=0}^{P-1} b_j K_j, \\ K_j = \tilde{f}(x_p + c_j h, \mathbf{Q}^*_{i,p} + h\sum_{k=0}^{P-1} a_{jk} K_k). \end{cases} \tag{3.10}$$

Additionally, in order to identify $\mathbf{Q}^*_{i,0}$, we require that the average stationary solution in S_i coincides with the cell average $\mathbf{Q}_i^n$ (Guerrero Fernández et al., 2022). Particularly, we apply a Gaussian quadrature rule of order P, with nodes x_p and weights w_p, to the average stationary solution integral and we enforce the equivalence at the discrete level. As a result, we compute $\mathbf{Q}^*_{i,0}$ by solving the following non-linear system of equations

$$w_0 \mathbf{Q}^*_{i,0} + \sum_{p=1}^{P-1} w_p \mathbf{Q}^*_{i,p}(\mathbf{Q}^*_{i,0}) = \mathbf{Q}_i^n. \tag{3.11}$$

Here, the solution to this system was found by applying the standard Newton method.

3.2.2 The well-balanced DET solver

In this section, we present the procedure for constructing a space-time polynomial $\mathbf{Q}_i^{ST,n}(x,t)$ that approximates the solution $\mathbf{Q}(x,t)$ within V_i^n and is employed in the evaluation of the integrals in eq. (3.4). Particularly, we apply a modified version of the Dumbser-Enaux-Toro (DET)

GRP solver (Dumbser et al., 2008) that is based on the calculation of the so-called deviations. The deviation $\mathbf{d}_i^n(x,t)$ is defined as the difference between the space-time polynomial $\mathbf{Q}_i^{ST,n}(x,t)$ and the stationary solution $\mathbf{Q}_i^*(x)$, namely

$$\mathbf{d}_i^n(x,t) = \mathbf{Q}_i^{ST,n}(x,t) - \mathbf{Q}_i^*(x), \quad \forall (x,t) \in V_i^n. \tag{3.12}$$

3

In order to compute integrands in eq. (3.4) at the desired time levels, we need to know the solution of the GRP for system in (3.3) with initial condition defined as

$$\mathbf{Q}(x,t^n) = \begin{cases} \mathbf{w}_{i-1}^n(x), & \text{if } x < x_{i-\frac{1}{2}}, \\ \mathbf{w}_i^n(x), & \text{if } x > x_{i-\frac{1}{2}}, \end{cases} \tag{3.13}$$

where $\mathbf{w}_i^n(x)$ is the reconstruction polynomial of order $P-1$ in S_i at time t^n. The DET solver (Dumbser et al., 2008) finds the solution to this GRP at the desired time points by first performing a space-time evolution procedure, and then solving classical RPs at those time points using the space-time predictions as initial conditions. In particular, locally evolved data in space and time, the space-time predictions $\mathbf{Q}_i^{ST,n}$, are computed through a local space-time discontinuous Galerkin finite element scheme of order P. Given the structure of the adopted numerical scheme, these predictions $\mathbf{Q}_i^{ST,n}$ are space-time polynomials $\mathbf{Q}_i^{ST,n}(x,t)$ evaluated at spatial and temporal quadrature nodes, i.e. $x_{i-\frac{1}{2}}, x_{i+\frac{1}{2}}$ and t^n, t^{n+1} for a second-order method, and $x_{i-\frac{1}{2}}, x_i, x_{i+\frac{1}{2}}$ and $t^n, t^{n+\frac{1}{2}}, t^{n+1}$ for a third-order method. The classical Riemann solver instead provides the solution of the GRP at the time points along interfaces where such solution is required for the computation of the numerical fluctuations $\mathbf{D}_{i\pm\frac{1}{2}}^{\pm}$ (3.8) and the reconstruction polynomials, by solving classical RPs and using space-time predictions at the previous time level on the left and on the right of the same interface as initial data. Before proceeding with the description of the DET solver, we underline that whenever we refer to a local quantity, we drop both the temporal superscript n and the spatial subscript i, keeping only the subscript h to recall that we are in the local framework, for example $\mathbf{Q}_h^{ST} = \mathbf{Q}_i^{ST,n}$.

The local framework is defined by the transformation of the computational volume V_i^n into the reference space-time element $V_h = [0,1] \times [0,1]$ with the reference coordinate ξ and τ as $x = x_{i-\frac{1}{2}} + \Delta x \xi$, and $t = t^n + \Delta t^n \tau$. Hence, problem (3.3) becomes

$$\begin{cases} \partial_\tau \mathbf{Q}_h^{ST} + \dfrac{\Delta t^n}{\Delta x} \mathbf{A}(\mathbf{Q}_h^{ST}) \partial_\xi \mathbf{Q}_h^{ST} - \dfrac{\Delta t^n}{\Delta x} \mathbf{A}(\mathbf{Q}_h^*) \partial_\xi \mathbf{Q}_h^* = \\ \qquad\qquad\qquad \Delta t^n \mathbf{S}(\mathbf{Q}_h^{ST}) - \Delta t^n \mathbf{S}(\mathbf{Q}_h^*), \\ \mathbf{Q}_h^{ST}(\xi,0) = \mathbf{w}_h(\xi). \end{cases} \tag{3.14}$$

We note that this change of coordinate does not affect the mesh spacing Δx or the time step Δt^n, as both are constant quantities. Since $\partial_\tau \mathbf{Q}_h^* = 0$, using relation (3.12), we replace the term $\partial_\tau \mathbf{Q}_h^{ST}$ with $\partial_\tau \mathbf{d}_h$. Additionally, we write the space-time predictor in terms of deviations as $\mathbf{Q}_h^{ST}(\xi,\tau) = \mathbf{d}_h(\xi,\tau) + \mathbf{Q}_h^*(\xi)$. As a result, we transform the unknown of our problem from $\mathbf{Q}_h^{ST}(\xi,\tau)$ to $\mathbf{d}_h(\xi,\tau)$. We also note that if both the non-conservative product $\mathbf{A}(\mathbf{Q})\partial_\xi \mathbf{Q}$ and the source term $\mathbf{S}(\mathbf{Q})$ are linear operators, then eq. (3.14) can be written only in terms of deviations $\mathbf{d}_h(\xi,\tau)$, without the stationary solution $\mathbf{Q}_h^*(\xi)$ explicitly appearing in the formulation.

Then, we multiply eq. (3.14) by a space-time basis function $\theta(\xi,\tau) \in \mathbb{P}_{m,m}$ with m the degree of the polynomial, and we integrate it over V_h. After applying integration by parts only in time, we obtain

$$\begin{aligned}
[\theta,\mathbf{d}_h]^1 - \langle \partial_\tau \theta, \mathbf{d}_h \rangle_{V_h} - [\theta,\mathbf{d}_h]^0 + \frac{\Delta t^n}{\Delta x}\langle \theta, \mathbf{A}(\mathbf{Q}_h^{ST})\partial_\xi \mathbf{Q}_h^{ST} \rangle_{V_h} \\
- \frac{\Delta t^n}{\Delta x}\langle \theta, \mathbf{A}(\mathbf{Q}_h^*)\partial_\xi \mathbf{Q}_h^* \rangle_{V_h} = \Delta t^n \langle \theta, \mathbf{S}(\mathbf{Q}_h^{ST}) \rangle_{Vh} - \Delta t^n \langle \theta, \mathbf{S}(\mathbf{Q}_h^*) \rangle_{Vh},
\end{aligned} \tag{3.15}$$

where we have used the following notation for the two scalar products of two functions $f(\xi,\tau)$ and $g(\xi,\tau)$

$$[f,g]^\tau = \int_0^1 f(\xi,\tau) g(\xi,\tau) d\xi, \quad \langle f,g \rangle_{V_h} = \int_0^1 \int_0^1 f(\xi,\tau) g(\xi,\tau) d\xi d\tau. \tag{3.16}$$

We now take the element $[\theta,\mathbf{d}_h]^0$ of eq. (3.15) at reference time $\tau = 0$ and we observe that it is completely defined by the initial condition. The initial condition (Dumbser et al., 2008) is

$$\mathbf{d}_{h,0}(\xi) = \mathbf{d}_h(\xi,0) = \mathbf{w}_h(\xi) - \mathbf{Q}_h^*(\xi), \tag{3.17}$$

where the stationary term $\mathbf{Q}_h^*(\xi)$ is known from previous computations.

Later, using the same basis function $\theta(\xi,\tau)$, we approximate the different quantities in (3.15) expanding them as

$$\mathbf{d}_h(\xi,\tau) = \sum_{l=1}^{P^2} \theta_l \widehat{\mathbf{d}}_l, \quad \mathbf{Q}_h^*(\xi) = \sum_{l=1}^{P^2} \theta_l \widehat{\mathbf{Q}^*}_l, \tag{3.18}$$

$$\mathbf{A}(\mathbf{Q}_h^{ST})\partial_\xi \mathbf{Q}_h^{ST}(\xi,\tau) = \sum_{l=1}^{P^2} \theta_l \widehat{\mathbf{A}\partial_\xi \mathbf{Q}}_l, \quad \mathbf{A}(\mathbf{Q}_h^*)\partial_\xi \mathbf{Q}_h^*(\xi) = \sum_{l=1}^{P^2} \theta_l \widehat{\mathbf{A}^*\partial_\xi \mathbf{Q}^*}_l, \tag{3.19}$$

$$\mathbf{S}(\mathbf{Q}_h^{ST})(\xi,\tau) = \sum_{l=1}^{P^2} \theta_l \widehat{\mathbf{S}}_l = \sum_{l=1}^{P^2} \theta_l \mathbf{S}(\widehat{\mathbf{Q}}_l) = \sum_{l=1}^{P^2} \theta_l \mathbf{S}(\widehat{\mathbf{d}}_l + \widehat{\mathbf{Q}^*}_l), \tag{3.20}$$

$$\mathbf{S}(\mathbf{Q}_h^*)(\xi) = \sum_{l=1}^{P^2} \theta_l \widehat{\mathbf{S}^*}_l = \sum_{l=1}^{P^2} \theta_l \mathbf{S}(\widehat{\mathbf{Q}^*}_l). \tag{3.21}$$

We observe that the term $\widehat{\mathbf{A}\partial_\xi \mathbf{Q}}_l$ is obtained by assuming that $\widehat{\mathbf{A}\partial_\xi \mathbf{Q}}_l = \mathbf{A}(\widehat{\mathbf{Q}}_l)\widehat{\partial_\xi \mathbf{Q}}_l$, and by computing the expansion coefficients of the spatial derivative as $\langle\theta_k,\theta_l\rangle_{V_h}\widehat{\partial_\xi \mathbf{Q}}_l = \langle\theta_k,\partial_\xi\theta_l\rangle_{V_h}\widehat{\mathbf{Q}}_l$ for $k = 1,\dots,P^2$ (Müller et al., 2016). Similarly, $\widehat{\mathbf{A}^*\partial_\xi \mathbf{Q}^*}_l = \mathbf{A}(\widehat{\mathbf{Q}^*}_l)\widehat{\partial_\xi \mathbf{Q}^*}_l$, and the spatial derivative is computed as $\langle\theta_k,\theta_l\rangle_{V_h}\widehat{\partial_\xi \mathbf{Q}^*}_l = \langle\theta_k,\partial_\xi\theta_l\rangle_{V_h}\widehat{\mathbf{Q}^*}_l$ for $k = 1,\dots,P^2$. In general, $\forall l = 1,\dots,P^2$, the expansion coefficients $\widehat{\mathbf{Q}^*}_l$, $\widehat{\mathbf{A}^*\partial_\xi \mathbf{Q}^*}_l$, and $\widehat{\mathbf{S}^*}_l$, , are known because of the knowledge of the stationary solution. The expansion coefficients $\widehat{\mathbf{Q}}_l$ instead can be written in terms of deviations as $\widehat{\mathbf{Q}}_l = \widehat{\mathbf{d}}_l + \widehat{\mathbf{Q}^*}_l$. Finally, the expansions coefficients related to the deviations $\widehat{\mathbf{d}}_l$, $\forall l = 1,\dots,P^2$, which are the resulting unknown of system (3.15), are found applying a fixed-point iteration procedure to the following system

$$
\begin{aligned}
&\left\{[\theta_k,\theta_l]^1 - \langle\partial_\tau\theta_k,\theta_l\rangle_{V_h}\right\}\widehat{\mathbf{d}}_l^{m+1} - \Delta t^n\langle\theta_k,\theta_l\rangle_{Vh}\mathbf{S}(\widehat{\mathbf{d}}_l^{m+1} + \widehat{\mathbf{Q}^*}_l) = \\
&[\theta_k,\psi_l]^0\widehat{\mathbf{d}}_{0l} - \frac{\Delta t^n}{\Delta x}\langle\theta_k,\theta_l\rangle_{V_h}\mathbf{A}(\widehat{\mathbf{d}}_l^m + \widehat{\mathbf{Q}^*}_l)\left\{\langle\theta_k,\theta_l\rangle_{V_h}\right\}^{-1}\langle\theta_k,\partial_\xi\theta_l\rangle_{V_h}(\widehat{\mathbf{d}}_l^m + \widehat{\mathbf{Q}^*}_l) \\
&+\frac{\Delta t^n}{\Delta x}\langle\theta_k,\theta_l\rangle_{V_h}\mathbf{A}(\widehat{\mathbf{Q}^*}_l)\left\{\langle\theta_k,\theta_l\rangle_{V_h}\right\}^{-1}\langle\theta_k,\partial_\xi\theta_l\rangle_{V_h}\widehat{\mathbf{Q}^*}_l - \Delta t^n\langle\theta_k,\theta_l\rangle_{Vh}\mathbf{S}(\widehat{\mathbf{Q}^*}_l),
\end{aligned}
\tag{3.22}
$$

for $k = 1,\dots,P^2$, where we have expanded the initial condition as $\mathbf{d}_{h,0}(\xi) = \sum_{l=1}^{P^2}\psi_l\widehat{\mathbf{d}}_{0l} = \sum_{l=1}^{P^2}\psi_l(\widehat{\mathbf{w}}_l - \widehat{\mathbf{Q}^*}_l)$, and where m represents the current iteration step. We underline that due to the non-linearity of the system we decided to evaluate the second term of the right-hand side at the known expansion coefficients $\widehat{\mathbf{d}}_l^m$ of the current iteration. Once the expansion coefficients are known, we finally retrieve the space-time predictions $\mathbf{Q}_i^{ST,n}$ in V_i^n. We remark that the modified version of the DET solver here described is equivalent to the original version of the DET solver if we assume that the stationary solution $\mathbf{Q}_i^*(x)$ is always zero.

3.2.3 Spatial reconstruction

In this section, we provide a brief overview of the GRP-based reconstruction procedure used to derive second- and third-order accurate spatial reconstruction polynomials $\mathbf{w}_i^n(x)$ (Montecinos et al., 2025). These polynomials serve as local reconstructed data that provide the initial condition for the GRP solver, which in turns computes high-order space-time predictions of the solution $\mathbf{Q}(x,t)$. As a result, they enable the construction of a high-order scheme in both space and time.

They are piecewise functions of degree $P-1$, with P being the order of the numerical method, defined on each computational cell S_i at time t^n. They are expressed in terms of the cell average of the solution at the current time step $\mathbf{Q}_i^n$, and in terms of left and right boundary states at the previous time step $\mathbf{Q}_{i-\frac{1}{2}}^{+,n-1}$ and $\mathbf{Q}_{i+\frac{1}{2}}^{-,n-1}$. These states arise from the solution of a classical RP at time $t^{n-1}+\Delta t^{n-1}$ at the interfaces $x_{i\pm\frac{1}{2}}$ between two neighboring cells, and are also used to compute the integrand in the time integral of the fluctuations (3.8). For the left interface $x_{i-\frac{1}{2}}$, the classical RP reads

$$\begin{cases} \partial_t \mathbf{Q} + \mathbf{A}(\mathbf{Q})\partial_x \mathbf{Q} = 0, \quad x \in \mathbb{R}, t > t^{n-1}, \\ \mathbf{Q}(x, t^{n-1}+\Delta t^{n-1}) = \begin{cases} \mathbf{Q}_{i-1}^{ST,n-1}(x_{i-\frac{1}{2}}, t^{n-1}+\Delta t^{n-1}) & \text{if } x < x_{i-\frac{1}{2}}, \\ \mathbf{Q}_{i}^{ST,n-1}(x_{i-\frac{1}{2}}, t^{n-1}+\Delta t^{n-1}) & \text{if } x > x_{i-\frac{1}{2}}, \end{cases} \end{cases} \tag{3.23}$$

where $\mathbf{Q}_{i-1}^{ST,n-1}$ and $\mathbf{Q}_{i}^{ST,n-1}$ are space-time predictions at time $t^{n-1}+\Delta t^{n-1}$ and related to cells S_{i-1} and S_i, respectively. Their computation is described in the previous section. The solution to RP (3.23) can be obtained using various methods (Toro, 2009). Here we applied the exact Riemann solver for the Burgers' equation, and a two-rarefaction approximate Riemann solver for the BFEs, which yielded to a non-linear system in the left boundary states unknowns $\mathbf{Q}_{i-\frac{1}{2}}^{\pm,n-1}$. The $-$ and $+$ superscripts on the left boundary states denote, respectively, values taken from the left and right of the interface. This distinction is essential, since at cell interfaces the solution of the considered RP can exhibit discontinuities. Details on how the non-linear system was solved are provided in section C.1 of the supplementary material. The solution to this problem internal to cell S_i, namely $\mathbf{Q}_{i-\frac{1}{2}}^{+,n-1}$, is then used to find the reconstruction polynomial $\mathbf{w}_i^n(x)$.

Due to the structure of our numerical method, the reconstruction polynomials $\mathbf{w}_i^n(x)$ need to be evaluated only in the quadrature nodes, i.e $x_{i-\frac{1}{2}}$ and $x_{i+\frac{1}{2}}$ for a second-order method, and $x_{i-\frac{1}{2}}, x_i$ and $x_{i+\frac{1}{2}}$ for a third-order method. In particular, for a second-order method, a first degree polynomial evaluated in the 2 quadrature nodes $x_{i\pm\frac{1}{2}}$ of the computational cell S_i at time t^n reads

$$\mathbf{w}_i^n(x_{i\pm\frac{1}{2}}) = \mathbf{Q}_i^n \pm \frac{1}{2}(\mathbf{Q}_{i+\frac{1}{2}}^{-,n-1} - \mathbf{Q}_{i-\frac{1}{2}}^{+,n-1}). \tag{3.24}$$

Similarly, for a third-order method, a second degree polynomial evaluated in the 3 quadrature nodes $x_p \in \{x_{i\pm\frac{1}{2}}, x_i\}$ of the computational cell S_i at time t^n reads

$$\mathbf{w}_i^n(x_p) = a + bx_p + cx_p^2, \tag{3.25}$$

where

$$a = \mathbf{Q}_{i-\frac{1}{2}}^{+,n-1}, \tag{3.26}$$

$$b = \frac{2}{\Delta x}(-2\mathbf{Q}_{i-\frac{1}{2}}^{+,n-1} - \mathbf{Q}_{i+\frac{1}{2}}^{-,n-1} + 3\mathbf{Q}_i^n), \tag{3.27}$$

and

$$c = \frac{3}{(\Delta x)^2}(\mathbf{Q}_{i-\frac{1}{2}}^{+,n-1} + \mathbf{Q}_{i+\frac{1}{2}}^{-,n-1} - 2\mathbf{Q}_i^n). \tag{3.28}$$

Both reconstruction polynomials are fully determined by either computing a slope or interpolating them through the boundary states $\mathbf{Q}_{i\pm\frac{1}{2}}^{\mp,n-1}$ associated with cell S_i, and by enforcing the conservation property, which ensures that the cell average of cell S_i at time t^n is $\mathbf{Q}_i^n$. Consequently, if the cell average is that of the steady-state solution on the same computational cell, and the boundary states lie on the same steady-state solution, then the resulting reconstruction polynomials evaluated in the quadrature nodes x_p coincide with the steady-state solution. We underline that this feature of the GRP-based reconstruction procedure applies only to first and second degree polynomials. Higher degree polynomials require additional information coming from neighboring cells $S_{i\pm1}$ for their complete identification (Montecinos et al., 2025). Thus, they may fail to coincide with the steady-state solution.

3.2.4 Summary of the method

Consider a non-conservative hyperbolic PDE system with source terms written as in (3.1). The following list summarizes how to compute its numerical solution with the proposed methodology:

1) Discretize the spatial domain Ω into N computational cells S_i, and the temporal domain $\mathscr{T}$ into K temporal cells T^n.

2) At each time step t^n and for each cell S_i, compute the steady-state solution of problem (3.1) using eq. (3.10) and eq. (3.11).

3) At each time step t^n and for each cell S_i, compute the spatial reconstruction polynomials using eq. (3.24) or eq. (3.25).

4) At each time step t^n and for each cell S_i, compute the space-time predictions using information from points 2) and 3), and the GRP solver presented in section 3.2.2.

5) At each time step t^n and for each cell S_i, use information from points 2) and 4) to approximate integrals (3.5), (3.6), (3.7), and (3.8).

6) At each time step t^n and for each cell S_i, update the solution using eq. (3.4).

7) Repeat points 2)-6) till the final simulation time is reached.

3.3 Numerical tests

This section presents the numerical tests conducted to evaluate the performance of the proposed high-order numerical method. Two representative test cases are considered: the scalar Burgers' equation and the hyperbolized BFEs system introduced in Müller et al. (2016). To carry out these tests, we employ both second- and third-order implementations of four different methods for comparison. The first is our method, which combines the GRP-based reconstruction with the well-balanced DET solver (GRP+DET-WB). The second method employs the GRP-based reconstruction, coupled with the original, non-well-balanced DET solver (GRP+DET). The third method combines the WENO reconstruction with the well-balanced DET solver (WENO+DET-WB). The fourth method is a reference approach based on the WENO reconstruction combined with the original DET solver (WENO+DET). More details about the WENO reconstruction can be found in Liu et al. (1994).

3.3.1 Scalar case: Burgers' equation

Let us replicate the test proposed by Guerrero Fernández et al. (2022), where we consider the following one-dimensional scalar Burgers' equation with algebraic nonlinear source term, expressed in quasi-linear form (3.1) as

$$\partial_t q + q\partial_x q = q^2, \quad x \in \Omega, \quad t \in \mathscr{T}, \tag{3.29}$$

with initial condition (see figure 3.1A) defined as

$$q(x,0) = \exp\big(x\big) + 0.3\exp\big(-200(x+0.5)^2\big), \quad x \in \Omega, \tag{3.30}$$

and left boundary condition as

$$q(x_A,t) = \exp\big(x_A\big), \quad t \in \mathscr{T}. \tag{3.31}$$

A transparent right boundary condition is also enforced. Stationary solutions of eq. (3.29) can be computed either analytically as

$$q(x) = \exp\big(x\big), \quad x \in \Omega, \tag{3.32}$$

or numerically by applying the procedure described in section 3.2.1.

The goal of this test is to demonstrate the ability of our numerical scheme to recover and preserve the stationary solution of eq. (3.29) when the initial condition (3.30) is given by a

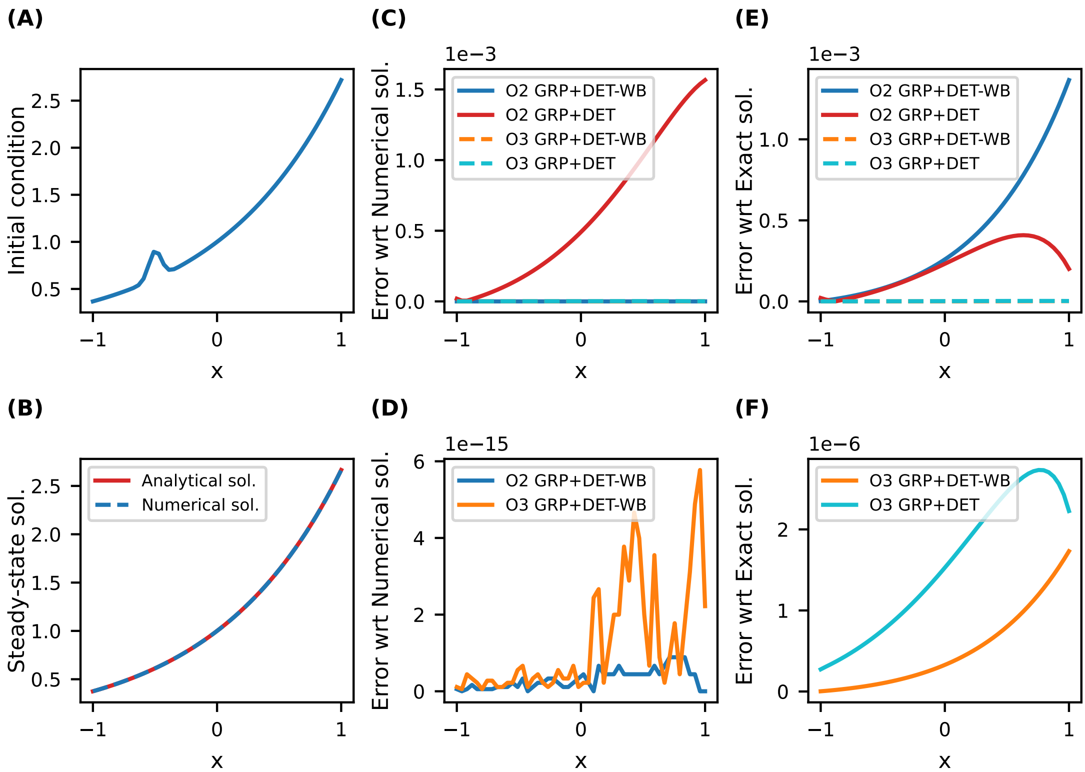

Figure 3.1: Burgers' problem. Initial condition (A), steady-state solution (B), and errors in space between the numerical solution and the steady-state solution obtained either numerically (C and D) or analytically (E and F). Results are shown for both second- and third-order implementations of the GRP+DET and the GRP+DET-WB methods.

small spatial perturbation of that stationary solution. We consider a computational domain $\Omega = [-1, 1]$, discretized through a mesh of $N = 50$ computational cells, and we stop our simulations at the final time $t^K = 40\,\mathrm{s}$. We use a CFL number of 0.9 to compute $\Delta t^n = \mathrm{CFL} \cdot \Delta x / v$, with

$$v = \max(||\mathbf{q}^n||_{L^\infty}, ||\mathscr{V}^n||_{L^\infty}), \tag{3.33}$$

where $\mathbf{q}$ is the vector containing the cell averages q_i^n of the solution in S_i at time t^n, and $\mathscr{V}$ is a vector containing the maximum, on each computational cell, between the left and right states $q_{i-\frac{1}{2}}^{+,n}$ and $q_{i+\frac{1}{2}}^{-,n}$ and their average $\mathscr{M} = 0.5(q_{i-\frac{1}{2}}^{+,n} + q_{i+\frac{1}{2}}^{-,n})$. The time step Δt^n is updated at each iteration of the method and, if necessary, when computing space-time predictions. In this way, we account for the highest wave speed that arises in the presence of shocks and rarefactions. Moreover, we solve equation (3.22) employing a maximum number of iterations equal to the order of accuracy of the method (Dumbser et al., 2008).

Table 3.1
L^1 and L^∞ error norms, and corresponding empirical convergence rates for a second- and third-order implementation of the numerical scheme. N is the number of computational cells.

N	L^1	L^∞	$O(L^1)$	$O(L^\infty)$	L^1	L^∞	$O(L^1)$	$O(L^\infty)$
	Order 2				Order 3			
32	1.9e-03	3.2e-03	-	-	3.8e-06	6.4e-06	-	-
64	4.9e-04	8.4e-04	2.0	1.9	4.8e-07	8.3e-07	3.0	2.9
128	1.2e-04	2.2e-04	2.0	2.0	6.1e-08	1.1e-07	3.0	3.0
256	3.1e-05	5.5e-05	2.0	2.0	7.6e-09	1.3e-08	3.0	3.0
512	7.8e-06	1.4e-05	2.0	2.0	9.6e-10	1.7e-09	3.0	3.0

In figures 3.1C and 3.1D, we show the absolute errors between the numerical solution of the steady-state problem obtained through an appropriate Runge-Kutta scheme, and the numerical solution of eq. (3.29) obtained using the GRP+DET-WB and the GRP+DET methods. Similarly, we display in figures 3.1E and 3.1F the errors between the analytical solution (3.32) and the numerical solution obtained using the GRP+DET-WB and the GRP+DET methods.

We also perform an empirical convergence test to verify whether our method reaches the expected order of accuracy. We report in table 3.1 L^1 and L^∞ error norms between the numerical solution obtained with the GRP+DET-WB method and the analytical solution (3.32), along with the corresponding empirical convergence rates.

3.3.2 System case: hyperbolized blood flow equations

Let us consider the hyperbolized BFEs system proposed in Müller et al. (2016), including now a gravity term. This system of PDEs can be written in quasi-linear form as in eq. (3.1), where we have

$$\mathbf{Q} = [A, q, \psi, A_0, h_0, E_e, E_c, p_r]^T, \tag{3.34}$$

$$\mathbf{A}(\mathbf{Q}) = \begin{bmatrix} 0 & 1 & 0 & 0 & 0 & 0 & 0 & 0 \\ c^2 - u^2 & 2u & \frac{A}{\rho}\partial_\psi \zeta & \frac{A}{\rho}\partial_{A_0} \zeta & \frac{A}{\rho}\partial_{h_0} \zeta & \frac{A}{\rho}\partial_{E_e} \zeta & \frac{A}{\rho}\partial_{E_c} \zeta & \frac{A}{\rho} \\ 0 & -1/\varepsilon & 0 & 0 & 0 & 0 & 0 & 0 \\ 0 & 0 & 0 & 0 & 0 & 0 & 0 & 0 \\ 0 & 0 & 0 & 0 & 0 & 0 & 0 & 0 \\ 0 & 0 & 0 & 0 & 0 & 0 & 0 & 0 \\ 0 & 0 & 0 & 0 & 0 & 0 & 0 & 0 \\ 0 & 0 & 0 & 0 & 0 & 0 & 0 & 0 \end{bmatrix}, \tag{3.35}$$

with $u = q/A$, and $c = \sqrt{\frac{A}{\rho}\partial_A \zeta}$, and where

$$\mathbf{S}(\mathbf{Q}) = \left[0, Rq/A + Ag_x, -\psi/\varepsilon, 0, 0, 0, 0, 0\right]^T. \tag{3.36}$$

x is the axial coordinate along the vessel, t is the time, $A(x,t)$ represents the cross-sectional area of the vessel lumen, $q(x,t)$ is the flow rate, and $\psi(x,t)$ is an auxiliary variable used in the hyperbolization process (Montecinos et al., 2014) along with the relaxation time $\varepsilon > 0$. $R(< 0)$ is the coefficient of the friction term, while $g_x(x)$ is the projection of gravity along the vessel's axis defining the gravity term. $A_0(x)$, $h_0(x)$, $E_e(x)$, $E_c(x)$, and $p_r(x)$ are spatial parameters, assumed to be either constant or continuously varying along the vessel's axis. These parameters characterize the vessel's wall mechanics through a nonlinear constitutive relation that links the cross-sectional area to the blood pressure. More details about the spatial parameters, the adopted pressure-area relation, and the system itself can be found in Müller et al. (2016). Additionally, details of the eigenstructure of this system are given in Müller et al. (2016), and more extensively in Montecinos et al. (2014); Müller et al. (2016). Finally, we recall that the computation of the boundary states for RP (3.23), associated with the hyperbolized BFEs, is carried out as described in section C.1 of the supplementary material.

To test our method on this PDE system, we considered two geometries. First, we used a single blood vessel to verify the empirical convergence of the method to the desired order of accuracy and to compare its efficiency to that of other numerical schemes. Later, we used an arterial network to assess the well-balanced property of the method over a complex geometry and its performance in transient scenarios. Specifically, we considered a reduced version of the anatomically detailed arterial network described in Blanco et al. (2015), ADAN86 (Blanco et al., 2020), which is an open network composed of 86 arteries that resemble the real human anatomy. Among all the arteries of ADAN86, we also considered the right internal carotid artery (ICA) as the single blood vessel on which run the first set of tests, due to its peculiar geometry.

The PDE system was solved in each artery of the ADAN86 network using an initial condition given by constant pressure equal to 60 mmHg, and constant zero flow rate. Additionally, three different types of boundary conditions were enforced. At the inlet of the ascending aorta, an inflow boundary condition was set. At the outlet of terminal vessels, either a Dirichlet boundary condition in cross-sectional area or an outflow boundary condition were used. Finally, at the joins between two or three arterial segments, junction coupling conditions were prescribed. Further details on the treatment of these boundary conditions and their assignment in the context of the proposed numerical scheme are given in Müller and Blanco (2015); Müller et al.

(2016); Müller et al. (2016). We emphasize that boundary and coupling conditions computed as reported in these references are used by the implemented GRP-based reconstruction, thereby obviating the need for more sophisticated techniques, such as ghost cell filling, to achieve high-order accuracy. We also underline that, given the high computational cost of computing (3.8) along junctions, we adopt the local time-stepping algorithm proposed in Müller et al. (2016), where, for all tests, the user-defined CFL value is 0.8.

3.3.2.1 Efficiency analysis for a single blood vessel (ICA test)

An efficiency analysis was performed to assess if our method was able to attain a prescribed error at low computational cost. To this end, we considered three different scenarios of increasing complexity, all defined on the same blood vessel, the ICA, and subject to identical boundary conditions. The difference among the scenarios arises solely from the choice of both the gravity term and the spatial parameters, in order to highlight the importance of combining appropriate reconstruction techniques with well-balanced solvers to achieve maximal efficiency.

The first scenario (S1) considers the parameters of the pressure-area relation to be constant along all the vessel axis. Specifically, $A_0 = 0.24$ cm^2, $h_0 = 0.05$ cm, $E_e = 3.6 \cdot 10^6$ Pa, and $E_c = 9 \cdot 10^8$ Pa. It also assumes the gravity projection g_x to be constant and equal to $981\,\mathrm{cm/s^2}$. For this first scenario, we compared the results obtained using a second-order implementation of the GRP+DET-WB, the GRP+DET, the WENO+DET-WB, and the WENO+DET methods.

The second scenario (S2) considers the parameters of the pressure-area relation to be variable and continuous in space (Blanco et al., 2015). Additionally, a smooth function of the gravity projection is taken into account

$$g_x(x) = |g| \big[\exp(-x) - \exp(-L) \big] , \tag{3.37}$$

where L is the axial length of the ICA, while $|g| = 981\,\mathrm{cm/s^2}$ is the gravitational acceleration modulus. In this second case, we only compared results obtained with the second-order GRP+DET-WB method, to those obtained with the second-order GRP+DET method, to better highlight the differences among the well-balanced and the non-well-balanced solvers.

The third and final scenario (S3) considers a variation to the second case, where the gravity projection is now a polyline. Here, we took into account the real 3D geometry of the ICA and we projected the gravitational acceleration on the vessel axis.

For all the scenarios, we assumed a final simulation time of 10 s, and a minimum number of 4 spatial computational cells that are doubled for each of the 4 considered mesh refinements. Additionally, we assumed a no-flow boundary condition at the inlet of the vessel, and fixed

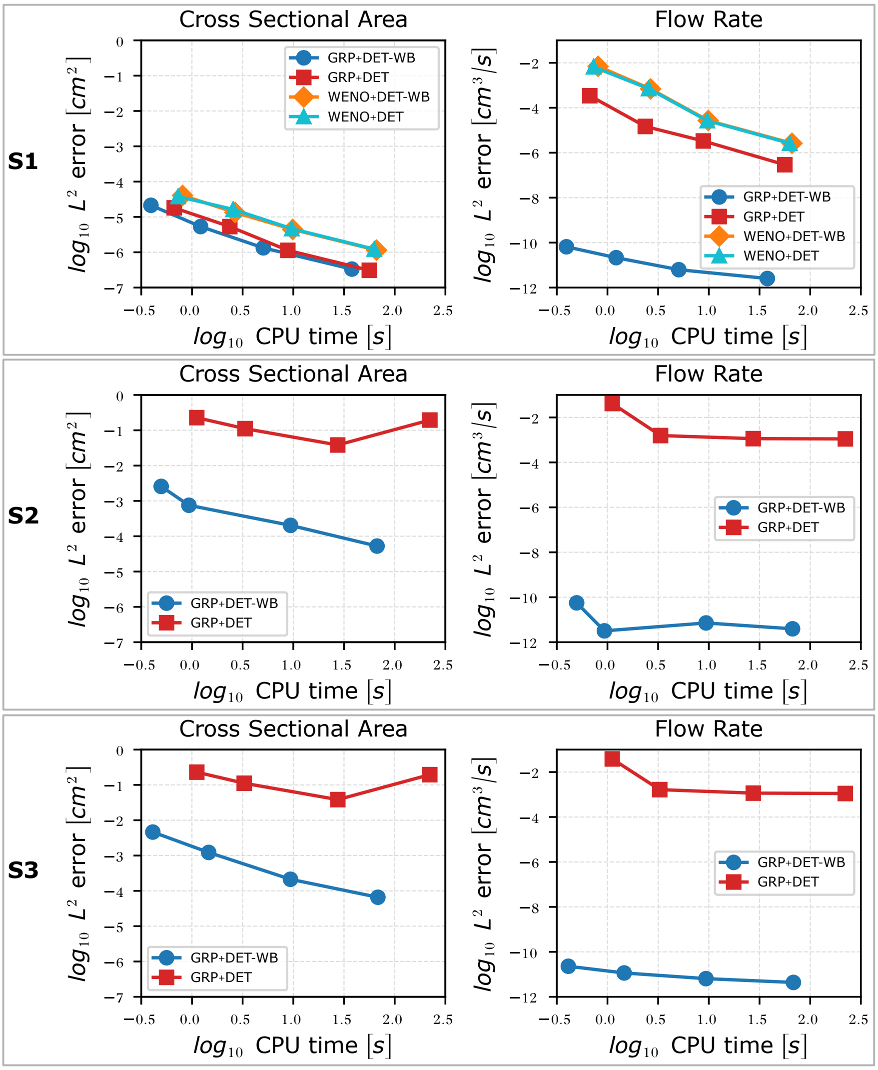

Figure 3.2: Efficiency plots for ICA test. CPU times versus L^2 error norms between the numerical solution and either the exact solution (S1 and S2) or a reference solution (S3), for all the considered scenarios and for 4 consecutive mesh refinements. Each row refers to a different scenario (S1, S2, and S3). Results are shown for both cross-sectional area (left panels) and flow rate (right panels) in logarithmic scale on both axes.

cross-sectional area at the outlet such that the corresponding pressure was 60 mmHg. In all the cases, we run our tests on a workstation that had a Intel Core i9 processor with 16 cores and 24 threads (3.2 GHz clock speed), and 64 GiB of RAM, using 1 thread per test.

Figure 3.2 shows the obtained results at the final simulation time for a second-order implementation of all the considered methods in terms of CPU time and L^2 error norms between

Table 3.2
L^1 and L^∞ error norms, and corresponding empirical convergence rates for the cross-sectional area $A(x,t)$ at the final simulation time and for scenarios S1, S2, and S3 for the ICA test, for a second- and a third-order implementation of the numerical scheme. N is the number of computational cells.

Variable	N	L^1	L^∞	$O(L^1)$	$O(L^\infty)$	L^1	L^∞	$O(L^1)$	$O(L^\infty)$
Scenario S1		Order 2				Order 3			
A [cm^2]	4	7.84e-05	5.92e-06	—	—	8.49e-08	6.28e-09	—	—
	8	1.96e-05	1.48e-06	2.0	2.0	1.08e-08	1.17e-09	2.97	2.42
	16	4.90e-06	3.72e-07	2.0	2.0	1.36e-09	1.68e-10	2.99	2.80
	32	1.23e-06	9.30e-08	2.0	2.0	1.74e-10	2.34e-11	2.97	2.84
Scenario S2		Order 2				Order 3			
A [cm^2]	4	8.59e-03	9.59e-04	—	—	5.90e-03	4.37e-04	—	—
	8	2.49e-03	2.85e-04	1.78	1.75	9.72e-04	1.13e-04	2.60	1.96
	16	6.71e-04	7.84e-05	1.89	1.86	1.36e-04	2.03e-05	2.84	2.47
	32	1.74e-04	2.04e-05	1.95	1.94	1.72e-05	2.82e-06	2.99	2.84
Scenario S3		Order 2				Order 3			
A [cm^2]	4	1.64e-02	1.64e-03	—	—	9.79e-04	1.16e-04	—	—
	8	4.04e-03	5.15e-04	2.02	1.67	8.38e-04	8.36e-05	0.22	0.47
	16	6.66e-04	9.75e-05	2.60	2.40	7.48e-05	1.36e-05	3.49	2.62
	32	2.05e-04	3.70e-05	1.70	1.40	3.17e-05	4.34e-06	1.24	1.65

the numerical solution and either the exact solution (S1 and S2), or a reference solution (S3) obtained by running a test with 4 times the number of computational cells considered in the final mesh refinement. For all tests, we show results in terms of cross-sectional area and flow rate.

3.3.2.2 Empirical convergence rates for ICA test

An empirical convergence test was carried out to verify whether the proposed method attains its expected theoretical order of accuracy. Convergence rates were computed for the ICA test cases obtained with the GRP+DET-WB method across the three scenarios (S1, S2, and S3). The errors between the computed numerical solutions and either the exact solution (S1 and S2) or a reference solution (S3) were evaluated in both L^1 and L^∞ norms. The results, reported in table 3.2, are given in terms of cross-sectional area. Errors for the flow rate are omitted, as they consistently remained below 10^{-10} cm^3/s.

3.3.2.3 Well-balance property for the ADAN86 geometry (deadman test)

This test is designed to verify if our method can accurately approximate a specific steady-state solution, characterized by zero flow throughout the network and a hydrostatic pressure distribution (i.e. the pressure varies linearly along the vertical axis of the body due to gravity, with higher values in lower regions, such as in the legs, and lower values in elevated regions, such as in the head).

To this end, we considered the ADAN86 network in the upright posture, enabling the simulation of hydrostatic pressure gradients induced by gravity. Then, we assumed the parameters of the pressure-area relation to be variable and continuous in space. In this test, the gravity term $g_x(x)$ was a polyline. Specifically, we took into account the real 3D geometry of the different vessels and we projected the gravitational acceleration on the vessels' axes. All blood vessels were discretized using a maximum mesh spacing of 1 cm, and the simulations were performed over 20 s. Finally, we assumed no-flow boundary conditions at both inlet and outlets of the terminal vessels.

Results are shown in figure 3.3 and figure C.2 of the supplementary material in terms of flow rate (top panel) and pressure (bottom panel). Specifically, the two networks in each panel display the errors at the final simulation time along the ADAN86 network between the deadman solution and the numerical solutions obtained with a second (and third) order implementation of the GRP+DET-WB and the GRP+DET methods. A focus on three vessels (left anterior cerebral artery, thoracic aorta, and left femoral artery) is provided in the middle of each panel, where results are reported for the midpoint of the vessels axis and for the last second of simulation. Additionally, figure 3.4 and figure C.3 of the supplementary material show the obtained pressure distribution along the network for both the applied methods of order two and three at the final simulation time. A focus on different vessels at different heights of the network is provided in the middle of the panel, where results are displayed for the midpoint of the chosen vessels axis.

3.3.2.4 Transient simulation for ADAN86

The final test we present aims to assess the capability of our method to accurately capture transient solutions in complex geometries. Specifically, we wanted to test its ability in retrieving pressure and flow rate curves that are commonly observed when modeling the cardiovascular system.

We considered the ADAN86 network in the upright posture and we assumed the parameters of the pressure-area relation to be variable and continuous in space. As in the previous test, the gravity projection $g_x(x)$ was defined as the projection of the gravitational acceleration along the vessels' axes. All blood vessels were discretized using a maximum mesh spacing of 2 cm, and the simulations were performed over 10 s. A periodic inflow boundary condition was prescribed at the aortic inlet (Blanco et al., 2015) to simulate the behavior of the heart (here not present), thereby reproducing the dynamics of the human cardiac cycle. Finally, an outflow boundary

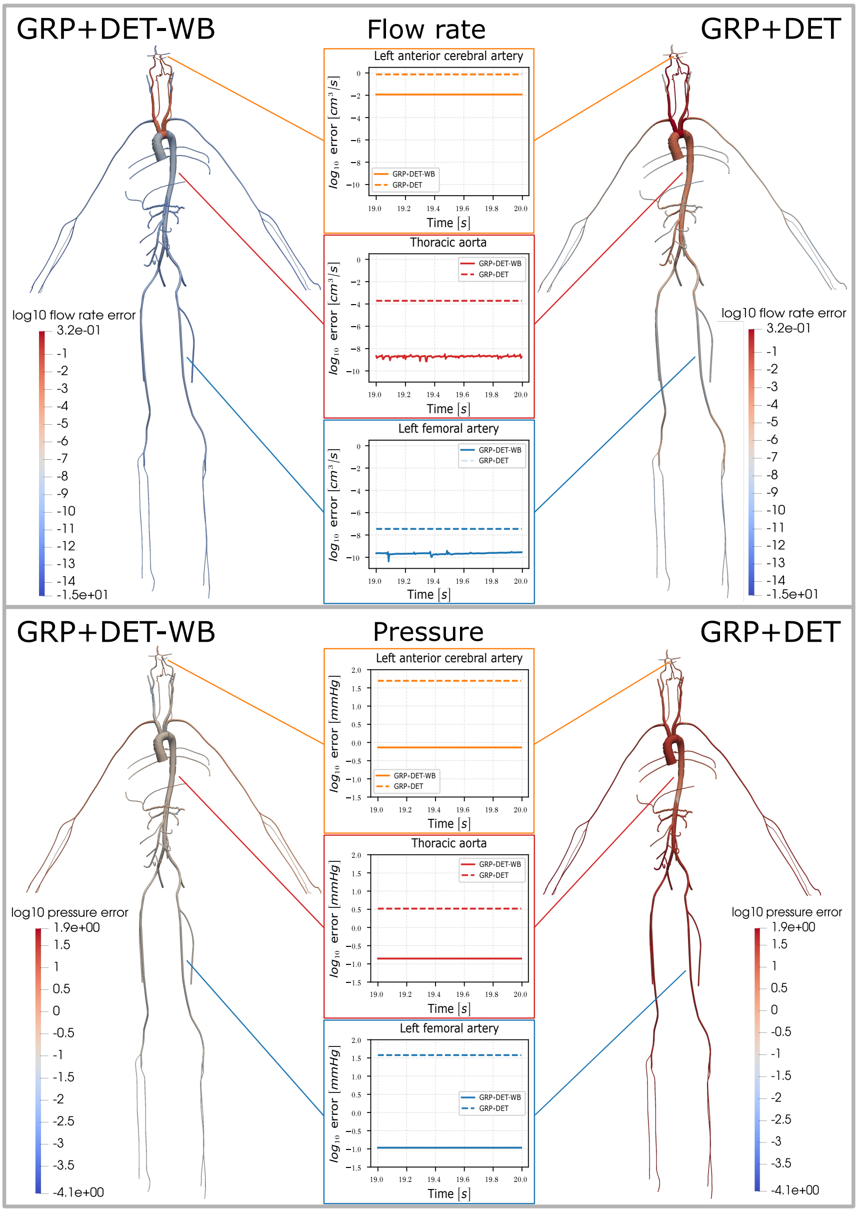

Figure 3.3: Deadman test. A representation of the ADAN86 network is shown. In the top panel, the colors indicate the errors between zero-flow solution and the second-order numerical solution computed with either the GRP+DET-WB, or the GRP+DET. In the bottom panel, the colors indicate the errors between the reference hydrostatic pressure distribution and the numerical solution computed with either the GRP+DET-WB, or the GRP+DET. A focus on three vessels is provided in the middle of both panels. All the results are shown in logarithmic scale.

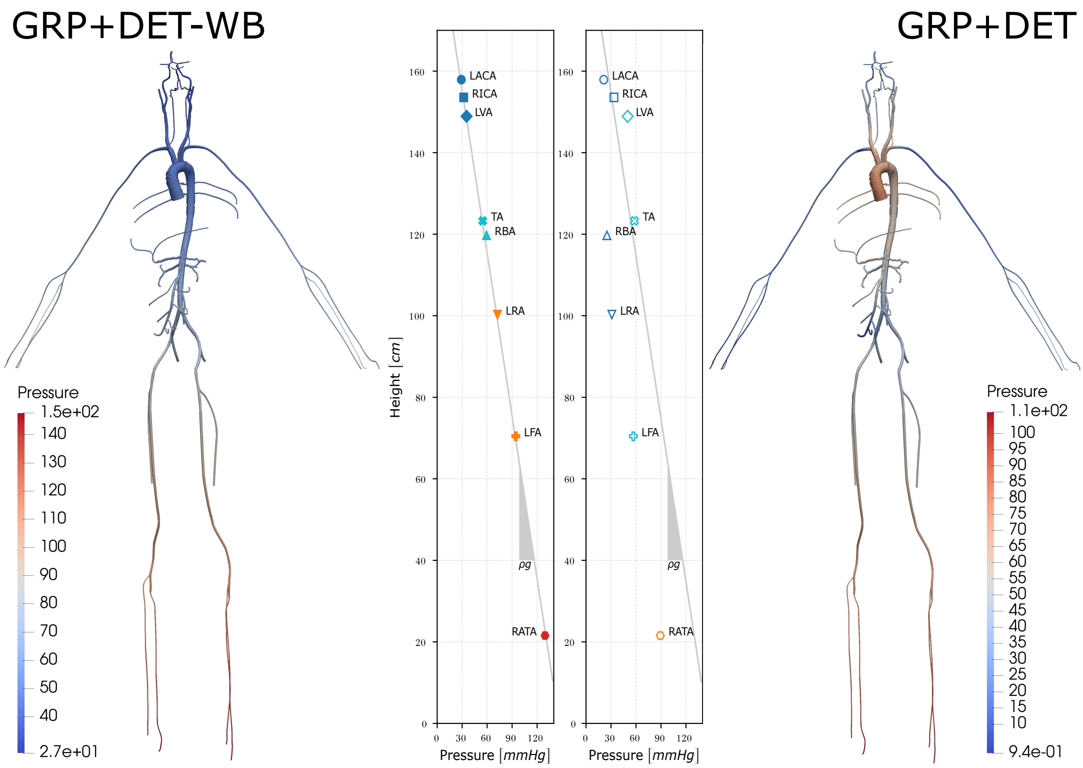

Figure 3.4: Pressure distribution. Pressure distribution at the final simulation time along the ADAN86 network obtained with a second-order implementation of both the GRP+DET-WB method (left) and the GRP+DET method (right). A focus on eight vessels is provided in the middle of the panel, showing how the GRP+DET-WB results respect the expected hydrostatic distribution indicated in light gray. The considered vessels are: LACA: left anterior cerebral artery, RICA: right internal carotid artery, LVA: left vertebral artery, TA: thoracic aorta, RBA: right brachial artery, LRA: left radial artery, LFA: left femoral artery, RATA: right anterior tibial artery.

condition was enforced by coupling terminal vessels to lumped parameters models that mimic the resistance and compliance of the venous system (Müller et al., 2016). We underline that the pressure of the venous system was assumed to be hydrostatically distributed with respect to the vertical axis of the body. In particular, we considered the aortic root to be our reference level.

Results are shown in figure 3.5 and figure C.4 of the supplementary material in terms of flow rate and pressure for three specific vessels (left anterior cerebral artery, thoracic aorta, and left femoral artery) at their midpoint along the final cardiac cycle of simulation. A reference solution, obtained by running the test with gravity set to zero, is also displayed.

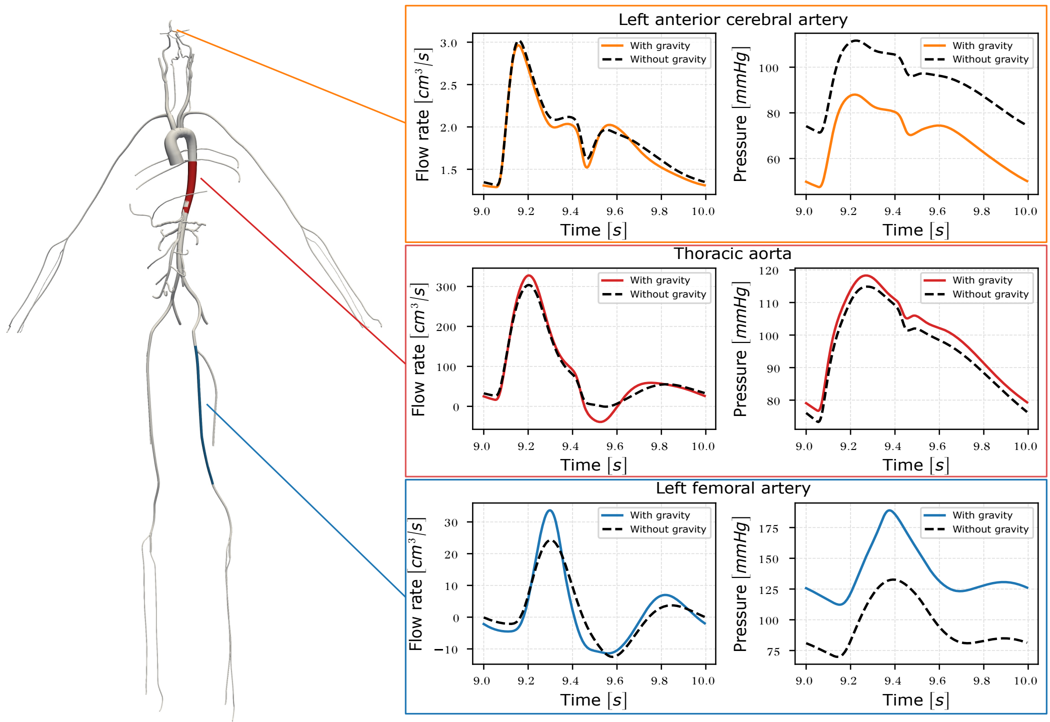

Figure 3.5: Transient test. Flow rate (left column) and pressure (right column) curves along the final cardiac cycle of simulation at the midpoint of three selected blood vessels: left anterior cerebral artery (orange), thoracic aorta (red), and left femoral artery (blue). Indication on the location of the vessels is shown in the ADAN86 network representation on the left. Black dashed lines represent the reference solution with no gravity in the different vessels.

3.4 Discussion

In this section, we discuss results obtained through the numerical tests outlined in section 3.3, assessing the accuracy and efficiency of our numerical method, and evidencing its limitations.

Empirical convergence results reported in tables 3.1 and 3.2 demonstrate that the GRP+DET-WB scheme converges with the expected order of accuracy to either the analytical steady-state solution or to a reference solution computed on a sufficiently fine mesh. Additionally, results reported in figure 3.1D confirm that the method is well-balanced when applied to find the steady-state solution of problem (3.29). This proves numerically that, as opposed to the standard WENO reconstruction, the GRP-based reconstruction is well-balanced up to the third order of accuracy by construction. Indeed, as mentioned in section 3.2.3, reconstruction polynomials are computed by enforcing that the boundary states associated with each cell are used either to compute the polynomials slopes or as interpolation points, and that the conservation property holds. Consequently, if the cell average is that of the steady-state solution on the same computational cell, and the boundary states lie on the same steady-state solution, then they are not perturbed by the reconstruction procedure.

This is also confirmed from the efficiency plots reported in figure 3.2. When considering scenario S1 (top row), we can notice that the choice of the spatial reconstruction plays a significant role: results obtained through the GRP+DET method present lower errors, with the same spatial discretization, than results obtained through the WENO+DET method. Moreover, the former are comparable, when considering the cross-sectional area, to results obtained through the GRP+DET-WB scheme. As a consequence, we can conclude that the only well-balancing errors introduced within the GRP+DET framework are those associated with the DET solver.

A comparison between numerical results and either the analytical solution of the problem or the reference solution computed on a sufficiently fine mesh (see figures 3.1E, 3.1F, and 3.2), shows that, while the GRP+DET-WB and GRP+DET methods perform similarly in simple cases such as the Burgers' equation and scenario S1 for the BFEs, there is an evident advantage in choosing a well-balanced scheme for more complex scenarios. When considering scenarios S2 and S3 for the BFEs, numerical errors for the cross-sectional area and the flow rate obtained through the GRP+DET-WB scheme are significantly lower than those obtained in the GRP+DET setup with analogous meshes, highlighting the higher efficiency of the well-balanced setup. The similar performance of the GRP+DET-WB and GRP+DET schemes in simple scenarios suggests that the approximation of steady-state solutions (see section 3.2.1) has a significant impact on the overall numerical errors introduced by the scheme. This poses the problem of choosing an ordinary differential equation solver of high enough accuracy to avoid the introduction of numerical errors that are comparable or higher than those introduced by the absence of well-balancing.

The ability of our numerical method to preserve stationary solutions is also particularly evident when the method is applied to solve the BFEs over a complex geometry like the ADAN86 network. In fact, observing figure 3.3, top panel, it is evident that the errors in flow rate between the exact solution given by zero-flow and the numerical solution are always higher for the GRP+DET case with respect to the GRP+DET-WB case. A minimum of two orders of magnitude difference between the solutions obtained with the two methods is always detected. Additionally, we observe that the maximum errors for the GRP+DET-WB case are found in the neck and head region, due to its intricate geometry. This region presents multiple vessels junctions, and blood vessels with high geometrical variability, which results in a gravity projection ranging from $-981\,\mathrm{cm/s^2}$ to $981\,\mathrm{cm/s^2}$ along the same vessel axis that can significantly influence the approximation of the solution. Similarly, observing the bottom panel of figure 3.3, we note that the errors in pressure between the deadman solution and the numerical solution are generally larger for the GRP+DET case with respect to the GRP+DET-WB case. These errors strongly affect the representation of the pressure distribution. In particular, we expect to see an hydrostatic pressure distribution along the network when a steady-state is reached, with a maximum pressure in the legs region that gradually decreases towards the cerebral region. This behavior is correctly reproduced in figure 3.4 by the GRP+DET-WB scheme, whereas the GRP-DET scheme fails to capture the hydrostatic distribution, leading to an incorrect approximation of the target solution with a maximal error of 100 mmHg.

Finally, from the pressure and flow-rate waveforms reported in figure 3.5, we observe that the effects of the gravity term are most apparent in the pressure curves. The flow-rate waveforms obtained with gravity are in good agreement with those computed without gravity, with only slight differences in curvature and peak values. In contrast, the pressure waveforms with gravity exhibit a vertical shift relative to those without gravity. This shift reflects the position of the vessel under consideration with respect to the aortic root, which serves as the reference level for the assumed hydrostatic pressure distribution of the venous system. These findings are consistent with previous observations reported in Fois et al. (2022); Murillo and Garcia-Navarro (2023), confirming that the proposed method is capable of performing transient simulations in complex scenarios, allowing an accurate reproduction of the behavior of the cardiovascular system.

3.5 Conclusion

In this work, we proposed a high-order well-balanced numerical scheme for the solution of non-conservative systems of hyperbolic PDEs with source terms. The method is based on the GRP reconstruction by Montecinos et al. (2025), which is well-balanced by construction up to third order of accuracy, provided that boundary states belong to the same family of the steady-state solution of the considered PDEs and the conservation property holds. In addition, it incorporates a modification of the DET solver (Dumbser et al., 2008) along the same lines as those proposed by Guerrero Fernández et al. (2022). Numerical tests performed on the Burgers' equation and on the hyperbolized BFEs (Müller et al., 2016) with friction, gravity and variable geometrical properties demonstrate the well-balanced property of the scheme and highlight its accuracy and efficiency in complex scenarios.

However, it is important to mention that in this work we employ the GRP-based reconstruction without making use of any limiter, which is linear in Godunov's sense. As a consequence, spurious oscillations might arise in the presence of discontinuities. A possible strategy to overcome this issue would be to employ an a-posteriori limiter such as the Multi-dimensional Optimal Order Detection (MOOD) strategy (Clain et al., 2011).

Chapter 4

Quantitative analysis of physiological responses to orthostatic stress during the head-up tilt test

4.1 Introduction

The gravitational field exerts a significant influence on the human body, representing one of the main factors affecting both cardiovascular function and the activity of the nervous system. As described in appendix A, when a healthy adult transitions from the supine to the standing position, approximately 500 ml of blood are redistributed from the thoracic region to the lower limbs. This redistribution alters blood flow, blood pressure, and cardiac function. Within a few seconds, control mechanisms of the autonomic nervous system are activated, triggering reflex responses that act to restore cardiovascular equilibrium (Widmaier et al., 2016). Although many aspects of these physiological responses have been characterized (Blomqvist and Stone, 1991; Hinghofer-Szalkay, 2011; Levick, 2009), their full extent remains incompletely understood. In particular, the magnitude and dynamics of the autonomic nervous system's compensatory actions have not been fully quantified (Ursino and Magosso, 2003). Furthermore, compared to the arterial circulation, the venous system has received considerably less attention, and the available literature contains limited data on the hemodynamic behavior of individual veins (Blomqvist and Stone, 1991).

Several experimental approaches have been proposed to study the physiological and pathological effects of orthostatic stress and to simulate the transition from supine to standing position under controlled conditions. Among the most common techniques are the head-up tilt test (HUT), the head-down tilt test (HDT), the active stand test, the NASA lean test, the bed-rest test, and the lower body negative pressure (LBNP) protocol (Finucane et al., 2019; Goswami et al., 2019; Kapoor et al., 1994; Teuschl et al., 2025; Traon et al., 2007). Each of these methods provides a controlled means of altering the hydrostatic pressure within the body, thereby enabling the investigation of cardiovascular regulation and autonomic responses to gravitational changes. These methods allow for precise control of the degree of orthostatic load and facilitate the measurement of key parameters such as heart rate, blood pressure, and venous return. Depending on the specific protocol, different aspects of cardiovascular control can be emphasized, for instance, the HUT test primarily evaluates autonomic reflexes and blood pressure regulation during passive tilting, while LBNP allows for the isolation of lower body venous pooling effects without changing body orientation (Goswami et al., 2025). Additionally, these techniques are often combined with various measurement methods to monitor cardiovascular function. Common examples include electrocardiography (ECG) for assessing heart rate and rhythm, Doppler ultrasound for evaluating blood flow velocity and vessel dynamics, and impedance plethysmography for estimating changes in blood volume and venous return. In this context, the combination of posture-based tests with non-invasive monitoring tools provides valuable insight into the dynamic responses of the cardiovascular and autonomic nervous systems under orthostatic stress (Yong et al., 2025).

Experimental data obtained from such protocols are essential for the development, validation, and parametrization of physiological models describing the interactions between autonomic regulation, vascular responses, and cardiac function during orthostatic stress. Reliable quantitative measurements allow the comparison between simulated and observed responses, enabling researchers to refine model parameters and improve the predictive accuracy of computational frameworks. In particular, accurate recordings of variables such as blood pressure, venous flow, and heart rate dynamics are crucial for reproducing the complex interactions between the circulatory and autonomic systems. The availability of high-quality experimental datasets thus represents a fundamental step toward building physiologically meaningful models capable of simulating human responses to gravitational challenges and supporting both clinical and aerospace applications (Alzaabi et al., 2025).

In this work, an experimental procedure was designed and carried out to characterize the influence of gravitational stress on hemodynamic responses. Particular emphasis was placed on the quantitative characterization of the venous circulation, providing novel experimental data that enhance the understanding of cardiovascular and autonomic regulation under different orthostatic conditions. The collected experimental data also provided the basis for the validation and parametrization of the ADAVN cardiovascular model. Specifically, we propose the use of a HUT test to characterize blood flow in different body districts. This test allows for a controlled and reproducible simulation of orthostatic stress, making it possible to monitor cardiovascular adjustments as the body transitions from a horizontal to an upright position. By analyzing flow parameters across various arterial and venous segments, the HUT test enables the assessment of how gravitational forces influence blood distribution and vascular function.

The structure of this chapter is organized as follows: in section 4.2, the experimental protocol is described, including details on ethical approval, participants' demographics, the experimental measurements performed, and the methods used for data analysis. Subsequently, in sections 4.3 and 4.4 the obtained results are presented and discussed, and the main limitations of the study are outlined. Finally, in section 4.5 conclusions are drawn.

4.2 Methods

In this section, we describe the methodological framework of the study, including the ethical approval process, the recruitment of 10 volunteers, the experimental protocol developed and applied, and the procedures used for data acquisition and analysis.

4.2.1 Ethical approval

Ethical approval was granted by the Northern B Health and Disability Ethics Committee, Auckland, New Zealand (19/NTB/125), by the Auckland District Health Board Research Review Committee (A+ 8687), and was registered with the Australian New Zealand Clinical Trials Registry (ACTRN12619001767190). All volunteers received a detailed verbal and written explanation of the study procedures before giving their written consent to participate in the study. The study was conducted according to the standards described in the latest revision of the Declaration of Helsinki (2013).

4.2.2 Participants

Ten healthy participants were enrolled in this study. All participants were between 20 and 40 years old, non-obese [body mass index (BMI) $< 30\,\mathrm{kg\,m^{-2}}$] and with a maximum height of 185 cm. All participants reported not being recreational drug users and hazardous alcohol users. People with a history or symptoms of pulmonary, metabolic and neurological diseases, as well as any acute or chronic disorders associated with alterations in cardiovascular structure or function, were excluded from this study. In addition, people with episodic recurrent syncope and low blood pressure values were not included. The demographic information of the participants is reported in table 4.1.

Table 4.1
Participants demographic. Values are expressed as mean ± maximum absolute deviation for continuous data and as frequency (percentage) for discrete variables.

Total number of participants	10
Number of women (%)	5 (50%)
Age (years)	28 ± 5
Weight (kg)	71.1 ± 10.5
Height (m)	1.73 ± 0.07
BMI ($kg\,m^{-2}$)	23.7 ± 2.5

4.2.3 Experimental protocol

The experimental protocol consisted of two visits to the laboratory on separate days. The purpose of the first visit was to make participants familiarize with the study protocol. During this visit, clinical information was collected, and demographic data were acquired.

The purpose of the second visit was to acquire the hemodynamic measurements of interest. Figure 4.1 shows a sketch of the timeline of this session. Before this second visit, participants were asked not to consume caffeine, not to exercise for 12 hours prior to the study, and not to consume alcohol for 24 hours prior to the study. Participants were also asked not to eat for 2 hours before the study, even if an early meal was encouraged. Upon arrival at the laboratory, participants were asked to lie on a tilt table, horizontally placed, in supine position. After instrumentation, the protocol consisted of three repeating phases. First, a rest period of 4 minutes was awaited, so that the vital parameters (heart rate, blood pressure, and arterial oxygen saturation) of the participants stabilized. Second, a period of 20-30 minutes followed, during which ultrasound and echocardiographic measurements were performed. Third, a final period of 3 minutes took place during which the bed was tilted. These three phases were repeated for each of the four selected angles of tilt, namely 0°, 30°, 60°, and 90°. The test was terminated when either all measurements were acquired or the participant was showing early signs of syncope.

This protocol in its whole was applied to 5 participants (3 men and 2 women) and showed a 60% rate of early signs of syncope when participants were tilted to 60° or 90°. For this reason, the protocol has been reduced by removing the two critical angles of tilt (60° and 90°) and it was applied in this reduced manner to the second half of the participants.

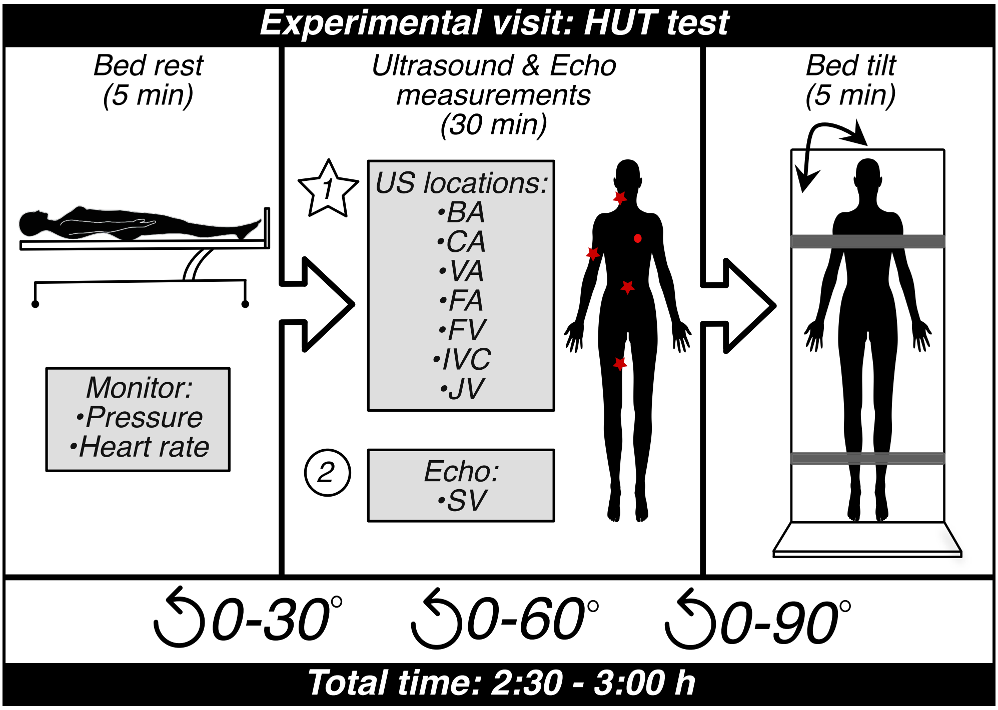

Figure 4.1: Second visit of the experimental protocol: sketch of the timeline. Schematic overview of the second experimental visit protocol, consisting of three phases: 5 min of baseline bed rest with heart rate and blood pressure monitoring, 30 min of ultrasound and echocardiographic measurements, and a final 5 min tilting phase. The tilting phase included three tilt angles: 30°, 60°, and 90°. The total duration of the session was approximately 2h 30 min to 3h. All abbreviations used in the figure are defined in table 4.2.

4.2.4 Experimental measurements

Participants were lying on a tilt table (MPVT, amtech) while heart rate (HR) was continuously monitored with a three-lead electrocardiogram (ADInstruments), and beat-to-beat blood pressure (BP) was measured with a finger photoplethysmography (Finometer PRO). Brachial artery BP measurements were recorded with an automated sphygmomanometer (BP+, Uscom) before tilting the participant to the next angle of tilt and used to validate finger BP values. Arterial oxygen saturation (SpO_2) was continuously monitored using a finger pulse oximeter (ADInstruments). A digital transcranial Doppler (ST3, Spencer Technology) was placed on a headset and used to continuously measure cerebral blood flow velocity, specifically in the mean cerebral artery (MCA). A 3D echocardiography (ACUSON SC 2000, Siemens) was performed for each angle of tilt to measure cardiac output (CO) and stroke volume (SV) by a single operator (G. M. Q.). Duplex Doppler ultrasound (uSmart 3300, Terason) was used for each angle of tilt to

Table 4.2
Abbreviations in alphabetical order.

Abbreviations	Extended name
BA	Right brachial artery
BP	Blood pressure
CO	Cardiac output
CVP	Central venous pressure
DBP	Diastolic blood pressure
FA	Right femoral artery
FV	Right femoral vein
HR	Heart rate
ICA	Right internal carotid artery
IJV	Right internal jugular vein
IVC	Inferior vena cava
MAP	Mean arterial pressure
MCA	Mean cerebral artery
PP	Pulse pressure
SBP	Systolic blood pressure
SV	Stroke volume
VA	Right vertebral artery
VV	Vertebral vein

acquire blood flow velocity and diameter of vessels at eight different locations: right brachial artery (BA), right femoral artery (FA), right internal carotid artery (ICA), right vertebral artery (VA), right femoral vein (FV), inferior vena cava (IVC), right internal jugular vein (IJV), and vertebral veins (VV) on the right side of the neck. The B-mode was used to locate the vessels and measure their diameter. In particular, it was ensured that the sample volume was positioned in the center of the vessel in order to cover the width of the vessel diameter. The pulse-wave mode was used to measure the velocities. All ultrasound measurements were performed by a single operator (K. N. T.). Ultrasound images were screen captured (DVI2USB3.0; Epiphan Video, Ottawa, ON, Canada) by a different operator (J-L. F.) and stored as digital MP4 files for offline analysis. A minimum time of 20 seconds for a continuous recording was adopted. For clarity, a summary of the abbreviations used is provided in table 4.2, while appendix D includes representative images of the experimental setup.

4.2.5 Data analysis

Cardiorespiratory and MCA velocity recordings were converted into digital signals at 1000 Hz (PowerLab 16/35 and LabChart version 8; ADInstruments), stored as text files, and then analyzed offline by a single operator (C. C.), who also processed the ultrasound video files. Each stored file referred to a participant in a specific tilting position, and the saved signals represented the experimental measurements of the participant at steady state. HR was extracted from the electrocardiogram signal by computing the number of consecutive R waves in a minute of recording. Finger BP was calibrated based on the systolic (SBP) and diastolic (DBP) sphygmomanometer measurements taken at the brachial level. In particular, the frequency of the pressure waves was kept unchanged, while the amplitude was scaled in order to match the sphygmomanometer pulse pressure (PP=SBP-DBP). The finger BP time series was then shifted to match the sphygmomanometer value of the mean arterial pressure (MAP=DBP+1/3*PP). From the calibrated finger BP, continuous signals of SBP and DBP were then extracted, and their averaged values were calculated over the full considered tilting period.

CO and SV were calculated from echocardiograpic images of the left ventricle, by averaging the data coming from multiple recordings at the same angle of tilt over multiple cardiac cycles.

Ultrasound video files were analyzed using an automated edge detection and wall tracking software (Cardiovascular Suite; Quipu, Italy), which provided blood flow velocity and vessel diameter measurements. These measurements represent temporal variations across the full recording period at a fixed spatial sampling point corresponding to the ultrasound probe location. Specifically, vessel diameter measurements were used to compute cross-sectional areas over time, assuming a circular vessel shape, and subsequently to derive the average cross-sectional area. The velocity data obtained represented peak blood velocity over time, which we used to calculate the mean blood velocity. Mean blood velocity was determined by dividing the peak blood velocity by two and then averaging these data over the recording period. As suggested by Evans (1985), when a parabolic velocity profile is assumed, the time-averaged mean velocity of pulsatile flow equals one-half of the time-averaged peak velocity, a relationship later experimentally validated by Li et al. (1993). Finally, blood flow was calculated as the product of the mean blood velocity and the mean vessel cross-sectional area. Another potentially informative feature of ultrasound measurements is the blood flow waveform. In the present study, however, we were unable to perform this analysis because we did not have automated tools in our possession that could denoise the recordings and extract the waveform.

4.3 Results

Results for the various quantities of interest across the entire participant population at all tilt angles are presented in figures 4.2 to 4.10. For each participant, the average data of the different quantities at all angles of tilt $0^\circ, 30^\circ, 60^\circ, 90^\circ$ were extracted and then normalized with respect to the average value at 0°.

If the normalizing factor was zero, the first non-null average value at greater tilt angles was used for normalization. These data (light dots in the figures) were then grouped by tilt angle, and the mean values (dark dots) and standard deviations (whiskers) were computed for the entire population. Unfortunately, the limited sample size, together with the fact that multiple participants presented early signs of syncope at high tilt angles (60° and 90°), further reduced the effective dataset and prevented the extraction of meaningful gender-specific insights.

Figures 4.2 and 4.3 present the mean values and standard deviations of SV and CO, respectively. Figure 4.4 displays the mean values and standard deviations of HR, while figure 4.5 shows those of BP time series. Figure 4.6 illustrates the mean values and standard deviations of blood flow, cross-sectional area, and blood flow velocity in the ICA and VA. Figure 4.7 presents the mean values and standard deviations of MCA blood velocity. Finally, figures 4.8, 4.9, and 4.10 display the mean values and standard deviations of blood flow, cross-sectional area, and blood flow velocity in IJV and VV, BA and FA, and FV and IVC, respectively.

4.4 Discussion

This section presents a comprehensive discussion of the obtained results, structured according to the type of data acquired.

4.4.1 Stroke volume

Our data reveal a clear trend in SV (see fig. 4.2), showing a decrease as the tilt angle increases. Venous pooling results in a reduction of central venous pressure (CVP). The CVP is the pressure at the entrance of the right atrium and is also known as the heart filling pressure. In fact, it is the pressure that determines the stretch of the resting right cardiac chambers. Therefore, the more the CVP is reduced, the less the fibers of the right atrium are stretched, resulting in a reduced blood volume admitted to the heart. Such a reduction affects the amount of blood ejected from the right ventricle and then admitted to the left atrium, translating into a reduced left ventricle SV (Blomqvist and Stone, 1991).

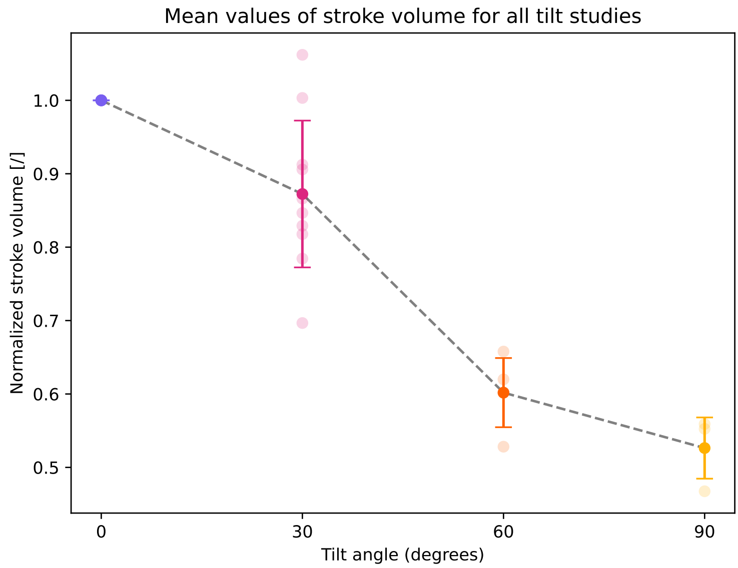

Figure 4.2: Mean values and standard deviations of SV for the complete population. Light dots represent normalized average data for each participant. Dark dots and whiskers represent mean values and standard deviations for the entire population at the considered angle of tilt. Results show a decrease in normalized SV relative to the 0° position as the tilt angle increases.

4

The progressive reduction of SV that we observe in our data (see fig. 4.2) is in line not only with the general behavior of the cardiovascular system just described, but also with the data coming from other experimental works. Møller et al. (2004) showed that a HUT test at 30° produces a SV reduction of 9% with respect to the 0° position, corresponding to the 12% decrease in SV that we observe at 30° (see fig. 4.2, red marker). Møller et al. (2004), along the same study, also observed a SV reduction of 49% at 60° with respect to the 0° position, which is slightly higher then the 40% decrease that we observe for the same tilt angle (see fig. 4.2, orange marker). Wang et al. (1960) and Edgell et al. (2012) instead showed that when the participants to their studies moved from supine to the standing position, the SV is reduced by 30-50%, agreeing with the 47% decrease in SV that we observe at 90° (see fig. 4.2, yellow marker).

4.4.2 Cardiac output

The mechanism affecting CO is the same as described in the previous paragraph (venous pooling). However, its impact on CO is mitigated by variations in the heart rate. In fact, CO represents the efficiency of the heart in maintaining adequate tissue perfusion in the human

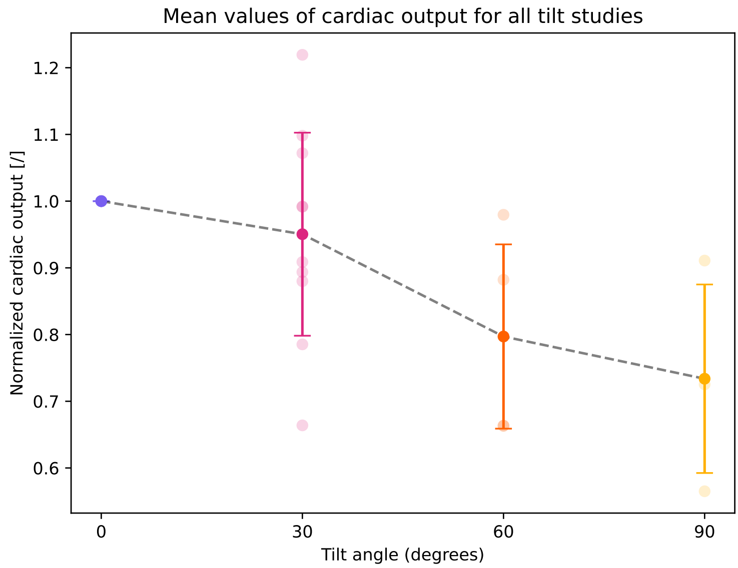

Figure 4.3: Mean values and standard deviations of CO for the complete population. Light dots represent normalized average data for each participant. Dark dots and whiskers represent mean values and standard deviations for the entire population at the considered angle of tilt. Results show a decrease in normalized CO relative to the 0° position as the tilt angle increases.

body and should be kept high enough to meet the metabolic demand. For this reason, a reduction in SV without an adequate response may result in a prominent decrease in CO and a consequent impairment of metabolic demand (Levick, 2009). To prevent such a catastrophic behavior, the autonomic nervous system triggers a response, by increasing the activity of the sympathetic division, that raises the HR and constricts the veins of the splanchnic circulation. While the first mechanism acts directly on the cardiac activity, the second mechanism is useful to prevent an excessive drop of the CVP and thus a further reduction of the SV. This response shifts blood from the congested venous system into the arterial system, promoting the venous return and avoiding the collapse of the cardiovascular system (Pocock et al., 2017). However, if the raise in HR is not enough to counterbalance the reduction in SV, a reduction in CO will still be observed, though less pronounced than the one seen in the SV.

This behavior of CO is evident in our results (see fig. 4.3), which show a progressive reduction with increasing tilt angle. In addition, our findings are consistent with those reported by other authors. Smith et al. (1970) observed a decrease in CO of the 20% with respect to the 0° position during a 20 min HUT test at 70°, which well compares with both the 20% decrease in CO that we observe at 60° (see fig. 4.3, orange marker) and the 27% decrease in CO that we observe at 90° (see fig. 4.3, yellow marker). Toska and Walløe (2002) observed a 17%

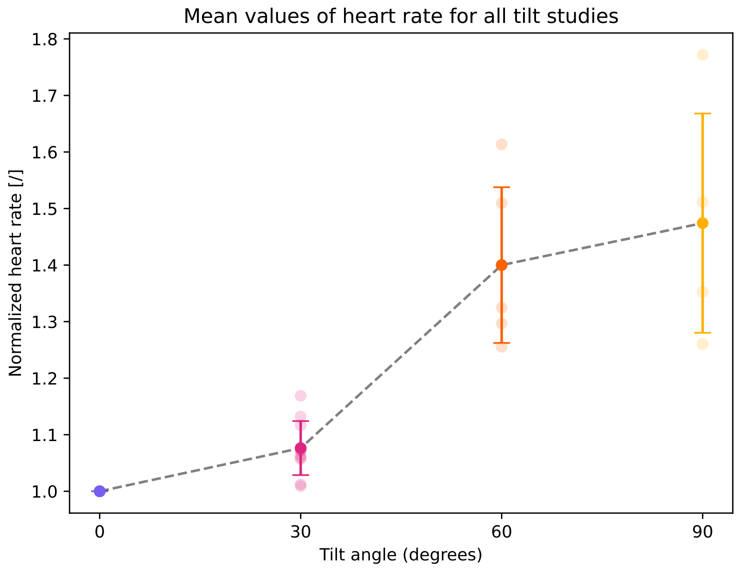

Figure 4.4: Mean values and standard deviations of HR for the complete population. Light dots represent normalized average data for each participant. Dark dots and whiskers represent mean values and standard deviations for the entire population at the considered angle of tilt. Results indicate that HR increases relative to the 0° position as the tilt angle increases.

decrease in CO during a 2 min HUT test at 30° with respect to the 0° position, while Møller et al. (2004) measured a decrease of 35% in CO during a 20 min HUT test at 60° with respect to the 0° position. Both these percentages are slightly higher compared to our results, where we observed a decrease in CO of 5% and 20% at 30° and 60°, respectively (see fig. 4.3, red and orange markers). Nevertheless, these differences may be due to the different experimental protocols adopted by these authors compared to ours.

4.4.3 Heart rate

The HR is controlled by the autonomic nervous system through multiple mechanisms that can increase or decrease the frequency of cardiac contractions depending on physiological demands. One of these mechanisms is mediated by the sympathetic division of the nervous system, which specifically promotes acceleration of the HR. As previously discussed, sympathetic activity increases to counteract the excessive drop in CO caused by venous pooling, resulting in a corresponding increase in HR (Widmaier et al., 2016).

Our data confirm this increase in HR (see fig. 4.4). In particular, we observe how HR increases while increasing the angle of tilt, confirming what just described in the previous paragraph. However, we also observe a more marked response of the sympathetic division, and hence in HR, at 60° compared to the other tilting angles (30° and 90°). In fact, we notice that the HR increases of 32% at 60° with respect to the 30° position (see fig. 4.4, orange marker), while it increases of about 7% at 30° with respect to the 0° position (see fig. 4.4, red marker), and similarly it increases of about 8% at 90° with respect to the 60° position (see fig. 4.4, yellow marker). This is due to two different mechanisms that involve sympathetic activity. At 30°, the action of gravity, which drags blood away from the heart, is moderate and can be easily counterbalanced by a slight growth of sympathetic activity. In contrast, at 60°, the action of gravity is stronger and a more powerful response is needed. At 90°, a mechanism similar to that observed at 60° remains active, but sympathetic activity may attain its peak level of responsiveness. This is due to the fact that the firing rate of the nerve fibers transmitting the information to the cells of the heart is not infinite, but it presents a plateau. When this plateau is reached, the sympathetic activity saturates and no further response is triggered rather than the one already delivered, which explains the small increase in HR from 60° to 90° (Levick, 2009). This behavior has also been reported by other authors (Møller et al., 2004; Smith et al., 1994; Zaidi et al., 2000), who observed HR responses similar to ours under experimental conditions comparable to those we employed, further confirming the consistency of our findings with previous observations.

4.4.4 Blood pressure

The compensatory mechanism triggered by the drop in venous return and SV is used not only to preserve a suitable CO but also, most importantly, to stabilize BP. In fact, BP plays an extremely important role in maintaining adequate tissue perfusion in different districts of the body based on the various blood vessels involved in the processes of transport and diffusion of oxygen, hormones, nutrients and waste products (Pittman, 2011). To stabilize BP, the human body relies on mechanical pressure receptors that signal changes in pressure to the central nervous system, which then triggers compensatory mechanism. Such receptors, commonly known as baroreceptors, can be divided into two groups based on their location. As described in appendix A, arterial baroreceptors are located in the aortic arch and carotid sinus, while low-pressure baroreceptors are found in large systemic veins, pulmonary vessels, and the walls of the right atrium and ventricles (Pocock et al., 2017). The arterial baroreceptors, as suggested by the name, are mechanoreceptors that are responsive to distention of the blood vessels due to changes in arterial BP. Specifically, they inform the central nervous system about changes in MAP, in PP, and in the rate of change of the BP. The low-pressure baroreceptors, also known as cardiopulmonary baroreceptors, instead are mechanoreceptors that sense changes in low BP. They are activated

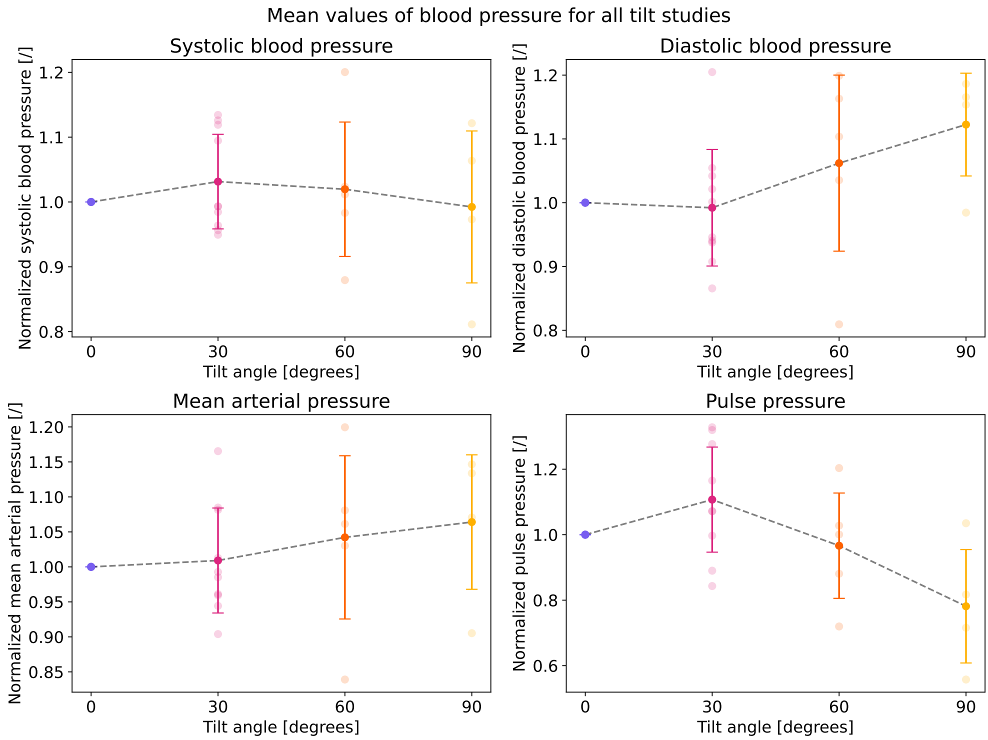

Figure 4.5: Mean values and standard deviations of BP time series for the complete population. Light dots represent normalized average data for each participant, while dark dots and whiskers indicate the mean values and standard deviations for the entire population at each tilt angle. From left to right and from top to bottom, the normalized quantities displayed are: systolic blood pressure (SBP), diastolic blood pressure (DBP), mean arterial pressure (MAP), and pulse pressure (PP). Results indicate that SBP remains constant regardless of the tilt angle, while DBP shows a marked increase relative to the 0° position as the tilt angle increases. Additionally, results reveal a slight increase in MAP and a pronounced decrease in PP, both relative to the 0° position and corresponding to an increase in tilt angles.

as well by the stretch of the blood vessels or by the stretch of the heart surface where they are located, and are primarily involved in the regulation of blood volume. Depending on the type of sensory information received by the central nervous system, different responses are activated. The combination of these responses return the general action of the compensatory mechanism, which involves changes in heart rate, as already seen, but also changes in cardiac contractility, and in vascular resistance (Widmaier et al., 2016).

Considering the specific case of the venous pooling and the consequent drop in SV, it is well known that such a change in blood volume produces not only a reduction in CO, as previously seen, but also a fall in PP and in MAP. The PP is the difference between SBP and DBP, and is approximately proportional to the SV and inversely proportional to the compliance of the aorta (Homan et al., 2023). Thus, a marked decrease in SV results in a decrease in PP. Similarly, MAP, which is the average BP along a single cardiac cycle, is approximately proportional to SV, HR and systemic vascular resistance. Thus, a significant reduction in SV may lead to a marked decrease in MAP, unless HR and vascular resistance are appropriately elevated to compensate (Widmaier et al., 2016). At the same time, venous pooling in the lower extremities leads to a redistribution of blood within the systemic circulation and an increase in the compliance of the thoracic veins, where venous pressure decreases. As a result, CVP temporarily falls. These pressure changes are detected by low-pressure baroreceptors located in the thoracic veins and atria, which trigger reflex responses that constrict the systemic veins and reduce their compliance. This compensatory mechanism enhances venous return to the heart and helps restore CVP, thereby limiting the decline in SV. In addition, the associated increase in venous tone contributes to a rise in DBP, which in turn reduces PP (Pocock et al., 2017).

Our data (see fig. 4.5) agree with the behavior of the cardiovascular system and the compensatory mechanism just introduced. Specifically, we observe that SBP presents fluctuations in the range of 3% for all angles of tilt (30°, 60°, and 90°) with respect to the 0° position, suggesting a constant behavior of this quantity (see fig. 4.5, top left panel). The DBP instead has a more marked raise, up to $+12\%$ at 90° with respect to the 0° position (see fig. 4.5, top right panel). MAP presents a slight increase reaching a maximum of $+6\%$ at 90° with respect to the 0° position (see fig. 4.5, bottom left panel). Finally, we observe a slight increase in the PP of $+10\%$ at 30° with respect to the 0° position, followed by a strong decrease that reaches a -22% at 90° with respect to the 0° position (see fig. 4.5, bottom right panel). The general BP behavior just analyzed is in line not only with the physiology described in the previous paragraphs, but also with what other authors observed in their experimental works (e.g. Smith et al., 1994; Vijayalakshmi et al., 2000), confirming again how our data align with such observations.

4.4.5 Cerebral inflow

The body activates multiple responses to maintain cardiovascular equilibrium, with their interplay ultimately determining the system's overall state and, consequently, the body's condition. Maintaining homeostasis and protecting vital organs, especially in the presence of disease, is essential. Among these organs, the brain plays a crucial role, processing information from the nervous system and coordinating various physiological responses (Widmaier et al., 2016). In order to preserve its normal functioning, the brain needs a continuous inflow of blood that supplies oxygen and nutrients to the brain tissues, and a continuous outflow of blood that removes waste products created by the brain activity. The quantification of blood flow in the brain is

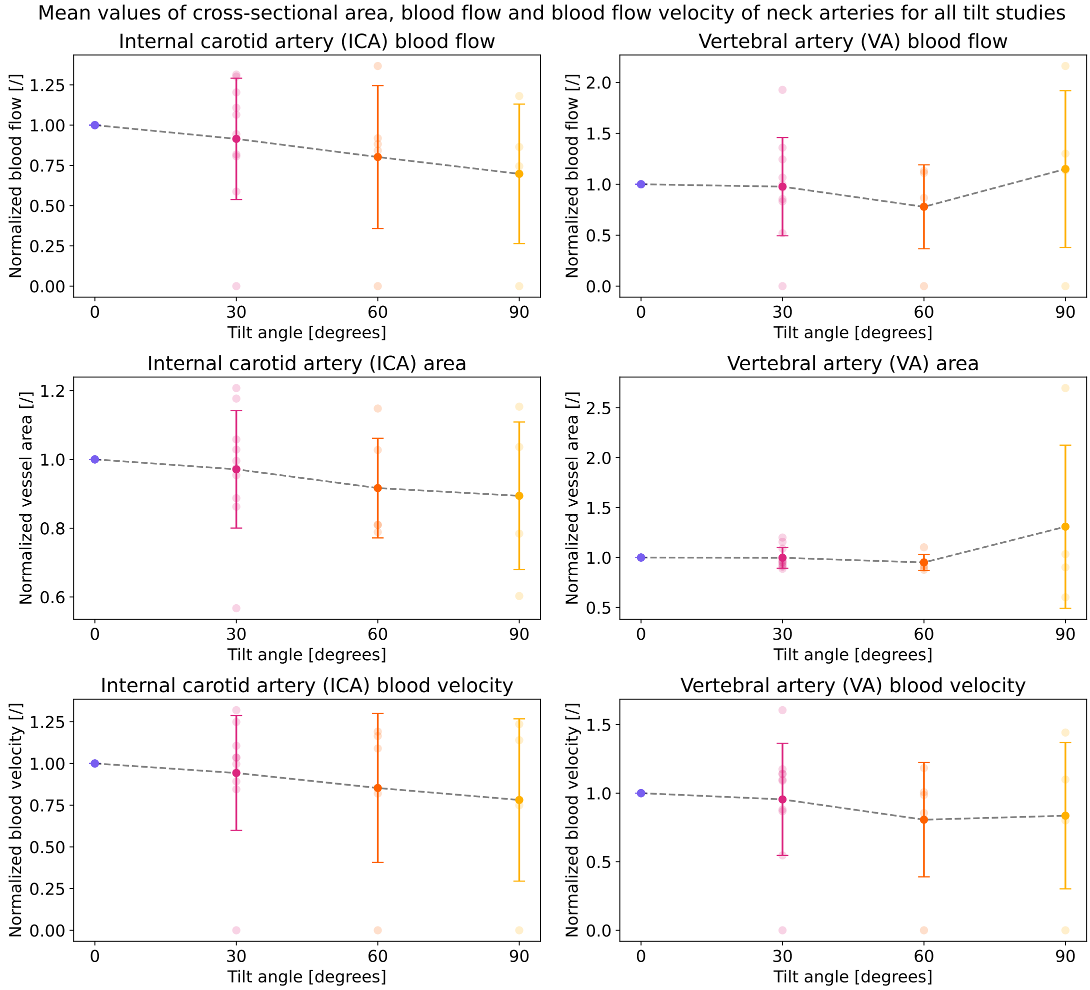

Figure 4.6: Mean values and standard deviations of blood flow, area and blood velocity of ICA and VA arteries for the complete population. Light dots represent normalized average data for each participant, while dark dots and whiskers indicate mean values and standard deviations for the entire population at each tilt angle. All quantities are normalized to their corresponding values at 0°. The first row presents blood flow data, the second row cross-sectional area, and the third row blood flow velocity. The left column corresponds to the ICA, the right to the VA. For the ICA, all three quantities decrease across all tilt angles. For the VA, they decrease at 30° and 60° but increase in blood flow and cross-sectional area at 90°.

not easy due to its position inside the skull. Nevertheless, we can inference some information analyzing other quantities.

The vessels that supply blood to the brain are divided in two groups. There are arteries that supply blood to the anterior brain, like the ICA, and there are arteries that supply blood to the posterior brain, like the VA. These arteries are then interconnected trough other arteries belonging to the circle of Willis, which guarantees an homogeneous blood supply to the different parts of the brain (Pocock et al., 2017). The amount of blood that flows through the ICA, the VA, and the arteries of the circle of Willis is controlled by the cerebral autoregulation, a control mechanism that maintains adequate blood supply to the brain in response to changes in the cerebral perfusion pressure. This control mechanism acts mainly by adjusting the resistance of the vessels that supply blood to the brain (Sagirov et al., 2023). However, the cerebral autoregulation does not work alone. It has been observed that during postural changes, from supine to upright, the cerebral autoregulation mechanisms are closely connected to the responses activated by the sympathetic nervous system previously described, and in particular they are inversely correlated (Nasr et al., 2014). Thus, analyzing the blood flow coming from the ICA and the VA can give us important information about the general blood supply to the brain and the behavior of the cerebral autoregulation.

Different studies (e.g. Ogoh et al., 2015; Sato et al., 2012; van Campen et al., 2018) analyzed the responses of blood flow to orthostatic stress in ICA and VA. The authors of these studies observed that the cerebral blood flow was reduced following an increase of orthostatic stress, due to a reduction of the flow in these vessels. van Campen et al. (2018) performed a 30 min HUT test at 70° and they observed a similar flow reduction in both ICA and VA at 70° with respect to the 0° position. On the contrary, Sato et al. (2012) performed a 9 min HUT test at 60° and they found no significant reduction in VA blood flow at 60° with respect to the 0° position, while ICA blood flow was reduced. Thus, these experimental studies suggest that while the blood flow in the ICA responds immediately to orthostatic stress, blood flow in the VA reduces only during severe orthostatic stress, giving rise to regional differences in the cerebral blood flow and in cerebral autoregulation responses between anterior and posterior vascular areas (Ogoh et al., 2015; Sato et al., 2012).

Our data (see fig. 4.6) display the behavior of the ICA and the VA under the different degrees of orthostatic stress experienced by the volunteers. We observe that the blood flow of the ICA decreases while increasing the angle of tilt (see fig. 4.6, top left panel). In particular, we observe a reduction of 9% at 30°, of 20% at 60°, and of 31% at 90° with respect to the 0° position. Similarly, the cross-sectional area reduces of 3% at 30°, of 8% at 60°, and of 11% at 90° with respect to the 0° position (see fig. 4.6, center left panel), while the blood velocity decreases of 6% at 30°, of 15% at 60°, and of 22% at 90° with respect to the 0° position (see fig. 4.6, bottom left panel). On the contrary, the VA presents a decrease in all the measured quantities at 30° and 60° with respect to the supine position similar to the one described for the ICA, but it presents an increase in both blood flow and cross-sectional area at 90° with respect to the 0° position. In fact, we measure an increase of 15% in blood flow and of 31% in cross-sectional area (see fig. 4.6, right panels). The VA blood velocity instead presents a decrease of 17% at 90° with respect to the 0° position, which however corresponds to an increase of 5% with respect to the 60° position (see fig. 4.6, bottom right panel).

Our data agree with what observed by Ogoh et al. (2015); Sato et al. (2012); van Campen et al. (2018). In fact, while at 30° and 60° there are no significant differences between ICA and VA behaviors, as in van Campen et al. (2018), at 90° we observe how the cerebral autoregulation responds differently on these two vessels, as in Sato et al. (2012). Specifically, our results suggest that the cerebral autoregulation is most responsive at 90°, rather than at 30° or 60°, because the blood supply at 90° falls below a critical threshold, signaling an inadequate level of perfusion. Therefore, at 90°, while the arterial baroreceptors triggers the increase in systemic vascular resistance through the vessels constriction, the cerebral autoregulation reduces the resistance of the vessels in the neck and head areas through a dilatation of these vessels, thus increasing the cross-sectional area, the blood velocity and the blood flow with respect to the previous angle of tilt (60°). However, while these changes are evident on the VA (see fig. 4.6, right panels), they are not observed on the ICA (see fig. 4.6, left panels), which may indicate that the arterial baroreceptors response dominates over the cerebral autoregulation response. It is also worth noting that, in a couple of individual cases, very low flow values were observed at intermediate tilt angles for both ICA and VA. These measurements likely reflect subject-specific physiological responses combined with the sensitivity limits of the acquisition procedure. Despite the presence of these outliers, they do not alter the overall trends reported here, which remain consistent across the study population.

An additional quantity that we considered to analyze the behavior of the blood flow in the brain is the blood velocity recorded in the MCA. The MCA originates from the ICA, thus it seems reasonable to think that a decrease in blood velocity of the ICA results in a decrease in blood velocity of the MCA. Our data (see fig. 4.7) agree with this behavior. In fact, we observe that at 30° the MCA blood velocity is almost constant, increasing of only 2% with respect to the 0° position, while at 60° and 90° it decreases of 11% and 17% with respect to the 0° position, respectively. Other works, like the one by Garrett et al. (2017), report similar results.

4.4.6 Cerebral outflow

Cerebral outflow refers to the volume of blood that drains from the brain through the veins, returning to the heart and lungs for oxygenation. It should equalize the cerebral inflow to guarantee the adequate removal of waste products from the brain. It is well known that there exist

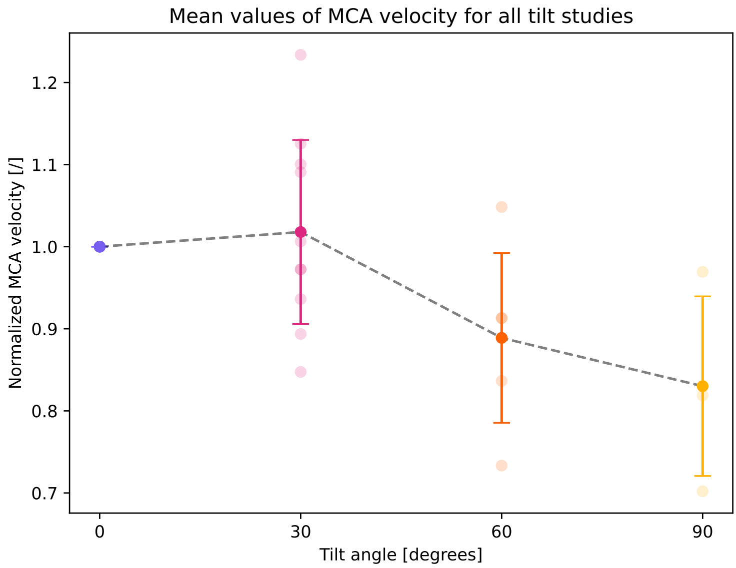

Figure 4.7: Mean values and standard deviations of MCA velocity time series for the complete population. Light dots represent normalized average data for each participant. Dark dots and whiskers represent mean values and standard deviations for the entire population at the considered angle of tilt. Results show a decrease in MCA velocity with respect to the 0° position and corresponding to an increase in the angle of tilt.

different venous pathways of drainage of the cerebral blood flow based on the body position considered. In a resting supine position, the primary pathway is through the IJVs. In the upright position, the IJVs partially collapse and the venous outflow from the brain is redirected to the VVs and other vessels of the extrajugular system such as the deep neck veins (Doepp et al., 2004). The differences in cerebral blood flow distribution, as well as the differences in the anatomy of the veins may affect the extrajugular outflow pathways making more prominent the outflow through a specific type of vein (e.g. VVs) over the others. In addition, Sagirov et al. (2023) observed that the IJVs start to collapse when the human body assumes a tilted position between 10° and 30°, thus a change in the type of outflow pathway from IJVs to extrajugular veins may be visible for high tilting angles, like in our case 60° and 90°.

Our data (see fig. 4.8) highlight this change in outflow pathway from IJVs to extrajugular veins. In fact, we observe a reduction of the blood flow through the right IJV (see fig. 4.8, top left panel) that reaches -26% at 30° with respect to the 0° position, and -63% at 90° with respect to the 0° position. At the same time, we also observe that the cross-sectional area decreases of 14% at 30° with respect to the 0° position, and of 78% at 90° with respect to the 0° position (see fig. 4.8, center left panel), while the blood velocity increases of 81% and 125% at

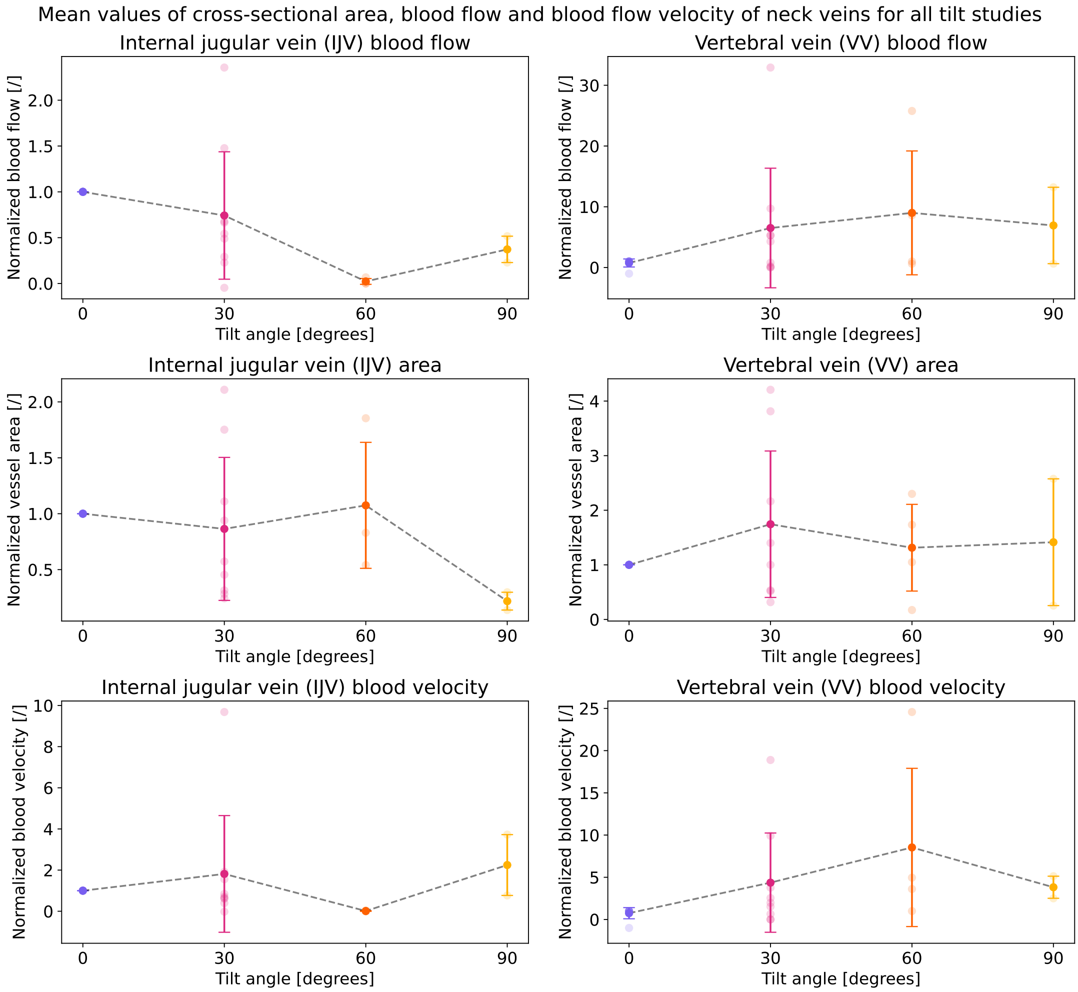

Figure 4.8: Mean values and standard deviations of blood flow, area and blood velocity of IJV and VV veins for the complete population. Light dots represent normalized average data for each participant. Dark dots and whiskers represent mean values and standard deviations for the entire population at the considered angle of tilt. The first row represents blood flow data, the second row represents cross-sectional area data, while the third row represents blood flow velocity data. Left column refers to IJV, right column refers to VV. Results highlight a shift in cerebral blood drainage from the IJV to the extra-jugular pathway. In fact, results of IJV show a decrease in blood flow with respect to the 0° position and corresponding to an increase in the angle of tilt. This decrease is mainly due to the venoconstriction that progressively reduces the cross-sectional area and increases the blood velocity. On the contrary, results of VV show an increase in blood flow with respect to the 0° position and corresponding to an increase in the angle of tilt, due to an increase in both cross-sectional area and blood velocity.

30° and 90° with respect to the 0° position, respectively (see fig. 4.8, bottom left panel). These changes are unlikely to be caused by the sympathetic activation previously discussed, as the effects of the sympathetic nervous system on veins are generally minimal. Instead, they appear to be consistent with the behavior of a passive collapse of the IJV resulting from a combination of factors. Among these, a key role may be attributed to the transmural pressure, defined as the difference between the pressure inside the vessel and the external surrounding pressure. When the transmural pressure approaches zero, the internal and external pressures nearly balance, causing the vessel to collapse. Because the external pressure is generally assumed to equal the atmospheric pressure (approximately zero), vessel collapse largely depends on the internal pressure. This pressure consists of two main components: the pressure generated by viscous forces associated with blood flow in the entire vascular system, and the hydrostatic pressure arising from the gravitational column of blood. Tilting of the body increases the hydrostatic component, thereby altering the balance between these pressures. When the hydrostatic pressure becomes comparable to or exceeds the viscous contribution, the resulting equilibrium may lead to passive vessel collapse (Holmlund et al., 2017). Focusing now on the 60° angle of tilt, we observe a 98% decrease in blood flow with respect to the 0° position, but we also notice an increase in cross-sectional area of 7% with respect to the 0° position and a decrease in blood velocity of 99% with respect to the 0° position. These changes in cross-sectional area and blood velocity at 60° appear to contrast with the trends observed at 30° and 90°. We believe that these anomalies are due to a shift in the location of the vessel collapse point relative to the probe's fixed position. Specifically, we hypothesize that, as at 90°, a 60° tilt is sufficient to induce vessel collapse. However, while the ultrasound probe was consistently positioned at the same anatomical site for all tilt angles, the collapse point itself shifts depending on the angle. As noted by Hinghofer-Szalkay (2011), the collapse point moves toward the more compliant end of the vessel, which, in this case, corresponds to the distal end of the IJV. In other words, our results suggest that the collapse point of the IJV shifts from head to heart, approaching the probe position as the tilt angle increases. This shift results in a greater distance between the probe and the collapse point at 60° than at 90°, explaining the nearly unchanged cross-sectional area at 60° relative to the 0° position, and the smaller cross-sectional area observed at 90° (see fig. 4.8, center left panel). Additionally, as the lumen at the collapse point narrows, the velocity of blood passing through this region increases in accordance with the continuity principle, whereas, as the lumen expands back toward its original size, the velocity correspondingly decreases. Consequently, when the probe is farther from the collapse point, as at 60°, the blood passing through the collapsed region slows down before reaching the probe, leading to the near-zero velocity observed. Conversely, when the collapse point lies closer to the probe, as at 90°, the blood has less distance to decelerate, resulting in the higher measured velocity (see fig. 4.8, bottom left panel).

As for the right VV, it presents a huge increase in blood flow (see fig. 4.8, top right panel), reaching +576% at 30° with respect to the 0° position, +825% at 60° with respect to the 0° position, and +617% at 90° with respect to the 0° position. These changes in blood flow are due to changes in cross-sectional area of the considered vessel and blood flow velocity. In fact, we also observe an increase in both cross-sectional area and blood velocity corresponding to an increase in the angle of tilt (see fig. 4.8, center and bottom right panels). The behavior of the VV, as well as that of the IJV, is consistent with a change in the venous outflow pathway, in agreement with both experimental observations and reports in the literature (Doepp et al., 2004). However, the specific extrajugular vessels involved in this process cannot be identified due to the lack of additional experimental data.

4.4.7 Peripheral arteries

The peripheral arteries that we insonated are the BA and the FA, and they are located at the beginning of the upper and lower limbs, respectively. These arteries are the main blood supply of arms and legs. Thus, studying these arteries can give us information about the behavior of the cardiovascular system in the limbs.

Looking at our data (see fig. 4.9), the first thing that we noticed is that at both 30° and 60°, the two arteries present a reduced blood flow with respect to the 0° position. In particular, the BA present a 35% decrease at both 30° and 60° with respect to the 0° position (see fig. 4.9, top left panel), while the FA present a 25% decrease at both 30° and 60° with respect to the 0° position (see fig. 4.9, top right panel). This behavior is in agreement with the reduction in CO and SV that we observed. In fact, upper and lower limbs are areas of the human body without vital organs, thus they are areas that can be sacrificed in terms of blood flow compared to other parts of the body, like the heart and the brain (Widmaier et al., 2016). The cross-sectional areas instead present a slight decrease around the supine values of about −3% and −1% for the BA at 30° and 60°, respectively (see fig. 4.9, center left panel), while an increase of about +13% and +6% is recorded for the FA at 30° and 60°, respectively, with respect to the 0° position (see fig. 4.9, center right panel). We believe that the observed changes in cross-sectional area in both BA and FA are primarily due to gravity-induced blood redistribution, modulated by autonomic compensatory mechanisms. During HUT, hydrostatic pressure increases in vessels below the heart and decreases in vessels above the heart. The BA, being near heart level, shows only minimal decreases in cross-sectional area, likely due to the relatively small hydrostatic pressure changes it experiences during tilts. In contrast, the FA expand more due to the hydrostatic pressure increase in the lower limbs. The non-linear changes with increasing tilt angle, such

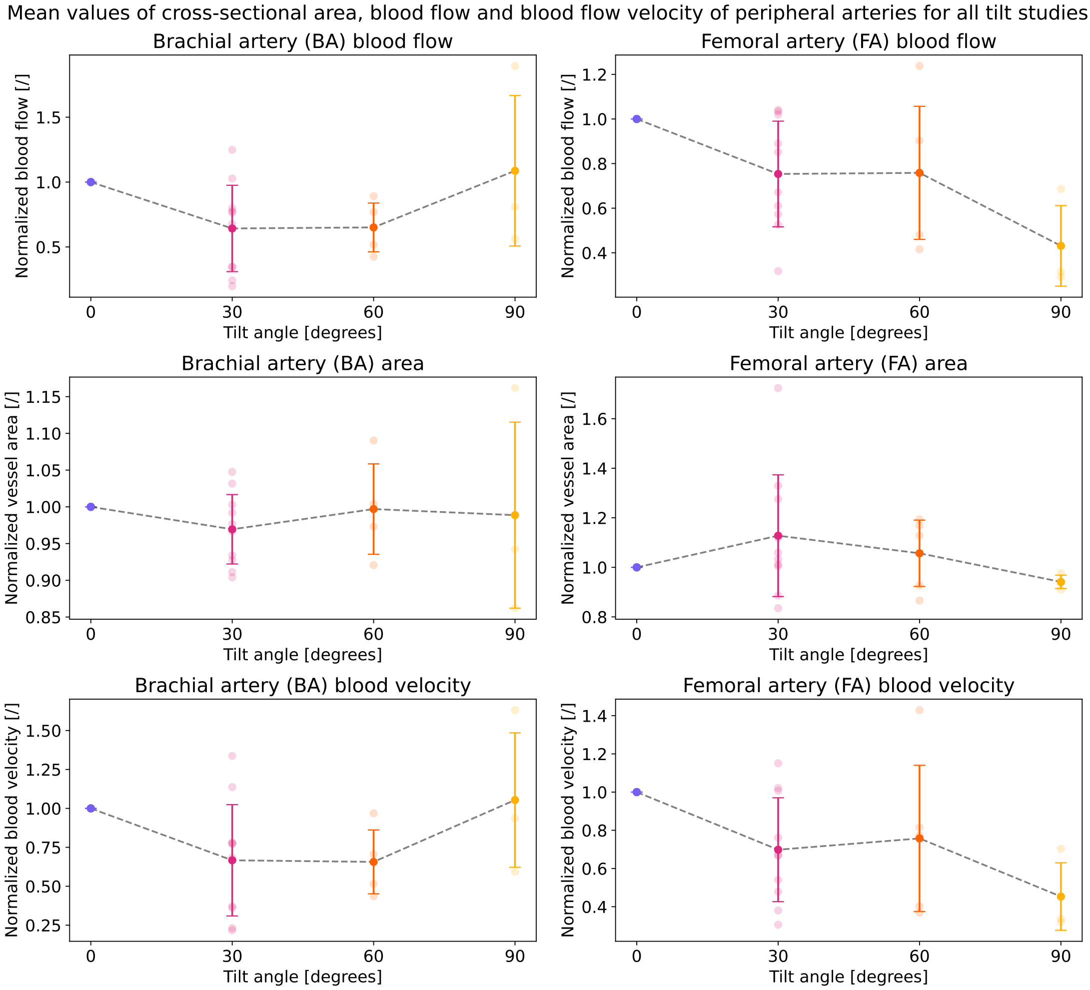

Figure 4.9: Mean values and standard deviations of blood flow, area and blood velocity of BA and FA arteries for the complete population. Light dots represent normalized average data for each participant. Dark dots and whiskers represent mean values and standard deviations for the entire population at the considered angle of tilt. The first row represents blood flow data, the second row represents cross-sectional area data, while the third row represents blood flow velocity data. Left column refers to BA, right column refers to FA. Results show a decrease in blood flow and blood velocity in both BA and FA at 30° and 60° with respect to the 0° position. Results also show a slight decrease in cross-sectional area of BA at 30° and 60° with respect to the 0° position, while an increase in cross-sectional area of FA is observed at 30° and 60° with respect to the 0° position. The results for the 90° position show a decrease in all quantities with respect to the 0° position in the FA, but an opposite behavior in the BA, with an increase in both blood flow and blood velocity, and an almost constant cross-sectional area with respect to the 0° position.

as the smaller FA increase at higher angles, likely reflect autonomic adjustments counteracting excessive expansion. As for the blood velocity, our data highlight a decrease in both vessels at 30° and 60° with respect to the 0° position. In particular, we recorded a decrease of 33% at both angles in the BA (see fig. 4.9, bottom left panel), and a decrease of 30% and 24% at 30° and 60°, respectively, with respect to the 0° position, in the FA (see fig. 4.9, bottom right panel). These reductions in velocity are consistent with the observed changes in cross-sectional area, blood flow, and the effects of gravity-induced blood redistribution. In the BA, the minimal decrease in diameter coupled with a substantial velocity reduction corresponds to the observed moderate reduction in blood flow to the upper limb during tilt. In the FA, despite an increase in area, velocity also decreases, likely reflecting venous pooling and contributing to the observed reduction in blood flow. At 90°, the behavior of the FA is more marked with respect to the previous angles of tilt (see fig. 4.9, right panels). In fact, we observe a reduction of the cross-sectional area of 6% with respect to the 0° position (see fig. 4.9, center right panel), of the blood flow of the 57% with respect to the 0° position (see fig. 4.9, top right panel), and of the blood velocity of 55% with respect to the 0° position (see fig. 4.9, bottom right panel). This marked response may reflect several complementary mechanisms. Autonomic compensatory mechanisms, which partially maintain flow at lower tilt angles, may reach their limit at 90°, preventing adequate vasoconstriction. Systemic reductions in venous return, stroke volume, and cardiac output contribute to the substantial decrease in blood flow of the FA. Finally, the body may actively redistribute blood to prioritize perfusion of vital organs, further decreasing flow to peripheral arteries like the FA. Together, these factors likely explain the pronounced reductions in FA area, velocity, and blood flow observed at 90°. Instead, the BA presents a different behavior compared with the FA. In fact, we observe an increase in both blood flow and velocity, while the area is almost constant (see fig. 4.9, left panels). We believe that in this case the cardiovascular response may reflect the body's prioritization of perfusion to vital regions. Because the BA is near heart level, hydrostatic pressure changes are minimal, allowing flow to increase without substantial changes in diameter. Additionally, autonomic adjustments may selectively maintain or slightly enhance flow in upper-body arteries while constricting lower-body vessels, effectively redistributing blood to critical areas. Reflex responses could also contribute to the observed increases in velocity and flow. Overall, these findings suggest that the BA behaves differently from the FA, highlighting regional differences in vascular regulation.

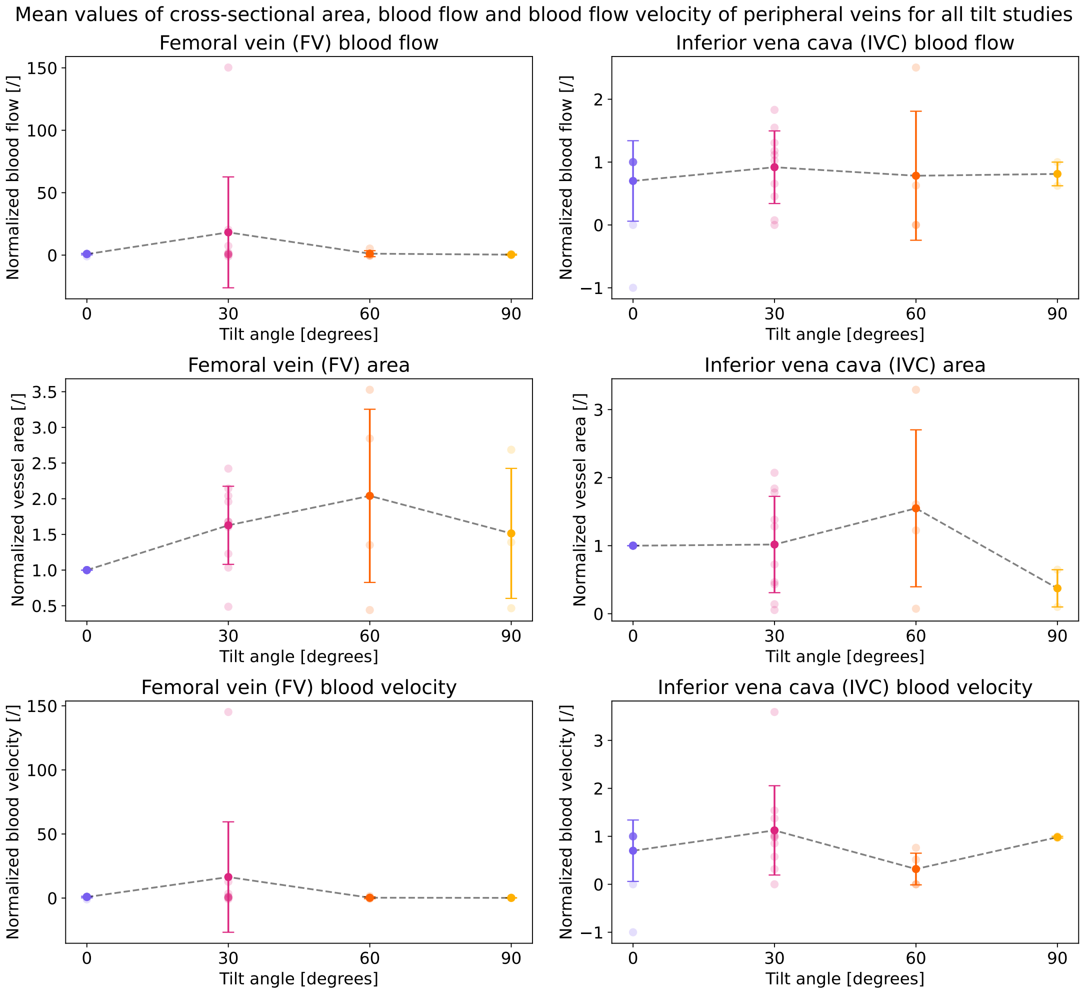

Figure 4.10: Mean values and standard deviations of blood flow, area and blood velocity of FV and IVC veins for the complete population. Light dots represent normalized average data for each participant. Dark dots and whiskers represent mean values and standard deviations for the entire population at the considered angle of tilt. The first row represents blood flow data, the second row represents cross-sectional area data, while the third row represents blood flow velocity data. Left column refers to FV, right column refers to IVC. Results of FV show a marked increase in cross-sectional area, a decrease in blood velocity, and oscillating blood flow. Results of IVC instead show an increase in blood flow, and oscillating cross-sectional area and blood velocity.

4.4.8 Other blood vessels: femoral vein and inferior vena cava

Finally, we analyze the behavior of two other blood vessels: the FV and the IVC (see fig. 4.10). The FV shows a pronounced increase in cross-sectional area, ranging from 63% to 104% at all tilt angles compared with the 0° position (see fig. 4.10, center left panel). Concurrently, blood velocity decreases by $50-65\%$ (see fig. 4.10, bottom left panel), while blood flow exhibits oscillations around the supine value at the same tilt angles (see fig. 4.10, top left panel). It should be noted that a potential outlier at 30° may affect the observed trend. We believe that this behavior reflects the effects of venous pooling in the lower limbs. In fact, the increase in cross-sectional area may allow the FV to accommodate the greater volume of blood shifted downward during tilt, while the reduced velocity and oscillatory flow may indicate that venous return is partially slowed and modulated by autonomic reflexes to maintain CVP and CO.

The IVC instead presents an increased blood flow reaching the $+22\%$ at 30°, $+8\%$ at 60° and $+11\%$ at 90° with respect the 0° position (see fig. 4.10, center right panel). At the same time, it also presents oscillating cross-sectional area and blood flow velocity of the order of $\pm 50\%$ in both cases with respect to the 0° position (see fig. 4.10, top and bottom right panels). We believe that these oscillations primarily reflect the influence of respiration (Mintz et al., 1981), which modulates venous return through cyclic changes in intrathoracic and intra-abdominal pressures. In addition, sympathetic venoconstriction, particularly within the splanchnic compartment, may actively modulate IVC flow by intermittently ejecting blood toward the thoracic cavity (Fudim et al., 2021), contributing to the observed variability and overall increase in mean flow during tilt. For one subject in the 0° position, a single measurement showed a local reversal of IVC flow (local backflow), likely driven by respiration-related pressure fluctuations in the absence of orthostatic stress. Nevertheless, this isolated measurement does not alter the overall trends observed across the study population.

4.4.9 Further considerations

The adopted experimental setup enabled a quantitative analysis of physiological responses to orthostatic stress. However, the study also presents certain limitations. The most significant among these is the limited number of volunteers who completed the full experimental protocol, which included tilts at $0°, 30°, 60°$, and $90°$. Expanding the sample size would enhance the statistical robustness of the results, allow for a more accurate assessment of inter-individual variability. Moreover, a larger cohort of participants would provide greater confidence in distinguishing systematic physiological trends from subject-specific effects, thereby improving the generalization of the findings. Future studies should also address technical and methodological aspects. First, the experimental protocol could be optimized by dividing the experimental session into multiple visits to reduce participant fatigue and mitigate potential long-term physiological drifts that may occur during prolonged testing. Second, ensuring consistent signal acquisition across sessions is crucial, as fluctuations in the participant's hemodynamic and respiratory states due to movement or postural adjustments can affect data quality. Additionally, integrating new measurements, such as respiratory activity and oxygen consumption, would provide valuable insight into coupled cardiovascular–respiratory dynamics, including cerebral blood flow regulation. Finally, refining data processing procedures would enable the extraction of additional information, such as blood flow waveforms, while minimizing measurement uncertainty and ensuring robust results for model validation. The type of computational model for which the experimental data are intended also plays a critical role, as it determines the specific data required for validation. Throughout this analysis, mean values obtained by averaging measurements across volunteers were used. This approach was adopted to characterize the general behavior of the cardiovascular system, independent of individual variability. However, it is important to recognize that such averaged behavior may not reflect the specific responses of any single participant. This highlights the importance of careful selection and interpretation of experimental data for model development.

4.5 Conclusion

Orthostatic stress is a major factor influencing the cardiovascular function, as it challenges the body's ability to maintain adequate blood flow and pressure during postural changes. The experimental work conducted in this study has provided valuable quantitative insights into the cardiovascular responses elicited by orthostatic stress across different tilt angles. By systematically recording hemodynamic quantities, this experiment has expanded the characterization of venous responses and provided new insight into autonomic regulation, while highlighting the interplay between vascular dynamics, autonomic regulation, and gravitational effects on blood distribution. The results demonstrate clear trends in both cardiac and venous–arterial responses, confirming previously reported findings while also providing new data that are otherwise scarce in the literature. They also offer essential information for the parametrization and validation of computational models of the cardiovascular system. At the same time, several limitations of the experimental work have been identified. Future studies should aim to address these limitations to improve both the type and quality of collected data. Finally, it is important to emphasize the nature of the data used for model validation: the current analysis relied on mean values averaged across volunteers to capture general cardiovascular behavior. While suitable for population-level modeling, this approach is not appropriate for personalized or subject-specific modeling. Careful consideration of these factors will be essential in future experimental and computational work aiming to deepen our understanding of cardiovascular responses to orthostatic stress. Overall, the experimental insights obtained here provide a critical foundation for the subsequent development and validation of the ADAVN model under orthostatic conditions, ensuring that simulations accurately reflect physiological responses across a range of postures.

Chapter 5

Modeling cardiovascular responses to orthostatic stress

5.1 Introduction

This final chapter brings together the key elements developed throughout this thesis: the tube law formulation, the numerical strategy designed to solve the governing equations, and the experimental data collected under controlled conditions. In the previous chapters, each of these components was investigated separately, allowing us to establish a solid theoretical foundation, a reliable computational framework, and a set of measurements suitable for validation. Here, they converge in a unified analysis aimed at understanding how our model behaves when confronted with physiologically relevant scenarios.

The focus of this chapter is on simulations that incorporate gravitational effects in both supine and upright postures. These two scenarios were chosen because they reveal how the cardiovascular system, and, by extension, our model, responds to changes in orthostatic stress introduced by posture. The transition from a supine to an upright position represents one of the most important physiological challenges, involving substantial changes in hydrostatic pressure distribution and cardiovascular regulation (Blomqvist and Stone, 1991). By comparing the predicted responses with experimental measurements, we evaluate the model's ability to reproduce key physiological trends under these conditions and identify the aspects that perform well, as well as those that require further improvement.

The first part of this chapter focuses on simulations performed in both supine and upright positions using the baseline parameter set. This baseline parameter set refers to the parameters used to perform the baseline simulations without gravity, which we are not going to modify throughout this work unless explicitly stated. By comparing the simulation outputs with literature data, we assess the extent to which the model captures expected physiological trends, such as pressure distributions and blood flow variations. This comparison enables us to identify the components of the model that robustly reproduce observed behavior, as well as those that exhibit limitations.

The second part introduces the upright simulation with manual calibration. In this context, manual calibration refers to the targeted adjustment of selected parameters, within physiologically reasonable bounds, to better match the experimental standing data. This procedure allows us to evaluate not only whether improved alignment with the measurements can be achieved, but also which parameters play the most influential role in shaping the model's response to orthostatic stress. The manually calibrated case therefore provides a complementary perspective, highlighting the strengths of the model structure while revealing potential sources of mismatch between simulation and experiment.

By synthesizing the theoretical, numerical, and experimental developments of the preceding chapters, this final analysis aims to offer an assessment of the model's current performance. At the same time, it outlines the most critical directions for future work, ultimately guiding the continued development of a physiologically consistent and experimentally validated modeling framework.

5.2 Methodology

In this section, we describe the methodological developments implemented to extend the ADAVN model for the study of posture-dependent hemodynamics. First, we outline the modifications introduced to incorporate gravitational effects into the governing equations and model formulation. Subsequently, we present the computational setup employed to simulate the cardiovascular responses to orthostatic stress under different body positions.

5.2.1 The ADAVN model: extension with gravity

The Anatomically Detailed Arterial-Venous Network (ADAVN) model provides a high-fidelity computational representation of the human cardiovascular system, enabling simulation of the entire circulation. Here, we summarize only the modifications introduced to incorporate gravitational effects, while the full model description is available in Blanco et al. (2015, 2020); HeMoLab (2013); Müller et al. (2023) and appendix A.

The first modification introduced in the ADAVN model is the capability to alter body orientation in 3D space. As described in appendix A, the vascular network is represented through vessel centerlines with defined 3D coordinates that reflect their anatomical orientation. Because the supine position serves as the reference configuration for these centerlines, we implemented a function that applies rigid-body transformations to the entire network, allowing the model to be rotated into any desired body orientation. Successively, the second modification that we introduced concerns the hemodynamic modeling itself. In the original 1D blood flow model, used to simulate hemodynamics in both arterial and venous networks, the gravitational term was neglected (i.e. $g_x(x) = 0$ in eq. (1.1)). In the present work, this term is redefined as a spatially varying parameter, whose value depends on the geometry and orientation of each blood vessel within the global vascular network. One of the advantages of the ADAVN framework is that it allows us to characterize the gravitational term in a more distributed and realistic manner across the network. These two features, the rigid-body transformation function and the non-zero gravitational term, enable the model to simulate hemodynamic responses to orthostatic stress across a range of postural conditions.

Another important component of the ADAVN model that we modified to account for gravitational effects is the microcirculation. Incorporating gravity into this part of the model is essential, as the microvascular compartments play a key role in determining local blood pressure, volume distribution, and capillary exchange. Under postural changes, arterioles, capillaries and venules experience hydrostatic pressure variations that influence venous return, making their proper representation crucial for accurately simulating the cardiovascular response to orthostatic stress. To capture these effects, the microcirculation, which in ADAVN is represented using 0D models, as described in chapter 1, was modified to include the hydrostatic pressure induced by gravity and to ensure consistent coupling with the 1D vascular network. A schematic representation of the microcirculation's 0D configuration, illustrating an example of a 1:1 arterio–venous connection, is shown in figure 5.1. Following the electrical analogy, pressure and blood flow in arterioles and venules are computed through the standard relations for resistive and capacitive elements (eqs. 1.2 and 1.3). We underline that two different types of microcirculation models were implemented, depending on how the unstressed volumes V_0 are defined. The first type is a linear model, which assumes that the unstressed volumes V_0, capacitances C_i, and resistances R_i, for arterioles (a), capillaries (av), and venules (v), are all constant parameters based on reference values, and their pressure–flow relationships are computed directly from equations 1.2 and 1.3. The second type is the nonlinear model, which assumes a nonlinear relationship between the pressure and the volume of the considered compartment (Celant et al., 2021), and is applied specifically to the venular compartments. In particular, the pressure–volume relationship considered in this nonlinear model, which replaces equation 1.3, is given by

$$P(t) = P_{ext} + P_{ref} + K\left[\left(\frac{V(t)}{V_{ref}}\right)^m - \left(\frac{V(t)}{V_{ref}}\right)^n\right], \tag{5.1}$$

where $m = 10.0$, $n = -1.5$, and $K = \frac{V_{ref}}{C_i(m-n)}$, with C_i denoting the constant reference capaci-

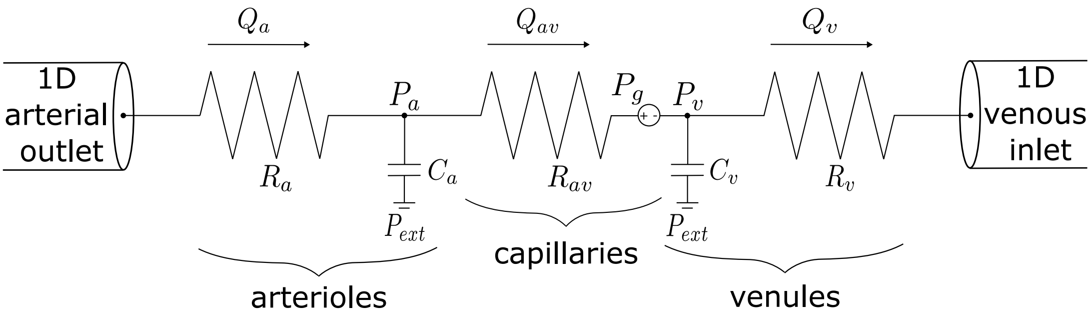

Figure 5.1: Microcirculation. 0D model of a 1:1 arterio–venous connection, with indication of arteriolar (*a*), venular (*v*), and capillaries (*av*) compartments. Each compartment presents a resistive element (*R*) with blood flow (*Q*) directed from the arterial to the venous side of the circulation. Arteriolar and venular compartments also present a capacitive element (*C*), while the capillaries compartment presents a generator of hydrostatic pressure (P_g).

tance used in the linear model. The parameters P_{ref} and V_{ref} represent the reference pressure and volume, respectively. They are assumed constant and are extrapolated from previous simulations using the linear model with $V_0 = 0$ in order to match the typical pressure and volume of the compartment under consideration. Equation 1.2 still applies in this nonlinear model, but here the resistances are no longer constant. Instead, they vary with volume according to

$$R(t) = R_{ref} \left(\frac{V_{ref}}{V(t)} \right)^2, \tag{5.2}$$

with R_{ref} denoting the constant reference resistance used in the linear model, which ensures consistency between the pressure–volume behavior of the compartments and their flow–resistance characteristics.

While gravitational effects are inherently included in the terminal arterial and venous segments, they are not directly accounted for in the microcirculation. To address this limitation, we introduced a hydrostatic pressure source immediately downstream of the capillary resistance R_{av}, as done in Snyder and Rideout (1969) and Fois et al. (2022), thereby incorporating the gravitational contribution within this specific segment. Specifically, the equation for the capillary flow Q_{av} was modified by adding a hydrostatic pressure term, computed as the scalar product between the gravitational acceleration vector $\bar{g}$ and the vector $\bar{l}$ connecting the outlet of the 1D terminal artery to the inlet of the 1D terminal vein associated with the given capillary. The governing equation for the capillary flow can thus be written as

$$Q_{av} = \frac{P_v - P_a + P_g}{R_{av}}, \tag{5.3}$$

where P_a and P_v are the arterial and venous pressures, computed with equation (1.3) or (5.1), R_{av} is the constant capillary resistance, and P_g is the newly introduced hydrostatic pressure, computed as

$$P_g = \rho \bar{g} \cdot \bar{l}, \tag{5.4}$$

with

$$\bar{l} = \begin{pmatrix} x_{a,outlet} \\ y_{a,outlet} \\ z_{a,outlet} \end{pmatrix} - \begin{pmatrix} x_{v,inlet} \\ y_{v,inlet} \\ z_{v,intlet} \end{pmatrix}. \tag{5.5}$$

5

This relation, together with equations 1.2 and 1.3 (or (5.1)), provides the complete set of equations governing the dynamics of the terminal microcirculatory compartments. These equations offer a simplified yet physiologically meaningful description of the pressure–volume dynamics within the terminal vessels and serve as the basis for coupling the microcirculation with the larger-scale 1D vascular network.

5.2.2 Simulation setups

In this section, we describe the computational configurations employed to simulate cardiovascular responses to orthostatic stress using our model. Specifically, we used an unpublished version of the ADAVN model, referred to as ADAVN86. This model was developed by Caterina Dalmaso, a fellow Ph.D. student in our research group, as part of her project. ADAVN86 is a reduced representation of the full 1D arterial and venous network, comprising the 86 main systemic and terminal arteries from the ADAN86 model (Blanco et al., 2020), 23 additional coronary arteries, and 189 veins from the ADAVN model, including 58 cerebral and 13 coronary veins (Müller et al., 2023). Consistently with the ADAVN framework, ADAVN86 also incorporates 30 venous valves and 53 Starling resistors. All other features of the ADAVN86 model not explicitly described here, such as the nonlinear tube law for the 1D vessels and the 0D models for the heart and lungs, are identical to those of the full ADAVN model. Further details can be found in Blanco et al. (2020); Müller et al. (2023), in chapter 2, and in appendix A. The ADAVN86 model was parametrized to closely match haemodynamic waveforms obtained through the ADAVN model in the thoracic and abdominal vasculature. The choice of using ADAVN86 instead of the full ADAVN model is primarily due to computational reasons, as the reduced network preserves the key physiological features relevant for orthostatic simulations while significantly lowering the computational cost.

The simulations were designed to reproduce key physiological conditions associated with orthostatic stress. We initially conducted three simulations, referred to as NoGravity, Hut00, and Hut90, whose main characteristics are summarized in table 5.1. The NoGravity simulation represents the baseline condition, reproducing the cardiovascular behavior in the supine position while neglecting the influence of gravity. This setup serves as a reference case for comparison with previously published versions of the model. The Hut00 simulation introduces a slight modification to the baseline. Here, the cardiovascular system is still modeled in the supine position, but the gravitational field is now applied to assess its effects under supine conditions. The Hut90 simulation represents the transition to an upright posture, corresponding to a head-up tilt of 90°. In this configuration, the full gravitational field acts along the body's longitudinal axis. This setup allows investigation of the cardiovascular adjustments required to maintain adequate perfusion under orthostatic stress, and provides a basis for evaluating the impact of gravity-induced blood redistribution on systemic hemodynamics. To achieve this configuration, the simulation was performed over a total period of 70 s: an initial 10 s in the supine position, followed by a 45 s transition phase to gradually reach the upright posture, and concluding with 15 s in the final upright position, to allow the system to settle into its periodic solution. For a given posture, the model converges to a unique periodic solution that does not depend on the initial conditions. However, the direct application of the full gravitational field while retaining the initial conditions and the parametrization calibrated for the supine position without gravity (NoGravity simulation) leads to large, non-physiological oscillations in several model variables during the initial seconds of the simulation. The inclusion of a gradual transient phase is therefore necessary to ensure numerical stability and smooth convergence of the solution. Moreover, the progressive rotation better reflects the experimental head-up tilt protocol presented in chapter 4, in which postural changes occur over a finite time rather than instantaneously. In principle, the transient phase could be avoided by adopting initial conditions and a parametrization specifically calibrated for the upright posture with gravity. However, this was not pursued here in order to preserve consistency with the supine calibration and to explicitly model the postural transition.

In addition to the previous simulations, we performed four further simulations designed to mimic the influence of the autonomic nervous system on cardiovascular regulation. These simulations were based on the Hut90 setup and thus correspond to the upright position under the full gravitational field. In these cases, the HR was increased by 23%, the maximal ventricular elastance was increased by 18% and the arteriolar resistances were raised by 40% to represent autonomic modulation. The total peripheral venous compliance, however, is less well characterized in literature. To account for this uncertainty, it was varied at four levels: baseline (0%), −10%, −20%, and −30%. All these percentage changes were chosen based on values reported in literature (Blomqvist and Stone, 1991; Hinghofer-Szalkay, 2011; Koubenec et al.,

Table 5.1
Simulation setups. Description of the simulation setups. Each case corresponds to a different combination of gravitational loading and body orientation for evaluating orthostatic effects. The second part of the table reports the corresponding calibration adjustments applied to heart rate (HR), maximal ventricular elastance (E), arteriolar resistances (R), and total peripheral venous compliance (C).

Simulation name	Gravity load	Body position	Calibration adjustments (%)			
			HR	E	R	C
NoGravity	No	Supine	0	0	0	0
Hut00	Yes	Supine	0	0	0	0
Hut90	Yes	Upright	0	0	0	0
Hut90_C00	Yes	Upright	+23	+18	+40	0
Hut90_C10	Yes	Upright	+23	+18	+40	−10
Hut90_C20	Yes	Upright	+23	+18	+40	−20
Hut90_C30	Yes	Upright	+23	+18	+40	−30

1978; Levick, 2009; Sagawa et al., 1977; Smith et al., 1994), with the range for venous compliance specifically intended to explore plausible physiological variability. The resulting simulations are referred to as Hut90_C00, Hut90_C10, Hut90_C20, and Hut90_C30, and their main characteristics are summarized in table 5.1. These configurations were specifically selected to reproduce typical physiological responses associated with orthostatic stress, allowing assessment of how changes in venous capacitance interact with cardiac and vascular adjustments to maintain hemodynamic stability.

The numerical method used to perform all the simulations is the one presented in chapter 3, with a CFL number of 0.8. All blood vessels were discretized using a maximum mesh spacing of 2 cm, and the parameters defining the vessel mechanics in the tube laws were assumed to be constant across all vascular segments. Additionally, the 1D arterial and venous networks were connected using the nonlinear model of microcirculation. The final simulation time for all cases was set to 70 s, and the results presented in the next section correspond to the last simulated cardiac cycle.

5.3 Results and discussion

In this section, we present and discuss the results obtained from the simulations previously introduced. First, we compare the outcomes for the supine position with and without gravity. Next, we examine the differences between the supine and upright positions under the influence of gravity. Finally, we discuss the results for the upright position with gravity following manual calibration.

Table 5.2
Blood volume distribution in supine position. Percentage blood volume distribution for NoGravity and Hut00 simulations, and their differences.

Compartment	NoGravity (%)	Hut00 (%)	Difference (%)
Heart	7.10	6.93	-0.17
Pulmonary circulation	6.79	6.64	-0.15
1D arteries	5.43	5.40	-0.03
1D veins	8.22	8.22	0.00
Terminal arteries	9.63	9.63	0.00
Terminal veins	62.33	62.72	0.38
Terminal coronary vessels	0.49	0.47	-0.02

5.3.1 Supine position simulations: Gravity vs. No gravity

The comparison between simulations performed in the supine position with and without gravity, Hut00 and NoGravity respectively, highlights the specific contributions of gravitational loading in a posture where hydrostatic effects are minimized with respect to the upright posture, but still present.

The first thing that we notice when we analyze the blood volume distribution in table 5.2 is that the inclusion of gravity produces only modest distributions across model's compartments. Most changes remain below 1% of the total blood volume, confirming that the supine orientation minimizes gravitational effects. The heart and pulmonary circulation show slightly reduced volumes in the Hut00 condition compared to NoGravity, with differences of approximately 0.17% and 0.15%, respectively. Similarly, a minor reduction is observed in both 1D arteries and coronary vessels, indicating that these arteries of the ADAVN86 network, which are explicitly solved using the 1D blood flow model, are only minimally affected. Conversely, the terminal venous compartment exhibits a small increase, about 0.38% when gravity is included, suggesting a subtle pooling tendency even in the supine posture. The 1D veins of the ADAVN86 network, also solved with the 1D blood flow model, and terminal arteries remain essentially unchanged, with differences close to zero.

Another relevant point is the comparison of cardiac and haemodynamic outputs. Table 5.3 presents the main variables from the NoGravity and Hut00 simulations alongside literature reference values. Overall, the two simulations exhibit similar behaviors, with most variables falling within or near the physiological ranges reported in the literature. However, the main focus here is on the effect of gravity in the supine position. In this sense, the results show that including gravity in the supine posture produces only minor differences. Pressures in the systemic circulation, including systolic, diastolic and mean arterial pressures, are comparable, with differences of only few millimeters of mercury between simulations. Central venous pressure

Table 5.3
Hemodynamic variables in supine position. Hemodynamic variables for NoGravity, Hut00, and reference conditions. MAP: mean arterial pressure, SBP: systolic blood pressure, DBP: diastolic blood pressure, MPAP: mean pulmonary arterial pressure, CVP: central venous pressure, LVSV: left ventricle stroke volume, CO: cardiac output, CBF: cerebral blood flow, CorBF: coronary blood flow.

Variable	NoGravity	Hut00	Ref. value	Reference
MAP (mmHg)	98.36	95.80	88 ±8	McEniery et al. (2005)
SBP (mmHg)	117.79	114.75	123 ±10	McEniery et al. (2005)
DBP (mmHg)	76.38	74.26	73 ±8	McEniery et al. (2005)
MPAP (mmHg)	15.03	14.66	14 ±3	Lau et al. (2016)
CVP (mmHg)	4.64	4.50	0 - 5	Levick (2009)
LVSV (mL)	78.29	76.56	40 - 120	Levick (2009)
CO (mL/s)	96.15	93.95	83.30 ±33.3	Cattermole et al. (2017)
CBF (mL/s)	15.66	15.40	12.18 ±2.12	Ford et al. (2005)
CorBF (mL/s)	5.10	4.87	4.50 ±1.36	Sakamoto et al. (2013)

and pulmonary pressure also align well, showing only minor deviations between the two simulations. Similarly, stroke volume and cardiac output show minimal differences, while cerebral blood flow and coronary blood flow remain consistent across both simulations. These findings indicate that, under supine conditions, gravitational loading has a very limited impact on cardiac and hemodynamic outputs, confirming that the Hut00 configuration accurately represents supine physiology and thereby supporting the use of the Hut00 configuration as a reliable baseline for further analyses.

A final aspect of interest is the shape of pressure and blood flow waveforms. Figure 5.2 presents these waveforms in six major vessels: three arteries (the internal carotid artery, ascending aorta, and femoral artery), and three veins (the inferior vena cava, internal jugular vein, and femoral vein). The waveforms from the NoGravity and Hut00 simulations show small differences in flow rates and arterial pressures, while larger differences are observed in venous pressures. These pressure variations are due to the relative positions of the vessels along the direction of the gravitational field, which are no longer coplanar, rather than reflecting any fundamental change in hemodynamic behavior. This spatial arrangement modifies the hydrostatic pressure acting on each vessel, leading to the observed differences in internal pressure. Overall, while the waveforms remain largely consistent between the NoGravity and Hut00 simulations, the two cases are not completely equivalent due to these pressure changes. Taken together, the analyses of volume distributions, hemodynamic variables, and waveforms show that, although the Hut00 simulation closely reproduces the behavior of the NoGravity simulation, and thus remains valid for representing the supine condition, it is not strictly equivalent to it. The small but systematic differences introduced by gravitational loading may influence subsequent analyses, highlighting the importance of explicitly including gravity in the model even in the supine

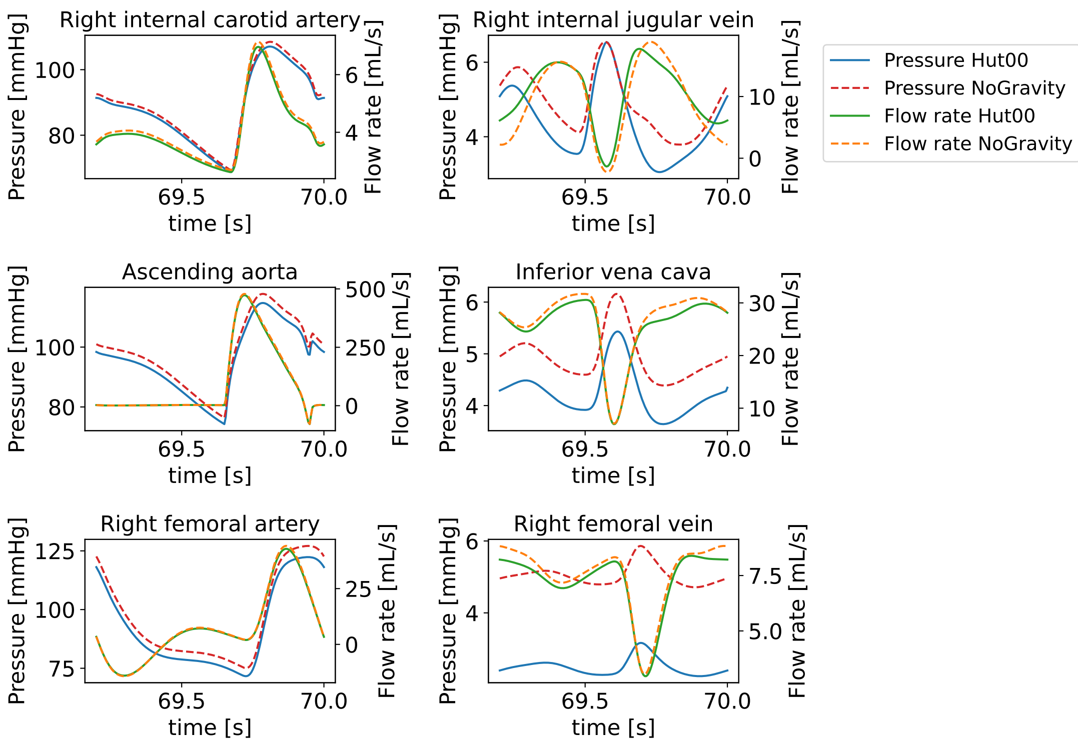

Figure 5.2: Supine waveforms. Pressure and blood flow waveforms along the final cardiac cycle of simulation at the midpoint of six selected vessels: right internal carotid artery, ascending aorta, right femoral artery, right internal jugular vein, inferior vena cava, and right femoral vein. Results are shown for supine position simulations with gravity (Hut00) and without gravity (NoGravity).

position.

5.3.2 Postural simulations: Supine vs. Upright

In this section, we compare simulations performed with gravity in two different body postures: the supine position (Hut00) and the upright position (Hut90). No model parameters are modified here between the two scenarios. The only difference between the two simulations is the orientation of the body, and therefore the direction of the gravitational field acting on the cardiovascular network. This setup allows us to isolate and characterize the purely mechanical effects of gravity on the cardiovascular system, providing a baseline understanding of how the model responds to postural changes before introducing physiological regulatory mechanisms.

A key aspect of the physiological response to a posture change is the redistribution of blood volume. When a person moves from the supine to the upright posture, approximately 340 to

560 mL of blood shifts from the thoracic region toward the lower extremities, primarily accumulating in the venous system (Smith et al., 1994). This gravitational pooling reduces central venous return and alters the filling conditions of the heart, ultimately influencing both systemic and pulmonary hemodynamics (Blomqvist and Stone, 1991).

In our simulations, where no regulatory mechanisms are included, the effects of this redistribution are captured.The comparison between Hut00 and Hut90 (see table 5.4) clearly shows a substantial redistribution of blood volumes across compartments. Most notably, the terminal venous compartment exhibits a marked increase of about 5.8% of the total blood volume in Hut90, reflecting significant venous pooling during standing. This shift is accompanied by large reductions in the volumes of central compartments. The heart and pulmonary circulation show decreases of 2.59% and 3.06%, respectively, indicating reduced thoracic blood content when standing. Smaller but consistent decreases also occur in the 1D arterial network and terminal arterial compartments. Conversely, the volumes of 1D veins and terminal coronary vessels show slight increases in Hut90, though their magnitude is much smaller than that observed in the terminal venous reservoir. To examine this behavior more closely, table 5.5 provides a detailed breakdown of blood distribution among the anatomical regions identified by the 1D blood vessels. In the arterial network, we see that the thoracic arterial volume decreases by 0.45%, while the volume in lower limbs increases by 0.05%. These changes indicate a downward redistribution of arterial blood, consistent with the gravitational shift of blood toward the lower body. In the venous network, the changes are even more pronounced. The venous volumes in the head, neck, and thorax decrease significantly by 0.54% and 0.13% respectively, whereas the lower limbs increase by 0.8% and the abdomen by 0.34%. This highlights that venous pooling predominantly occurs in the lower extremities, which is the primary reservoir for gravitationally shifted blood during standing. It is also worth noting that, while the percentages reported in tables 5.4 and 5.5 indicate that our model correctly captures the general tendency for venous pooling when standing, the absolute magnitude of blood volume shift is slightly lower than the physiological value of approximately 340-560 mL (Smith et al., 1994). Specifically, our simulations show a comprehensive pooling of 6.3% of the total blood volume in the lower extremities, corresponding to roughly 300 mL. We attribute this reduced value to two factors: first, the vascular network in our model contains fewer vessels than the human body, and second, the total blood volume considered in the simulations is around 4.8 L, which is slightly below the typical 5 L of a healthy adult (Klabunde, 2021).

The volume shifts have clear hemodynamic consequences. As shown in Table 5.6, moving from supine to upright results in marked decreases in stroke volume, from 76.56 mL to 46.93 mL, and in cardiac output, from 93.95 mL/s to 56.22 mL/s. These reductions re-

Table 5.4
Blood volume distribution in different postures. Percentage blood volume distribution for Hut00 and Hut90, and their differences.

Compartment	Hut00 (%)	Hut90 (%)	Difference (%)
Heart	6.93	4.33	-2.59
Pulmonary circulation	6.64	3.57	-3.06
1D arteries	5.40	4.81	-0.59
1D veins	8.22	8.69	0.47
Terminal arteries	9.63	9.61	-0.02
Terminal veins	62.72	68.51	5.80
Terminal coronary vessels	0.47	0.48	0.01

Table 5.5
Blood distribution among 1D anatomical regions. Percentage distribution of 1D arterial and venous blood volume among the different model's anatomical regions in Hut00 and Hut90. Percentages are computed with respect to the total arterial and venous blood volume (%), as well as the total blood volume (% TBV).

Region	Compartment	Hut00 (%)	Hut90 (%)	Hut00 (% TBV)	Hut90 (% TBV)	Difference (% TBV)
1D Arteries						
Head and neck	Arterial	5.52	5.32	0.30	0.26	-0.04
Back and spinal cord	Arterial	2.09	2.12	0.11	0.10	-0.01
Thorax	Arterial	44.66	40.88	2.41	1.97	-0.45
Abdomen and pelvis	Arterial	22.65	23.73	1.22	1.14	-0.08
Upper limbs	Arterial	10.31	10.38	0.56	0.50	-0.06
Lower limbs	Arterial	14.77	17.56	0.80	0.84	0.05
1D Veins						
Head and neck	Venous	17.47	10.34	1.44	0.90	-0.54
Back and spinal cord	Venous	0.00	0.00	0.00	0.00	0.00
Thorax	Venous	6.33	4.54	0.52	0.39	-0.13
Abdomen and pelvis	Venous	34.70	36.76	2.85	3.19	0.34
Upper limbs	Venous	5.09	4.73	0.42	0.41	-0.01
Lower limbs	Venous	36.41	43.63	2.99	3.79	0.80

flect the diminished venous return caused by gravitational pooling in the lower extremities. In turn, these changes strongly affect blood pressure behavior: mean arterial pressure drops from 95.80 mmHg to 63.25 mmHg, systolic blood pressure decreases from 114.75 mmHg to 77.86 mmHg, and diastolic pressure falls from 74.26 mmHg to 47.43 mmHg. Pulmonary arterial pressure similarly decreases from 14.66 mmHg to 8.70 mmHg, while central venous pressure drops from 4.50 mmHg to 2.41 mmHg. Together, these changes indicate that the reduced venous return lowers cardiac preload, highlighting impaired cardiopulmonary filling during upright posture.

The substantial reductions in stroke volume and cardiac output would, under physiological conditions, be partly compensated by reflex tachycardia and peripheral vasoconstriction. In the

Table 5.6
Hemodynamic variables in different positions. Hemodynamic variables for Hut00, Hut90, and reference conditions. MAP: mean arterial pressure, SBP: systolic blood pressure, DBP: diastolic blood pressure, MPAP: mean pulmonary arterial pressure, CVP: central venous pressure, LVSV: left ventricle stroke volume, CO: cardiac output, CBF: cerebral blood flow, CorBF: coronary blood flow.

Variable	Hut00	Hut90	Ref. value	Reference
MAP (mmHg)	95.80	63.25	88 $\pm$8	McEniery et al. (2005)
SBP (mmHg)	114.75	77.86	123 $\pm$10	McEniery et al. (2005)
DBP (mmHg)	74.26	47.43	73 $\pm$8	McEniery et al. (2005)
MPAP (mmHg)	14.66	8.70	14 $\pm$3	Lau et al. (2016)
CVP (mmHg)	4.50	2.41	0 - 5	Levick (2009)
LVSV (mL)	76.56	46.93	40 - 120	Levick (2009)
CO (mL/s)	93.95	56.22	83.30 $\pm$33.3	Cattermole et al. (2017)
CBF (mL/s)	15.40	5.81	12.18 $\pm$2.12	Ford et al. (2005)
CorBF (mL/s)	4.87	3.21	4.50 $\pm$1.36	Sakamoto et al. (2013)

present simulations, however, these mechanisms are not implemented, so the observed drops are larger than would be expected in vivo. Nevertheless, the trends are consistent with the early phase of orthostatic stress, during which blood volume from the thorax is rapidly shifted toward the lower extremities, causing a transient reduction in venous return and a temporary drop in systemic arterial pressures.

These hemodynamic changes have also direct implications for blood flow. Cerebral blood flow decreases substantially, from 15.40 mL/s to 5.81 mL/s, which in reality would normally trigger autoregulatory mechanisms to maintain brain perfusion. Coronary blood flow also declines, from 4.87 mL/s to 3.21 mL/s, which would normally limit myocardial oxygen delivery under physiological conditions. The pronounced drops in cerebral and coronary perfusion in the model indicate the absence of compensatory processes, such as cerebral autoregulation and baroreflex-mediated vasoconstriction, which are essential for an accurate representation of upright posture.

These results illustrate the purely mechanical consequences of blood volume redistribution during postural change in the absence of regulatory mechanisms: lower-body venous pooling reduces central venous return, decreases cardiac preload, lowers stroke volume and cardiac output, and leads to a drop in systemic pressures. Cerebral and coronary perfusion also decline, reflecting the direct impact of gravity on organ perfusion. Importantly, these effects are exaggerated relative to physiological conditions because no autonomic or local compensatory mechanisms are included. This analysis demonstrates how the model responds to postural changes purely from a mechanical perspective, providing a baseline for assessing the role of regulatory mechanisms in subsequent simulations.

5.3.3 Upright position simulations: Effects of manual calibration

In this section, we present the comparison between the upright simulation (Hut90) and its manually calibrated counterpart (Hut90_C). The specific parameter changes applied in the calibrated case are summarized in table 5.1 for reference. As shown in the previous section, the uncalibrated Hut90 model captures the immediate, mechanically driven trends associated with the transition to standing, particularly those occurring before the activation of autonomic control mechanisms. However, the observed hemodynamic responses deviate from physiological behavior due to the absence of baroreflex and cardiopulmonary reflex regulation. To address this limitation, we performed a preliminary manual calibration designed to mimic the primary effects of these autonomic controls. This calibration serves as a first approximation of how baroreflex-mediated adjustments to heart rate, vascular resistance, and venous tone, as well as cardiopulmonary reflex contributions, would modify the system's response. However, while the autonomic effects on heart rate, ventricular elastance, and vascular resistance have been quantified in the literature, much less information is available regarding reflex-induced changes in venous tone. For this reason, in our calibration we applied established average values for the known regulated variables, while exploring venous compliance reductions across a plausible range of percentage adjustments to account for its limited experimental characterization. This strategy enables us to first isolate the effects of the documented autonomic adjustments and then evaluate how modifications in venous tone, still poorly characterized experimentally, shape the overall hemodynamic response. By comparing Hut90 with Hut90_C, we aim to assess the potential impact that these regulatory mechanisms would have on our model and to evaluate whether such adjustments improve the physiological plausibility of the upright position simulations.

Figure 5.3 illustrates the effects of the manual calibration by showing the relative changes in stroke volume, cardiac output, arterial pressure (mean, systolic, and diastolic), and central venous pressure with respect to the supine simulation (Hut00), comparing the uncalibrated upright simulation (Hut90) with its calibrated versions (Hut90_C). The figure also includes the experimental measurements obtained from the head-up tilt test, which were analyzed in chapter 4, providing a reference for evaluating the physiological plausibility of the simulations. The first notable observation is that, in the configuration where venous compliance is not modified (Hut90_C00), the calibration of heart rate, ventricular elastance, and vascular resistance produces a markedly different response across the considered hemodynamic variables. In the experimental data, stroke volume is expected to decrease by approximately 47% upon standing. Consistently, the calibrated simulation (Hut90_C00) closely reproduces this reduction, whereas

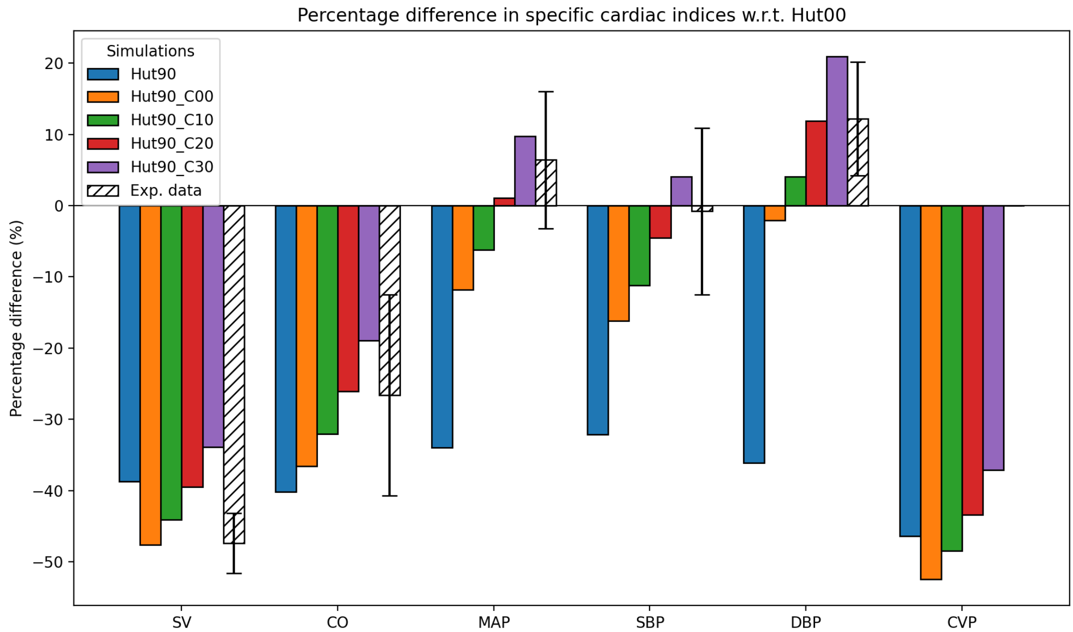

Figure 5.3: Calibration effects on hemodynamic variables using the nonlinear model of microcirculation. Relative changes in key hemodynamic variables with respect to the supine condition (Hut00) for the upright simulation (Hut90) and its calibrated versions (Hut90_C00, Hut90_C10, Hut90_C20, Hut90_C30) when the nonlinear model of the microcirculation is adopted. SV: stroke volume, CO: cardiac output, MAP: mean arterial pressure, SBP: systolic blood pressure, DBP: diastolic blood pressure.

the uncalibrated Hut90 underestimates it, showing only a −38% change. Cardiac output, which experimentally decreases by about 25%, is overestimated in both simulations: −40% in Hut90 and −37% in Hut90_C00. Nevertheless, the calibrated case shows a smaller deviation from the supine condition, indicating partial improvement relative to Hut90. Arterial pressures (mean, systolic, and diastolic) decrease in both simulations, contrary to the experimental trend, where they are expected to increase or remain stable. Again, the calibrated simulation exhibits a smaller relative drop, suggesting a trend toward the experimental behavior. This divergence highlights how the calibrated adjustments act through different mechanisms. The increase in heart rate and vascular resistance in Hut90_C00 helps stabilize stroke volume and partially align it with measured values. However, the unchanged venous compliance limits venous return, preventing adequate maintenance of cardiac output and arterial pressures. These results indicate that, while the manual calibration can reproduce some aspects of the experimental response, notably stroke volume, additional modifications, particularly in venous tone, are necessary to fully capture the physiological behavior observed during the head-up tilt test.

Table 5.7
Blood volume distribution in the upright posture. Percentage blood volume distribution for Hut90 and Hut90_C20, and their differences.

Compartment	Hut90 (%)	Hut90_C20 (%)	Difference (%)
Heart	4.33	4.61	0.28
Pulmonary circulation	3.57	4.35	0.78
1D arteries	4.81	5.59	0.78
1D veins	8.69	8.72	0.03
Terminal arteries	9.61	9.78	0.17
Terminal veins	68.51	66.45	-2.06
Terminal coronary vessels	0.48	0.51	0.03

When venous compliance is progressively reduced in the calibrated simulations (Hut90_C10, Hut90_C20, and Hut90_C30), the hemodynamic response moves closer to what would be expected from an active increase in venous tone. Compared with Hut90_C00, the reduction in compliance limits gravitational pooling in the lower extremities and partially restores central venous pressure and ventricular filling. Consequently, stroke volume, cardiac output, and central venous pressure change progressively across Hut90_C10 to Hut90_C30, with their deviations from the supine baseline becoming less negative. This trend illustrates the impact of venous tone on central blood volume redistribution during orthostatic stress, though the degree of compliance reduction does not necessarily correspond to the best agreement with experimental data for every variable.

The presence of an enhanced venous return is further supported by the results reported in Table 5.7, which compare the blood volume distributions between the Hut90 and Hut90_C20 simulations. Overall, the Hut90_C20 condition shows slightly higher volumes in the heart, pulmonary circulation, and terminal arteries compared to Hut90, while the terminal veins exhibit a modest reduction. This indicates a more efficient redistribution of blood toward the central circulation under the Hut90_C20 condition. The differences, although small, highlight subtle shifts in compartmental blood volume that may contribute to improved venous return and cardiac filling.

Correspondingly, the arterial pressure variables in figure 5.3 follow a similar compensatory pattern. MAP, SBP, and DBP steadily rise as venous compliance decreases, indicating improved systemic perfusion and a more effective counteraction of the orthostatic fall in arterial pressure. Although none of the calibrated cases fully match the experimental data in chapter 4, the improvements are clearly visible. In particular, the Hut90_C20 case shows the closest agreement with the targeted reflex-mediated adjustments, suggesting that enhanced venous tone plays a key role in moderating the hemodynamic destabilization observed in the upright posture.

It is worth noting, however, that the present calibration relies on significant assumptions regarding venous compliance. In the absence of detailed experimental data on how venous tone changes quantitatively during orthostatic stress, it is difficult to determine whether a uniform reduction of, for example, $10-30\%$ of the total peripheral venous compliance is physiologically justified. In reality, venoconstriction is likely to be regionally heterogeneous (Raffetto et al., 2010), with different vascular beds exhibiting distinct autonomic sensitivities. A more anatomically targeted adjustment of venous compliance might therefore enhance the realism of the simulated response and yield an improved match with expected physiological trends. Moreover, the use of a nonlinear model for the microcirculation may influence how changes in compliance are distributed across the vascular tree. In a nonlinear model, where a nonlinear pressure-volume relationship is used, compliance is not constant but varies with pressure. As a consequence, a global reduction in compliance does not produce a uniform proportional change in volume across all venous segments. Instead, vessels operating on the steeper portion of the pressure–volume curve may exhibit large volume changes for a small pressure variation, whereas vessels operating near a plateau may show minimal response to the same modification. Thus, the same percentage decrease in nominal compliance can lead to heterogeneous and model-dependent effects, potentially amplifying pooling in some regions while attenuating it in others. This raises the possibility that part of the observed behavior results from model-intrinsic redistribution mechanisms rather than purely physiological processes. These considerations indicate that the role of venous compliance remains an open question. Future work will need to explore more detailed formulations of venous tone regulation and to investigate how localized changes in compliance interact with nonlinear microcirculatory dynamics. Such refinements will be essential for determining whether the improvements observed in the current calibrated simulations are capturing the true physiological response or simply reflecting an approximate compensatory adjustment within the model.

To further investigate the role of microcirculatory dynamics, figure 5.4 reports the results of the same set of calibrated simulations using a linear formulation for the microcirculation. In this case, the impact of reducing total venous compliance is markedly different. Even when venous compliance is decreased substantially, the calibrated simulations exhibit hemodynamic responses that remain very similar to the Hut90_C00 case, with no meaningful recovery in stroke volume, cardiac output, or arterial pressures. This behavior indicates that a uniform global reduction in venous compliance is not effective when the microcirculation is modeled linearly, suggesting that physiological improvements in preload likely depend on local redistribution of compliance rather than a simple global change. In contrast, the nonlinear model inherently produces these region-specific changes in compliance, which can amplify or attenuate the in-

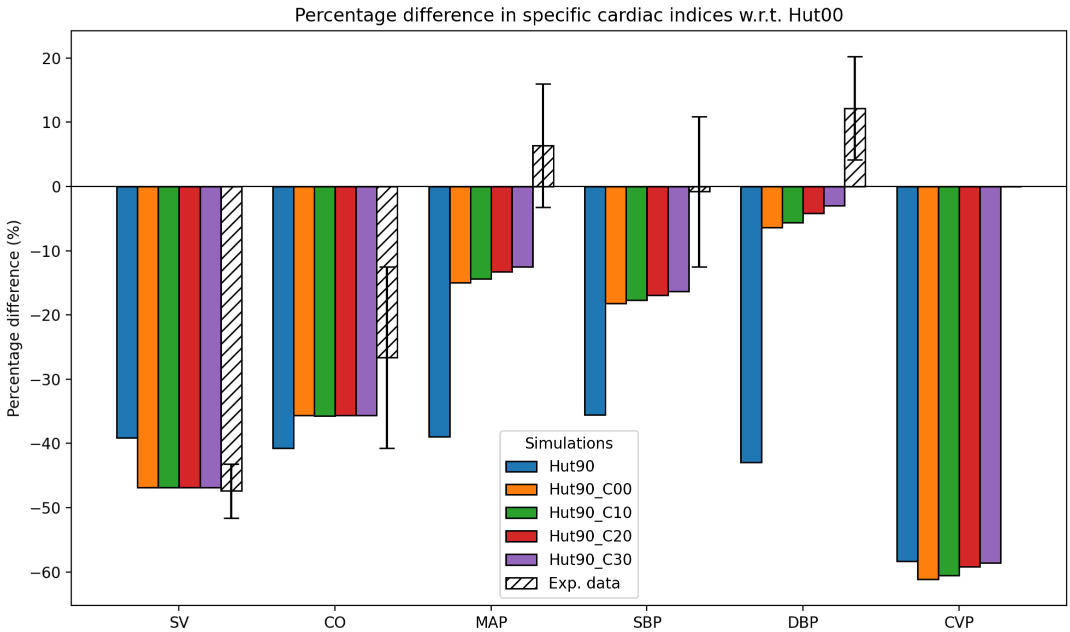

Figure 5.4: Calibration effects on hemodynamic variables using the linear model of microcirculation. Relative changes in key hemodynamic variables with respect to the supine condition (Hut00) for the upright simulation (Hut90) and its calibrated versions (Hut90_C00, Hut90_C10, Hut90_C20, Hut90_C30) when the linear model of the microcirculation is adopted. SV: stroke volume, CO: cardiac output, MAP: mean arterial pressure, SBP: systolic blood pressure, DBP: diastolic blood pressure.

fluence of a global compliance reduction depending on where each vascular segment lies along the pressure-volume curve. In other words, the linear model appears to require anatomically targeted adjustments, mirroring actual regional differences in venous tone, for venoconstriction to produce the expected hemodynamic effects, while the nonlinear model implicitly incorporates a form of distributed response that the linear model cannot reproduce. This reinforces the idea that the interaction between venous compliance and microcirculatory mechanics is nontrivial and that capturing realistic orthostatic adaptations will require future refinements involving regional control of venous properties and more detailed vascular reflex modeling.

Finally, in figure 5.5 we visualize the pressure distribution of the Hut90_C20 simulation, obtained with the nonlinear microcirculation model, directly on the anatomical network. This representation makes evident how strongly the hydrostatic component shapes the global pressure field in the upright posture, with a clear decline in pressure along vessels located above heart level and a corresponding increase in the lower extremities. However, the resulting distribution does not fully resemble the characteristic pressure profile observed in actual standing humans, especially in the the central and upper regions. For comparison, an example of the expected physiological pressure distribution in the upright posture can be found in Levick (2009) and Hinghofer-Szalkay (2011). In physiological conditions, several regulatory and structural factors act together to buffer raw hydrostatic gradients and prevent extreme cranio-caudal pressure drops. These include baroreflex-mediated adjustments in vascular tone, as previously seen, active modulation of cardiac function, and respiratory-driven intrathoracic pressure variations, all of which redistribute pressures more evenly across the circulation (Smith et al., 1994). Furthermore, intracranial and intra-abdominal pressures are not constant in vivo but adapt dynamically during orthostasis, influencing venous return, cerebrovascular pressures, and abdominal venous capacitance (Grillner et al., 1978; Moncur et al., 2024). In the present model, despite the manual calibration, these mechanisms are either absent or represented in a simplified manner, and gravitational effects on the heart and pulmonary circulation are not fully captured. As a result, the computed pressure field reflects the unregulated mechanical effects of gravity on the vascular network, rather than the physiologically modulated profile observed in standing individuals. Taken together, all these results confirm that the model successfully reproduces the primary mechanical effects of gravity on the cardiovascular system, while highlighting that further refinements are required to capture the full physiological regulation of pressure during orthostatic stress.

5.4 Conclusion

In this chapter, we investigated the hemodynamic response to postural changes using the ADAVN86 cardiovascular model. We first compared simulations in the supine position with and without gravity (Hut00 and NoGravity, respectively), exploring the impact of considering gravity in supine position. We then analyzed blood volume redistribution and its impact on key hemodynamic variables when moving from the supine (Hut00) to the upright (Hut90) posture without control mechanisms. Our simulations captured the general trends of venous pooling in the lower extremities, reductions in central venous return, decreases in stroke volume and cardiac output, and the corresponding effects on systemic and pulmonary pressures. However, these effects were exaggerated compared with physiological observations due to the absence of baroreflex and cardiopulmonary regulatory mechanisms.

To explore the role of autonomic regulation, we then introduced a preliminary manual calibration (Hut90_C) that mimics baroreflex and cardiopulmonary reflex adjustments, including heart rate, ventricular elastance, and vascular resistance. By progressively modifying venous

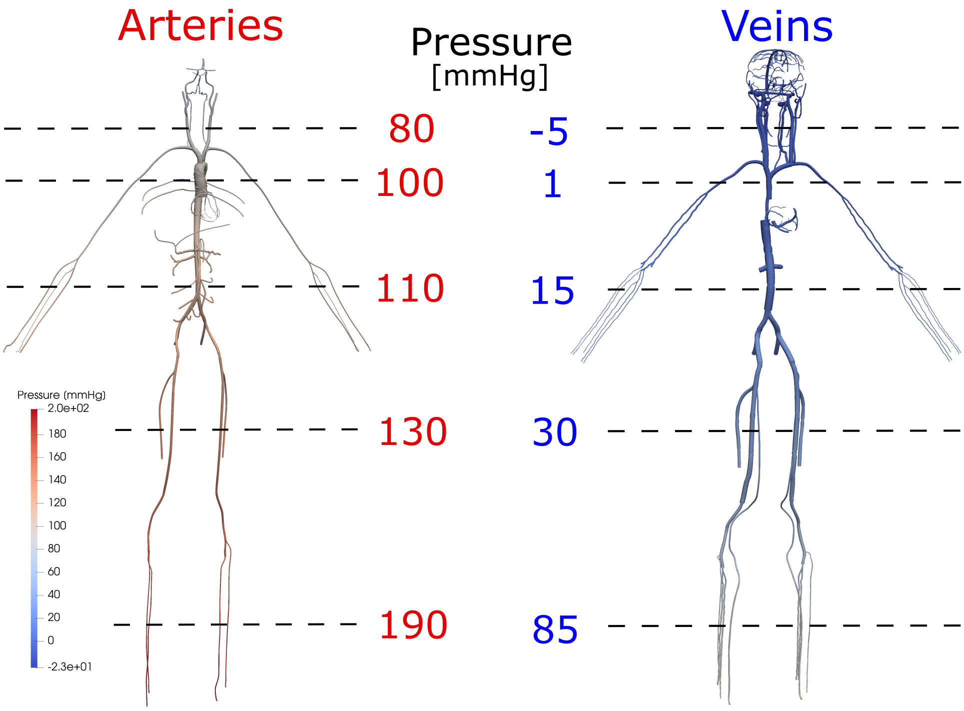

Figure 5.5: Pressure distributions. Network-based pressure rendering for the upright simulation (Hut90_C20), illustrating the pronounced hydrostatic gradient induced by gravity.

compliance, we showed that enhanced venous tone plays a key role in mitigating the hemodynamic destabilization caused by upright posture. Comparisons with a linear microcirculation model further revealed that local redistribution mechanisms are crucial for capturing the effects of venous tone on hemodynamics. These results emphasize the importance of both preload restoration and regional redistribution of venous compliance in reproducing physiologically plausible responses.

Finally, we visualized the pressure distribution of the best calibrated simulation (Hut90_C20), showing how gravity alone shapes the cranio-caudal pressure gradient in the upright posture. While the model captures the primary mechanical effects of gravity, the absence of dynamic intracranial, intrathoracic, and intra-abdominal pressures, as well as regulatory mechanisms, leads to exaggerated gradients compared with physiological observations. This highlights that, although the mechanical baseline is well represented, further refinements are needed to fully reproduce the regulated pressure distributions seen in vivo.

The simulation results are promising: they reproduce key features of orthostatic stress, illustrate the contribution of autonomic reflexes, and provide insight into the interaction between vascular compliance and hydrostatic effects. At the same time, these findings highlight clear directions for future developments. Key improvements include more detailed modeling of regional venous compliance, integration of full baroreflex and cardiopulmonary reflex control, and incorporation of non-constant pressures. Additional validation using experimental waveform measurements will be essential to strengthen model reliability. A more comprehensive discussion of future work and broader research directions is presented in chapter 6.

Chapter 6

Conclusion

This research project has focused on the development of a multiscale 1D-0D cardiovascular model that accounts for gravitational effects. Particularly, we aimed at extending the Anatomically Detailed Arterial-Venous Network (ADAVN) model by incorporating gravity into its framework. Although the methodology developed here is general and applicable to other 1D–0D cardiovascular models, the ADAVN model presents specific challenges, most notably the representation of the venous system with a 1D model, whose highly nonlinear behavior adds significant complexity when gravity is introduced. To address this aim, three major challenges were identified and investigated:

- the establishment of a mathematically convenient and physically consistent formulation of the tube law,
- the numerical methodology employed to ensure its stable and efficient solution,
- the representation of physiological processes, such as those mediated by control mechanisms, which are essential for reproducing realistic adaptive responses to postural changes.

This chapter revisits each of these elements, summarizing the key findings and discussing how they collectively contribute to extending the ADAVN model to include gravitational effects from theoretical, numerical, and physiological perspectives.

6.1 Mathematical formulation of the tube law

A key step in extending the ADAVN model with gravity involved establishing a mathematically convenient and physically consistent pressure–area relationship for the venous 1D segments. Since every 1D blood flow model relies on a tube law to close the system, particular attention was given to evaluating whether the formulation adopted in the ADAVN model for the venous system is suitable both in terms of parametrization and in its ability to preserve the hyperbolic nature of the governing equations, which is crucial for the modeling framework we aim to employ.

To this end, two tube law formulations were selected and examined in detail. Their mathematical properties, such as hyperbolicity and genuine non-linearity of characteristic fields, were analyzed to ensure that the 1D blood flow model preserves these properties when each tube law is employed. Following this analysis, both formulations were parametrized to reproduce ovine and human in vitro data. Particular attention was given to how constraining certain parameters to admissible ranges affects each tube law's ability to fit experimental data, as discussed in chapter 2. Importantly, our results show that the viscoelastic tube law, adopted in the ADAVN model, retains the desired mathematical properties of the 1D blood flow equations despite the imposed parametrization. This makes it a robust and reliable formulation for further model development.

6.2 Numerical methodology

A second important aspect of this project involved the development of a numerical method capable of solving the extended 1D blood flow model with gravity efficiently and stably. Incorporating gravitational terms in the system of equations requires careful numerical treatment to avoid instabilities and the computation of inaccurate solutions. Specifically, it requires the use of a well-balanced numerical method tailored to the newly introduced gravity source term.

To address this, we implemented a well-balanced high-order path-conservative numerical scheme. This method correctly computes steady-state solutions in presence of geometric- and algebraic-type source terms, such as the one resulting from incorporating gravity in the 1D model, while also accurately reproducing transient dynamics. The well-balanced property is particularly crucial for preserving hydrostatic pressure distributions, as demonstrated in chapter 3, where the method was applied to the 1D blood flow model with gravity on the ADAN86 network.

By ensuring accuracy in both steady-state and dynamic conditions, the numerical framework developed in this project enables reliable simulations of gravitational effects across different postures. This foundation is essential for integrating the physiological processes discussed in the following section and for achieving physiologically meaningful cardiovascular predictions.

6.3 Acquisition of experimental data

A final key aspect of this project involved representing the physiological mechanisms underlying cardiovascular responses to orthostatic stress. While many responses of the cardiovascular system are well-characterized, certain processes remain poorly understood. This lack of detailed physiological understanding and available data, particularly regarding the venous circulation and the autonomic nervous system regulation, poses a significant challenge for accurate model development. Accurately capturing these responses is essential for simulating realistic hemodynamic adaptations during postural changes.

To this end, we conducted a head-up tilt (HUT) test, as described in chapter 4, to measure relevant cardiovascular quantities under controlled orthostatic stress. The resulting data provided valuable insights into the dynamics of venous return, baroreflex-mediated autonomic adjustments, and overall cardiovascular function. In particular, the analysis revealed clear trends, including decreases in stroke volume, cardiac output, and cerebral inflow with increasing angle of tilt, accompanied by compensatory rises in heart rate and diastolic pressure, as well as a shift in cerebral venous drainage from the internal jugular to vertebral pathways. Together, these findings quantitatively describe how gravitational stress redistributes blood and activates autonomic regulation. All these experimental observations were then used to refine our understanding of the cardiovascular behavior and will serve as a basis for integrating physiological control mechanisms into the ADAVN model.

6.4 Modeling cardiovascular responses to orthostatic stress

In chapter 5, the three aspects developed throughout this work were brought together within the ADAVN model. This integration enabled the first simulations of cardiovascular responses to orthostatic stress in different postures using a highly detailed 1D arterial network coupled with a fully 1D venous network. These results represent an important step toward achieving a physiologically consistent multiscale model capable of capturing both the underlying hemodynamic responses and the adaptive regulatory mechanisms involved in orthostatic stress.

The simulations presented in chapter 5 reproduced the trends associated with orthostatic loading. In particular, the model captured the onset of venous pooling in the lower extremities following head-up tilting, as well as the associated redistribution of pressures and volumes across the arterial and venous systems. While the magnitude of venous pooling was overestimated, reflecting the absence of autonomic regulatory mechanisms, these results nonetheless provide insight into the passive mechanical effects of gravity within the extended framework. The simulations also explored the contribution of autonomic regulation, highlighting in particular the role of venous tone in mitigating the hemodynamic destabilization induced by upright posture.

Taken together, these findings indicate that the extended ADAVN model offers a promising foundation for multiscale simulations of the physiological responses to orthostatic stress. Although further refinement is needed to achieve fully quantitative accuracy, the results obtained here establish the feasibility and potential of the proposed approach.

6.5 Limitations and future works

Building on the foundations established in this thesis, several directions for future developments can be identified. Having constructed a multiscale 1D–0D cardiovascular framework that accounts for gravity, the subsequent steps arise naturally from both the capabilities achieved and the new physiological questions that the model enables us to address.

A first priority is the integration of autonomic regulatory mechanisms. Having now characterized the purely passive response of the circulation to gravitational loading, the model is in a position where the addition of baroreflex and cardiopulmonary reflex control mechanisms becomes both feasible and essential. Their inclusion will enable quantitatively realistic compensatory responses and will transform the current simulations from exploratory mechanistic tests into physiologically complete scenarios. In parallel, the present implementation of gravitational loading, successfully incorporated in both the 1D arterial and 1D venous networks, should be extended to all 0D compartments, including the heart and the pulmonary circulation. This generalization will ensure full internal coherence of pressures across central and peripheral regions and will make it possible to study global hemodynamic responses that remain inaccessible under the current partial treatment.

The increased fidelity in representing orthostatic responses gained so far also highlights the importance of further refining the microcirculation compartments. The current results reveal that global hemodynamic behavior is highly sensitive to the representation of venous peripheral compliance. Strengthening this component emerges as a natural next step, enabling the model to capture the subtle interplay between vascular capacitance, volume redistribution, and postural changes. Similarly, the cerebrovascular compartment warrants further development to surpass the limiting hypothesis of a constant intracranial pressure. Introducing a cerebrospinal fluid module would complete the physiological picture, allowing the framework to reproduce cerebral blood flow regulation, intracranial pressure dynamics, and their modulation during orthostatic stress.

Although this thesis introduced and successfully applied a dedicated numerical methodology for handling the inclusion of gravitational effects, future extensions of the model may challenge the current method. As the physiological complexity of the framework increases, particularly with regulatory mechanisms and intracranial dynamics, further developments or refinements of the numerical method may become necessary to ensure stability, efficiency, and accuracy.

In addition to these extensions, further refinements of the model's physiological complexity will be important. This includes incorporating additional mechanisms such as hormonal and metabolic regulatory pathways, as well as respiratory influences on venous return. Expanding the framework in this way would also allow exploration of inter-subject variability and the effects of anatomical or functional differences on orthostatic responses.

With these numerical, structural and regulatory components in place, a major objective will be to conduct orthostatic stress simulations using the complete ADAVN model and to compare the resulting hemodynamic responses with those generated by the reduced ADAVN86 network. The present thesis has established both modeling environments, laying a consistent foundation on which the next developments can build. Consequently, future works will be able to explicitly quantify how anatomical detail influences orthostatic behavior and to what extent simplified networks can reproduce clinically relevant responses. Progress on these fronts will also benefit from the acquisition of additional experimental data. The current study lacks a sufficiently detailed waveform analysis, which we believe is essential for demonstrating the impact of gravity on cardiovascular hemodynamics. Accordingly, waveform measurements from head-up-tilt protocols, particularly pressure and flow recordings at multiple anatomical sites, will be crucial both for parameter identification and for validating the full wave-dynamic behavior that the multiscale model is designed to capture.

Ultimately, once the regulatory framework and enhanced physiological aspects are incorporated, the model will be equipped to explore scenarios that were previously beyond reach. In particular, the availability of clinical recordings of syncope events provides a unique opportunity to test whether the extended ADAVN model can reproduce the onset, progression, and recovery phases associated with orthostatic intolerance. Reaching this stage will allow the model to move beyond simulating passive gravitational responses and begin to capture transient and pathological episodes, thereby significantly expanding its applicability to clinically relevant scenarios and realizing the full potential of the multiscale 1D–0D cardiovascular framework developed in this thesis.

6.6 Concluding remarks

Working on the extension of the ADAVN model to include gravitational effects and orthostatic stress responses has been both challenging and rewarding. Beyond the technical achievements, developing robust numerical methods, characterizing tube laws, and integrating physiological processes, this work has highlighted the intricate interplay between vascular mechanics, autonomic regulation, and body posture in determining cardiovascular function.

Personally, this project has reinforced my appreciation for the complexity of the cardiovascular system and the importance of combining experimental observations with computational modeling. It has also emphasized the value of systematically integrating theory, data, and numerical implementation to produce models that are both mathematically and physiologically meaningful.

From a scientific perspective, the results obtained provide a foundation for further studies of orthostatic stress, syncope, and related physio-pathological conditions. More broadly, this work contributes to the development of anatomically and physiologically detailed models capable of supporting future research and clinical investigations of cardiovascular behavior. Ultimately, this work highlights the importance of a multiscale approach to modeling the cardiovascular system, offering new opportunities to explore both normal physiology and disease mechanisms under a variety of conditions.

Appendix **A**

Background

This appendix outlines the fundamental physiological concepts and the modeling framework necessary for understanding the cardiovascular mechanisms investigated in this work. It begins with an overview of the human cardiovascular system, describing its anatomy and function in sustaining circulatory equilibrium. The subsequent section explores the physiological effects of orthostatic stress, emphasizing the hemodynamic adaptations and autonomic responses elicited by postural transitions. Finally, the appendix examines the state of the art in the ADAVN model, providing a detailed basis for interpreting its cardiovascular behavior and responses within the context of this work.

A.1 The human cardiovascular system

The cardiovascular system (CVS) is essential to human physiology. Its primary task is to deliver oxygen and nutritive molecules to tissues, to carry hormones, enzymes, antibodies and other substances and to remove carbon dioxide and metabolic waste produced by cells to recycle or expulsion centers (Levick, 2009).

The CVS consists of the heart, a network of blood vessels, and the blood. The heart is a hollow organ that can be found at the center of the thoracic cavity, between the two lungs. As it can be seen in figure A.1, showing a schematic representation of the heart anatomy, this organ is internally subdivided into four chambers: left and right atria, and left and right ventricles. Left chambers are separated from right chambers by a septum, which is a wall of cardiac tissue that prevents oxygenated blood handled by heart left side to mix with de-oxygenated blood handled by heart right side (Martini et al., 2012). Atria receive blood from veins and make it flow to ventricles through cardiac valves. Similarly, ventricles return blood to arteries, making it flow through other cardiac valves. There are four cardiac valves in total. The mitral valve lies between the left atrium and the left ventricle, while the tricuspid valve is located between the right atrium and the right ventricle. The aortic valve is positioned at the outlet of the left

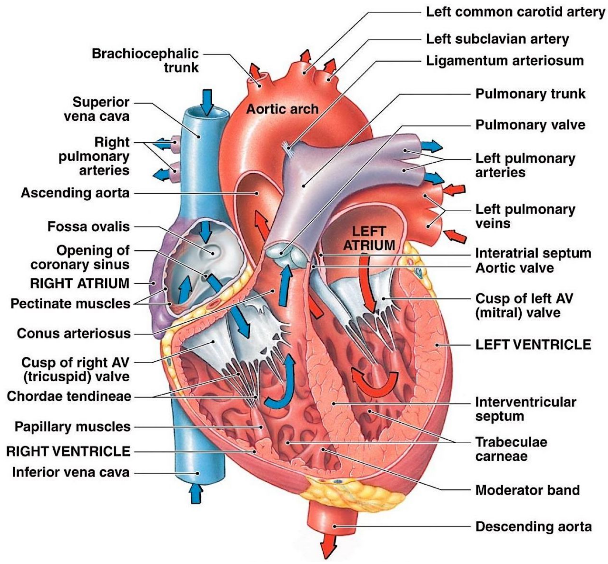

Figure A.1: Schematic representation of the heart anatomy with an indication of the route of the blood flow. Taken from Martini et al. (2012).

ventricle, separating it from the aorta, while the pulmonary valve is found at the outlet of the right ventricle, separating it from the pulmonary artery. Each of these valves is made of thin membranes that open and close at each cardiac beat, responding to the pressure differences between the two chambers they divide. Their function is to favor the flow of blood in a single direction, preventing backflow (Widmaier et al., 2016).

The heartbeat originates from an electrical impulse generated by the sinus-atrial node, which spreads to all the cardiac cells triggering their coordinated contraction. This mechanism ensures the cyclic contraction and relaxation of the atria and ventricles, enabling blood to flow from atria to ventricles, from ventricles into the great arteries, and from the systemic veins back into the atria (Klabunde, 2021). The phase of cardiac contraction is called systole, while the phase of cardiac relaxation is called diastole. The alternation of these two phases produces an intermittent blood ejection into the arterial system, inducing an arterial pressure that is pulsatile and that drives systemic perfusion. Figure A.2 illustrates this phenomenon using a Wiggers diagram. The Wiggers diagram, together with the values reported below, refers to a healthy adult in supine position at rest. The hemodynamic changes occurring in the standing position, and the resulting effects of orthostatic stress, are addressed in the next section. Under these normal resting conditions, systemic arterial pressure decreases from approximately 120 mmHg in systole to 80 mmHg during diastole (see the red curve in figure A.2), whereas pulmonary arterial pressure falls from about 25 mmHg in systole to 10 mmHg in diastole. In

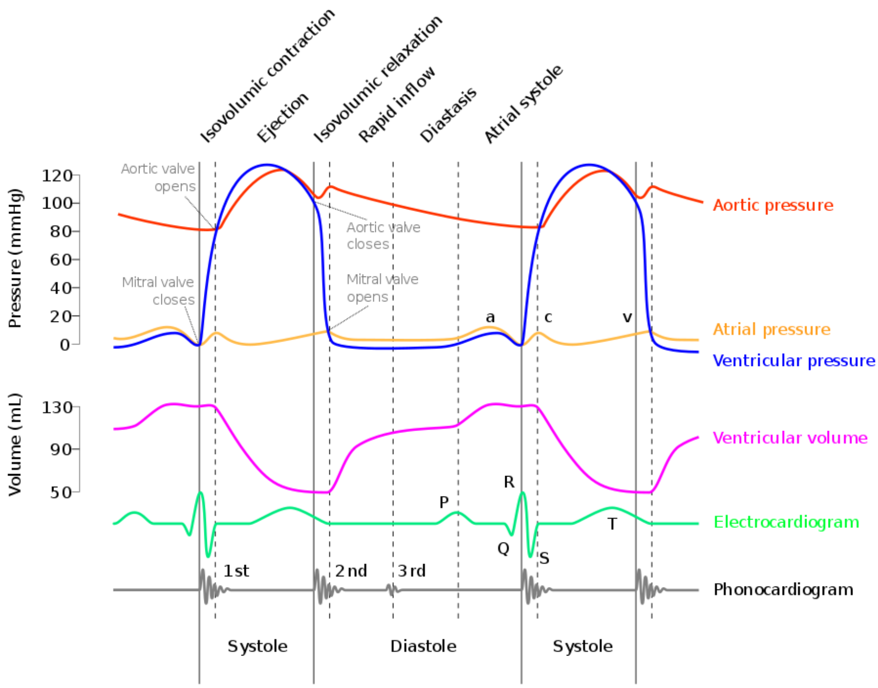

Figure A.2: A Wiggers diagram, representing some of the most important heart values over an entire cardiac cycle for a healthy adult in supine position at rest. Adapted from Levick (2009).

contrast, pressure in the great veins is only a few mmHg (Levick, 2009). This steep pressure difference between arteries and veins provides the driving force for blood flow throughout the circulatory system. Blood pressure is therefore a fundamental hemodynamic parameter of clinical significance across multiple medical fields (Pocock et al., 2017). The gradual decline in pressure across the arterial tree results from the resistance of large arteries, with the sharpest drop occurring at the level of the arterioles, where microcirculation begins and arteries transition into veins (Widmaier et al., 2016).

Within the CVS, two distinct circulations can be identified: the systemic circulation, which supplies oxygenated blood to the body, and the pulmonary circulation, which ensures gas exchange in the lungs (Levick, 2009). In both circulations, arteries transport blood away from the heart, capillaries connect arteries to veins while allowing substance exchanges with the surrounding cells, and veins return blood back to the heart, thereby completing a loop. Arteries and veins differ not only for the direction of blood flow (away from the heart for arteries, and toward the heart for veins), but most importantly in the structural composition of their walls, which reflects their distinct functional roles (Widmaier et al., 2016). As shown in figure A.3, arteries have thick walls, principally made by elastin, collagen, and smooth muscle cells, which are de-

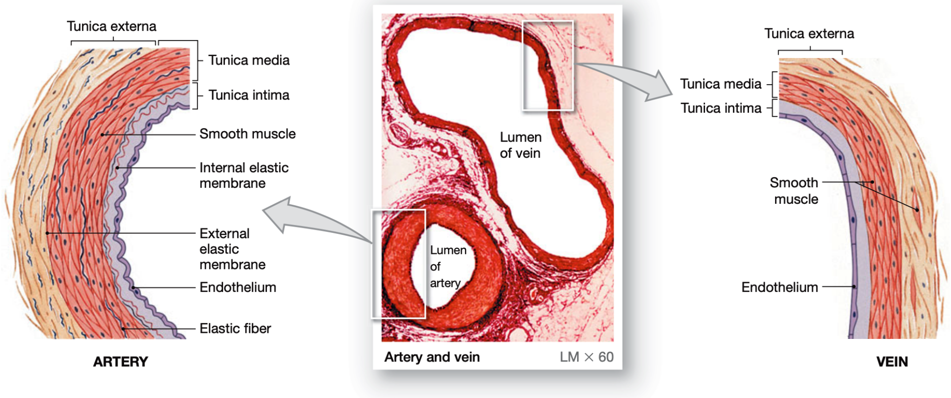

Figure A.3: Schematic representation of the vessels wall structure. Taken from Martini et al. (2012).

signed to withstand and propagate the high pulsatile pressure generated by the heart. The elastic and collagen fibers in the elastic tissue of the arterial wall absorb the high pressure waves from each heartbeat, providing the structural strength needed to resist the high pressures of blood flow. At the same time, these fibers expand during systole to store the energy generated by the heart and then recoil during diastole to push blood out of the arteries. This mechanism is essential to ensure an efficient blood circulation, maintaining a relatively steady flow and pressure in the arteries throughout the cardiac cycle thanks to its dampening effects, while preventing the pulsatile flow from the heart from causing damage to the more delicate downstream vessels. Finally, smooth muscle cells allow for vasoconstriction and vasodilation (narrowing and widening of the vessel lumen, respectively) to control blood pressure and direct blood flow to specific tissues as needed (Widmaier et al., 2016). In contrast, veins have thinner walls with less smooth muscle cells and connective tissue, and they generally exhibit a wider internal diameter, which allow them to collapse or expand to hold blood. This large deformation capacity grants veins the ability to accommodate substantial changes in blood volume with only minimal alterations in pressure. They also frequently contain valves that prevent backflow, particularly in the lower limbs. Almost the 70 % of the total blood volume in the human body is in fact in the venous system. This great capacity earned veins with the name of capacitance vessels, highlighting their role as low-pressure reservoirs returning blood to the heart (Martini et al., 2012).

The ability of both arteries and veins to adjust their lumen depends on the vascular tone, namely the degree of constriction experienced by a blood vessel relative to its maximally dilated state (Klabunde, 2021). An increase in vascular tone causes vasoconstriction, thereby reducing local blood flow. Conversely, a decrease in vascular tone leads to vasodilation, as the blood pressure distends the relaxed vessel wall. Such adjustments in vascular tone play a central role in regulating regional blood flow, capillary filtration, arterial blood pressure, and central venous pressure (Levick, 2009). These changes are mediated by alterations in the resistance of peripheral arteries, veins, arterioles, and venules. Basal vascular tone, in turn, reflects a dynamic equilibrium between competing vasoconstrictive and vasodilatory influences. Its regulation involves two classes of processes: extrinsic factors, originating outside the organ or tissue in which the blood vessel resides, and intrinsic factors, arising from the vessel itself or its surrounding tissue. Extrinsic factors primarily regulate systemic arterial pressure by modulating vascular resistance to flow, whereas intrinsic factors adjust local blood flow to match the metabolic demands of surrounding tissue. This distinction establishes a hierarchy of control processes, with intrinsic regulation acting at the local level and extrinsic regulation exerting global influence (Klabunde, 2021). Among intrinsic factors, autoregulation of blood flow is particularly important. It protects organ perfusion against fluctuations in arterial blood pressure by maintaining a nearly constant local blood flow despite changes in pressure. Although autoregulation functions within a limited pressure range, it can be reset by metabolic vasodilators to operate at a different baseline flow level (Levick, 2009). Another noteworthy factor is the autonomic nervous system, which represents one of the major extrinsic determinants of the vascular tone. It governs vascular tone as part of its broader role in controlling the involuntary functions of the human body, such as breathing, digestion, thermo-regulation, bladder function, heart rate, and blood pressure. It also plays a central role in activating compensatory responses to orthostatic stress, as is discussed in the next section (Robertson et al., 2012).

A.2 The effects of orthostatic stress on the human cardiovascular system

Orthostatic stress can be defined as the set of changes caused by gravity on the human body (Robertson et al., 2012). When a person moves from the supine position to standing, multiple physiological systems activate to maintain stability and equilibrium of the human functions in the new posture. The musculoskeletal system engages to support the body's weight and maintain balance, the nervous system coordinates sensory input and motor responses to prevent falls, the respiratory system modifies breathing to support oxygen delivery during the shift in posture, and the CVS regulates blood flow and blood pressure to maintain adequate tissue perfusion (Levick, 2009). If these coordinated responses are inadequate, symptoms such as dizziness, fatigue, or impaired motor control may occur. Studying orthostatic stress thus highlights the complex interplay of these physiological systems working together to counteract the effects of gravity in everyday life (Widmaier et al., 2016).

Focusing on the CVS, during the transition from a supine to a standing position, approximately 500 mL of blood are displaced by gravity from the thorax into the veins of the lower limbs. This process, known as *venous pooling*, decreases intrathoracic blood volume by about 20 % within 15 s, thereby altering cardiac function. Particularly, the central venous pressure, namely the pressure in the venae cavae near the right atrium, drops from around 6 mmHg to nearly 0 mmHg. As a result, veins below the heart level become markedly distended to accommodate the redistributed blood and their pressure increases proportionally to their distance from the heart, venous return to the heart declines, and the stroke volume, which is the amount of blood ejected by the ventricle per beat, falls by 30-40 % (Hinghofer-Szalkay, 2011; Levick, 2009). To counteract these substantial changes, rapid compensatory mechanisms, mediated primarily by the autonomic nervous system, adjust heart rate, cardiac contractility, and vascular tone. When these responses are insufficient, orthostatic intolerance may occur, manifesting as dizziness, lightheadedness, or fainting episodes (Blomqvist and Stone, 1991). Therefore, understanding the effects of orthostatic stress and studying the compensatory mechanisms behavior provides valuable insight into circulatory control and the body's ability to adapt to postural challenges. Notably, however, the full extent of the physiological responses to orthostatic stress still remains not completely understood, reflecting the complex interplay of multiple body systems and external factors that influence cardiovascular function (Robertson et al., 2012).

These compensatory responses are initiated by reflexes of the autonomic nervous system, which are triggered by a variety of stimuli detected through specialized receptors located both within and outside the circulation. The principal sensors are arterial baroreceptors, situated in the walls of the carotid sinuses and the aortic arch, and cardiopulmonary receptors, distributed in the atrial and ventricular walls, the coronary arteries, and the pulmonary artery (Widmaier et al., 2016). Arterial baroreceptors respond to changes in vessel wall stretch, allowing them to detect fluctuations in mean arterial pressure as well as the rate at which these pressure changes occur. Cardiopulmonary receptors sense mechanical deformation of the heart's surface, allowing them to monitor central venous pressure and cardiac filling changes. Signals from both receptor groups are transmitted to the brainstem, where they are integrated to generate appropriate autonomic reflexes: the baroreceptor reflex and the cardiopulmonary reflex (Pocock et al., 2017).

The baroreceptor reflex, or baroreflex, is a rapid negative feedback system that stabilizes blood pressure by sensing arterial pressure changes through arterial baroreceptors. When a sudden drop in arterial pressure occurs, the reflex responds by increasing the activity of the

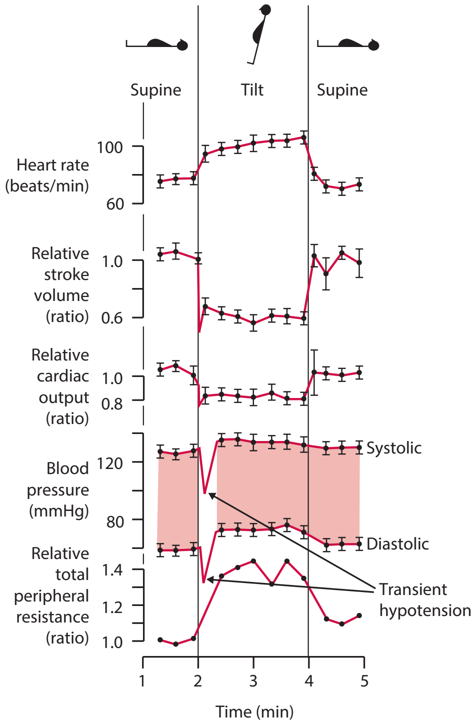

Figure A.4: Schematic representation of the cardiovascular responses to orthostatic stress generated by the baroreceptor reflex and the cardiopulmonary reflex. Taken from Levick (2009).

sympathetic nervous system and reducing the activity of the parasympathetic nervous system. The sympathetic and parasympathetic branches are two of the three divisions of the autonomic nervous system. The sympathetic branch is typically associated with the body's *fight-or-flight* response, preparing the organism for action in situations of stress or danger. Its activation promotes widespread vasoconstriction, shunting blood away from organs not necessary to the immediate survival of the organism and redirecting it toward those involved in intense physical activity. Conversely, the parasympathetic branch supports *rest-and-digest* functions, favoring recovery and energy conservation. Its stimulation reduces heart rate and facilitates processes such as digestion (Robertson et al., 2012). The balance between sympathetic and parasympathetic activity, and thus the effectiveness of the baroreflex, is dynamically modulated by the central nervous system, for example during exercise, or may be altered by pathological conditions that impair receptor function, such as cardiovascular diseases. Nevertheless, the baroreceptor reflex remains a crucial mechanism for buffering short-term fluctuations in arterial pressure, thereby contributing to the stabilization of the CVS (Widmaier et al., 2016). A typical demonstration of its importance occurs when a healthy adult transitions from the supine to the upright posture. This postural change produces a transient hypotension, namely a temporary fall in arterial pressure, which lasts only a few seconds before the baroreflex is activated. The reflex response triggers vasoconstriction, increasing total peripheral resistance by approximately 40 %, along with a rise in heart rate of 15–20 beats/min and in cardiac contractility up to 25 %, all contributing to the restoration of arterial pressure (Blomqvist and Stone, 1991; Levick, 2009; Sagawa et al., 1977). A schematic representation of these responses is shown in figure A.4.

The cardiopulmonary reflex is a regulatory mechanism that monitors blood volume distribution and cardiac filling through the cardiopulmonary receptors located in the heart's surface and in the pulmonary artery wall. As a healthy adult stands up from a supine position, venous return and cardiac filling momentarily decline, prompting reflex compensatory responses aimed at preserving circulatory stability. First, heart rate is increased to favor the transfer of blood from the congested venous system into the arterial system, thereby sustaining cardiac output. Second, sympathetic activity to the kidneys is reduced, promoting renal vasodilation and enhanced fluid excretion, which contributes to the regulation of plasma volume and, in turn, the stabilization of arterial pressure. Together, these adjustments help limit the decline in cardiac output and maintain arterial pressure at levels slightly higher than those observed in the supine position (Klabunde, 2021).

The preservation of normal blood pressure over long periods also depends on the maintenance of adequate blood volume Martini et al. (2012). Beyond the rapid neural adjustments provided by the baroreceptor and cardiopulmonary reflexes, which operate within milliseconds to seconds, slower endocrine mechanisms acting over minutes to weeks are essential for sustaining cardiovascular stability during prolonged orthostatic stress. The integration of these short- and long-term control mechanisms allows the body to adapt not only to the initial hemodynamic challenge of standing but also to sustain the upright posture (Widmaier et al., 2016). However, the effectiveness of these mechanisms varies considerably among individuals, influenced by factors such as age, hydration status, physical conditioning, and genetic predisposition, which explains why susceptibility to orthostatic intolerance is highly variable across populations (Blomqvist and Stone, 1991). Additionally, when coordination between these neural and endocrine mechanisms is inadequate, orthostatic intolerance may persist, giving rise to chronic disorders such as orthostatic hypotension or postural orthostatic tachycardia syndrome (POTS) (Robertson et al., 2012). Given the complexity of these intertwined mechanisms, numerical methods, ranging from lumped-parameter to multiscale computational models of the circulation, are invaluable for simulating physiological responses and deepening our understanding of cardiovascular regulation under orthostatic stress.

A.3 The ADAVN model

The Anatomically Detailed Arterial-Venous Network (ADAVN) model (Blanco et al., 2015, 2020; HeMoLab, 2013; Müller et al., 2023) is a computational model of the human CVS, which was originally developed to study the complete circulation with high anatomical fidelity. It is a closed-loop multiscale model that comprises a 1D description of the hemodynamic in large arteries and veins, and a 0D description of the rest of the CVS, including the cardiac function, the microcirculation connecting arteries to veins, the pulmonary system, the intracranial pressure and the valve dynamics. Particularly, the ADAVN model includes 1598 arteries, covering the majority of the large blood vessels listed in anatomical atlases, and 189 veins. An illustration of the complete vascular network is provided in figure 1.2, while a zoom on the thoracic cavity is shown in figure 1.3. Each vessel is described by a set of points in the 3D space that identifies its centerline (black polylines in figure 1.3B), ensuring that the 3D position of the vessel's centerline is always available. This characterization is, to the best of our knowledge, unique, since no other 1D model achieves this level of detail in representing blood vessels. Furthermore, as it can be seen in figure 1.3A, it allows us to remove the coplanarity hypothesis, namely the assumption that the entire vascular network lies in a single plane, thus enabling a more anatomically realistic 3D representation of the vascular geometry. This spatial detail also makes it possible to account for gravitational effects under any rigid orientation of the body, including the supine and the standing positions, thereby broadening the range of physiological conditions that can be studied. It is worth noting, however, that vessel spatial orientation is not explicitly included in the model, except through the effect of gravity as determined by the body's overall orientation.

Blood flow in all the vessels of both arterial and venous networks is described with the 1D blood flow model presented in system (1.1). The relationship between the vessel cross-sectional area $A(x,t)$ and the internal pressure $p(x,t)$, the tube law, is described as follows:

$$p(x,t) = p_{ext}(x,t) + p_{tm}(x,t), \tag{A.1}$$

where $p_{ext}(x,t)$ is the external pressure that accounts for the force exerted by tissues or extravascular fluids on the vessel, while $p_{tm}(x,t)$ is the transmural pressure that is the pressure effectively being supported by vessel's wall stresses. In this work, the external pressure is assumed constant, while the transmural pressure assumes two different formulations depending on the type of the considered vessel. For arteries, the adopted law follows the formulation proposed by Blanco et al. (2015), while, for veins, the tube law is taken from Müller and Toro (2014). These distinct formulations enable the model to accurately represent the mechanical differences between arterial and venous vessels within the 1D hemodynamic framework.

Another important component of the ADAVN model is the microcirculation. The microcirculation represents the portion of the vascular system composed of the smallest blood vessels, including arterioles, venules, and capillaries, which form the critical interface between the arterial and venous sides of the circulation. Here, it is represented using 0D models. Specifically, in ADAVN, terminal models are structured in a way that allows each 1D terminal artery to be connected to a maximum of two 1D terminal veins, whereas each 1D terminal vein may receive blood from multiple 1D terminal arteries. Each of these arterio–venous connections is represented by a multiple resistance–capacitance (RCRCR) circuit, where the central resistance models the capillary segment connecting the arterial and venous sides. A schematic representation of this 0D configuration, illustrating an example of a 1:1 arterio–venous connection, is shown in figure 5.1. A similar approach is used to represent also the coronary bed, namely the microcirculation at the coronary level. However, the 0D model used here differs in order to account for the specificity of blood flow dynamics in the cardiac microcirculation. In particular, the central resistance connecting arterioles to venules is substituted with the circuit proposed in Mynard et al. (2014) representing the multi-layer structure of the cardiac tissue.

The heart and its four cardiac valves are modeled following the approach proposed by Mynard et al. (2012). This 0D model represents each cardiac chamber as an elastic compartment characterized by a time-varying elastance, thereby capturing the pressure–volume relationship that governs cardiac contraction and relaxation. Instead, the pressure–flow relationship across an open valve is approximated by the Bernoulli equation. Valve dynamics depend on the instantaneous pressure difference and the valve state, representing the degree of opening. Valve motion begins when the instantaneous pressure difference exceeds a threshold value and smoothly approaches zero as the valve reaches its fully open or closed position, ensuring physiologically consistent transitions. The same valvular model is also applied to represent venous valves. In this case, the 0D model representing the valve is placed between two one-dimensional segments representing a vein, rather then between two cardiac chambers. Furthermore, this same model is slightly modified to represent Starling resistors, nonlinear resistances that mimic the collapsible behavior of intracranial veins near dural sinuses (Müller et al., 2023). When the dural sinus pressure falls below the intracranial pressure, the resistor effectively decouples the upstream and downstream veins, temporarily halting venous outflow and reproducing the physiological collapse mechanism observed in cerebral circulation.

The interaction between the cerebral vasculature and intracranial pressure is also incorporated into the model. Specifically, it follows the 0D formulation proposed by Ursino and Lodi (1997), which describes the coupling between cerebral blood flow and intracranial dynamics. However, in this preliminary stage of model development with gravitational influences, the intracranial pressure is assumed to remain constant, serving as a fixed parameter of the model.

Finally, the ADAVN model presents also the pulmonary circulation, described according to Sun et al. (1997). This 0D representation comprises three lumped compartments, including arteries, capillaries, and veins, each modeled as a compliance–inertance-resistance (CLR) element. In each compartment, the pressure–volume relationship is expressed as an exponential function of the compartmental volume, enabling a physiologically realistic description of pulmonary hemodynamics.

Given the complexity of the model and the combination of multiple 1D and 0D components used to represent the CVS, the ADAVN model incorporates several types of coupling conditions to ensure effective interaction and information exchange between the different submodels. At vessel junctions, conservation of mass and total pressure continuity are enforced to guarantee hemodynamic consistency across connected segments. At the interfaces between 1D and 0D domains, coupling is achieved through relations derived from generalized Riemann invariants, namely quantities preserved along characteristics for hyperbolic systems of PDEs, supplemented by additional mass and energy conservation conditions enforced at the discrete level. Full details about coupling conditions can be found in Müller et al. (2016) and in Müller and Toro (2014).

A final modeling aspect concerns the parametrization of ADAVN. In this work, the parametrization follows the values and formulations reported in the original references (Blanco et al., 2015, 2020; Müller et al., 2023). Unless otherwise specified in the relevant chapters of this work, no modifications have been made to the original parameter sets. This ensures that the results presented here remain directly comparable with previous studies and reflect the baseline configuration of the established model.

Appendix **B**

Supplementary material to Chapter 2

Table B.1
Averaged estimated parameters of the viscoelastic tube law for V2 estimation case.

Vess.	Num.*	K [kPa]	m [–]	n [–]	Γ [Pa s m]
Sheep systemic arteries					
AA	12	1.04	10.00	-1.50	13.75
BT	11	1.90	10.00	-1.50	18.96
CA	11	46.23	10.00	-1.50	93.91
DDA	11	7.78	10.00	-1.50	41.83
FA	11	11.25	10.00	-1.50	22.63
MDA	11	2.48	10.00	-1.50	19.72
PDA	11	2.01	10.00	-1.50	15.98
Sheep pulmonary arteries					
LPA	11	0.35	10.00	-1.50	4.63
PT	10	0.31	10.00	-1.50	4.82
Sheep veins at high (H) pressure					
HVCI	5	60.10	10.00	-1.50	214.30
HVCS	8	38.96	10.00	-1.50	140.23
HVF	5	22.62	10.00	-1.50	28.46
HVJ	8	30.38	10.00	-1.50	70.87
Sheep veins at low (L) pressure					
LVCI	10	7.26	10.00	-1.50	6.85
LVCS	12	1.73	10.00	-1.50	8.61
LVF	30	5.10	10.00	-1.50	4.12
LVJ	10	2.45	10.00	-1.50	7.84
Human vessels					
Fem	30	27.00	10.00	-1.50	49.02
Saf	20	26.19	10.00	-1.50	10.36

*Number of available sets of data for each type of vessel

Table B.2
Averaged estimated parameters of the viscoelastic tube law for V3 estimation case.

Vess.	Num.*	K [kPa]	m [–]	n [–]	Γ [Pa s m]
Sheep systemic arteries					
AA	12	61.73	0.50	0.00	13.25
BT	11	77.13	0.50	0.00	18.55
CA	11	1118.40	0.50	0.00	93.83
DDA	11	231.43	0.50	0.00	41.53
FA	11	309.42	0.50	0.00	22.57
MDA	11	104.99	0.50	0.00	19.29
PDA	11	90.48	0.50	0.00	15.55
Sheep pulmonary arteries					
LPA	11	12.33	0.50	0.00	4.62
PT	10	11.34	0.50	0.00	4.80
Sheep veins at high (H) pressure					
HVCI	5	1443.86	0.50	0.00	214.01
HVCS	8	954.26	0.50	0.00	139.84
HVF	5	566.34	0.50	0.00	28.41
HVJ	8	739.41	0.50	0.00	70.80
Sheep veins at low (L) pressure					
LVCI	10	186.58	0.50	0.00	6.74
LVCS	12	60.95	0.50	0.00	8.49
LVF	30	134.18	0.50	0.00	4.07
LVJ	10	82.20	0.50	0.00	7.65
Human vessels					
Fem	30	654.62	0.50	0.00	48.91
Saf	20	636.63	0.50	0.00	10.30

*Number of available sets of data for each type of vessel

Table B.3
Averaged estimated parameters of the viscoelastic tube law for V4 estimation case.

Vess.	Num.*	K [kPa]	m [−]	n [−]	Γ [Pa s m]
Sheep systemic arteries					
AA	12	2107.74	7.37	-7.24	13.69
BT	11	1656.61	13.24	-5.01	19.24
CA	11	1642.17	50.06	-119.39	93.80
DDA	11	3165.27	9.62	0.52	41.89
FA	11	2709.82	13.85	-29.50	22.58
MDA	11	1309.26	9.89	-18.53	19.70
PDA	11	857.79	12.47	-19.24	16.07
Sheep pulmonary arteries					
LPA	11	3426.68	26.59	26.59	4.66
PT	10	3779.99	14.26	14.26	4.86
Sheep veins at high (H) pressure					
HVCI	5	2708.33	20.35	-49.90	214.15
HVCS	8	3932.77	12.38	-1.06	140.48
HVF	5	866.30	36.36	-128.80	28.39
HVJ	8	4066.46	15.74	-1.30	70.86
Sheep veins at low (L) pressure					
LVCI	10	2906.49	53.66	-10.16	7.04
LVCS	12	1042.70	14.71	-15.95	8.70
LVF	30	2074.47	20.11	-61.35	4.17
LVJ	10	1367.72	16.60	5.65	8.08
Human vessels					
Fem	30	3390.90	35.58	-61.58	49.14
Saf	20	2030.91	52.48	-53.74	10.50

*Number of available sets of data for each type of vessel

B

Table B.4
Averaged estimated parameters of the elastic tube law for E1 estimation case.

Vess.	Num.*	K [kPa]	m [–]	n [–]	Γ [Pa s m]
Sheep systemic arteries					
AA	12	1.92	7.94	-0.71	0.00
BT	11	1.18	14.46	-1.09	0.00
CA	11	231.98	13.89	-1.48	0.00
DDA	11	9.88	11.14	-0.18	0.00
FA	11	43.01	8.95	-0.91	0.00
MDA	11	5.09	8.14	-1.09	0.00
PDA	11	2.19	10.56	-1.64	0.00
Sheep pulmonary arteries					
LPA	11	0.02	35.74	0.00	0.00
PT	10	0.13	20.56	0.00	0.00
Sheep veins at high (H) pressure					
HVCI	5	274.17	7.53	-1.60	0.00
HVCS	8	90.53	12.92	-0.25	0.00
HVF	5	97.90	5.58	-2.00	0.00
HVJ	8	38.02	20.02	-0.50	0.00
Sheep veins at low (L) pressure					
LVCI	10	19.30	64.05	-0.80	0.00
LVCS	12	0.93	14.78	-1.33	0.00
LVF	30	3.96	21.19	-0.80	0.00
LVJ	10	0.73	18.69	-0.40	0.00
Human vessels					
Fem	30	79.48	18.04	-0.97	0.00
Saf	20	41.94	42.13	-1.20	0.00

*Number of available sets of data for each type of vessel

Table B.5
Averaged estimated parameters of the elastic tube law for E2 estimation case.

Vess.	Num.*	K [kPa]	m [—]	n [—]	Γ [Pa s m]
Sheep systemic arteries					
AA	12	1.03	10.00	-1.50	0.00
BT	11	1.88	10.00	-1.50	0.00
CA	11	46.13	10.00	-1.50	0.00
DDA	11	7.74	10.00	-1.50	0.00
FA	11	11.21	10.00	-1.50	0.00
MDA	11	2.46	10.00	-1.50	0.00
PDA	11	1.99	10.00	-1.50	0.00
Sheep pulmonary arteries					
LPA	11	0.35	10.00	-1.50	0.00
PT	10	0.31	10.00	-1.50	0.00
Sheep veins at high (H) pressure					
HVCI	5	59.90	10.00	-1.50	0.00
HVCS	8	38.87	10.00	-1.50	0.00
HVF	5	22.56	10.00	-1.50	0.00
HVJ	8	30.29	10.00	-1.50	0.00
Sheep veins at low (L) pressure					
LVCI	10	7.25	10.00	-1.50	0.00
LVCS	12	1.70	10.00	-1.50	0.00
LVF	30	5.09	10.00	-1.50	0.00
LVJ	10	2.42	10.00	-1.50	0.00
Human vessels					
Fem	30	26.79	10.00	-1.50	0.00
Saf	20	26.17	10.00	-1.50	0.00

*Number of available sets of data for each type of vessel

B

Table B.6
Averaged estimated parameters of the elastic tube law for E3 estimation case.

Vess.	Num.*	K [kPa]	m [–]	n [–]	Γ [Pa s m]
Sheep systemic arteries					
AA	12	61.36	0.50	0.00	0.00
BT	11	76.75	0.50	0.00	0.00
CA	11	1116.08	0.50	0.00	0.00
DDA	11	230.46	0.50	0.00	0.00
FA	11	308.58	0.50	0.00	0.00
MDA	11	104.32	0.50	0.00	0.00
PDA	11	89.98	0.50	0.00	0.00
Sheep pulmonary arteries					
LPA	11	12.29	0.50	0.00	0.00
PT	10	11.31	0.50	0.00	0.00
Sheep veins at high (H) pressure					
HVCI	5	1439.15	0.50	0.00	0.00
HVCS	8	951.97	0.50	0.00	0.00
HVF	5	564.91	0.50	0.00	0.00
HVJ	8	737.28	0.50	0.00	0.00
Sheep veins at low (L) pressure					
LVCI	10	186.43	0.50	0.00	0.00
LVCS	12	60.23	0.50	0.00	0.00
LVF	30	133.82	0.50	0.00	0.00
LVJ	10	81.41	0.50	0.00	0.00
Human vessels					
Fem	30	649.82	0.50	0.00	0.00
Saf	20	636.01	0.50	0.00	0.00

*Number of available sets of data for each type of vessel

Table B.7
Averaged estimated parameters of the elastic tube law for E4 estimation case.

Vess.	Num.*	K [kPa]	m [–]	n [–]	Γ [Pa s m]
Sheep systemic arteries					
AA	12	2697.51	6.85	-7.11	0.00
BT	11	2242.90	12.31	-2.30	0.00
CA	11	1613.42	46.08	-118.27	0.00
DDA	11	4071.37	7.57	2.69	0.00
FA	11	2720.88	13.43	-28.23	0.00
MDA	11	1768.51	9.13	-15.11	0.00
PDA	11	869.77	12.00	-15.81	0.00
Sheep pulmonary arteries					
LPA	11	2982.01	26.56	26.56	0.00
PT	10	4031.61	14.02	14.02	0.00
Sheep veins at high (H) pressure					
HVCI	5	2789.18	18.67	-51.56	0.00
HVCS	8	3984.47	11.20	-0.40	0.00
HVF	5	834.91	35.58	-128.05	0.00
HVJ	8	3879.75	15.59	-2.21	0.00
Sheep veins at low (L) pressure					
LVCI	10	2312.49	56.40	-135.08	0.00
LVCS	12	1285.00	14.37	-16.75	0.00
LVF	30	2288.13	19.42	-76.38	0.00
LVJ	10	1931.50	15.73	5.68	0.00
Human vessels					
Fem	30	3482.06	30.97	-56.81	0.00
Saf	20	2087.20	49.14	-48.32	0.00

*Number of available sets of data for each type of vessel

B

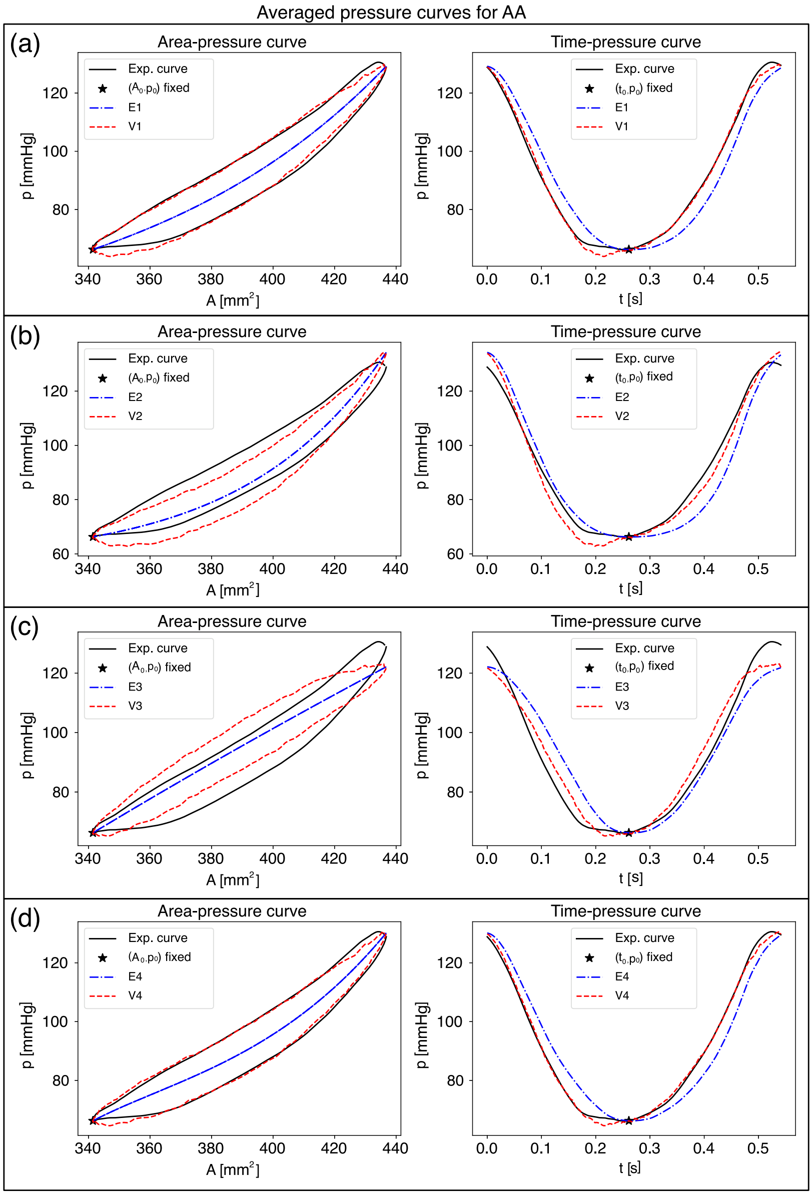

Figure B.1: Fitted pressure curves for AA. Comparison between experimental and fitted pressure curves for all the estimation cases of an example dataset of AA. Black solid lines represent averaged experimental area-pressure and time-pressure curves, blue dash-dot lines represent the fitted curves obtained considering the elastic cases E1-E4, while red dashed lines represent the fitted curves obtain considering the viscoelastic cases V1-V4.

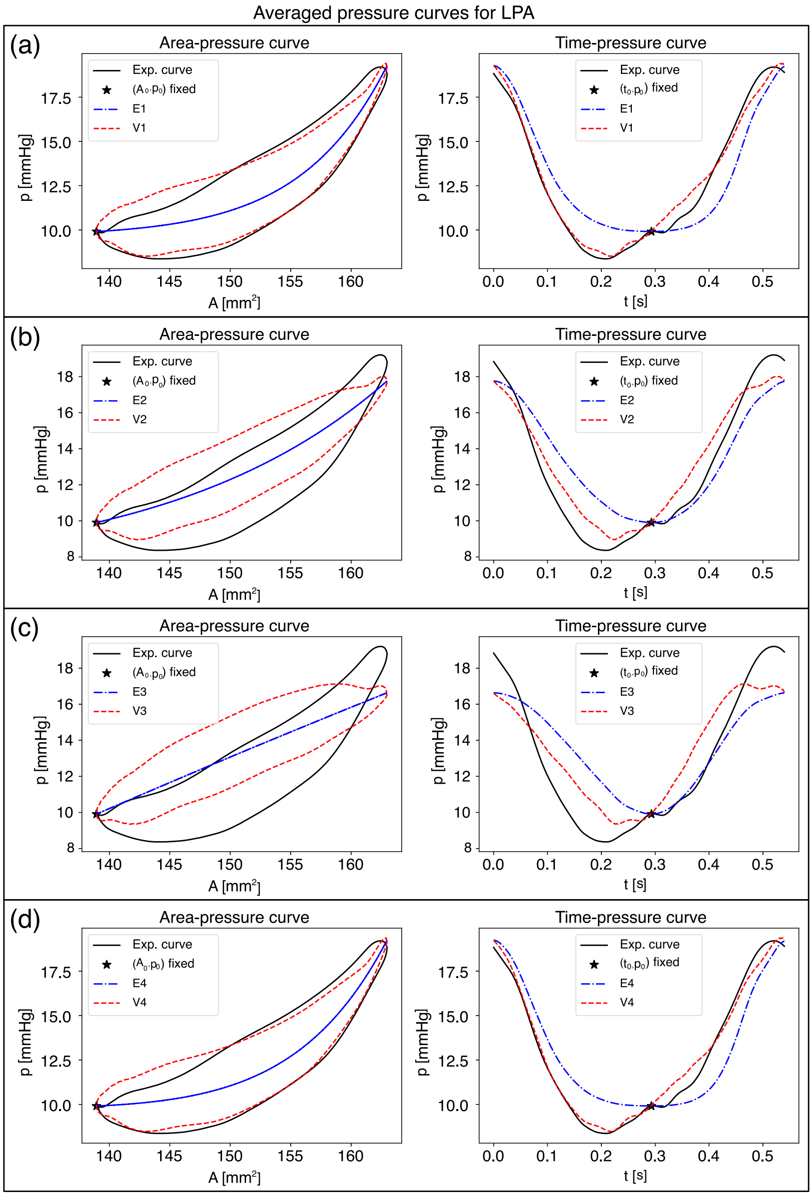

Figure B.2: Fitted pressure curves for LPA. Comparison between experimental and fitted pressure curves for all the estimation cases of an example dataset of LPA. Black solid lines represent averaged experimental area-pressure and time-pressure curves, blue dash-dot lines represent the fitted curves obtained considering the elastic cases E1-E4, while red dashed lines represent the fitted curves obtain considering the viscoelastic cases V1-V4.

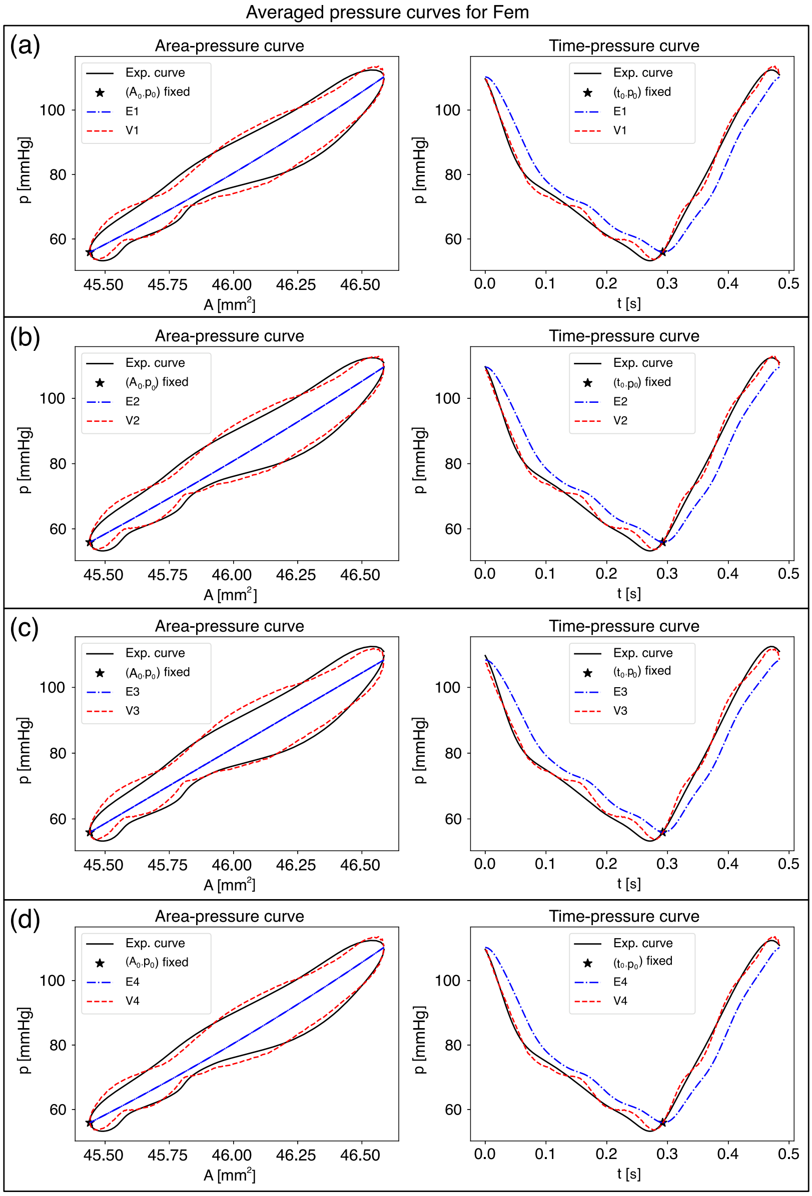

Figure B.3: Fitted pressure curves for Fem. Comparison between experimental and fitted pressure curves for all the estimation cases of an example dataset of Fem. Black solid lines represent averaged experimental area-pressure and time-pressure curves, blue dash-dot lines represent the fitted curves obtained considering the elastic cases E1-E4, while red dashed lines represent the fitted curves obtain considering the viscoelastic cases V1-V4.

Appendix **C**

Supplementary material to Chapter 3

C.1 Solution to RP (3.23) for the BFEs

Let us consider the following classical RP for the hyperbolized BFEs presented in the main manuscript at eq. (3.34)-(3.36)

$$\partial_t \mathbf{Q} + \mathbf{A}(\mathbf{Q})\partial_x \mathbf{Q} = \mathbf{0}, \quad x \in \mathbb{R}, t > 0 \tag{C.1}$$

with initial condition

$$\mathbf{Q}(x,0) = \begin{cases} \mathbf{Q}_L, & \text{if } x < x_{i+\frac{1}{2}}, \\ \mathbf{Q}_R, & \text{if } x > x_{i+\frac{1}{2}}. \end{cases} \tag{C.2}$$

$\mathbf{Q}_L$ and $\mathbf{Q}_R$ are constant states defined to both side of the cell interface $x_{i+\frac{1}{2}}$.

Our goal is to solve this RP under the condition that the flow is subcritical. Assuming a subcritical flow is equivalent to asking that the fluid velocity u is smaller than the wave propagation speed c, namely $\lambda_1 < 0$ and $\lambda_8 > 0$. Indeed, we recall that the hyperbolized BFEs present 8 waves (Montecinos et al., 2014), with associated eigenvalues given by

$$\lambda_1(\mathbf{Q}) = u - c, \quad \lambda_{2,\dots,7}(\mathbf{Q}) = 0, \quad \lambda_8(\mathbf{Q}) = u + c. \tag{C.3}$$

Within the subcritical regime, there is only a possible wave configuration in the $x-t$ half plane (see figure C.1) given by 4 constant states, namely $\mathbf{Q}_L, \mathbf{Q}_{*L}, \mathbf{Q}_{*R}, \mathbf{Q}_R$ (Spilimbergo et al., 2021). $\mathbf{Q}_L$ is left constant state (known) that is separated from the state $\mathbf{Q}_{*L}$ by the left family of waves associated to λ_1. Similarly, $\mathbf{Q}_R$ is right constant state (known) that is separated from the state $\mathbf{Q}_{*R}$ by the right family of waves associated to λ_8. Both left and right families of waves can generate either shock waves or rarefactions (Montecinos et al., 2014). Finally, $\mathbf{Q}_{*L}$ and $\mathbf{Q}_{*R}$ are the two unknown states that are separated by contact discontinuities. In order to identify these two unknown states, and thus solve the RP, we need to establish appropriate jump conditions across the family of waves to connect the unknown states $\mathbf{Q}_{*L}$, $\mathbf{Q}_{*R}$ between them and to the initial conditions $\mathbf{Q}_L$, and $\mathbf{Q}_R$.

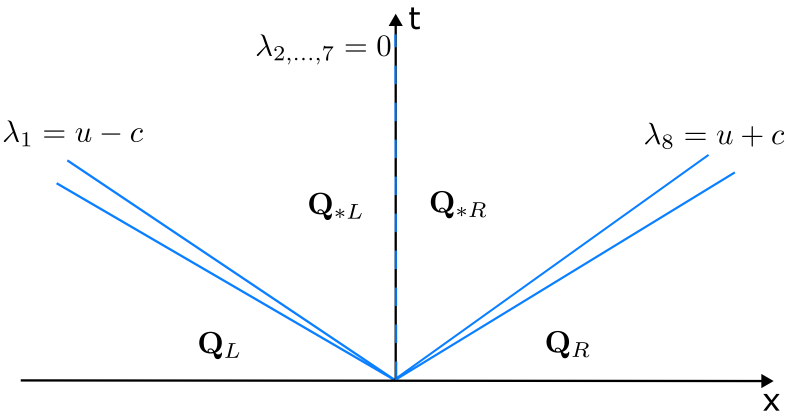

Figure C.1: Wave configuration. Representation of the wave configuration in the $x-t$ half plane.

The solution to this RP can be obtained using various methods (Toro, 2009). Here we apply a two-rarefaction approximate Riemann solver. Specifically, we assume that the waves associated to λ_1 and λ_8 are rarefactions, and we use the related Riemann invariants to identify the unknowns (Montecinos et al., 2014; Spilimbergo et al., 2021). The application of the solver to our problem yields

$$A_{0,L} = A_{0,*L}, \quad h_{0,L} = h_{0,*L}, \quad E_{e,L} = E_{e,*L}, \quad E_{c,L} = E_{c,*L}, \quad p_{r,L} = p_{r,*L}, \tag{C.4}$$

$$A_{0,R} = A_{0,*R}, \quad h_{0,R} = h_{0,*R}, \quad E_{e,R} = E_{e,*R}, \quad E_{c,R} = E_{c,*R}, \quad p_{r,R} = p_{r,*R}, \tag{C.5}$$

and

$$\begin{cases} \psi_L + A_L/\varepsilon = \psi_{*L} + A_{*L}/\varepsilon, \\ u_{*L} = u_L - \int_{A_L}^{A_{*L}} \frac{\tilde{c}_T(\xi)}{\xi} d\xi, \\ \psi_R + A_R/\varepsilon = \psi_{*R} + A_{*R}/\varepsilon, \\ u_{*R} = u_R + \int_{A_R}^{A_{*R}} \frac{\tilde{c}_T(\xi)}{\xi} d\xi, \\ q_{*L} = q_{*R}, \\ p_{*L} + \frac{1}{2}\rho u_{*L}^2 = p_{*R} + \frac{1}{2}\rho u_{*R}^2. \end{cases} \tag{C.6}$$

The equivalences in eq. (C.4) and (C.5) identify the first set of unknowns, while the system in eq. (C.6) leads us to the determination of the remaining six variables, namely $A_{*L/R}$, $q_{*L/R}$, and $\psi_{*L/R}$.

In order to solve system (C.6), we first apply the midpoint rule to the two integrals appearing in it. Specifically, we have

$$\int_{\hat{A}}^{A} \frac{\tilde{c}_T(\xi)}{\xi} d\xi \cong (A-\hat{A}) \left[\frac{\tilde{c}_T\left(\frac{A+\hat{A}}{2}\right)}{\frac{A+\hat{A}}{2}} \right], \tag{C.7}$$

with $\hat{A} = A_L, A_L$, and $A = A_{*L}, A_{*R}$. Later, we assume that the integrand function between $\hat{A}$ and A is flat enough to write that

$$\frac{\tilde{c}_T\left(\frac{A+\hat{A}}{2}\right)}{\frac{A+\hat{A}}{2}} \approx \frac{\tilde{c}_T(\hat{A})}{\hat{A}}. \tag{C.8}$$

As a result, system (C.6) becomes

$$\begin{cases} \psi_L + A_L/\varepsilon = \psi_{*L} + A_{*L}/\varepsilon, \\ u_{*L} = u_L + \tilde{c}_T(A_L) - (A_{*L}/A_L) \cdot \tilde{c}_T(A_L), \\ \psi_R + A_R/\varepsilon = \psi_{*R} + A_{*R}/\varepsilon, \\ u_{*R} = u_R - \tilde{c}_T(A_R) + (A_{*R}/A_R) \cdot \tilde{c}_T(A_R), \\ q_{*L} = q_{*R}, \\ p_{*L} + \frac{1}{2}\rho u_{*L}^2 = p_{*R} + \frac{1}{2}\rho u_{*R}^2. \end{cases} \tag{C.9}$$

We observe that the first 4 equations of the system can all be written in terms of A_{*L} and A_{*R}, namely

$$\begin{cases} \psi_{*L} = g_1(A_{*L}), \\ \psi_{*R} = g_2(A_{*R}), \\ u_{*L} = h_1(A_{*L}), \\ u_{*R} = h_2(A_{*R}), \\ q_{*L} = q_{*R}, \\ p_{*L} + \frac{1}{2}\rho u_{*L}^2 = p_{*R} + \frac{1}{2}\rho u_{*R}^2, \end{cases} \tag{C.10}$$

where g_1, g_2, h_1, h_2 are known. Additionally, we also note that $q = Au$, which allows us to write the fifth equation as

$$A_{*L}u_{*L} = A_{*R}u_{*R}, \tag{C.11}$$

and to identify a relation between A_{*L} and A_{*R}. Specifically, the previous equation represents an ellipse of the form

$$\frac{\tilde{c}_T(A_R)}{A_R} A_{*R}^2 + (u_R - \tilde{c}_T(A_R))A_{*R} + \frac{\tilde{c}_T(A_L)}{A_L} A_{*L}^2 - (u_L + \tilde{c}_T(A_L))A_{*L} = 0. \tag{C.12}$$

Writing thus A_{*R} as a function of A_{*L}, i.e. $A_{*R} = f(A_{*L})$, which represent the solution to the ellipse, we can now write all the equations of system (C.10) in terms of the same unknown

$$\begin{cases} \psi_{*L} = g_1(A_{*L}), \\ \psi_{*R} = g_2(f(A_{*L})), \\ u_{*L} = h_1(A_{*L}), \\ u_{*R} = h_2(f(A_{*L})), \\ A_{*R} = f(A_{*L}), \\ p_{*L} + \frac{1}{2}\rho h_1^2(A_{*L}) = p_{*R} + \frac{1}{2}\rho h_2^2(f(A_{*L})). \end{cases} \tag{C.13}$$

Finally, after this long manipulation of the original system (C.6), we observe that system (C.13) is characterized by a single non-linear equation (the last one) in terms of the unknown A_{*L}, and multiple equivalences. Thus, applying a standard Newton method to the last equation, it allows us to identify A_{*L} and successively to retrieve the remaining unknowns.

C.2 Additional results related to the third-order implementation of the method

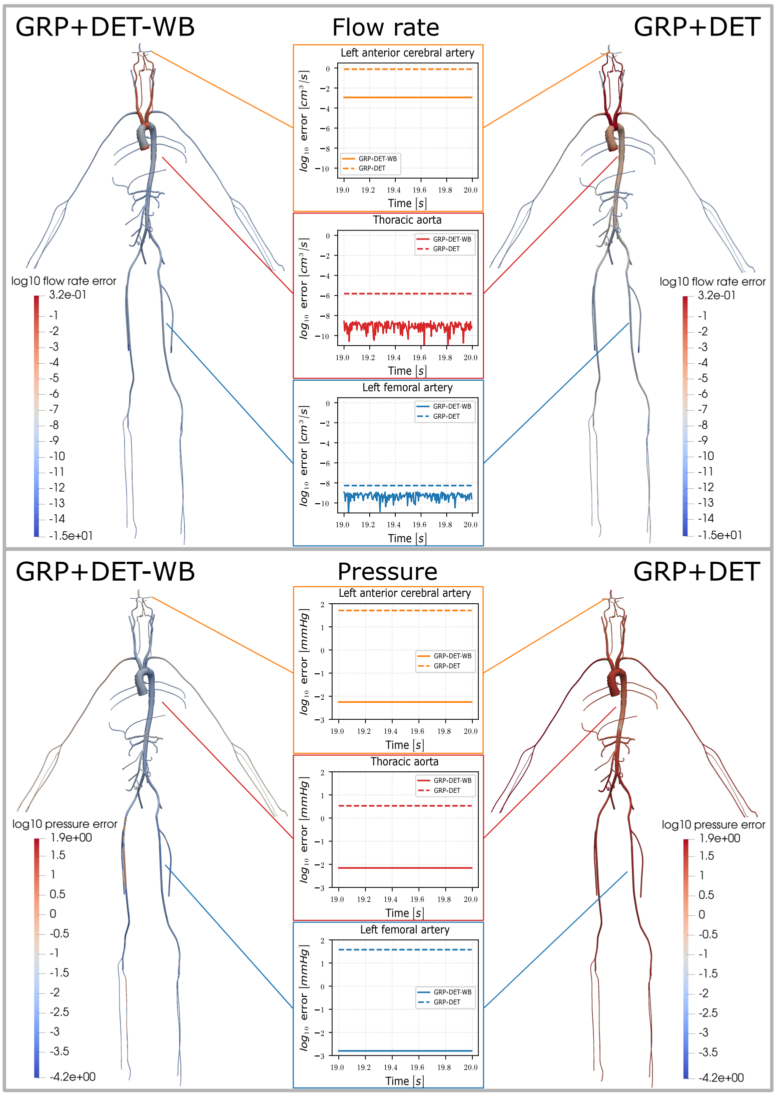

Figure C.2: Deadman test. A representation of the ADAN86 network is shown. In the top panel, the colors indicate the errors between zero-flow solution and the third-order numerical solution computed with either the GRP+DET-WB, or the GRP+DET. In the bottom panel, the colors indicate the errors between the reference hydrostatic pressure distribution and the numerical solution computed with either the GRP+DET-WB, or the GRP+DET. A focus on three vessels is provided in the middle of both panels. All the results are shown in logarithmic scale.

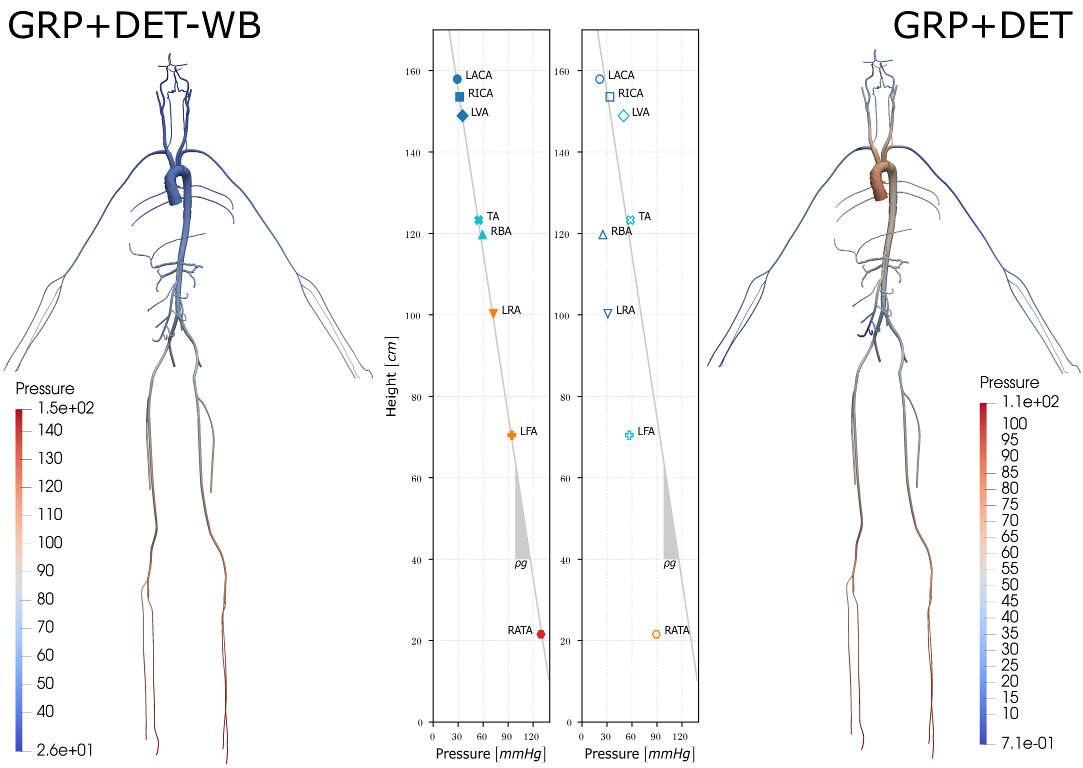

Figure C.3: Pressure distribution. Pressure distribution at the final simulation time along the ADAN86 network obtained with a third-order implementation of both the GRP+DET-WB method (left) and the GRP+DET method (right). A focus on eight vessels is provided in the middle of the panel, showing how the GRP+DET-WB results respect the expected hydrostatic distribution indicated in light gray. The considered vessels are: LACA: left anterior cerebral artery, RICA: right internal carotid artery, LVA: left vertebral artery, TA: thoracic aorta, RBA: right brachial artery, LRA: left radial artery, LFA: left femoral artery, RATA: right anterior tibial artery.

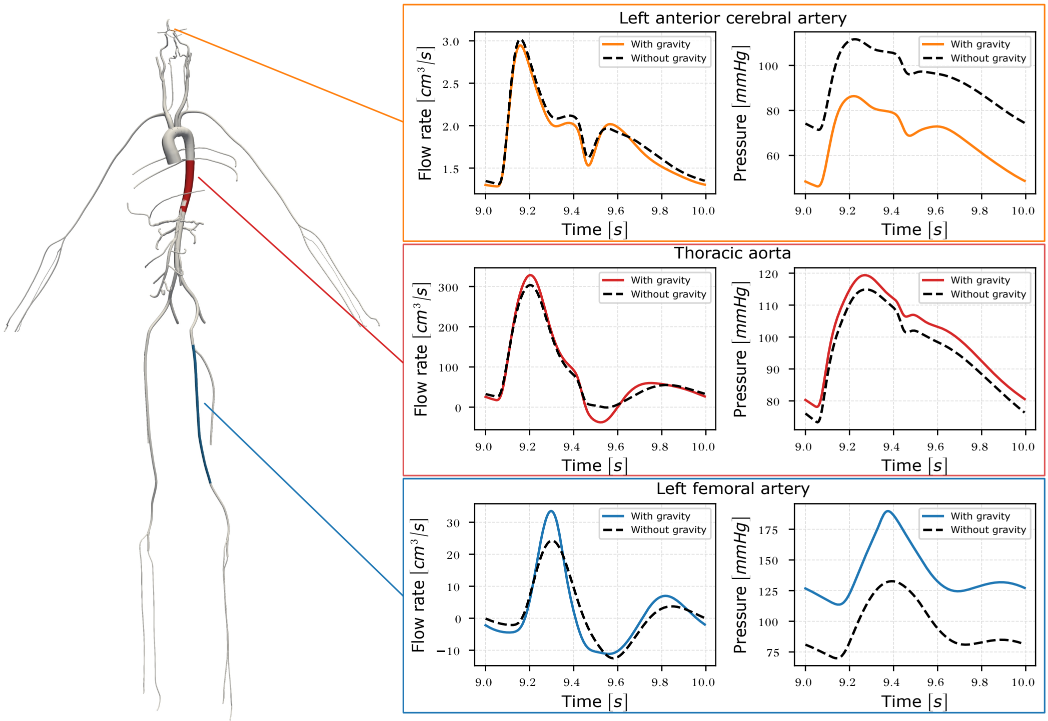

Figure C.4: Transient test. Flow rate (left column) and pressure (right column) curves along the final cardiac cycle of simulation at the midpoint of three selected blood vessels: left anterior cerebral artery (orange), thoracic aorta (red), and left femoral artery (blue). Indication on the location of the vessels is shown in the ADAN86 network representation on the left. Black dashed lines represent the reference solution with no gravity in the different vessels.

Appendix ***D***

Supplementary material to Chapter 4

Figure D.1: Experimental devices. Tilt table.

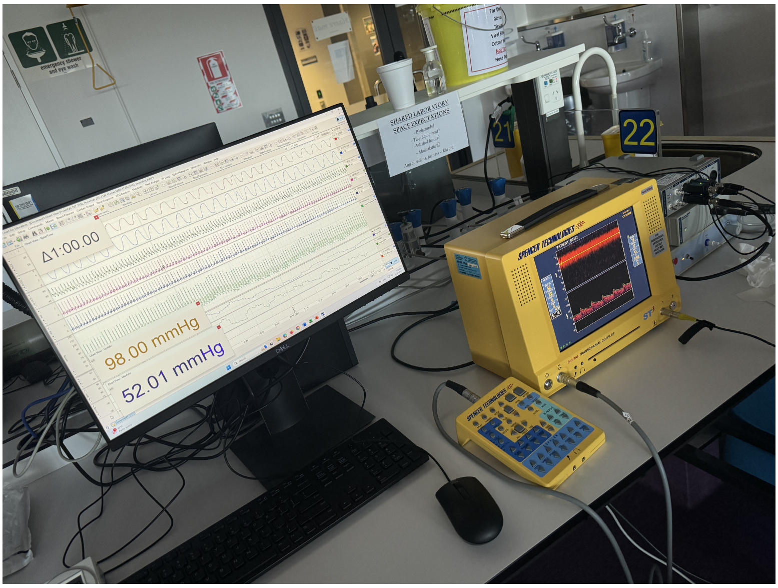

Figure D.2: Experimental devices. LabChart software recording real time data.

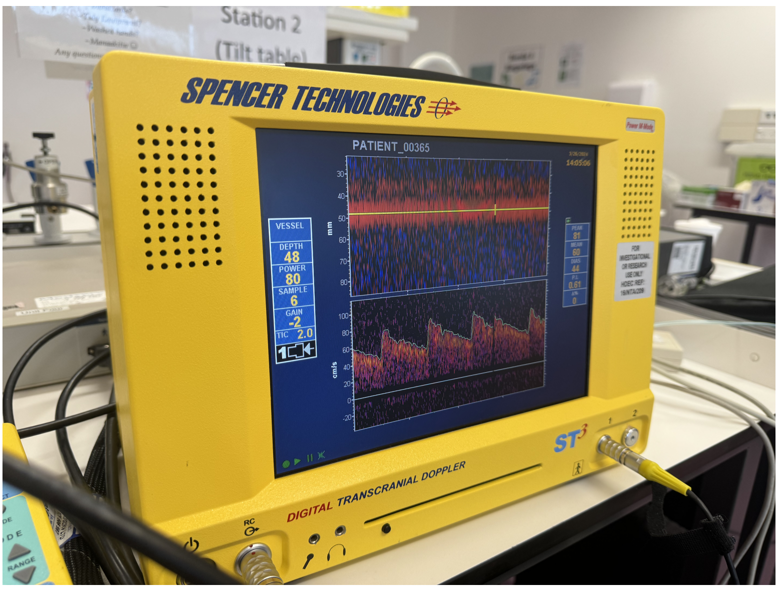

Figure D.3: Experimental devices. Digital transcranial Doppler.

Figure D.4: Experimental setup. Data recording of a volunteer positioned at 0°.

Figure D.5: Experimental setup. 3D echocardiography and duplex Doppler ultrasound of the femoral artery of a volunteer positioned at 60°.

D

Figure D.6: Experimental setup. 3D echocardiography of a volunteer positioned at 60°.

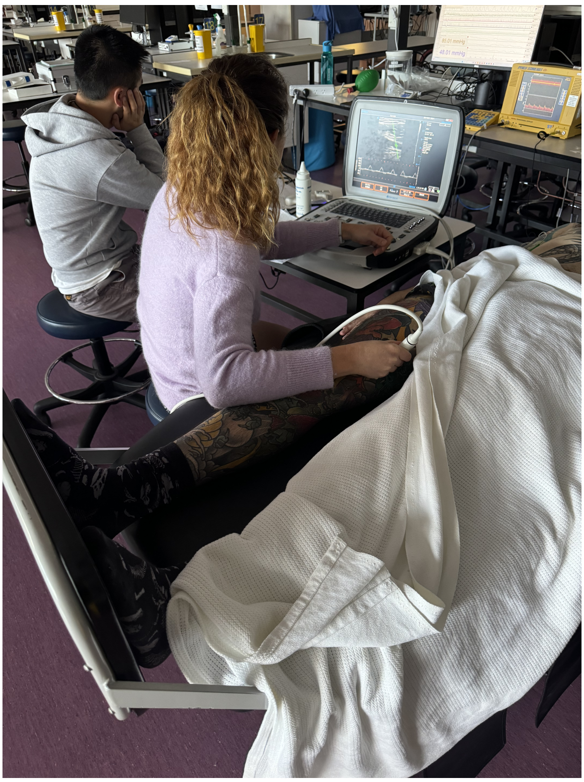

Figure D.7: Experimental setup. Duplex Doppler ultrasound of the femoral artery of a volunteer positioned at 60°.

References

J. Alastruey, A. W. Khir, K. S. Matthys, P. Segers, S. J. Sherwin, P. R. Verdonck, K. H. Parker, and J. Peiró. Pulse wave propagation in a model human arterial network: assessment of 1-D visco-elastic simulations against in vitro measurements. *J. Biomech.*, 44(12):2250–2258, 2011.

A. Albanese, L. Cheng, M. Ursino, and N. W. Chbat. An integrated mathematical model of the human cardiopulmonary system: model development. *Am. J. Physiol. Heart. Circ. Physiol.*, 310:H899–H921, 2016.

A. A. Alzaabi, F. M. Alzaabi, R. W. Siddiqui, T. W. Siddiqui, and M. M. Sami. Review of microgravity's impact on cardiovascular and nervous systems in space exploration. *npj Microgravity*, 11:77, 2025.

F. Argus, D. Zhao, T. P. Babarenda Gamage, M. P. Nash, and G. D. Maso Talou. Automated model calibration with parallel mcmc: Applications for a cardiovascular system model. *Front. Physiol.*, 13:1018134, 2022.

A. P. Avolio. Multi-branched model of the human arterial system. *Med. Biol. Eng. Comput.*, 18:709–718, 1980.

C. Battista, D. Bia, Y. Z. Germán, R. L. Armentano, M. A. Haider, and M. S. Olufsen. Wave propagation in a 1D fluid dynamics model using pressure-area measurements from ovine arteries. *J. Mech. Med. Biol.*, 16(02): 1650007, 2016.

J. P. Berberich, P. Chandrashekar, and C. Klingenberg. High order well-balanced finite volume methods for multi-dimensional systems of hyperbolic balance laws. *Comput. Fluids*, 219:104858, 2021.

A. Bermudez and M. E. Vazquez. Upwind methods for hyperbolic conservation laws with source terms. *Comput. Fluids*, 23(8):1049–1071, 1994.

A. Bermudez, X. López, and M. E. Vázquez-Cendón. Numerical solution of non-isothermal non-adiabatic flow of real gases in pipelines. *J. Comp. Phys.*, 323:126–148, 2016.

G. Bertaglia, V. Caleffi, and A. Valiani. Modeling blood flow in viscoelastic vessels: the 1D augmented fluid–structure interaction system. *Comput. Methods Appl. Mech. Eng.*, 360:112772, 2020.

D. Bia, Y. Zócalo, R. L. Armentano, J. Camús, E. de Forteza, and E. Cabrera-Fischer. The adventitia reduces left ventricular dynamic afterload via smooth muscle activation-dependent mechanisms. *Revista Española de Cardiología*, 60(5):501–509, 2007.

D. Bia, Y. Zócalo, E. I. Cabrera-Fischer, S. Wray, and R. L. Armentano. Quantitative analysis of the relationship between blood vessel wall constituents and viscoelastic properties: dynamic biomechanical and structural in vitro studies in aorta and carotid arteries. *Physiology Journal*, 2014:142421, 2014.

D. Bia Santana, R. L. Armentano, Y. Zócalo, H. Pérez Cámpos, E. I. Cabrera-Fischer, S. Graf, M. Saldias, W. Silva, and I. Alvarez. Functional properties of fresh and cryopreserved carotid and femoral arteries, and of venous and synthetic grafts: comparison with arteries from normotensive and hypertensive patients. *Cell Tissue Banking*, 8 (1):43–57, 2007.

P. J. Blanco and L. O. Müller. One-dimensional blood flow modeling in the cardiovascular system. from the conventional physiological setting to real-life hemodynamics. *Int. J. Num. Meth. Biomed. Eng.*, 41:e70020, 2025.

P. J. Blanco, M. R. Pivello, S. A. Urquiza, and R. A. Feijóo. On the potentialities of 3D-1D coupled models in hemodynamics simulations. *J. Biomech.*, 42(7):919–930, 2009.

P. J. Blanco, S. M. Watanabe, M. A. R. F. Passos, P. A. Lemos, and R. A. Feijóo. An anatomically detailed arterial network model for one-dimensional computational hemodynamics. *IEEE Trans. Biomed. Eng.*, 62(2):736–753, 2015.

P. J. Blanco, L. O. Müller, S. M. Watanabe, and R. A. Feijóo. On the anatomical definition of arterial networks in blood flow simulations: comparison of detailed and simplified models. *Biomech. Model Mechan.*, 19:663–1678, 2020.

C. G. Blomqvist and H. L. Stone. *Handbook of Physiology, The Cardiovascular System III. Chapter 28: Cardiovascular adjustments to gravitational stress*. NASA. Lyndon B. Johnson Space Center, Spacelab Life Sciences 1: Reprints of Background Life Sciences Publications, 1991.

E. Boileau, P. Nithiarasu, P. J. Blanco, L. O. Müller, F. E. Fossan, L. R. Hellevik, W. P. Donders, W. Huberts, M. Willemet, and J. Alastruey. A benchmark study of numerical schemes for one-dimensional arterial blood flow modelling. *Int. J. Num. Meth. Biomed. Engng.*, 31:e02732, 2015.

A. Bonfiglio, K. Leungchavaphongse, R. Repetto, and J. H. Siggers. Mathematical modeling of the circulation in the liver lobule. *J. Biomech. Eng.*, 132(11):111011, 2010.

M. A. Branch, T. F. Coleman, and Y. Li. A subspace, interior, and conjugate gradient method for large-scale bound-constrained minimization problems. *SIAM J. Sci. Comput.*, 21(1):1–23, 1999.

A. Bressan. *Hyperbolic systems of conservation laws: the one-dimensional Cauchy problem*. Oxford University Press, 2000.

J. Britton and Y. Xing. Well-balanced discontinuous Galerkin methods for the one-dimensional blood flow through arteries model with man-at-eternal-rest and living-man equilibria. *Comput. Fluids*, 203:104493, 2020.

B. S. Brook, S. A. E. G. Falle, and T. J. Pedley. Numerical solutions for unsteady gravity-driven flows in collapsible tubes: evolution and roll-wave instability of a steady state. *J. Fluid Mech.*, 396:223–256, 1999.

A. C. Burton. Relation of structure to function of the tissues of the wall of blood vessels. *Physiol. Rev.*, 34(4): 619–642, 1954.

H. T. Caddy, L. J. Kelsey, L. P. Parker, Green D. J., and Doyle B. J. Modelling large scale artery haemodynamics from the heart to the eye in response to simulated microgravity. *npj Microgravity*, 10(7), 2024.

A. Canestrelli, A. Siviglia, M. Dumbser, and E. F. Toro. Well-balanced high-order centred schemes for non-conservative hyperbolic systems. Applications to shallow water equations with fixed and mobile bed. *Adv. Water Resour.*, 32(6)(6):834–844, 2009.

S. Canić, J. Tambaca, G. Guidoboni, A. Mikelic, C. J. Hartley, and D. Rosenstrauch. Modeling viscoelastic behavior of arterial walls and their interaction with pulsatile blood flow. *SIAM J. Appl. Math.*, 67(1):164–193, 2006.

C. G. Caro, T. J. Pedley, R. C. Schroter, and W. A. Seed. *The mechanics of the circulation*. Cambridge university press, 2012.

M. Castro, J. M. Gallardo, J. A. López-GarcÍa, and C. Parés. Well-balanced high order extensions of Godunov method for linear balance laws. *SIAM J. Numer. Anal.*, 46(2):1012–1039, 2008.

M. J. Castro and C. Parés. Well-balanced high-order finite volume methods for systems of balance laws. *J. Sci. Comput.*, 82(2):48, 2020.

M. J. Castro Díaz, T. Chacón Rebollo, E. D. Fernández-Nieto, and C. Parés. On well-balanced finite volume methods for nonconservative nonhomogeneous hyperbolic systems. *SIAM J. Sci. Comput.*, 29(3):1093–1126, 2007.

C. Cattaneo. A form of heat-conduction equations which eliminates the paradox of instantaneous propagation. *C.R. Acad. Sci.*, 247:431, 1958.

G. N. Cattermole, P. Y. M. Leung, G. Y. L. Ho, P. W. S. Lau, C. P. Y. Chan, S. S. W. Chan, and et al. The normal ranges of cardiovascular parameters measured using the ultrasonic cardiac output monitor. *Physiol. Rep.*, 5: e13195, 2017.

M. Celant, E. F. Toro, and L. O. Müller. Total effective vascular compliance of a global mathematical model for the cardiovascular system. *Symmetry*, 13:1858, 2021.

T. Chacón Rebollo, A. Domınguez Delgado, and E. D. Fernández Nieto. A family of stable numerical solvers for the shallow water equations with source terms. *Comput. Method. Appl. M.*, 192(1-2):203–225, 2003.

P. Chandrashekar and M. Zenk. Well-balanced nodal discontinuous Galerkin method for Euler equations with gravity. *J. Sci. Comput.*, 71(3):1062–1093, 2017.

S. Clain, S. Diot, and R. Loubère. A high-order finite volume method for systems of conservation laws-Multi-dimensional Optimal Order Detection (MOOD). *J. Comp. Phys.*, 230(10):4028–4050, 2011.

C. Colombo. Mathematical properties-preserving parameter estimation for a blood flow model using ovine and human in vitro data. Master's thesis, University of Trento, 2021.

United States Naval Reserve Council. Guide for the care and use of laboratory animals, 1996.

G. Dal Maso, P. G. Le Floch, and F. Murat. Definition and weak stability of nonconservative products. *J. Math. Pure Appl.*, 74(6):483–548, 1995.

O. Delestre and P.-Y. Lagrée. A well-balanced finite volume scheme for blood flow simulation. *Int. J. Numer. Meth. Fl.*, 72(2):177–205, 2013.

V. Desveaux, M. Zenk, C. Berthon, and C. Klingenberg. A well-balanced scheme to capture non-explicit steady states in the Euler equations with gravity. *Int. J. Num. Meth. Fl.*, 81(2):104–127, 2016.

F. Doepp, S. J. Schreiber, T. von Münster, J. Rademacher, and R. Klingebiel J. M. Valdueza. How does the blood leave the brain? A systematic ultrasound analysis of cerebral venous drainage patterns. *Neuroradiology*, 46: 565–570, 2004.

Z. Duanmu, W. Chen, H. Gao, X. Yang, X. Luo, and N. A. Hill. A one-dimensional hemodynamic model of the coronary arterial tree. *Front. Physiol.*, 10:853, 2019.

M. Dumbser, C. Enaux, and E. F. Toro. Finite volume schemes of very high order of accuracy for stiff hyperbolic balance laws. *J. Comput. Phys.*, 227:3971–4001, 2008.

V. G. Eck, J. Sturdy, and L. R. Hellevik. Effects of arterial wall models and measurement uncertainties on cardiovascular model predictions. *J. Biomech*, 50:188–194, 2017.

H. Edgell, A. D. Robertson, and R. L. Hughson. Hemodynamics and brain blood flow during posture change in younger women and postmenopausal women compared with age-matched men. *J. Appl. Physiol.*, 112:1482–1493, 2012.

D. H. Evans. On the measurement of the mean velocity of blood flow over the cardiac cycle using Doppler ultrasound. *Ultrasound Med. Biol.*, 11:735–741, 1985.

C. Finucane, V.K. van Wijnen, C.W. Fan, C. Soraghan, L. Byrne, B. E. Westerhof, R. Freeman, A. Fedorowski, M. P. M. Harms, W. Wieling, and R. Kenny. A practical guide to active stand testing and analysis using continuous beat-to-beat non-invasive blood pressure monitoring. *Clin. Auton. Res.*, 29:427–441, 2019.

J. Flores, J. Alastuey, and E. Corvera Poiré. A novel analytical approach to pulsatile blood flow in the arterial network. *Ann. Biomed. Eng.*, 44(10):3047–3068, 2016.

M. Fois, S. V. Maule, M. Giudici, M. Valente, L. Ridolfi, and S. Scarsoglio. Cardiovascular response to posture changes: Multiscale modeling and in vivo validation during head-up tilt. *Front. Physiol.*, 13:826989, 2022.

M. D. Ford, N. Alperin, S. H. Lee, D. W. Holdsworth, and D. A. Steinman. Characterization of volumetric flow rate waveforms in the normal internal carotid and vertebral arteries. *Physiol. Meas.*, 26:477–488, 2005.

L. Formaggia, D. Lamponi, and A. Quarteroni. One-dimensional models for blood flow in arteries. *J. Eng. Math.*, 47(3):251–276, 2003.

L. Formaggia, A. Quarteroni, and A. Veneziani. *Cardiovascular Mathematics. Modeling and simulation of the circulatory system*. Springer, 2009.

M. Fudim, P. P. Ponikowski, D. Burkhoff, M. E. Dunlap, P. A. Sobotka, J. Molinger, M. R. Patel, G. M. Felker, A. F. Hernandez, S. E. Litwin, B. A. Borlaug, A. Bapna, H. Sievert, V. Y. Reddy, Z. J. Engelman, and S. J. Shah. Splanchnic nerve modulation in heart failure: Mechanistic overview, initial clinical experience, and safety considerations. *Eur. J. Heart. Fail.*, 23(7):1076–1084, 2021.

Y. C. Fung. *Biomechanics. Circulation*. Springer, 1997.

E. Gaburro, M. J. Castro, and M. Dumbser. Well-balanced Arbitrary-Lagrangian-Eulerian finite volume schemes on moving nonconforming meshes for the Euler equations of gas dynamics with gravity. *Mon. Not. R. Astro. Soc.*, 477(2):2251–2275, 2018.

Z. K. Garrett, J. Pearson, and A. W. Subudhi. Postural effects on cerebral blood flow and autoregulation. *Physiol. Rep.*, 5(4):e13150, 2017.

D. A. Gerlach, J. Manuel, A. Hoff, H. Kronsbein, F. Hoffmann, K. Heusser, H. Ehmke, J. Jordan, J. Tank, and F. Beissner. Medullary and hypothalamic functional magnetic imaging during acute hypoxia in tracing human peripheral chemoreflex responses. *Hypertension*, 77(4):1372 – 1382, 2021.

B. Ghitti, C. Berthon, M. H. Le, and E. F Toro. A fully well-balanced scheme for the 1D blood flow equations with friction source term. *J. Comput. Phys.*, 421:109750, 2020.

I. Gómez-Bueno, M. J. Castro, and C. Parés. High-order well-balanced methods for systems of balance laws: a control-based approach. *Appl. Math. Comput.*, 394:125820, 2021.

L. Gosse. A well-balanced flux-vector splitting scheme designed for hyperbolic systems of conservation laws with source terms. *Comput. Math. Appl.*, 39(9-10):135–159, 2000.

N. Goswami, A. P. Blaber, H. Hinghofer-Szalkay, and V. A. Convertino. Lower body negative pressure: Physiological effects, applications, and implementation. *Physiol. Rev.*, 99(1):807–851, 2019.

N. Goswami, A. P. Blaber, G. Valenti, H. Hinghofer-Szalkay, J. Evans, D. M. Bailey, J. Vernikos, A. Choukér, D. A. Green, O. White, J. J. W. A. van Loon, and V. A. Convertino. Gravity, microgravity and artificial gravity: Physiological effects, implementation and applications. *Physiol. Rev.*, 2025.

J. M. Greenberg, A. Y. Leroux, R. Baraille, and A. Noussair. Analysis and approximation of conservation laws with source terms. *SIAM J. Numer. Anal.*, 34(5):1980–2007, 1997.

S. Grillner, J. Nilsson, and A. Thorstensson. Intra-abdominal pressure changes during natural movements in man. *Acta Physiol. Scand.*, 103(3):275–283, 1978.

L. Grosheintz-Laval and R. Käppeli. High-order well-balanced finite volume schemes for the Euler equations with gravitation. *J. Comput. Phys.*, 378:324–343, 2019.

E. Guerrero Fernandez, M. J. Castro Diaz, and T. Morales de Luna. A second-order well-balanced finite volume scheme for the multilayer shallow water model with variable density. *Mathematics*, 8(5):848, 2020.

E. Guerrero Fernández, M.J. Castro Díaz, M. Dumbser, and T. Morales de Luna. An arbitrary high order well-balanced ADER-DG numerical scheme for the multilayer shallow-water model with variable density. *J. Sci. Comp.*, 90(1):52, 2022.

E. Guerrero Fernández, C. Escalante, and M. J. Castro Díaz. Well-balanced high-order discontinuous Galerkin methods for systems of balance laws. *Mathematics*, 10(1):15, 2022.

A. Harten. ENO schemes with subcell resolution. *J. Comp. Phys.*, 83(1):148–184, 1989.

T. Heldt, E. B. Shim, R. D. Kamm, and R. G. Mark. Computational modeling of cardiovascular response to orthostatic stress. *J. Appl. Physiol.*, 92:1239–1254, 2002.

HeMoLab. ADAN-WEB application. `http://hemolab.lncc.br/adan-web`, 2013.

H. Hinghofer-Szalkay. Gravity, the hydrostatic indifference concept and the cardiovascular system. *Eur. J. Appl. Physiol.*, 111:163–174, 2011.

P. Holmlund, E. Johansson, S. Qvarlander, A. Wåhlin, K. Ambarki, L.-O. D. Koskinen, J. Malm, and A. Eklund. Human jugular vein collapse in the upright posture: implications for postural intracranial pressure regulation. *Fluids Barriers CNS*, 14:17, 2017.

T. D. Homan, S. J. Bordes, and E. Cichowski. *Physiology, Pulse Pressure*. StatPearls Publishing, 2023.

T. J. R. Hughes and J. Lubliner. On the one dimensional theory of blood flow in the larger vessels. *Math. Biosci.*, 18:161–170, 1973.

W. N. Kapoor, M. A. Smith, and N. L. Miller. Upright tilt testing in evaluating syncope: a comprehensive literature review. *Am. J. Med.*, 97(1):78–88, 1994.

R. Käppeli and S. Mishra. Well-balanced schemes for the Euler equations with gravitation. *J. Comput. Phys.*, 259: 199–219, 2014.

R. E. Klabunde. *Cardiovascular physiology concepts*. Wolters Kluwer, 3rd edition, 2021.

H. J. Koubenec, W.D. Risch, and O.H. Gauer. Effective compliance of the circulation in the upright sitting posture. *Pflugers Arch.*, 374(2):121–124, 1978.

E. M. T. Lau, L. Godinas, O. Sitbon, D. Montani, L. Savale, X. Jaïs, and et al. Resting pulmonary artery pressure of 21–24 mmhg predicts abnormal exercise haemodynamics. *Pulm. Vasc. Dis.*, 47:1436–1444, 2016.

J. R. Levick. *An Introduction to Cardiovascular Physiology*. Hodder Arnold, 2009.

G. Li, O. Delestre, and L. Yuan. Well-balanced discontinuous Galerkin method and finite volume WENO scheme based on hydrostatic reconstruction for blood flow model in arteries. *Int. J. Numer. Meth. Fl.*, 86(7):491–508, 2018.

S. Li, P. R. Hoskins, T. Anderson, and W. N. McDicken. Measurement of mean velocity during pulsatile flow using time-averaged maximum frequency of Doppler ultrasound waveforms. *Ultrasound Med. Biol.*, 19(2):105–113, 1993.

F. Liang, D. Guan, and J. Alastruey. Determinant factors for arterial hemodynamics in hypertension: theoretical insights from a computational model-based study. *J. Biomech. Eng.*, 140(3):01, 2018.

X.-D. Liu, S. Osher, and T. Chan. Weighted essentially non-oscillatory schemes. *J. Comput. Phys.*, 115(1):200–212, 1994.

F. H. Martini, J. L. Nath, and E. F. Bartholomew. *Fundamentals of anatomy and physiology*. Pearson Education, Inc., 9th edition, 2012.

C. M. McEniery, Yasmin, I. R. Hall, A. Qasem, I. B. Wilkinson, J. R. Cockcroft, and ACCT Investigators. Normal vascular aging: Differential effects on wave reflection and aortic pulse wave velocity: The anglo-cardiff collaborative trial (acct). *J. Am. Coll. Cardiol.*, 46:1753–1760, 2005.

F. M. Melchior, R. S. Srinivasan, and J. B. Charles. Mathematical modeling of human cardiovascular system for simulation of orthostatic response. *Am. J. Physiol.*, 262(6 Part 2):H1920–H1933, 1992.

G. S. Mintz, M. N. Kotler, W. R. Parry, A. S. Iskandrian, and S. A. Kane. Real-time inferior vena caval ultrasonography: normal and abnormal findings and its use in assessing right-heart function. *Circulation*, 64(5):1018–1025, 1981.

S. Møller, A. Nørgaard, J. H. Henriksen, E. Frandsen, and F. Bendtsen. Effects of tilting on central hemodynamics and homeostatic mechanisms in cirrosis. *Hepatology*, 40(4):811–819, 2004.

E. M. Moncur, L. D'Antona, A. L. Peters, G. Favarato, S. Thompson, C. Vicedo, L. Thorne, L. D. Watkins, B. L. Dayc, A. K. Toma, and M. J. Bancroft. Ambulatory intracranial pressure in humans: Icp increases during movement between body positions. *Brain Spine*, 4:102771, 2024.

G. I. Montecinos and E. F. Toro. Reformulations for general advection–diffusion–reaction equations and locally implicit ader schemes. *J. Comput. Phys.*, 275:415–442, 2014.

G. I. Montecinos, L. O. Müller, and E. F. Toro. Hyperbolic reformulation of a 1D viscoelastic blood flow model and ADER finite volume schemes. *J. Comput. Phys.*, 266:101–123, 2014.

G. I. Montecinos, E. F. Toro, and L. O. Müller. A generalized Riemann problem-based compact reconstruction method for finite volume schemes. *Comput. Fluids*, Submitted, 2025.

J. Murillo and P. Garcia-Navarro. A Roe type energy balanced solver for 1D arterial blood flow and transport. *Comput. Fluids*, 117:149–167, 2015.

J. Murillo and P. Garcia-Navarro. Numerical coupling of 0D and 1D models in networks of vessels including transonic flow conditions. Application to short-term transient and stationary hemodynamic simulation of postural changes. *Int. J. Numer. Method Biomed. Eng.*, 39(11):e3751, 2023.

J. Murillo, A. Navas-Mantilla, and P. Garcia-Navarro. Formulation of exactly balanced solvers for blood flow in elastic vessels and their application to collapsed states. *Comput. Fluids*, 186:74–98, 2019.

J. Mynard, M. Davidson, D. Penny, and J. Smolich. Scalability and in vivo validation of a multiscale numerical model of the left coronary circulation. *Am. J. Physiol. Heart Circ. Physiol.*, 306:H517–H528, 2014.

J. P. Mynard and J. J. Smolich. One-dimensional haemodynamic modeling and wave dynamics in the entire adult circulation. *Ann. Biomed. Eng.*, 43(6):1443–1460, 2015.

J. P. Mynard, M. Davidson, D. Penny, and J. Smolich. A simple, versatile valve model for use in lumped parameter and one-dimensional cardiovascular models. *Int. J. Num. Meth. Biomed. Eng.*, 28:626–641, 2012.

L. O. Müller and P. J. Blanco. A high order approximation of hyperbolic conservation laws in networks: Application to one-dimensional blood flow. *J. Comp. Phys.*, 300:423–437, 2015.

L. O. Müller and E. F. Toro. Well-balanced high-order solver for blood flow in networks of vessels with variable properties. *Int. J. Numer. Meth. Biomed. Engng.*, 29:1388–1411, 2013.

L. O. Müller and E. F. Toro. A global multiscale mathematical model for the human circulation with emphasis on the venous system. *Int. J. Numer. Methods Biomed. Eng.*, 30(7):681–725, 2014.

L. O. Müller, P. J. Blanco, S. M. Watanabe, and R. A. Feijóo. A high-order local time stepping finite volume solver for one-dimensional blood flow simulations: application to the ADAN model. *Int. J. Numer. Meth. Biomed. Engng.*, 32(10):e02761, 2016.

L. O. Müller, G. Leugering, and P. J. Blanco. Consistent treatment of viscoelastic effects at junctions in one-dimensional blood flow models. *J. Comput. Phys.*, 314:167–193, 2016.

L. O. Müller, S. M. Watanabe, E. F. Toro, R. A. Feijóo, and P. J. Blanco. An anatomically detailed arterial-venous network model. Cerebral and coronary circulation. *Front. Physiol.*, 14:1162391, 2023.

N. Nasr, M. Czosnyka, A. Pavy-Le Traon, M. A. Custaud, X. Liu, G. V. Varsos, and V. Larrue. Baroreflex and cerebral autoregulation are inversely correlated. *Circulation*, 78(10):2460–2467, 2014.

J. Nocedal and S. J. Wright. *Numerical Optimization*. Springer, 1999.

S. Noelle, N. Pankratz, G. Puppo, and J. R. Natvig. Well-balanced finite volume schemes of arbitrary order of accuracy for shallow water flows. *J. Comput. Phys.*, 213(2):474–499, 2006.

S. Ogoh, K. Sato, K. Okazaki, T. Miyamoto, A. Hirasawa, T. Sadamoto, and M. Shibasaki. Blood flow in internal carotid and vertebral arteries during graded lower body negative pressure in humans. *Exp. Physiol.*, 100(3): 259–266, 2015.

M. Olufsen, H. Tran, and J. Ottesen. Modeling cerebral blood flow control during posture change from sitting to standing. *CVET*, 4, 2004.

C. Parés and C. Parés-Pulido. Well-balanced high-order finite difference methods for systems of balance laws. *J. Comput. Phys.*, 425:109880, 2021.

C. Parés. Numerical methods for nonconservative hyperbolic systems: a theoretical framework. *SIAM J. Numer. Anal.*, 44(1):300–321, 2006.

T. J. Pedley, B. S. Brook, and R. S. Seymour. Blood pressure and flow rate in the giraffe jugular vein. *Philos. Trans. R. Soc. London, Ser. B*, 351(1342):855–866, 1996.

R. N. Pittman. *Regulation of Tissue Oxygenation*. Morgan and Claypool Life Sciences, 2011.

G. Pocock, C. D. Richards, and D. A. Richards. *Human Physiology*. Oxford University Press, 5th edition, 2017.

A. Quarteroni. *Modellistica numerica per problemi differenziali*. Springer, 2012.

A. Quarteroni, M. Tuveri, and A. Veneziani. Computational vascular fluid dynamics: problems, models and methods. *Comput. Visualization Sci.*, 2:163–197, 2000.

A. Quarteroni, A. Manzoni, and C. Vergara. The cardiovascular system: Mathematical modeling, numerical algorithms, clinical applications. *Acta Numer.*, 26:365–590, 2017.

J. D. Raffetto, X. Qiao, K. G. Beauregard, A. F. Tanbe, A. Kumar, V. Mam, and R. A. Khalil. Functional adaptation of venous smooth muscle response to vasoconstriction in proximal, distal, and varix segments of varicose veins. *J. Vasc. Surg.*, 51(4):962–971, 2010.

P. Reymond, F. Merenda, F. Perren, D. Rüfenacht, and N. Stergiopulos. Validation of a one-dimensional model of the systemic arterial tree. *Am. J. Physiol. Heart Circ. Physiol.*, 297(1):H208–H222, 2009.

D. W. Robertson, I. Biaggioni, G. Burnstock, P. Low, and J. F. R. Paton. *Primer on the Autonomic Nervous System.* Academic Press, 3rd edition, 2012.

K. Sagawa, H. Suga, A. A. Shoukas, and K. M. Bakalar. End-systolic pressure/volume ratio: A new index of ventricular contractility. *Am. J. Cardiol.*, 40:748–753, 1977.

A. F. Sagirov, T. V. Sergeev, A. V. Shabrov, A. Y. Yurov, N. L. Guseva, and E. A. Agapova. Postural influence on intracranial fluid dynamics: an overview. *J. Physiol. Anthropol.*, 42(5):1–13, 2023.

S. Sakamoto, S. Takahashi, A. U. Coskun, M. I. Papafaklis, A. Takahashi, S. Saito, and et al. Relation of distribution of coronary blood flow volume to coronary artery dominance. *Am. J. Cardiol.*, 111:1420–1424, 2013.

K. Sato, J. P. Fisher, T. Seifert, M. Overgaard, N. H. Secher, and S. Ogoh. Blood flow in internal carotid and vertebral arteries during orthostatic stress. *Exp. Physiol.*, 97(12):1272–1280, 2012.

H. Saxton, T. Schenkel, I. Halliday, and X. Xu. Personalised parameter estimation of the cardiovascular system: Leveraging data assimilation and sensitivity analysis. *J. Comput. Sci.*, 74:102158, 2023.

I. Sazonov and P. Nithiarasu. A novel, fft-based one-dimensional blood flow solution method for arterial network. *Biomech. Model. Mechanobiol.*, 18:1311–1334, 2019.

Y. Shi, P. Lawford, and R. Hose. Review of zero-D and 1-D models of blood flow in the cardiovascular system. *Biomed. Eng. Online*, 33, 2011.

A. Siviglia and M. Toffolon. Steady analysis of transcritical flows in collapsible tubes with discontinuous mechanical properties: implications for arteries and veins. *J. Fluid Mech.*, 736:195–215, 2013.

A. Siviglia, D. Vanzo, and E. F. Toro. A splitting scheme for the coupled Saint-Venant-Exner model. *Adv. Water Resour.*, 159:104062, 2022.

H. Smith, J. E. Bush, V. T. Wiedmeier, and F. E. Tristani. Application of impedance cardiography to the study of postural stress in the human. *J. Appl. Physiol.*, pages 29–133, 1970.

J. J. Smith, C. M. Porth, and M. Erickson. Hemodynamic response to the upright posture. *J. Clin. Pharmacol.*, 34: 375–386, 1994.

M. F. Snyder and V. C. Rideout. Computer simulation studies of the venous circulation. *IEEE Trans. Biomed. Eng.*, 16(4):325–334, 1969.

A. Spilimbergo, E. F. Toro, and L. O. Müller. One-dimensional blood flow with discontinuous properties and transport: mathematical analysis and numerical schemes. *Commun. Comput. Phys.*, 29(3):649–697, 2021.

D. A. Steinman. Image-based computational fluid dynamics modeling in realistic arterial geometries. *Ann. Biomed. Eng.*, 30:483–497, 2002.

Y. Sun, M. Beshara, R. Lucariello, and S. Chiaramida. A comprehensive model for right-left heart interaction under the influence of pericardium and baroreflex. *Am. J. Physiol.*, 272:H1499–H1515, 1997.

C. A. Taylor and C. A. Figueroa. Patient-specific modeling of cardiovascular mechanics. *Annu. Rev. Biomed. Eng.*, 11:109–134, 2009.

Y. Teuschl, A. Fanciulli, A. Pavy-Le Traon, M. Habek, R. D. Thijs, A. R. Pavelic, and W. Struhal. Is the NASA Lean Test a suitable tool to diagnose cardiovascular autonomic disorders? *Clin. Auton. Res.*, 35:529–531, 2025.

E. F. Toro. *Riemann Solvers and Numerical Methods for Fluid Dynamics*. Springer, 2009.

E. F. Toro and A. Siviglia. Flow in collapsible tubes with discontinuous mechanical properties: mathematical model and exact solutions. *Commun. Comput. Phys.*, 13(2):361–385, 2013.

K. Toska and L. Walløe. Dynamic time course of hemodynamic responses after passive head-up tilt and tilt back to supine position. *J. Appl. Physiol.*, 92:1671–1676, 2002.

A. Pavy-Le Traon, M. Heer, M. V. Narici, J. Rittweger, and J. Vernikos. From space to earth: advances in human physiology from 20 years of bed rest studies (1986–2006). *Eur. J. Appl. Physiol.*, 101:143–194, 2007.

M. Ursino and C. Lodi. A simple mathematical model of the interaction between intracranial pressure and cerebral hemodynamics. *J. Appl. Physiol.*, 82, 1997.

M. Ursino and E. Magosso. Short-term autonomic control of cardiovascular function: a mini-review with the help of mathematical models. *J. Integr. Neurosci.*, 2(2):219–247, 2003.

D. Valdez-Jasso, D. Bia, Y. Zócalo, R. L. Armentano, M. A. Haider, and M. S. Olufsen. Linear and nonlinear viscoelastic modeling of aorta and carotid pressure–area dynamics under in vivo and ex vivo conditions. *Ann. Biomed. Eng.*, 39(5):1438–1456, 2011.

M. van Assen, A. Tariq, A. C. Razavi, C. Yang, I. Banerjee, and C. N. De Cecco. Fusion modeling: Combining clinical and imaging data to advance cardiac care. *Circulation: Cardiovascular Imaging*, 16(12):e014533, 2023.

C. L. M. C. van Campen, F. W. A. Verheugt, and F. C. Visser. Cerebral blood flow changes during tilt table testing in healthy volunteers, as assessed by doppler imaging of the carotid and vertebral arteries. *Clin. Neurophysiol. Pract.*, 3:91–95, 2018.

K. van Heusden, J. Gisolf, W. J. Stok, S. Dijkstra, and J. M. Karemaker. Mathematical modeling of gravitational effects on the circulation: importance of the time course of venous pooling and blood volume changes in the lungs. *Am. J. Physiol. Heart Circ. Physiol.*, 291:H2152–H2165, 2006.

B. van Leer. Towards the ultimate conservative difference scheme. V. A second-order sequel to Godunov's method. *J. Comp. Phys.*, 32(1), 1979.

P. Vijayalakshmi, S. Veliath, and M. Mohan. Effect of head-up tilt on cardiovascular responses in normal young volunteers. *Indian J. Physiol. Pharmacol.*, pages 467–472, 2000.

Y. Wang, R. J. Marshall, and J. T. Shepherd. The effect of changes in posture and of graded exercise on stroke volume in man. *J. Clin. Invest.*, 39(7):1051–1061, 1960.

E. P. Widmaier, H. Raff, and K. T. Strang. *Vander's Human Physiology*. McGraw-Hill Education, 14th edition, 2016.

N. Xiao, J. Alastruey, and C. Figueroa. A systematic comparison between 1-D and 3-D hemodynamics in compliant arterial models. *Int. J. Num. Meth. Biomed. Engng.*, 30:204–231, 2014.

Q. Yong, L. Yang, A. Kardos, and Y. Zhao. Non-invasive cardiovascular and vital signs monitoring techniques: review, challenges, and perspectives. *Measurement*, 258, 2025.

A. Zaidi, D. Benitez, P. A. Gaydecki, A. Vohra, and A. P. Fitzpatrick. Haemodynamic effects of increasing angle of head up tilt. *Heart*, 83:181–184, 2000.

X. Zhang, S. Noda, R. Himeno, and H. Liu. Gravitational effects on global hemodynamics in different postures: A closed-loop multiscale mathematical analysis. *Acta Mech. Sin.*, 33(3):595–618, 2017.

A. Zingaro, C. Vergara, L. Dedé, F. Regazzoni, and A. Quarteroni. A comprehensive mathematical model for cardiac perfusion. *Sci. Rep.*, 13:14220, 2023.

Y. Zócalo, D. Bia, F. M. Pessana, and R. L. Armentano. Changes in vein dynamics ranging from low to high pressure levels as a determinant of the differences in vein adaptation to arterial hemodynamic conditions. *Artificial Organs*, 31(7):575–580, 2007.

Y. Zócalo, D. Bia, E. I. Cabrera-Fischer, S. Wray, C. Galli, and R. L. Armentano. Structural and functional properties of venous wall: Relationship between elastin, collagen, and smooth muscle components and viscoelastic properties. *ISRN Physiology*, 2013:906031, 2013.